UC Berkeley
UC Berkeley Electronic Theses and Dissertations

Title
Woven Crystalline Covalent Organic Frameworks

Permalink
https://escholarship.org/uc/item/0np1s62c

Author
Liu, Yuzhong

Publication Date
2018

Peer reviewed|Thesis/dissertation

Woven Crystalline Covalent Organic Frameworks

by

Yuzhong Liu

A dissertation submitted in partial satisfaction of the

requirements for the degree of

Doctor of Philosophy

in

Chemistry

in the

Graduate Division

of the

University of California, Berkeley

Committee in charge:
Professor Omar M. Yaghi, Chair
Professor Kenneth N. Raymond
Professor Jeffrey A. Reimer

Summer 2018

Abstract

Woven Crystalline Covalent Organic Frameworks

By

Yuzhong Liu

Doctor of Philosophy in Chemistry

University of California, Berkeley

Professor Omar M. Yaghi, Chair

Described in this dissertation is the designed synthesis and characterization of a new class of materials – woven crystalline covalent organic frameworks (COFs). Molecular building units are stitched together through strong bonds in a process termed reticular synthesis. In conjunction with metal-templated synthesis woven frameworks are obtained. The products of this reticulation are extended covalently linked one-dimensional (1D) organic molecules that mutually interweave at regular intervals to construct crystalline two- and three-dimensional (2D and 3D) architectures. The mechanical entanglement between the constituents (*i.e.* 1D chains) allows for large spatial deviations to take place without the breaking of covalent bonds, leading to unusual mechanical properties and ultimately to materials with exceptional resilience and dynamics.

In Chapter I, a general introduction of covalent organic frameworks (COFs) and their designed synthesis based on the fundamental concepts of reticular synthesis is given. Since the discovery of COFs in 2005, a plethora of COF structures with various structure types have been synthesized by reticulating judiciously selected building blocks of desirable connectivity and geometry. The structural tunability and crystallinity of COFs make them the ideal candidates for the synthetic realization of woven extended structures. The metal templation strategy, widely explored in the field of supramolecular chemistry, employs metal ions as templates to pre-organize organic linkers into desirable orientations, which can then be reticulated into woven extended frameworks. These metal ions also serve as the crossing points (points of registry) of the resultant woven threads, and upon demetaltion, the threads have high degrees of freedom to move about these points of registry without undoing the weaving.

Chapter II describes the implementation of the design strategy of COFs toward the successful synthesis of the first woven material, COF-505. A copper(I)-bisphenanthroline core, a well-established template in the field of supramolecular chemistry, was functionalized with aldehyde groups and used as a building block for COF synthesis. Specifically, the tetratopic and tetrahedrally-shaped complex was reacted with a linear ditopic benzidine (BZ) linker through reversible imine condensation to form a 3D crystalline framework, COF-505, of **dia** topology. The structure was determined with atomic precision, by a combined 3D electron diffraction tomography (3D-EDT) and powder X-ray diffraction (PXRD) approach. On a fundamental level, COF-505 is constructed from organic helices that are covalently linked within the thread, while neighboring helices are held woven with copper(I) ions serving as the points of registry. Upon

removal of these copper(I) templates, the threads are endowed with large degrees of freedom to move about the crossing points, which results in a ten-fold increase of elasticity, as observed by nanoindentation using atomic force microscopy (AFM). Owing to the entanglement of the threads, the underlying topology of the structure remains intact upon demetalation. Copper(I) ions can be added back to the demetalated material to recover the structure of the as-synthesized COF; the demelation and remetalation process can be performed in a reversible manner.

In Chapter III, the design principle of woven COFs expanded to structures with large guest accessible internal void space within the structure. It was speculated that this parameter determines the magnitude of the thread movement upon demetalation. The original COF-505 was found to have a two-fold interpenetrated and consequently dense structure. Since it was believed that this might restrict the dynamics of the threads, two strategies were devised to prevent the formation of interpenetration in derivative woven structures: (i) A shorter ditopic linker, *p*-phenylenediamine (PDA), was employed instead of BZ to yield COF-504. The decreased pore size of the structure has limited internal space thus preventing framework interpenetration. (ii) Alternatively a non-interpenetrated framework can be formed using BZ as the linker when a bulky anion (diphenylphosphinate) was employed during COF synthesis. Post-synthetic anion exchange with smaller BF_4^- counterions yielded COF-506, a non-interpenetrated analogue of COF-505. The porosity of the two frameworks was investigated by vapor and dye adsorption, which confirmed the guest accessibility of their interior. In COF-506, the member of the series with the largest guest accessible void space, demetalation was found to affect structural dynamics within the structure. Spatial dislocations of the threads within the demetalated COF-506 structure allow for uptake of dye molecules that exceed the pore size of its metalated counterpart.

As the crystallinity of COFs heavily relies on the full reversibility of bond formation during the solvothermal synthesis, COF formation conditions can be highly specific for one type of linkage, or even one particular framework. The development of solid-state anthracene photodimerization as a new linkage for COF synthesis is detailed in Chapter IV. The key feature of this strategy is to pre-organize photoreactive anthracene monomers in a face-to-face manner in the solid state. This arrangement allows for exclusively lateral [4 + 4] cycloaddition reactions in the solid state upon UV exposure to target single-crystal-to-single-crystal transformation through C-C bond formation. To employ this approach to the synthesis of woven COFs the copper(I)-bisphenanthroline core was functionalized with anthracene moieties that serve as points of extension. Various packing modes resulted from different crystallization conditions, however only the undesirable face-to-edge anthracene stacking was observed. Fluorine atoms were subsequently installed on the 1, 2, 3, and 4 positions of the anthracene units which effectively enhanced the cofacial interaction of neighboring anthracenes, but no reactivity towards dimerization was observed upon UV treatment. Further studies of the molecular analogue, 1,2,3,4-tetralfuoro-9-phenylanthracene, revealed that the dimerization was only observed in solution, but not in the solid state, which could be attributed to the large energy cost of phenyl rotation and movement upon formation of the C9-C10 bond. Future work should thus focus on the functionalization of the 2 position of anthracene which is remote from the reaction site for dimerization.

Chapter V focuses on the discovery of higher modes of entanglement beyond woven structures. By reacting the tetrahedral aldehyde-functionalized copper(I) bisphenanthroline complex with square planar 4',4''',4''''',4'''''''-(ethene-1,1,2,2-tetrayl)tetrakis(([1,1'-biphenyl]-4-amine)) linkers (TBPA), the first interlocking COF-500 was synthesized. COF-500 is comprised

of entangled 1D corner-sharing ladders and crystallized in a **pts** topology. Interlocking structures are fundamentally different from woven structures as their entanglement is based on closed rings which ensures that the entities remain entangled. Upon demetalation, the structure became less open, indicated by the decreased nitrogen sorption capacity. Elucidation of structural change accompanying this process is provided by solid-state photoluminescence measurement. Fluorescence of the material was turned on after demelataion and this can be attributed to restricted rotation of the phenyl rings of TBPA when the interlocked ladders move towards each other within the rigid ring systems. THF vapor adsorption studies highlight the dynamic behavior of these interlocked ladders as the demetalated material has a similar THF uptake with COF-500, in a manner that is analogues to swelling of polymers. A significant decrease of fluorescence response further confirms opening-up of demetalated structure in the presence of THF.

Finally, in Chapter VI, a library of woven topologies were identified. By translating the geometries into linear line segments (sticks) joined at corners in their optimal embeddings, 2D and 3D woven and polycatenated structures can be viewed as an extended family of molecular knots and links. Based on mathematical calculations, the most plausible topologies that can be woven were systematically enumerated. Ripe synthetic targets of 2D and 3D weavings and polycatenanes were also provided.

Table of Contents

Acknowledgements

To my grandmother and my parents

江南忆，最忆是杭州。

山寺月中寻桂子，郡亭枕上看潮头。

何日更重游！

——白居易《忆江南词三首》

Chapter I

Introduction to Woven Covalent Organic Frameworks

1.1 Covalent organic frameworks

Covalent organic frameworks (COFs) are a class of crystalline materials that are constructed by reticulating molecular organic building units through strong covalent bonds.[1] COFs are formed with full reversibility of bond formation, leading to the thermodynamic product of the reticulation.[2] The reversibility of the directional bonds in combination with the use of rigid organic building blocks allows for obtaining COFs in crystalline form which allows for the precise elucidation of their structures.

Weaving of threads has been the most commonly practiced approach to making fabric throughout human history. Learning how to weave long organic molecules in a similar manner would be an important step toward the synthesis of extended materials with exceptional mechanical properties. To implement the weaving design and introduce dynamics into otherwise rigid structures, lower-dimensionality objects (*e.g.* 1D threads, 1D ladders, 2D sheets, etc.) can be mechanically entangled through metal templation to construct 2D or 3D frameworks. The structural tunability and crystallinity of COFs make them the ideal candidates for the synthetic realization of woven extended structures. Functionalized metal complexes can be incorporated as building blocks during the framework construction and the crystallinity of the resulting frameworks provides a handle on structure elucidation with atomic precision to ensure the woven nature of the resulting materials.

In this chapter, COF design principles, along with linkages reported so far will be presented. Metal templated synthesis in discrete supramolecular systems will then be covered as a transition into the discussion of the application of the same template strategy to the synthesis of extended woven structures with unique dynamics and mechanical properties.

1.2 Design principles of COFs

The chemistry of linking rigid molecular building blocks by strong chemical bonds into highly ordered extended structures, reticular chemistry, has yielded new classes of materials including metal organic frameworks (MOFs)[3], and their organic counterpart, COFs[1,4]. The directionality of covalent bonds, particularly in COFs, provides a means of controlling the assembly of building units based on the geometry of the molecular building units.

In 2005 this design principle lead to the discovery of the first COFs.[5] COF-5, shown in Figure 1.1, is synthesized through the condensation reaction of a triangular-shaped linker, hexahydroxytriphenylene (HHTP), and linear phenyl diboronic acid (BDBA) to form cyclic five-membered boronic esters. The HHTP linker is designed by functionalizing the triphenylene core with six hydroxyl substituents. Two adjacent hydroxyl groups constitute a catechol group to be reacted with boronic acid. The triangular geometry of the linker remains unchanged during the COF synthesis as the overall boronic ester bond angle is 180° and is directional. As a result of

linking of triangles, COF-5 was crystallized as a 2D framework of **hcb** topology with hexagonal pores. The augmented topology illustration is shown here and figures below highlight the geometry of the vertices and how they relate to the designed synthesis of frameworks by reticular chemistry.
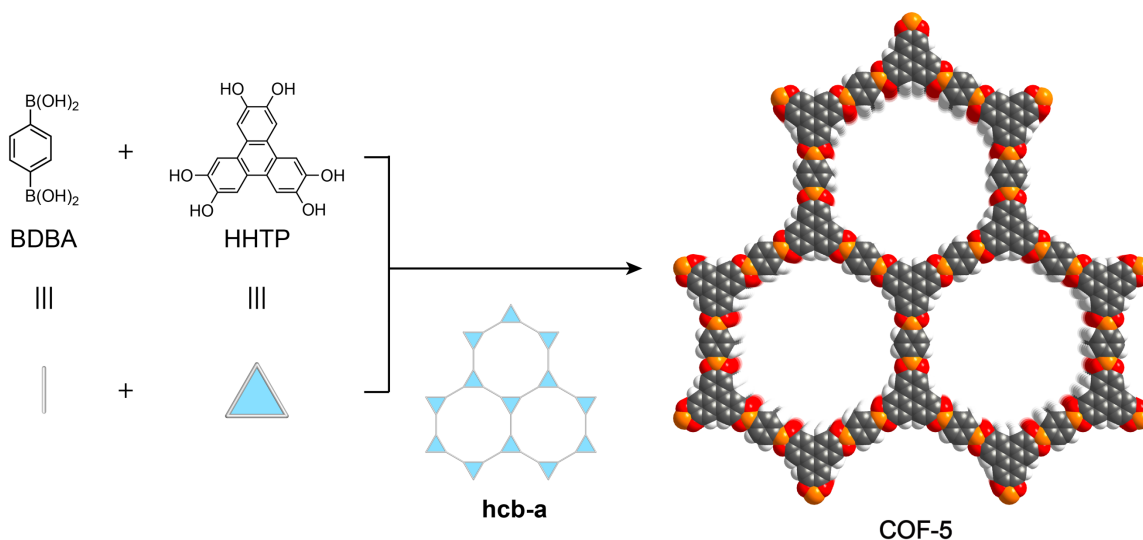
Figure 1.1. Structural representation of COF-5 of **hcb** topology (short for honeycomb). The framework is constructed through the condensation reaction of linear ditopic BDBA with trigonal tritopic HHTP.

When the same triangular HHTP linker is reticulated with a tetrahedral-shaped linker, TBPM, (boronic acid functionalized tetraphenylmethane) one of the first reported crystalline 3D COFs, COF-108,[6] is obtained. In this case there are two possible structure types that could result from the linking of these building units into an extended structure – **ctn** and **bor**. When no crystals suitable for single-crystal X-ray diffraction studies are obtained the structural solution for COFs relies on powder diffraction. To determine the topology of COF-108, calculated models based on the **bor** and **ctn** networks were constructed by placing the TBPM units at the tetrahedral nodes and the HHTP linkers at the triangular nodes of the tiling, followed by geometry optimization and energy minimization of the resulting structure. Comparison of the simulated PXRD patterns of the two models (**ctn** and **bor**) with the experimental data indicates that COF-108 crystallized in a **bor** net. This example highlights two important aspects of the reticular synthesis of COFs: (i) Possible structure types are predicted based on the principles of reticular chemistry (Here, the possible outcome of the structure type was narrowed down to two possibilities, **bor** and **ctn**); (ii) the crystallinity of the framework provides a useful handle for unambiguous structural determination.
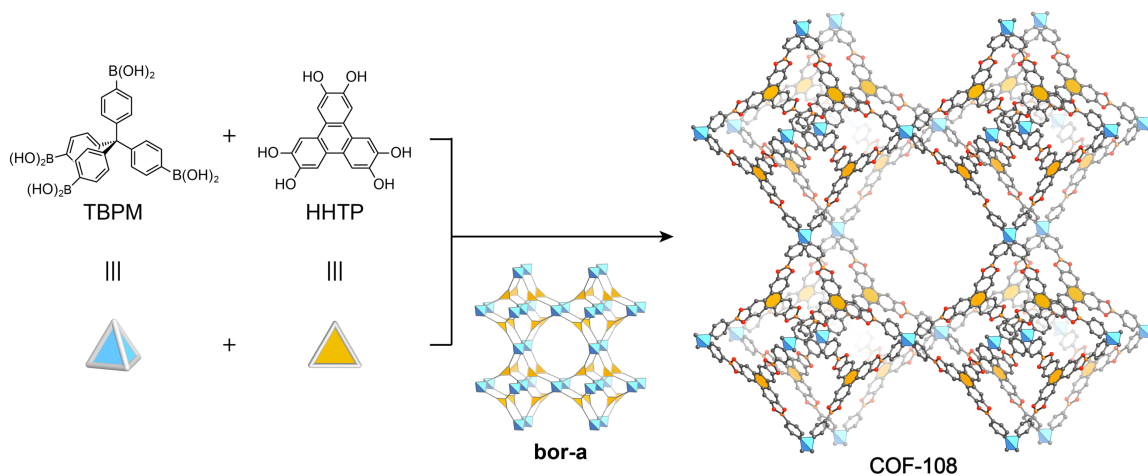
Figure 1.2. Framework structure of COF-108 with an underlying **bor** net (boracite).

In addition to the judicious choice of building blocks, the choice of reactions that can be used as linkages have also been explored. In the synthesis of COF-320 reversible imine formation, a well-established reaction in the context of dynamic covalent chemistry, was utilized..[7] Unlike the aforementioned boron-based linkages, imine bonds are stable to water at a neutral pH and the chemical stability of resulting frameworks is thus greatly improved. In COF-320 imine-functionalized tetraphenylmethane (TAM) was reacted with a linear ditopic aldehyde linker, BDA, to form a 3D **dia** (diamond) net. Here, the crystal size of the material was large enough for electron diffraction studies allowing for solving the structure unambiguously and with atomic resolution.
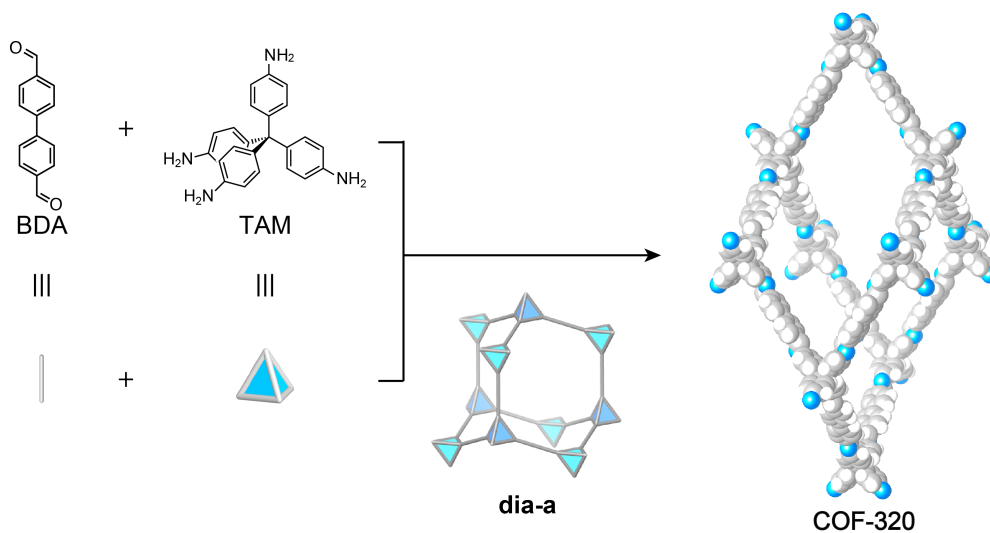
Figure 1.3. Synthetic scheme and single-crystal structure of COF-320, solved by electron diffraction of single crystals.

1.3 Linkages and their crystallization conditions

An important requirement in the context of the crystallization of COFs is that the chemical reactions involved in the framework formation have a high degree of reversibility under suitable

synthetic conditions. As such, self-correction mechanisms discovered in the realm of dynamic covalent chemistry[8] were found applicable and yield highly ordered and crystalline materials as the thermodynamically favorable product. The reactions used in the synthesis of COFs that are reported so far can be classified in terms of the linkages they form (Scheme 1.1): (i) B–O (boroxine,[5,9] boronate ester,[5,10] borosilicate,[11] and spiroborate[12]), (ii) C=N (imine,[13] hydrazone,[14] and squaraine[15]), (iii) $C=N_{(aromatic)}$ (triazine[16] and phenazine[17]), (iv) C=C (alkene[18]), (v) C–N (β-ketoenamine,[19] imide,[20] and amide[21]), (vi) B=N (borazine[22]) and (vii) N=N (azodioxy[23]).

The aforementioned boronate ester formation and B_3O_3 boroxine linkages formed by self-condensation of boronic acid were the first reactions used to make highly crystalline 2D and 3D COFs. In a sealed reaction vessel, a mixture of starting materials and appropriate solvent will be heated above the boiling point of H_2O. Since both reactions involve a dehydration step, the use of a closed reaction system keeps the H_2O formed upon reaction in the system thus maintaining reversible conditions critical for crystallite growth. Borosilicate COFs can be synthesized under similar reaction conditions. While COFs containing B-O bonds exhibit an excellent thermal stability, they are prone to hydrolysis and bases, due to the Lewis acidity of the boron centers in the structure.

Major efforts have since been dedicated to enhancing the chemical stability of the linkage and consequently of the resulting frameworks. First, imine linkages were developed for the synthesis of COFs in the presence of acetic acid as a catalyst. As a result, the chemical stability is greatly enhanced and imine COFs remain intact even in boiling water. Similar reactions between aldehyde and hydrazide groups yielded hydrazone-linked COFs in which the hydrogen-bonding interactions between the oxygen atoms in the alkoxyl chains and the hydrogens in the –CONH– units could further stabilize the framework structure. Additionally, reacting 2,4,6-trihydroxybenzene-1,3,5-tricarbaldehyde with aryl amines can form imine linkage, which tautomerize into a β-ketoenamine moiety which is again less prone to nucleophilic attacks.

Since crystalline frameworks are made under synthetic conditions that favor reversibility of the bond formation, as a general trend, structures yielded by using harsh conditions are often more chemically stable. Ring-fusing reactions between quinone and amine derivatives catalysed by acids can form phenazine-linked COFs where the backbone is highly conjugated and stable to various solvents and even to acids and bases. The self-condensation of aromatic nitriles synthesized at an elevated temperature of 400 °C in molten salts or at room temperature in the presence of a strong acid catalyst, such as trifluoromethyl sulfonic acid, form crystalline covalent triazine frameworks, which is one of the most stable linkages reported so far. Recently, a fully-conjugated conductive framework with C=C double bonds was synthesized through a cyano-assisted condensation reaction between aldehydes and cyano-functionalized methyl groups in the presence of NaOH.

By stitching rigid building blocks through strong directional bonds, the construction of architecturally stable frameworks has been realized in crystalline form. In such structures flexibility is restricted. To introduce dynamics into such otherwise rigid frameworks and thus generate materials with exceptional mechanical properties, supramolecular entanglement, in addition to covalent bonds, has been included as a part of the design strategy to build molecular weaving architectures fully described and characterized in this dissertation.

Scheme 1.1. Linkages that have been utilized to link building blocks into COF structures. The linkages have been divided into B–O, C=N, C=N$_{(Ar)}$, C–N, B=N, and C=C bond forming reactions.

B-O bond formation

boronate ester
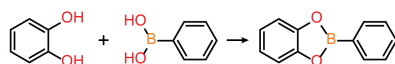
boroxine
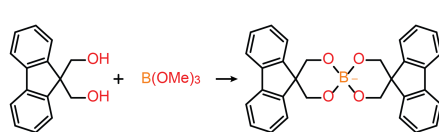
borate
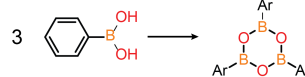
borosilicate
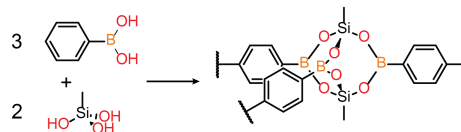
C=N bond formation

imine
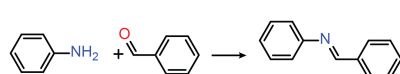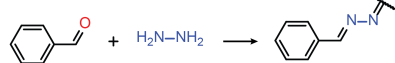
hydrazone
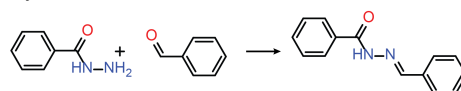
azine

squaraine
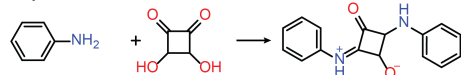
C=N$_{Ar}$ bond formation

triazine
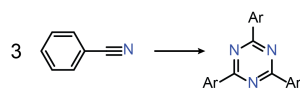
phenazine
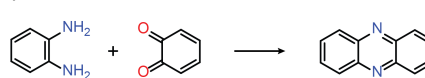
oxazole
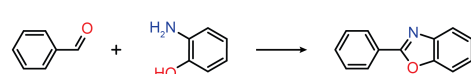
C-N bond formation

imide
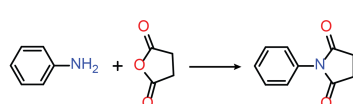
β-ketoenamine
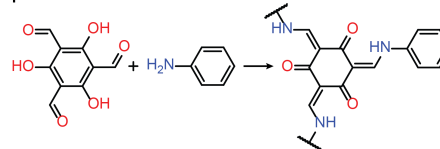
amide
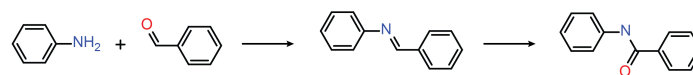
C=C bond formation

alkene
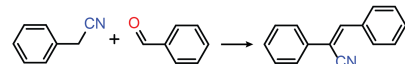
B=N bond formation

borazine

1.4 Molecular knots, links, and mechanical bond
1.4.1 Historical prospects

The designed synthesis of interlocking molecules (*e.g.* knots, catenanes and rotaxanes) is well documented in the chemical literature.[24–32] The first proof-of-concept work in the field was reported in 1960 with the successful synthesis of a [2]catenane by statistical interlocking of molecular macrocycles.[33] In 1964, the first directed synthesis of a catenane was demonstrated by introducing a covalent template to bring the two molecular components in place.[34] Upon subsequent cleavage of this covalent template, the catenated molecule was obtained in higher yields as compared to the previously reported statistical approach. However, both the early statistical and directed synthetic approaches to mechanically interlocked molecules suffered from low overall yields and/or lengthy synthetic procedures. Catenanes thus remained in the realm of laboratory curiosities rather than molecular constructs that could be practically exploited.

1.4.2 Metal-ion templated synthesis

The breakthrough in the field took place in 1983 when a metal-template approach was disclosed to construct higher-order supramolecular architectures.[35] This enabled catenanes to be made on a significant scale for the first time. In the synthesis, the metal complex orients the individual ligands to ensure spatial overlap to create crossing points (points of registry), which allows for efficient ring closure and the synthesis of entangled architectures in high yield. Here, the approach employed a tetrahedrally-coordinated Cu(I) complex with two hydroxy-functionalized 2,9-diphenyl-1,10-phenanthroline (dpp) ligands. The Cu(I) ion serves as the point of registry, and the ligands are positioned in an embracing fashion to facilitate efficient formation of the entanglement. Subsequent ring closing Williamson ether macrocyclization generated the [2]catenand in 42% yield. The Cu(I) ions could be removed quantitatively from the catenand with potassium cyanide to afford the metal-free [2]catenane (Figure 1.4).
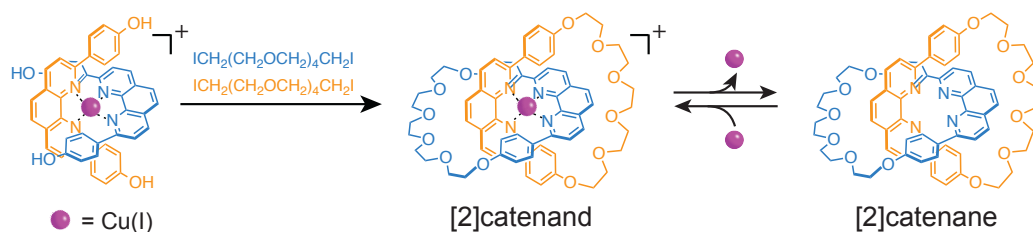
Figure 1.4. Cu(I)-bisphenanthroline-templated synthesis of a [2]catenane.

Developments in dynamic covalent bond forming reactions were also exploited towards the synthesis of interlocked molecules. Molecular Borromean rings were stitched together through the one-pot reaction of six dialdehydes, six diamines, and six Zn(II) ions using reversible imine formation under thermodynamic control (Figure 1.5).[26] The Borromean ring topology was confirmed by X-ray crystallography, which further corroborated that the combination of π-π stacking interactions and metal coordination likely directed the assembly process. The Zn(II) templates could be removed from the structure by reduction of the imine bonds with sodium borohydride (NaBH$_4$), followed by treatment with ethylenediaminetetraacetic acid (EDTA) to afford the demetalated Borromean rings.[36]
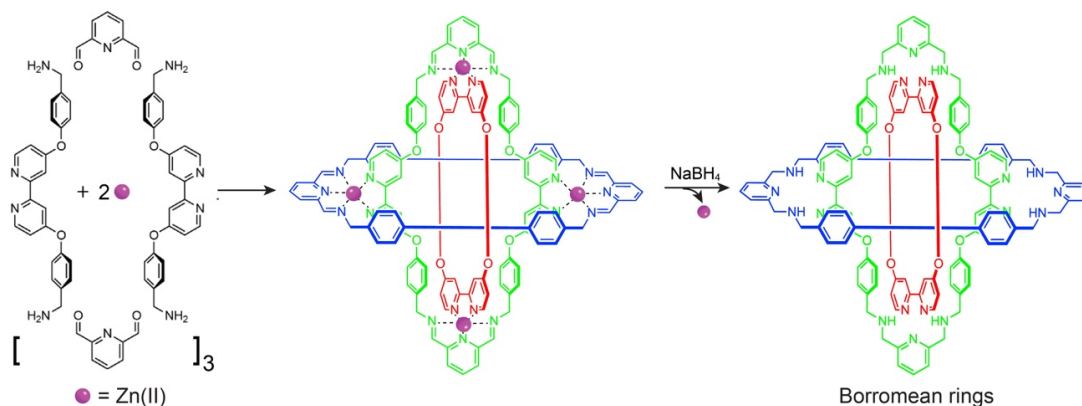
Figure 1.5. Synthetic route for the formation of molecular Borromean rings. Atoms in red and blue rings are omitted for clarity; only the green ring contains all the atoms and bonds present in the macrocycles.

In addition to higher yields and shorter synthetic routes associated with metal templated synthesis, specific orientation of the ligands due to complexation enables the rational design of synthetic pathways to more complex topologies. As a result the ability of synthetic chemists to construct increasingly complex molecular structures has since then progressed remarkably resulting in a plethora of highly sophisticated supramolecular architectures.[2-9]

1.4.3 Mechanical entanglement

As the mechanical bond is not shared between atoms, it only becomes relevant when talking about the spatial arrangement of individual molecular entities. It should be noted that these entangled entities are held together mechanically, not chemically, which allows for large-amplitude molecular motion of the individual units in respect to each other without the breaking of covanelt bonds. While benefiting from the degrees of freedom, separate parts are still refrained within certain boundaries (*e.g.* the size of the ring in catenanes, the length of the chains in rotaxanes, etc.) to ensure that the supramolecular constructs remain entangled. On the molecular level, this approach has proved fruitful for the development of molecular machines[37,38], muscles[39], and rotors[40,41] where during a switching process, only weak non-covalent bonds are broken and reformed again in a fully reversible and highly controllable fashion.

The first and most simple molecular switch that was studied was a catenane containing two different interlocking rings (Figure 1.6).[42] One of the rings possesses a bidentate chelating ligand, dpp, while the other one contains a dpp and a tridentate 2,2':6',2"-terpyridine (tpy) ligand. As a result, a metal ion can be coordinated tetrahedrally with two dpp ligand or in a 5-coordinate octahedral distorted geometry with one dpp and one tpy ligand. During synthesis, the Cu(I) ion is coordinated to two dpp ligands. Electrochemical oxidation of Cu(I) to Cu(II) leads to the formation of an unstable 4-coordinate Cu(II) intermediate which rearranges to a 5-coordinate Cu(II) species, in which the metal is ligating to one dpp and one tpy ligand, following circumrotation of one ring relative to the other. The original catenate can be recovered upon reduction of Cu(II) to Cu(I). Because of the mechanical entanglement between the two entities, they can be switched repeatedly and reversibly.
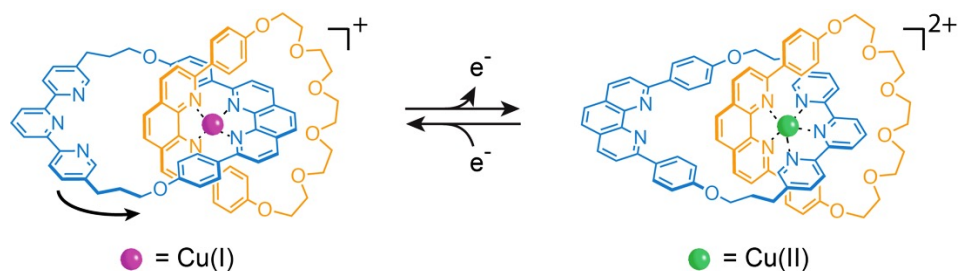
Figure 1.6. Electrochemically induced molecular ring rearrangements based on oxidation and reduction of the Cu(I)/Cu(II) redox couple.

A similar concept was adopted to expand and contract the molecular length of a [c2]daisy chain (Figure 1.7), designed to mimic the motion of muscles.[43] The rings of the daisy chain contain bidentate dpp ligands, while the corresponding threads bear bidentate dpp and tridentate tpy ligands. The pairing of ring and thread ligands around different templates affords different coordination geometries determined by the valency of the transition metal. The phenanthroline ligands of each component pair up tetrahedrally around Cu(I) ions. Upon removal of Cu(I) and addition of Zn(II) ions, which prefer a pentacoordinate complex, lead to a pentacoordinate complex involving dpp and tpy ligands and thus to a contracted version of this structure. The reversible contraction and expansion of the suparmoecular construct imitates the behavior of sarcomere (muscle fibril) and therefore is termed a 'molecular muscle'.
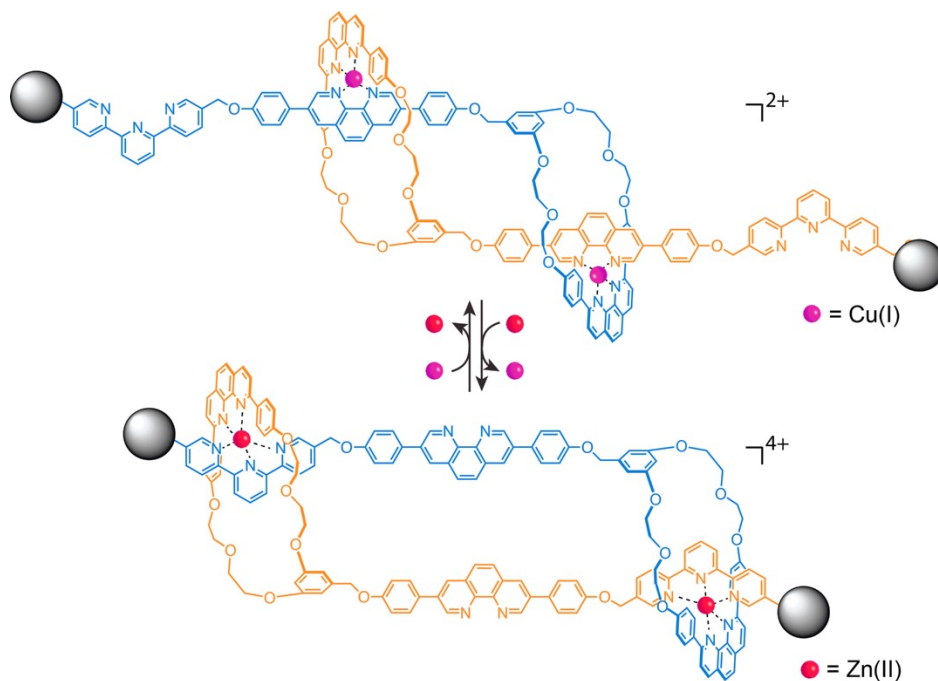
Figure 1.7. Control over [c2]Daisy chain contraction and expansion by using transition metal ions Cu(I) or Zn(II).

Towards this end, incorporation of these interlocked molecules with specific properties (*e.g.* mechanical strength or elasticity) as building blocks to make extended structures with higher-order entanglement can lead to materials displaying interesting behavior originating both from the

intrinsic chemical nature of the molecular units themselves, as well as from emerging properties resulting from their global interlocking scaffold.[44,45] As a consequence, potential applications of catenanes are no longer restricted to the realm of molecular chemistry, but can now further include extended structures such as covalent organic frameworks (COFs), which can display mechanical or dynamic properties of interest.

1.5 Woven crystalline COFs

Weaving of long threads is one of the oldest and most enduring methods of making fabrics that are so soft that they can be worn, yet robust enough to not tear apart easily. Linking molecular building units by strong bonds through reticular synthesis into woven framework structures would represent a powerful strategy to transfer this concept into the realm of synthetic chemistry. The mechanical entanglement between individual threads endows them with the ability to move in a reversible and controllable fashion. This holds great promise for materials with exceptional mechanical properties and dynamics. Atomically defined woven materials have long been sought after but it remains a challenge to construct highly ordered weaving patterns and to assemble their regular crossings by design.

Examples in chemical structures have been reported as woven or polycatenated networks.[46–51] These examples while certainly interesting with respect to their unique structure types were not systematically targeted and are not the result of structural design but much rather products of fortuity. Furthermore, there is currently no strict definition in the literature as to what constitutes a building unit (thread) of woven or polycatenated structures. Here we will focus on the design and synthesis of networks where the interactions within each thread (chemical bonding) are sufficiently different from the interactions between them (weak, non-covalent interactions).

To successfully design the weaving of threads into 2D and 3D chemical structures, long covalently linked molecules (*i.e.*, 1D units) must be able to cross at regular intervals. It would also be desirable if such crossings serve as points of registry, so that the threads can have many degrees of freedom to move away from and back to such points without collapsing the overall structure.

1.5.1   General synthetic strategy of woven structures

The metal-templated synthetic strategy in conjunction with the design principles of reticular synthesis[52] can be employed to target such woven structures (Figure 1.8). Here again we start with a molecular metal complex with functionalized organic ligands, but instead of forming discrete molecules by non-propagating ring closing reactions, it is linked to form 2D and 3D framework structures through the formation of strong, directional bonds. The directionality of the bonds is crucial as, together with the adjustment of angles and metrics of the molecular constituents, it allows for the resulting woven structures to be designed with regard to their underlying topology.

Metal coordination has been used extensively studied as a template strategy in the field of supramolecular chemistry. Preorganization of molecular components into a desirable orientation by metal complexation has allowed for the designed synthesis of interlocking molecules in high yields. Synthetic chemists have since learned to intertwine discrete molecular entities into

entangled architectures with increasing complexity limited only by imagination. This template strategy has recently been implemented in the synthesis of woven extended structures. By linking building units that contain a metal complex core, 2D and 3D frameworks can be constructed where long threads of covalently linked molecules are interwoven at regular intervals templated by the metal ions. Upon demetalation, the threads have high degrees of freedom for spatial deviation to take place between them while preserving the overall structure, endowing the material with exceptional mechanical properties and dynamics.
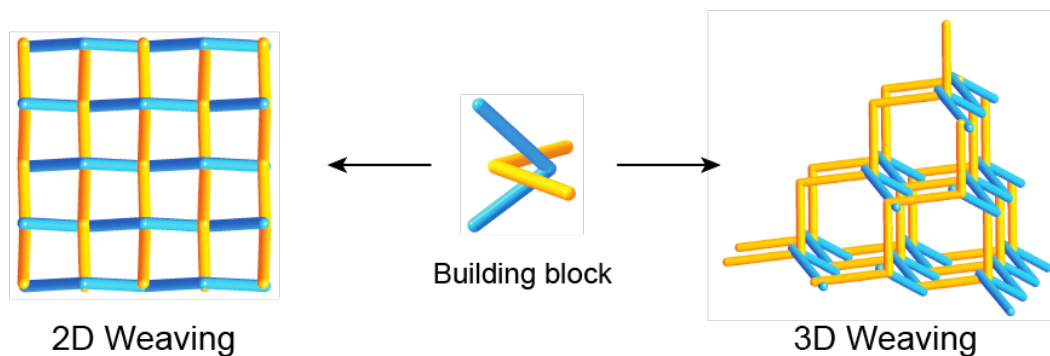
Figure 1.8. Synthesis of 2D and 3D woven extended structures by linking of a woven molecular building block.

In COF structures, the woven long threads are comprised of only organic units linked through strong covalent bonds. This is important because after removing the metal ion templates, the bonding within each thread is remarkably stronger than the mechanical entanglements between them which ensures the chemical and structural integrity of the materials. The individual woven threads therefore experience high degrees of freedom for spatial deviations to take without collapsing the structure. Such freedom allows for reversible remetalation/demetalation, which exerts a reversible control over the mechanical properties of materials.

1.6 References

(1)   Diercks, C. S.; Yaghi, O. M. *Science* **2017**, *355*, eaal1585.

(2)   Wallace, D. C. *Thermodynamics of Crystals*; Dover Publications: Mineola, New York, 1998.

(3)   Furukawa, H.; Cordova, K. E.; O'Keeffe, M.; Yaghi, O. M. *Science* **2013**, *341*, 1230444.

(4)   Waller, P. J.; Gándara, F.; Yaghi, O. M. *Acc. Chem. Res.* **2015**, *48*, 3053.

(5)   Cote, A. P.; Benin, A. I.; Ockwig, N. W.; O'Keeffe, M.; Matzger, A. J.; Yaghi, O. M. *Science.* **2005**, *310*, 1166.

(6)   El-Kaderi, H. M.; Hunt, J. R.; Mendoza-Cortés, J. L.; Côté, A. P.; Taylor, R. E.; O'Keeffe, M.; Yaghi, O. M. *Science* **2007**, *316*, 268.

(7)   Zhang, Y. B.; Su, J.; Furukawa, H.; Yun, Y.; Gándara, F.; Duong, A.; Zou, X.; Yaghi, O. M. *J. Am. Chem. Soc.* **2013**, *135*, 16336.

(8)   Rowan, S. J.; Cantrill, S. J.; Cousins, G. R. L.; Sanders, J. K. M.; Stoddart, J. F. *Angew. Chem. Int. Ed.* **2002**, *41*, 898.

(9)   Wan, S.; Guo, J.; Kim, J.; Ihee, H.; Jiang, D. *Angew. Chem. Int. Ed.* **2009**, *48*, 5439.

(10)   Spitler, E. L.; Dichtel, W. R. *Nat. Chem.* **2010**, *2*, 672.

(11)   Hunt, J. R.; Doonan, C. J.; LeVangie, J. D.; Côté, A. P.; Yaghi, O. M. *J. Am. Chem. Soc.* **2008**, *130*, 11872.

(12)   Du, Y.; Yang, H.; Whiteley, J. M.; Wan, S.; Jin, Y.; Lee, S. H.; Zhang, W. *Angew. Chem. Int. Ed.* **2016**, *55*, 1737.

(13)   Uribe-Romo, F. J.; Hunt, J. R.; Furukawa, H.; Klöck, C.; O'Keeffe, M.; Yaghi, O. M. *J. Am. Chem. Soc.* **2009**, *131*, 4570.

(14)   Uribe-Romo, F. J.; Doonan, C. J.; Furukawa, H.; Oisaki, K.; Yaghi, O. M. *J. Am. Chem. Soc.* **2011**, *133*, 11478.

(15)   Nagai, A.; Chen, X.; Feng, X.; Ding, X.; Guo, Z.; Jiang, D. *Angew. Chem. Int. Ed.* **2013**, *52*, 3770.

(16)   Katekomol, P.; Roeser, J.; Bojdys, M.; Weber, J.; Thomas, A. *Chem. Mater.* **2013**, *25*, 1542.

(17)   Guo, J.; Xu, Y.; Jin, S.; Chen, L.; Kaji, T.; Honsho, Y.; Addicoat, M. A.; Kim, J.; Saeki, A.; Ihee, H.; et al. *Nat. Commun.* **2013**, *4*, 2736.

(18)   Jin, E.; Asada, M.; Xu, Q.; Dalapati, S.; Addicoat, M. A.; Brady, M. A.; Xu, H.; Nakamura, T.; Heine, T.; Chen, Q.; et al. *Science* **2017**, *676*, 673.

(19) Deblase, C. R.; Silberstein, K. E.; Truong, T. T.; Abruña, H. D.; Dichtel, W. R. *J. Am. Chem. Soc.* **2013**, *135*, 16821.

(20) Fang, Q.; Zhuang, Z.; Gu, S.; Kaspar, R. B.; Zheng, J.; Wang, J.; Qiu, S.; Yan, Y. *Nat. Commun.* **2014**, *5*.

(21) Waller, P. J.; Lyle, S. J.; Osborn Popp, T. M.; Diercks, C. S.; Reimer, J. A.; Yaghi, O. M. *J. Am. Chem. Soc.* **2016**, *138*, 15519.

(22) Jackson, K. T.; Reich, T. E.; El-Kaderi, H. M. *Chem. Commun.* **2012**, *48*, 8823.

(23) Beaudoin, D.; Maris, T.; Wuest, J. D. *Nat. Chem.* **2013**, *5*, 830.

(24) Dietrich-Buchecker, C.; Sauvage, J.-P. *J. Am. Chem. Soc.* **1984**, *106*, 3043.

(25) Dietrich-Buchecker, C. O.; Sauvage, J. -P. *Angew. Chemie Int. Ed.* **1989**, *28*, 189.

(26) Chichak, K. S.; Cantrill, S. J.; Pease, A. R.; Chiu, S.-H.; Cave, G. W. V.; Atwood, J. L.; Stoddart, J. F. *Science* **2004**, *304*, 1308.

(27) Wood, C. S.; Ronson, T. K.; Belenguer, A. M.; Holstein, J. J.; Nitschke, J. R. *Nat. Chem.* **2015**, *7*, 354.

(28) Ponnuswamy, N.; Cougnon, F. B. L.; Pantoş, G. D.; Sanders, J. K. M. *J. Am. Chem. Soc.* **2014**, *136*, 8243.

(29) Beves, J. E.; Danon, J. J.; Leigh, D. A.; Lemonnier, J. F.; Vitorica-Yrezabal, I. J. *Angew. Chemie - Int. Ed.* **2015**, *54*, 7555.

(30) Ayme, J.-F.; Beves, J. E.; Leigh, D. A.; McBurney, R. T.; Rissanen, K.; Schultz, D. *Nat. Chem.* **2011**, *4*, 15.

(31) Leigh, D. A.; Pritchard, R. G.; Stephens, A. J. *Nat. Chem.* **2014**, *6*, 978.

(32) Danon, J. J.; Krüger, A.; Leigh, D. A.; Lemonnier, J.; Stephens, A. J.; Vitorica-yrezabal, I. J.; Woltering, S. L. *Science* **2017**, *162*, 159.

(33) E. Wassermann. *J. Am. Chem. Soc.* **1960**, *82*, 4433.

(34) Schill, G.; Lüttringhaus, A. *Angew. Chem. intertiat. Edil.* **1964**, *3*, 546.

(35) Dietrich-Buchecker, C. O.; Sauvage, J. P.; Kintzinger, J. P. *Tetrahedron Lett.* **1983**, *24*, 5095.

(36) Peters, A. J.; Chichak, K. S.; Cantrill, S. J.; Stoddart, J. F. *Chem. Commun.* **2005**, No. 27, 3394.

(37) Armaroli, N.; Balzani, V.; Collin, J. P.; Gaviña, P.; Sauvage, J. P.; Ventura, B. *J. Am. Chem. Soc.* **1999**, *121*, 4397.

(38) Tock, C.; Frey, J.; Sauvage, J. P. In *Molecular Switches, Second Edition (eds B. L. Feringa and W. R. Browne)*; Wiley-VCH Verlag GmbH & Co. KGaA, Weinheim, Germany, 2011.

(39) Bruns, C. J.; Stoddart, J. F. *Acc. Chem. Res.* **2014**, *47*, 2186.

(40) Koumura, N. ; Zijlstra, R. W. J.; Delden, R. A.; Van ; Harada, N. ;; Feringa, B. L. *Nature* **1999**, *401*, 152.

(41) Schalley, C. A.; Beizai, K.; Vögtle, F. *Acc. Chem. Res.* **2001**, *34*, 465.

(42) Livoreil, A.; Dietrich-Buchecker, C. O.; Sauvage, J. P. *J. Am. Chem. Soc.* **1994**, *116*, 9399.

(43) Jiménez, M. C.; Dietrich-buchecker, C.; Sauvage, J. *Angew. Chem. Int. Ed. Engl.* **2000**, *1*, 3284.

(44) Takata, T. *Polym. J.* **2006**, *38*, 1.

(45) Okumura, Y.; Ito, K. *Adv. Mater.* **2001**, *13*, 485.

(46) Lewandowska, U.; Zajaczkowski, W.; Corra, S.; Tanabe, J.; Borrmann, R.; Benetti, E. M.; Stappert, S.; Watanabe, K.; Ochs, N. A. K.; Schaeublin, R.; et al. *Nat. Chem.* **2017**, *9*, 1068.

(47) Li, Y.-H.; Su, C.-Y.; Goforth, A. M.; Shimizu, K. D.; Gray, K. D.; Smith, M. D.; zur Loye, H.-C. *Chem. Commun.* **2003**, No. 14, 1630.

(48) Han, L.; Zhou, Y. *Inorg. Chem. Comm.* **2007**, *11*, 385.

(49) Champsaur, A. M.; Mézière, C.; Allain, M.; Paley, D. W.; Steigerwald, M. L.; Nuckolls, C.; Batail, P. *J. Am. Chem. Soc.* **2017**, *139*, 11718.

(50) Wang, Z.; Błaszczyk, A.; Fuhr, O.; Heissler, S.; Wöll, C.; Mayor, M. *Nat. Commun.* **2017**, *8*, 14442.

(51) Thorp-Greenwood, F. L.; Kulak, A. N.; Hardie, M. J. *Nat. Chem.* **2015**, *7*, 526.

(52) Yaghi, O. M.; O'Keeffe, M.; Ockwig, N. W.; Chae, H. K.; Eddaoudi, M.; Kim, J. *Nature* **2003**, *423*, 705.

Chapter II

The First Woven COF-505

2.1 Introduction

Weaving, the mutual interlacing of long threads is one of the oldest and most enduring methods of making fabric, but this important design concept is yet to be emulated in extended chemical structures. Learning how to link molecular building units by strong bonds through reticular synthesis[1] into weaving forms would be a boon to making materials with exceptional mechanical properties and dynamics. In order to successfully design weaving of chains into two- and three-dimensional (2D and 3D) chemical structures (Figure 2.1a and b), long threads of covalently linked molecules (*i.e.* 1D units) must be able to cross at regular intervals. It would also be desirable if such crossings serve as points-of-registry so that the threads can have many degrees of freedom to move away and back to such points without collapsing the overall structure. Structures have been made by weaving metal-organic chains[2], but designing well-defined materials and assembling their structures by weaving is challenging, and weaving in crystalline inorganic or covalent organic extended structures is undeveloped.
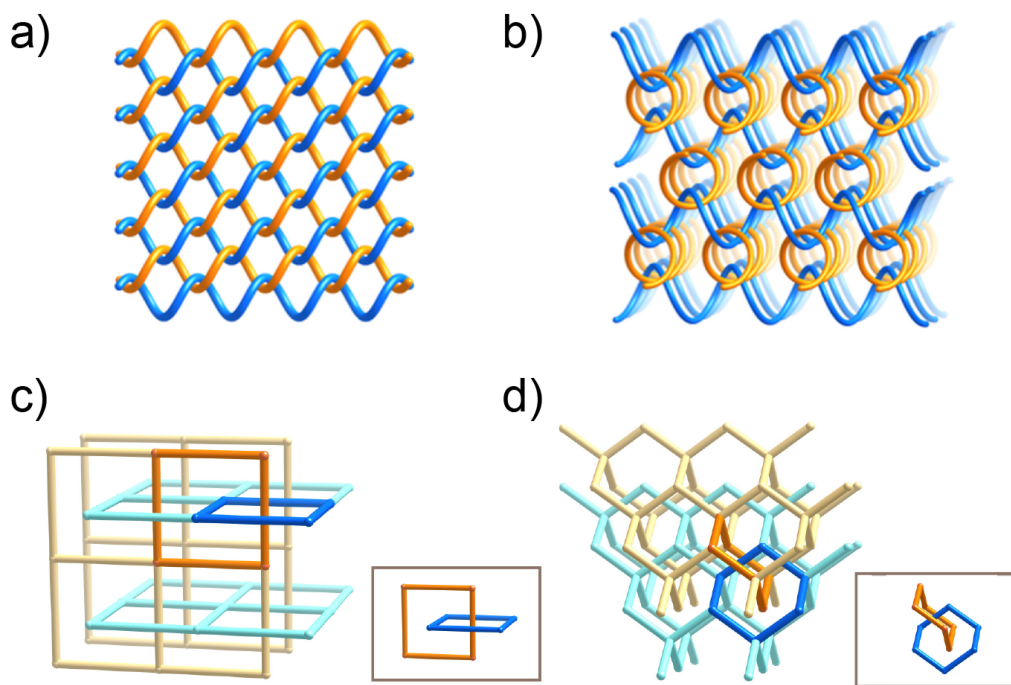
Figure 2.1. Weaving and entanglement. Illustrations of weaving of threads in two- (**a**) and three-dimensions (**b**), compared with entanglements of sheets (**c**), three-dimensional arrangements (**d**), and their interlocking of rings (insets).

Herein, a general strategy is reported along with its implementation for the designed synthesis of a woven material- covalent organic framework-505, COF-505. This COF has helical organic threads interlacing to make a weaving crystal structure with the basic topology of Figure 2.1B, and show that this material has an unusual behavior in elasticity. Although terms such as interweaving[3], polycatenated[2] and interpenetrating[4-6] have been used to describe interlocking of 2D and 3D extended objects [Figure 2.1c and d], most commonly found in MOFs, the term weaving should be used to describe exclusively the interlacing of 1D units to make 2D and 3D structures [Figure 2.1a and b]. Weaving differs from the commonly observed interpenetrating and polycatenated frameworks as the latter is topologically interlocking (*i.e.* interlocking rings, Figure 2.1c and d, insets), while the weaving constructs have many more degrees of freedom for enormous spatial deviations, by each of the threads, to take place independently and still preserve the underlying topology. Such freedom may enable reversible control over the mechanical properties of materials.

2.2 Experimental methods

All starting materials and solvents, unless otherwise specified, were obtained from Aldrich Chemical Co. and used without further purification. Tetrahydrofuran (HPLC grade, Aldrich) was passed through a PureSolv MD 7 Solvent Purification System before use. 4,4'-(1,10-Phenanthroline-2,9-diyl)dibenzaldehyde was synthesized according to published literature.[7,8] All reactions were performed at ambient laboratory conditions, and no precautions taken to exclude atmospheric moisture, unless otherwise specified. Pyrex glass tube charged with reagents and flash frozen with liquid N_2 were evacuated using a Schlenk line by fitting the open end of the tube inside a short length of standard rubber hose that was further affixed to a ground glass tap which could be close to insolate this assembly from dynamic vacuum when the desired internal pressure was reached. Tubes were sealed under the desired static vacuum using an oxygen propane torch. Elemental microanalyses were performed at the University of California, Berkeley, College of Chemistry. Solution ^{1}H nuclear magnetic resonance (NMR) spectra were recorded on a Bruker AVQ-400 (400 MHz) spectrometer operating with an Avance electronics console.

2.2.1 Synthesis

Scheme 2.1. Synthetic route to make 4,4'-(1,10-phenanthroline-2,9-diyl)dibenzaldehyde (PDB) according to literature[7,8] and subsequent complexation to afford Cu(PDB).
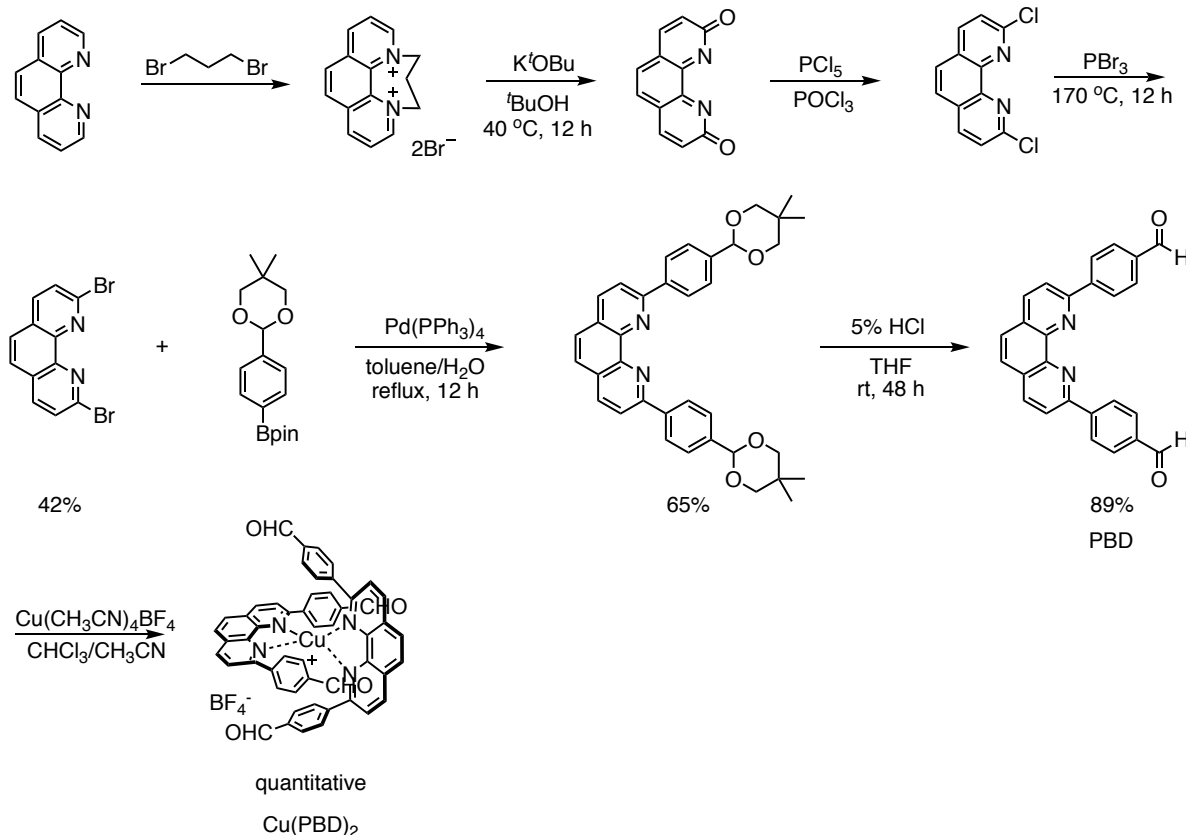
Scheme 2.2. Alternative synthetic route to make PDB ligand using lithium-halogen exchange by *t*-BuLi and electrophilic attack onto phenanthroline, modified from literature.[9]
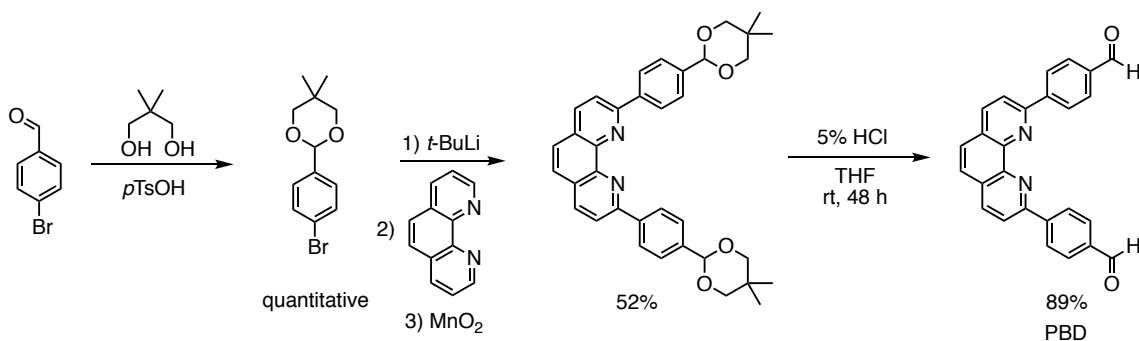
Synthesis of Cu(I)-bis[4,4'-(1,10-phenanthroline-2,9-diyl)dibenzaldehyde] tetrafluoroborate [Cu(PDB)₂]: [Cu(CH₃CN)₄]BF₄ (157 mg, 0.500 mmol) was dissolved in anhydrous CH₃CN (8 mL) under a N₂ atmosphere and added to a solution of 4,4'-(1,10-phenanthroline-2,9-diyl)dibenzaldehyde (388 mg, 1.00 mmol) in CHCl₃ (16 mL), affording a dark red solution, which

was stirred at room temperature for 30 min. The solution was then concentrated under vacuum to afforded an analytically pure compound as a red solid (545 mg, quantitative). ^{1}H NMR (400 MHz, CDCl$_3$) δ 9.69 (s, 4 H), 8.29 (d, ^3J = 7.9 Hz, 8 H), 8.18 (d, ^3J = 8.4 Hz, 4 H), 8.07 (d, ^3J = 8.4 Hz, 4 H), 7.70 (d, ^3J = 7.9 Hz, 8 H), 7.60 (s, 4 H). ESI-MS for [C$_{52}$H$_{32}$CuN$_4$O$_4$]$^+$ (Calcd. 839.17): m/z =839.17 ([M]$^+$, 100%); Elemental analysis: Calcd. For C$_{100}$H$_{68}$BCuF$_4$N$_8$: C, 67.36; H, 3.48; N, 6.04%. Found: C, 66.34; H, 3.37; N, 5.81%.

Synthesis and activation of COF-505: A Pyrex tube measuring 10 × 8 mm (o.d × i.d) was charged with Cu(PDB)$_2$ (15 mg, 0.016 mmol), BZ (6.0 mg, 0.032 mmol), 1 mL of anhydrous THF and 0.1 mL of 6 M aqueous acetic acid solution. The tube was flash frozen at 77 K (liquid N$_2$ bath), evacuated to an internal pressure of 50 mTorr and flame sealed. Upon sealing, the length of the tube was reduced to 18-20 cm. The reaction was heated at 120 °C for 72 h yielding a brown solid at the bottom of the tube which was isolated by centrifugation and washed with anhydrous THF and dried at 120 °C under 50 mTorr for 12 h. This material is insoluble in water and common organic solvents such as hexanes, methanol, acetone, tetrahydrofuran, *N,N*-dimethylformamide, and dimethyl sulfoxide, indicating the formation of an extended structure. Yield: 18.7 mg, 94.4% based on Cu(PDB)$_2$. Elemental analysis: for For C$_{76}$H$_{48}$BCuF$_4$N$_8$·4H$_2$O: Calcd. C, 70.45; H, 4.36; N, 8.65%. Found: C, 70.13; H, 4.03; N, 8.50%.

Synthesis of the molecular analogue of COF-505, Cu(I)-bis[(1*E*,1'*E*)-1,1'-((1,10-phenanthroline-2,9-diyl)bis(4,1-phenylene))bis(*N*-([1,1'-biphenyl]-4-yl)methanimine)] tetrafluoroborate [Cu(PBM)$_2$]: A mixture of Cu(PDB)$_2$ (50.0 mg, 0.108 mmol) and 4-phenyl-aniline (110 mg, 0.648 mmol) in anhydrous *p*-xylene and CHCl$_3$ 1:1 mixture (15 mL) was stirred under reflux with a Dean-Stark apparatus over 24 h. A dark grey solid was precipitated by adding additional *p*-xylen after cooling down the mixture to room temperature, which was then collected by filtration and dried under vacuum (49 mg, 99% yield). ^{1}H NMR (600 MHz, DMSO-d_6) δ 8.81 (d, ^3J = 8.1 Hz, 4 H), 8.33 (s, 4 H), 8.19 (d, ^3J = 8.2 Hz, 4 H), 8.12 (s, 4 H), 7.76 (d, ^3J = 7.8 Hz, 8 H), 7.72 (d, ^3J = 7.5 Hz, 8 H), 7.60 (d, ^3J = 7.9 Hz, 8 H), 7.49 (t, ^3J = 7.7 Hz, 8 H), 7.39 (s, 4 H),7.37 (d, ^3J = 7.5 Hz, 8 H), 7.13 (d, ^3J = 7.7 Hz, 8 H). ESI-MS for [C$_{100}$H$_{68}$CuN$_8$]$^+$ (Calcd. 1444.49): m/z =1444.48 ([M]$^+$, 100%); Elemental analysis: Calcd. For C$_{100}$H$_{68}$BCuF$_4$N$_8$: C, 78.40; H, 4.47; N, 7.31%. Found: C, 76.25; H, 4.55; N, 6.92%.

Scheme 2.3. Synthesis of the molecular analogue of COF-505, Cu(PBM)$_2$.
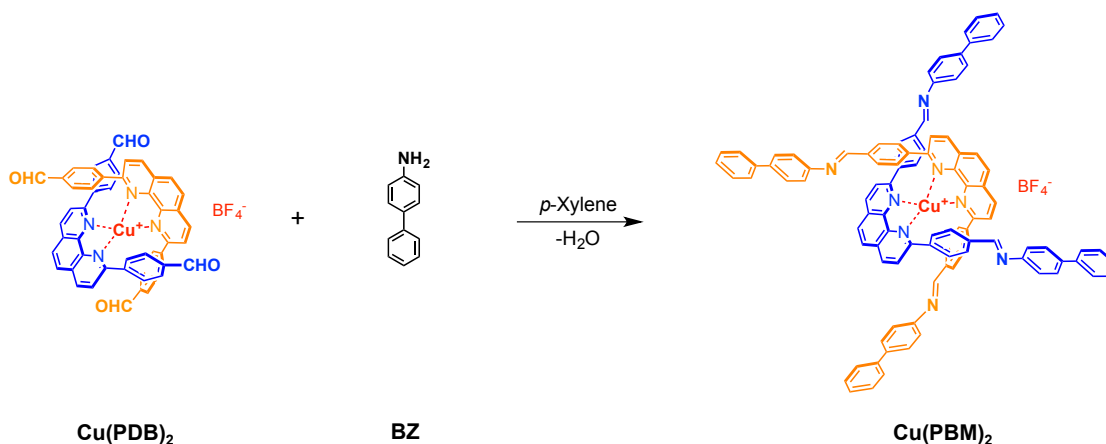
2.2.2 Single-crystal X-ray diffraction

Single-crystals of the complex Cu(PDB)$_2$ were crystallized by the slow diffusion of hexane vapor into a CH$_2$Cl$_2$ solution of the complex. A red block-shaped crystal (0.150 × 0.120 × 0.100 mm) was mounted on a Bruker D8 Venture diffractometer equipped with a fine-focus Mo target X-ray tube operated at 40 W power (40 kV, 1 mA) and a PHOTON 100 CMOS detector. The specimen was cooled to -123 °C using an Oxford Cryosystem chilled by liquid nitrogen. Bruker APEX2 software package was used for data collection; SAINT software package was used for data reduction; SADABS was used for absorption correction; no correction was made for extinction or decay. The structure was solved by direct methods in a triclinic space group $P\bar{1}$ with the SHELXTL software package and further refined with least squares method. All non-hydrogen atoms were refined anisotropically, all hydrogens were generated geometrically. The details of crystallography data are shown in Table 2.1 and 2.2.

The geometry around the copper can be described as distorted tetrahedral with approximate C$_2$ symmetry. The C$_2$ symmetry is indicated by the six N-Cu-N bond angles and the four Cu-N bonds in similar lengths (Table 2.2). The C$_2$ axis bisects the N1B-Cu-N1A angle, thus relating the two phenanthroline ligands and resulting in approximate molecular C$_2$ symmetry. A significant feature of the structure is the π-stacking interactions at 3.4 Å and 3.8 Å between phenanthrolines A and B and phenyl groups E and C, respectively (Figure 2.2). In addition, intermolecular phenyl-phenyl π-stacking interactions at 4.0 Å are also present, resulting in phenyl-phenanthroline-phenyl-phenyl-phenanthroline-phenyl π-stacks in the unit cell.

Table 2.1. Crystal data and structure refinement of Cu(PDB)$_2$.

Chemical formula	$C_{53}H_{34}BCl_2CuF_4N_4O_4$
Formula weight	1012.09
Wavelength	0.71073 Å
Crystal system	Triclinic
Space group	*P*-1
Unit cell dimensions	$a = 12.987(5)$ Å $\alpha = 88.288(7)°$
	$b = 12.995(5)$ Å $\beta = 81.131(7)°$
	$c = 14.074(5)$ Å $\gamma = 67.000(6)°$
Volume	2159.1(13) Å^3
Z	2
Absorption coefficient	0.703 mm^{-1}
Crystal size	$0.150 \times 0.120 \times 0.100$ mm^3
Theta Min-Max	1.465 to 25.427°
Reflections collected	73691
Independent reflections	7942 [*R*(int) = 0.0510]
Completeness to theta = 25.000°	100.0 %
Goodness-of-fit on *F*^{2}	1.046
Final *R* indices [*I* > 2σ(*I*)]	$R_1 = 0.0358$, $wR_2 = 0.0961$
R indices (all data)	$R_1 = 0.0399$, $wR_2 = 0.0999$
Largest diff. peak and hole	0.782 and -0.485 e.Å^{-3}

Table 2.2. Selected Structural Data for Complex of Cu(PDB)$_2$.

Distances / Å

N(1)-Cu(1)	2.0624(18)
N(2)-Cu(1)	2.0626(18)
N(3)-Cu(1)	2.1011(18)
N(4)-Cu(1)	2.0349(18)

Angles / °

N(4)-Cu(1)-N(1)	142.26(7)
N(4)-Cu(1)-N(2)	126.80(7)
N(1)-Cu(1)-N(2)	82.22(7)
N(4)-Cu(1)-N(3)	81.55(7)
N(1)-Cu(1)-N(3)	123.16(7)
N(2)-Cu(1)-N(3)	95.82(7)
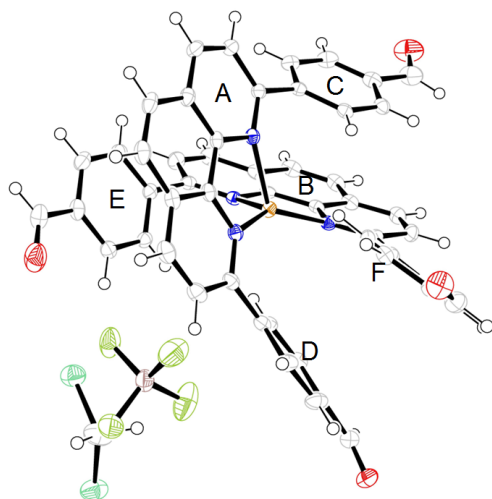
Figure 2.2. ORTEP drawing of the crystal structure of Cu(PDB)$_2$. Thermal ellipsoids are shown with 50% probability.

2.2.3 Fourier transform infrared spectroscopy

The FT-IR spectra of starting materials, molecular analogue, and activated COFs were collected on a Bruker ALPHA FT-IR Spectrometer equipped with ALPHA's Platinum ATR single reflection diamond ATR module, which can collect IR spectra on neat samples. The signals are given in wavenumbers (cm^{-1}) and described as: very strong (vs), strong (s), medium (m), shoulder (sh), weak (w), very weak (vw) or broad (br).
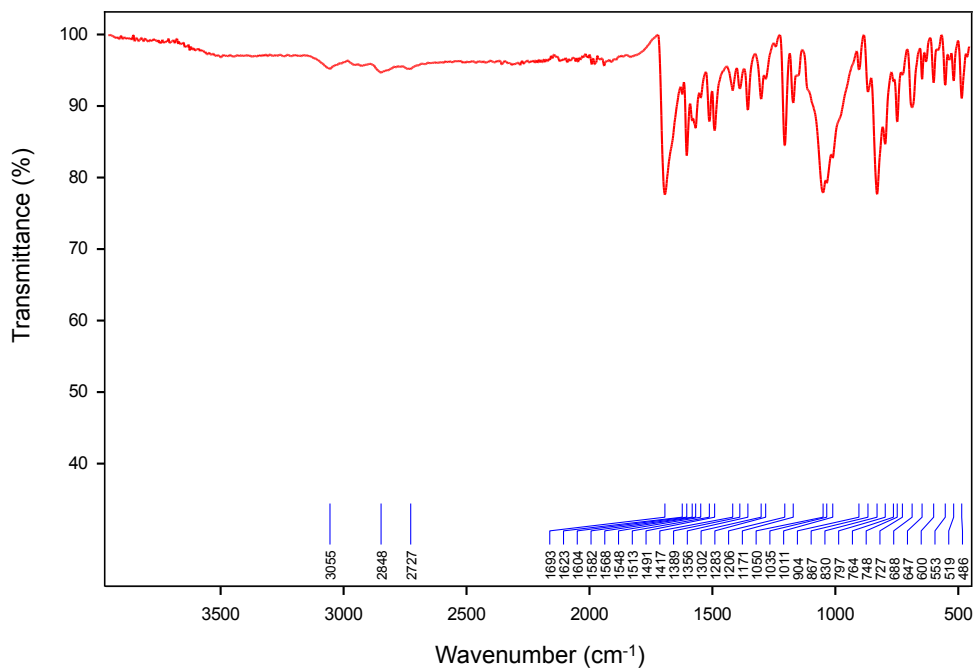
Figure 2.3. FT-IR spectrum of Cu(PDB)$_2$.
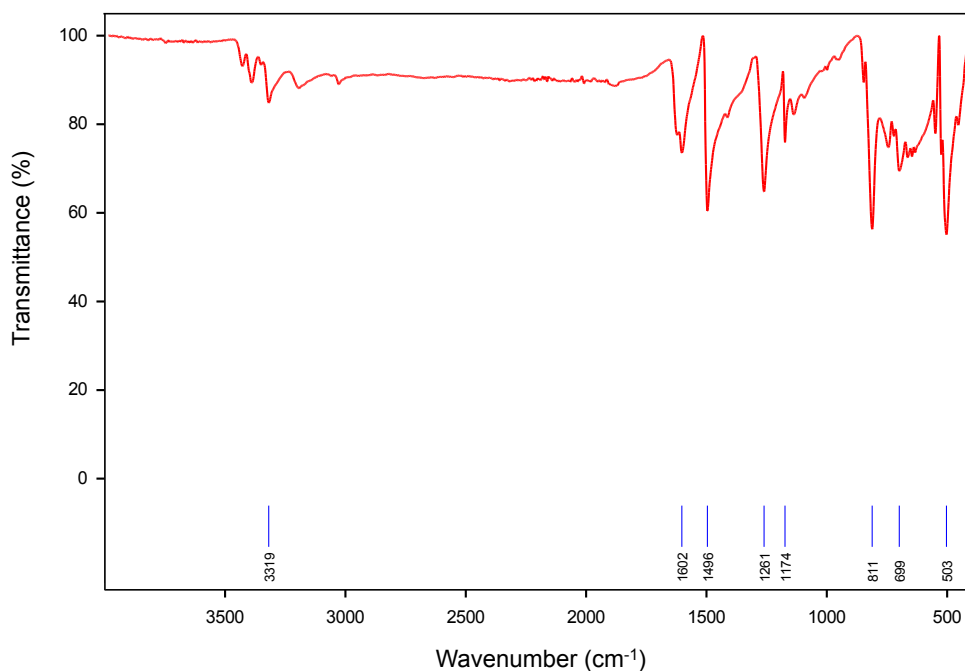
Figure 2.4. FT-IR spectrum of BZ.

YL-3-165
Instrument type and / or accessory
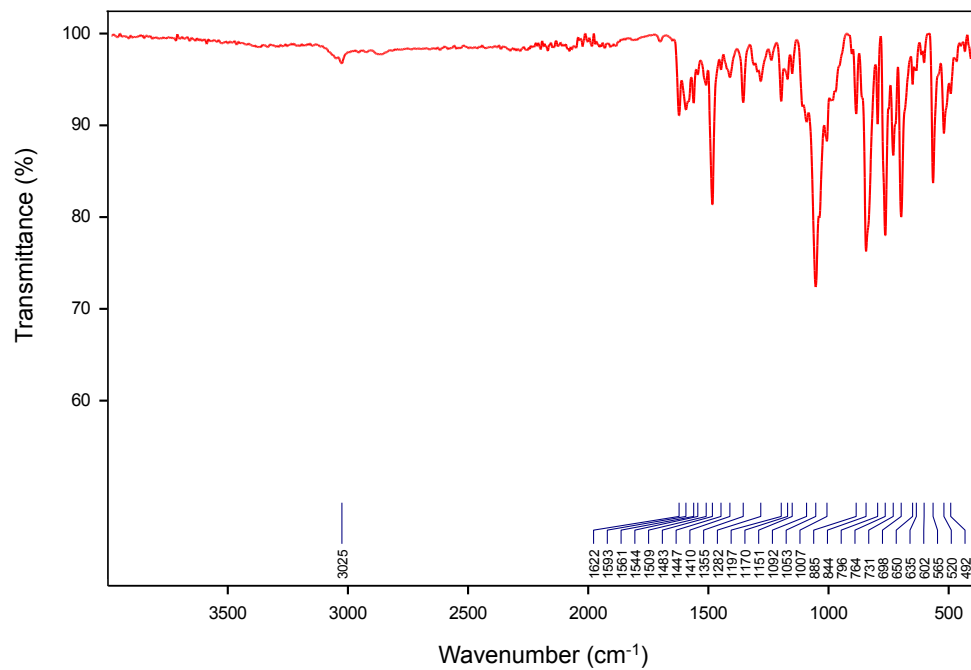
Figure 2.5. FT-IR spectrum of molecular analogue Cu(PBM)$_2$.

YL-3-133-5
Instrument type and / or accessory
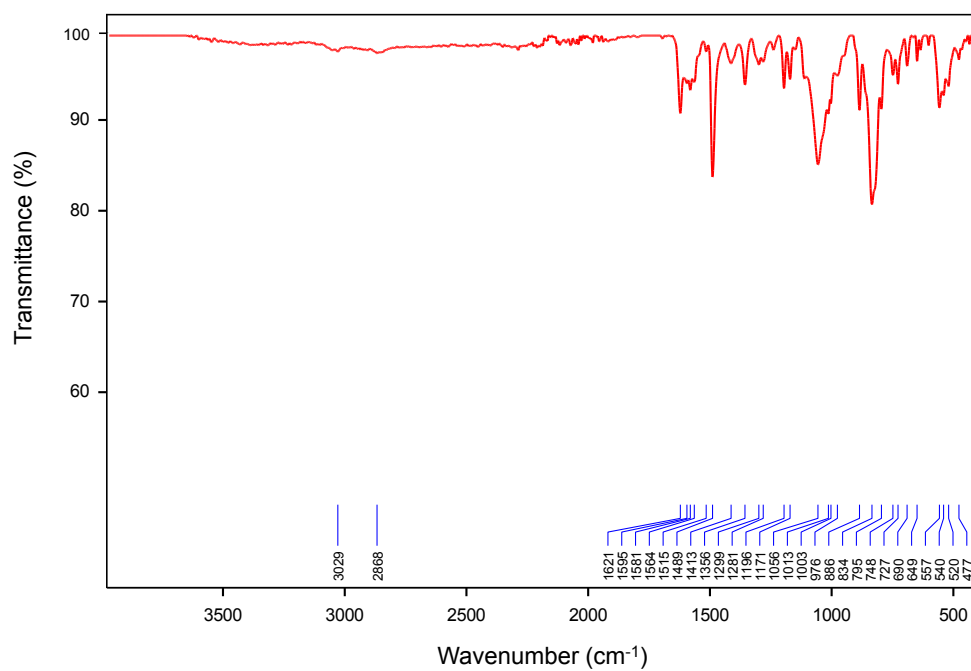
Figure 2.6. FT-IR spectrum of activated COF-505.
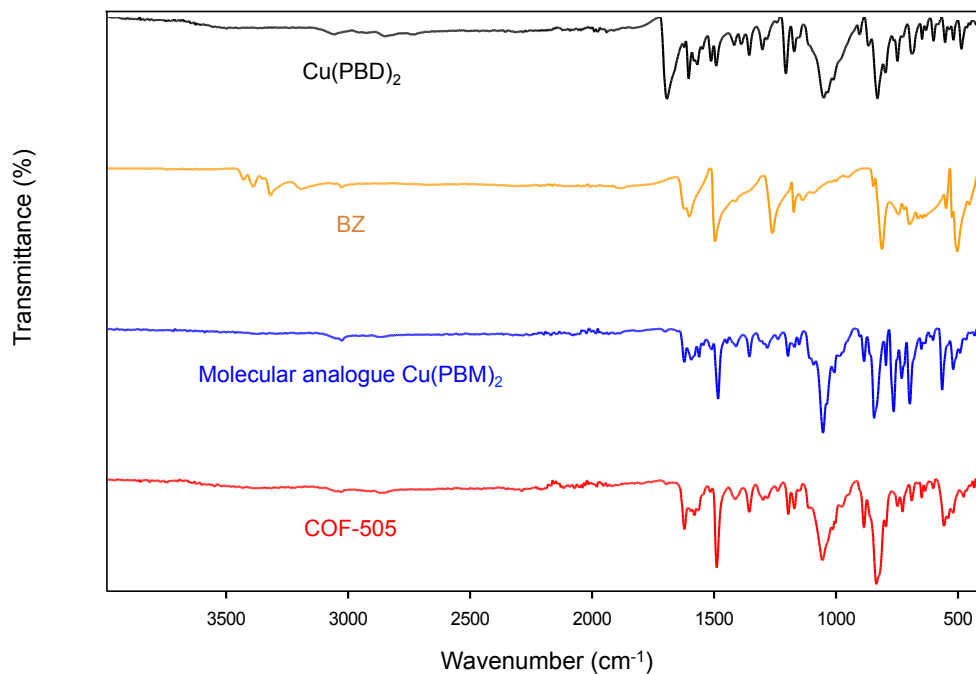
Figure 2.7. Stack plot of FT-IR spectra for the comparison between starting materials, molecular analogue, and activated COF-505.

Table 2.3. Peak assignment for the FT-IR spectrum of COF-505. Notes and discussion are provided to correlate the spectra of starting material.

Peak (cm^{-1})	Assignment and Notes
3029 (vw)	Aromatic C-H stretch from phenyl rings in complex Cu(PDB)$_2$. Present in model compound Cu(PBM)$_2$.
2868 (vw)	Alkene C-H stretching from imine. Present in Cu(PBM)$_2$.
1621 (m)	Imine C=N stretching. Present in Cu(PBM)$_2$. This bond is confirmed by the disappearance of the ν_{N-H} stretching mode from tetraanilylmethane (3319 cm^{-1}) and of the $\nu_{C=O}$ stretching mode from biphenyldicarboxaldehyde (1693 cm^{-1}).
1595 (m)	Aromatic C=C ring stretching from benzidine.
1581 (m)	Aromatic C=C ring stretching from phenyl rings in complex Cu(PDB)$_2$.
1564 (m)	Aromatic C=C ring stretching from Cu(PDB)$_2$.
1515 (m)	Aromatic C=C ring stretching from Cu(PDB)$_2$.
1489 (s)	Aromatic C−C ring stretching from Cu(PDB)$_2$.
1413 (w)	Aromatic C−C ring stretching from Cu(PDB)$_2$.
1356 (m)	Aromatic C−C ring stretching from Cu(PDB)$_2$.
1299 (w)	Aromatic ring stretching from Cu(PDB)$_2$.
1281 (w)	Aromatic ring stretching from Cu(PDB)$_2$.
1196 (m)	Imine C−C=N−C stretching. This mode is the stretching of the C−C and C−N single bonds.
1171 (m)	C-Ph breathing and C-C stretching from benzidine, characteristic of biphenyl.
1056 (w)	B−F stretching from BF$_4$ anions.
1013 (sh)	Aromatic C−H in-plane bending from phenyl rings in Cu(PDB)$_2$.
1003 (sh)	Aromatic C-H in-plane bending from phenyl rings in Cu(PDB)$_2$.
976 (sh)	Aromatic C-H in-plane bending from phenyl rings in Cu(PDB)$_2$.
886 (m)	Aromatic C-H phenyl ring substitution bands from biphenyl rings in benzidine.
834 (s)	Aromatic ring stretching from Cu(PDB)$_2$.
795 (m)	Aromatic ring stretching from Cu(PDB)$_2$.
748 (m)	Aromatic ring C-H out-of-plane bending from Cu(PDB)$_2$.
727 (m)	Aromatic ring C-H out-of-plane bending from Cu(PDB)$_2$.
690 (w)	Aromatic ring C-H out-of-plane bending from Cu(PDB)$_2$.
649 (w)	Aromatic ring C-H out-of-plane bending from Cu(PDB)$_2$.
557 (m)	Aromatic ring C-H out-of-plane bending from Cu(PDB)$_2$.
540 (m)	Aromatic ring C-H out-of-plane bending from BZ.
520 (m)	Aromatic ring C-H out-of-plane bending from Cu(PDB)$_2$.
477 (w)	Aromatic ring C-H out-of-plane bending from BZ.

2.2.4 Solid-State nuclear magnetic resonance spectroscopy

Solid-state nuclear magnetic resonance (NMR) spectra were recorded at ambient pressure on a Bruker AV-500 spectrometer using a standard Bruker magic angle-spinning (MAS) probe with 4 mm (o.d.) zirconia rotors. The magic angle was adjusted by maximizing the number and amplitudes of the signals of the rotational echoes observed in the ^{79}Br MAS FID signal from KBr. The transmitter frequnce of ^{13}C NMR is 125.80 MHz.

The solid-state ^{13}C NMR spectra were acquired using cross-polarization (CP) MAS technique with the ninety degree pulse of ^{1}H with 4.2 μs pulse width. The CP contact time was 2 ms. High power two-pulse phase modulation (TPPM) ^{1}H decoupling was applied during data acquisition. The decoupling frequency corresponded to 32 kHz. The MAS sample spinning rates was 11 kHz. Recycle delays between scans were 2 s. The ^{13}C chemical shifts are given relative to neat tetramethylsilane as zero ppm, calibrated using the methylene carbon signal of adamantane assigned to 38.48 ppm as secondary reference[10].

The experimental setup for cross-polarization and polarization inversion (CPPI) spectral editing is the same as the CPMAS experiment. Pulse sequences are included in work by Zilm and co-workers[11]. Spectral editing parameters were determined as ^{1}H with 6 μs pulse width, cross-polarization times of 2 ms, and a polarization inversion time of 40 μs.
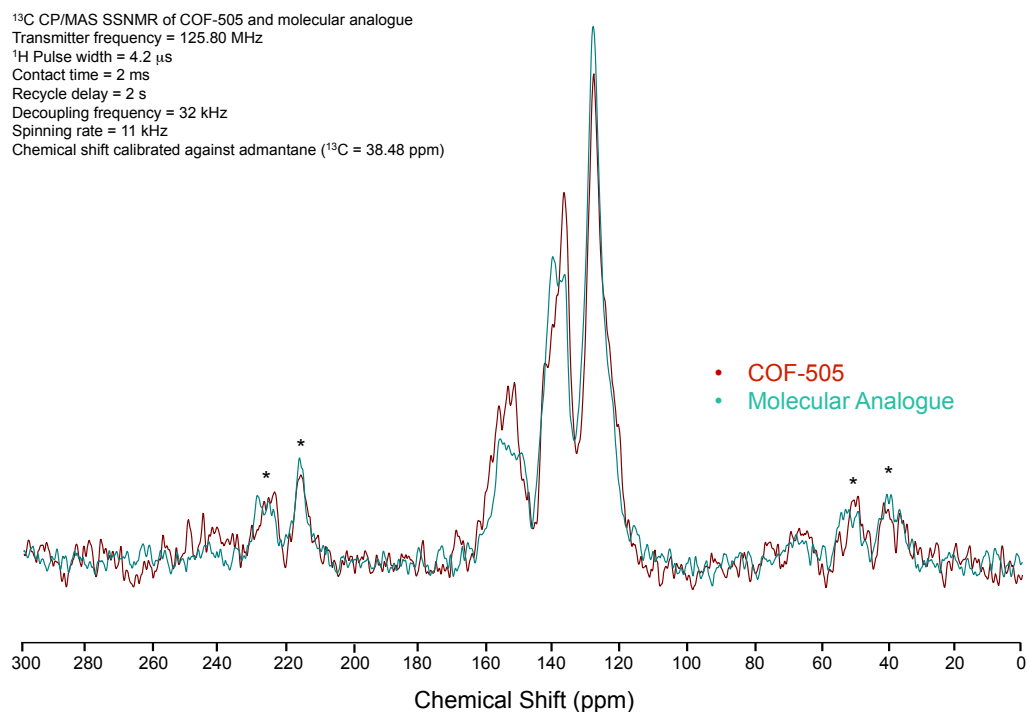
Figure 2.8. Solid-state ^{13}C CP/MAS NMR spectrum of COF-505 and its molecular analogue.
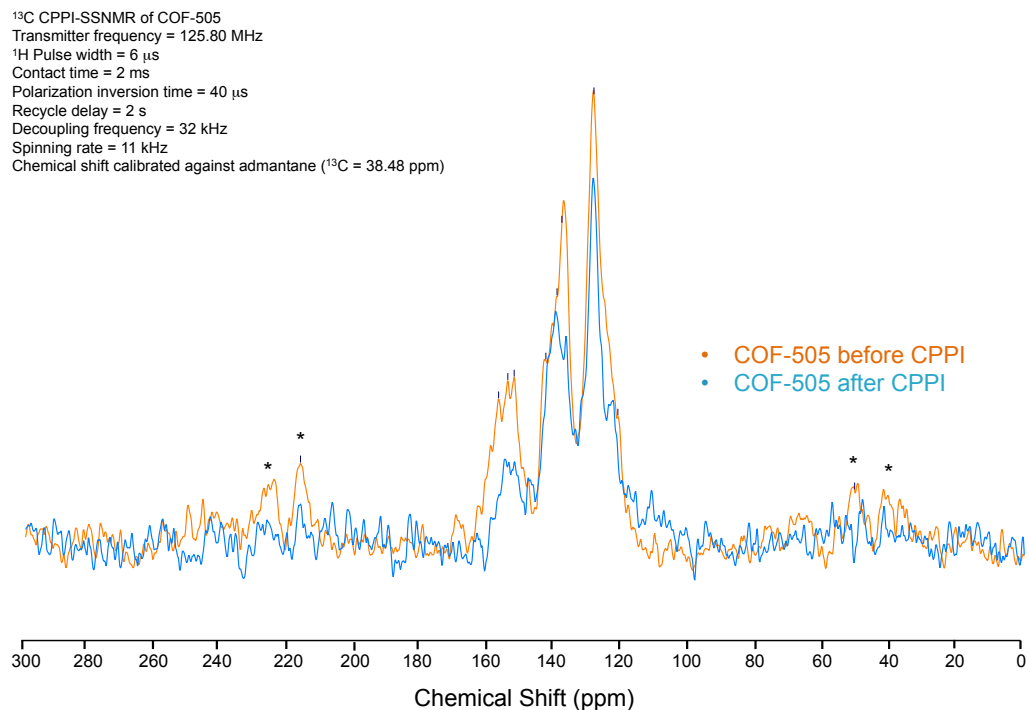
Figure 2.9. Solid-state ^{13}C NMR spectrum of COF-505 before and after CPPI technique.

2.2.5 Scanning electron microscopy

Samples of COF-505 for SEM study were prepared by dropcasting the acetone dispersion of the material onto a 1 cm^2 silicon wafer. SEM images were recorded on a Zeiss Gemini Ultra-55 Analytical scanning electron microscope with accelerating voltage of 5 kV with a working distance of 5 mm. Primary crystallites of size of 0.2 × 0.2 μm were aggregated into spheres with diameter of approximately 2 μm. No other forms were observed in the surveyed samples, and from morphology of primary crystallites, it is speculated that they are the same phase.
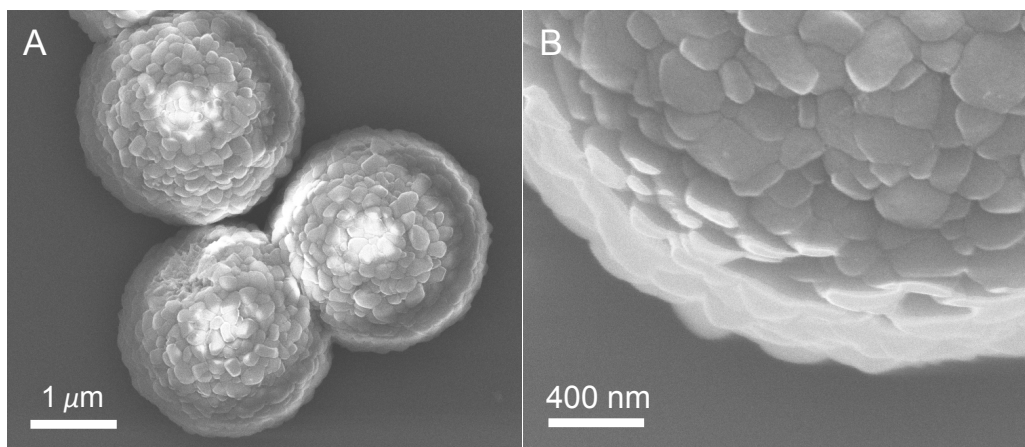
Figure 2.10. Morphology of COF-505 by SEM. (**a**) Crystalline spheres from aggregated crystallites. (**b**) Crystal plates on the surface of a sphere.

2.2.6 Structural determination

Electron diffraction analyses by transmission electron microscopy. A cold field emission JEM-2100F equipped with a DELTA C_s corrector operated at 60 kV was used for HRTEM imaging. Since COF materials are electron beam sensitive, the electron beam damage to the specimen was minimized as much as possible (in this study, the beam density during the observations was less than 500 electrons/(nm^2·s)). A Gatan 894 CCD camera was used for digital recording of the HRTEM images. A single HRTEM image with an exposure time of 2 seconds or a sequence of images (up to 20 frames) was recorded, with a 1 or 2 seconds exposure time for each. After drift compensation, some frames can be superimposed to increase the signal-to-noise (SN) ratio for display. HRTEM images are filtered by a commercial software named HREM-Filters Pro (HREM Research Inc. Japan).

COF-505 crystals were dispersed into ethanol by ultrasonic oscillation and dropped on a carbon film supported TEM grid. 3D electron diffraction tomography (3D-EDT) data were collected on a JEOL JEM-2100, with LaB6 filament and the control of EDT-collect program[12]. The data was further processed by EDT-process program.[12]

Table 2.4. Plane group of projection along [1-10] and multiplicities of general site for five different space groups.

Space group	*Cm2a*	*Cmma*	*Cmca*	*Cc2a*	*Ccca*
Plane group projected along [1-10]	*pg*	*pg*	*pgg*	*pgg*	*pmg*
Multiplicity for general site	8	16	16	8	16

Powder X-ray diffraction analysis. Powder X-ray diffraction data of complex and benzidine were collected using a Bruker D8-advance θ-θ diffractometer in parallel beam geometry employing Cu Kα1 line focused radiation at 1600 W (40 kV, 40 mA) power and equipped with a position sensitive detector with at 6.0 mm radiation entrance slit. Samples were mounted on zero background sample holders by dropping powders from a wide-blade spatula and then leveling the sample with a razor blade. The best counting statistics were achieved by collecting samples using a 0.02° 2θ step scan from 1 – 40° with exposure time of 5 s per step.

PXRD of COF-505 was obtained by wide angle X-ray scattering (WAXS) using Pilatus 2M (Dectris) instrument on beamline 7.3.3 at the Advanced Light Source, Lawrence Berkeley National Laboratory (λ = 1.24 Å). The sample-detector distance and beam center were calibrated using silver behenate. 1-D scattering profiles were reduced from the 2-d data using the Nika package for IGOR Pro (Wavemetrics). The 1-D plot shown in this material are plotted from WAXS data converted to 2θ values assuming λ = 1.5406 Å (Cu Kα1).
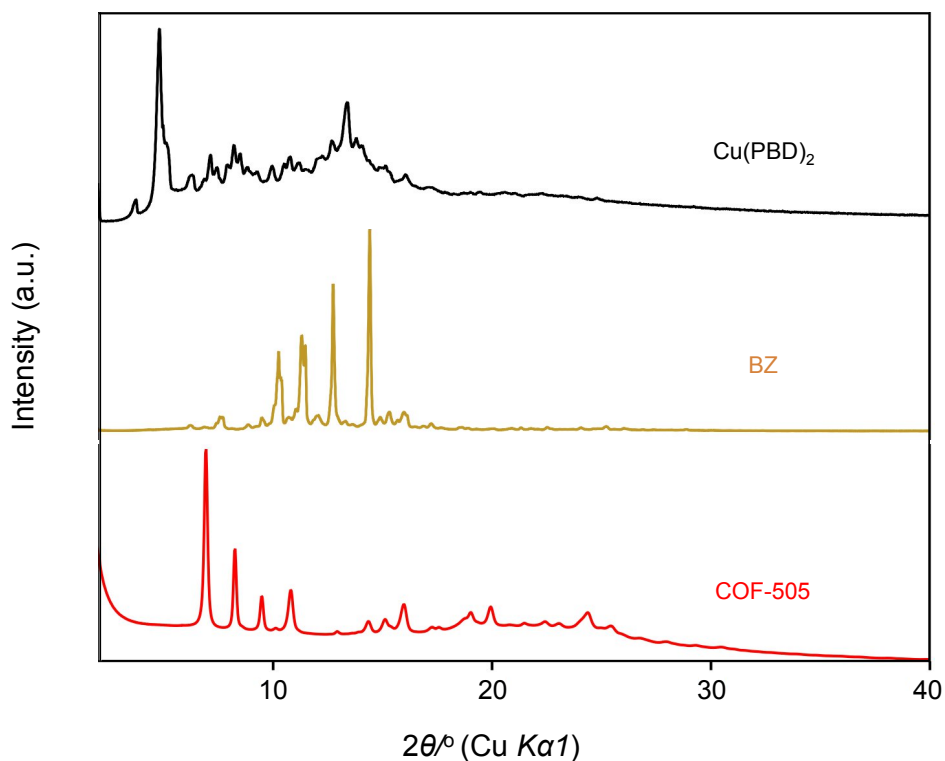
Figure 2.11. PXRD comparison of Cu(PDB)$_2$, BZ, and COF-505.
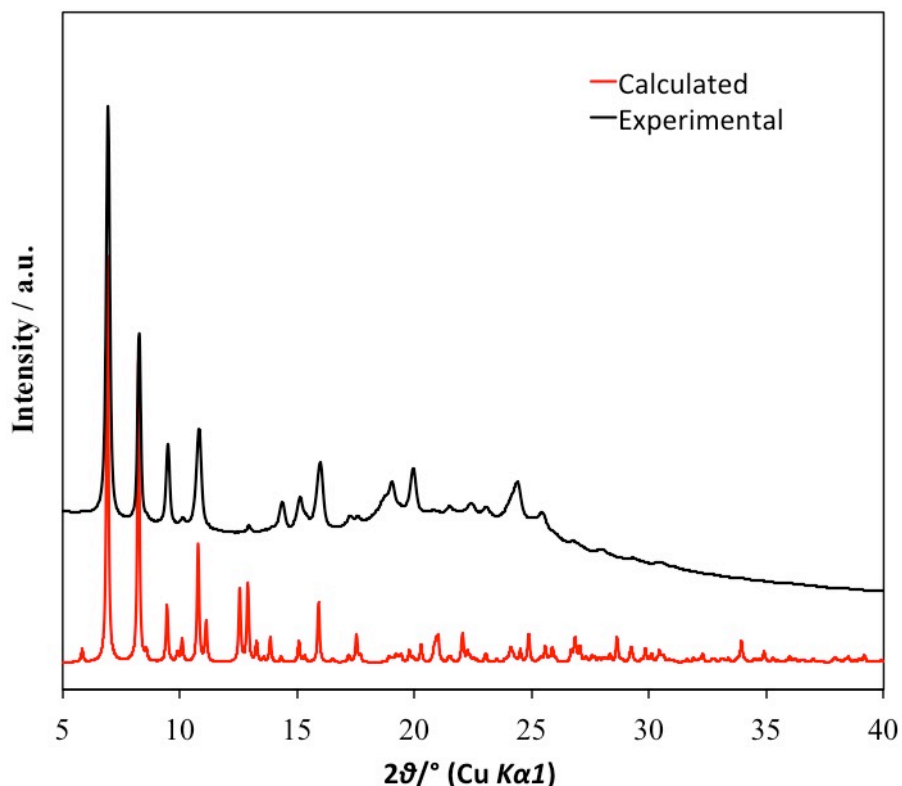
Figure 2.12. Comparison of experimental and calculated PXRD pattern from COF-505 structure.

Structural Modeling. Unit cell parameters and possible space groups were determined with the electron diffraction experiments. The unit cell parameters were refined against the PXRD pattern with a Pawley refinement (a = 18.6419 Å, b = 21.4075 Å, c = 30.2379 Å, orthorhombic, space group $Cc2a$). The initial positions of copper ions were obtained at the maxima of reconstructed 3D potential map from Fourier analysis of HRTEM image. A crystal model was build accordingly with the use of Materials Studio v6.0. Eight complex Cu(PDB)$_2$ molecules were put into one unit cell as a rigid body with copper positions fixed. The orientation of complex was initially refined using PXRD pattern. To make it an extended structure and according to the spectroscopic characterization, one Cu(PDB)$_2$ was connected to its four neighbors through BZ molecules. Then the crystal structure was optimized through a combination of energy and geometrical minimization and PXRD Rietveld refinement. Anions BF$_4^-$ were finally introduced into the model to compensate the charge of the Cu complexes, and to account for the missing electron density from electron diffraction studies. Since the position of the BF$_4^-$ anions does not affect the overall framework, the accurate positions of the anions are not assigned. The structure was further refined with the Rietvled method (Rwp = 6.23%, Rp = 4.35%).

The chemical content in one unit cell is B$_8$C$_{608}$Cu$_8$F$_{32}$H$_{384}$N$_{64}$, consisting of eight symmetrically equivalent Cu(PDB)$_2$, BZ and BF$_4$ units. The geometry of Cu(PDB)$_2$ in COF-505 was similar to that in its molecular crystal. The building units Cu(PDB)$_2$ are connected to each other through imine bonds with biphenyl linkers BZ. The closest distance between two Cu atoms is 8.5 Å. This short distance does not allow the connection between these two Cu(PDB)$_2$ and two mutually weaving nets are formed. The continuous connection of PDB and BZ units forms a helical

29

thread along [110] or [-110] directions. As a result, COF-505 is a weaving framework consisted of helical threads.

The two frameworks are mutually weaving in a way that is different to the commonly observed interpenetration and polycatenation modes. In the normally observed 2-fold **dia** interpenetration, every 6-ring of one network is crossed by one and only one edge of the other network. However, some 6-rings are crossed by three edges of the other network and some edges pass though more than one rings in COF-505 network. This mode of polycatenation and interpenetration makes the particular weaving pattern in the structure COF-505.[13]

2.2.7 Thermogravimetric analysis

Samples were run on a TA Instruments Q-500 series thermal gravimetric analyzer with samples held in a platinum pan under nitrogen atmosphere. A ramp rate of 5 °C/min was used.
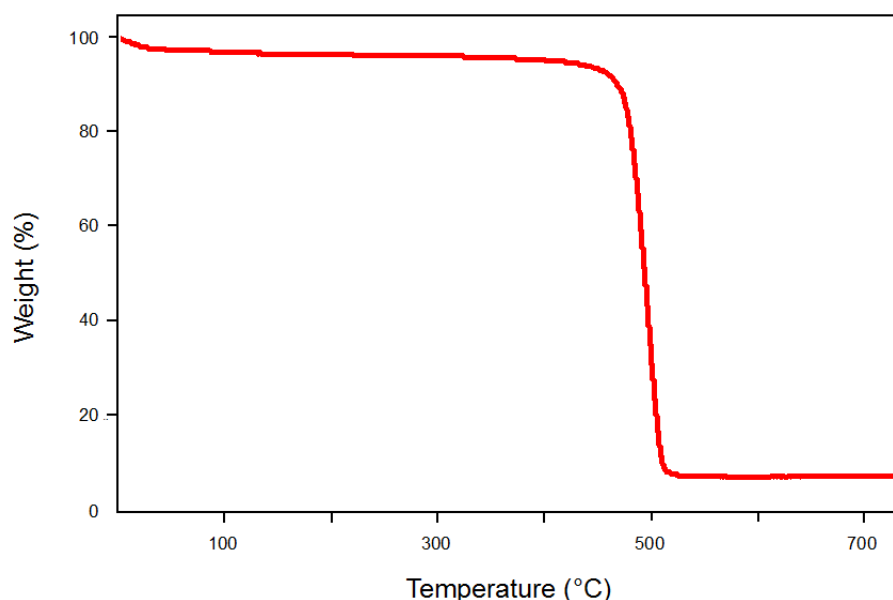
Figure 2.13. TGA trace for activated COF-505.

2.2.8 procedure for demetalation and remetaltion

To a suspension of COF-505 powder was added a 0.3 M KCN solution in a 1:5 mixture of MeOH and H_2O, and was heated at 90 °C. The solution was replaced by a fresh solution of KCN every 24 h and this procedure was repeated three times. Control experiment without KCN solution was also conducted under otherwise identical conditions. Subsequently, both samples were washed with anhydrous CH_3OH and dried at 120 °C under 50 mTorr for 12 h. The demetalated material was observed to be pale-yellow in color, in contrast to the dark brown color of COF-505 (Figure 2.14).

The remetalation process was carried out in similar conditions with the complexation reaction to yield complex Cu(PDB)$_2$. Dried powder of the demetalated material was immersed in anhydrous CHCl$_3$, to which was added a 0.01 M Cu(CH$_3$CN)BF$_4$ solution in CH$_3$CN. This mixture was stirred for 12 h under N$_2$ at room temperature and dark brown color was recovered (Figure 2.14).
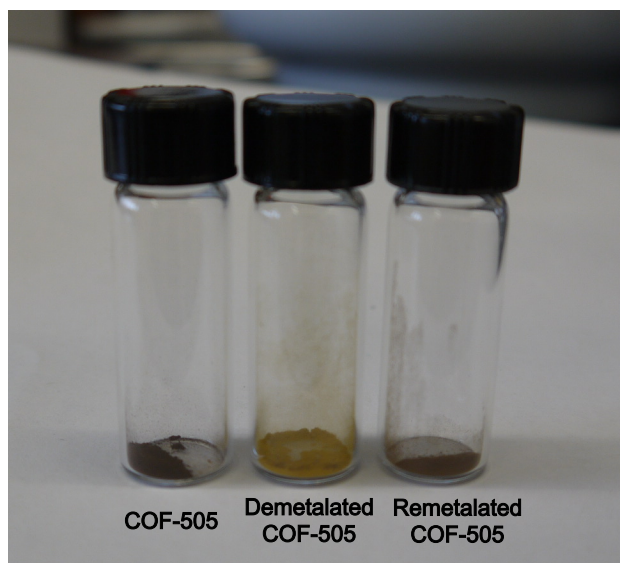
Figure 2.14. Powder of COF-505 (left), demetalated COF-505 (middle), and remetalated COF-505 (right). The sample changed color from dark brown to yellow as it was demetalated and after remetalation, the dark color was recovered.
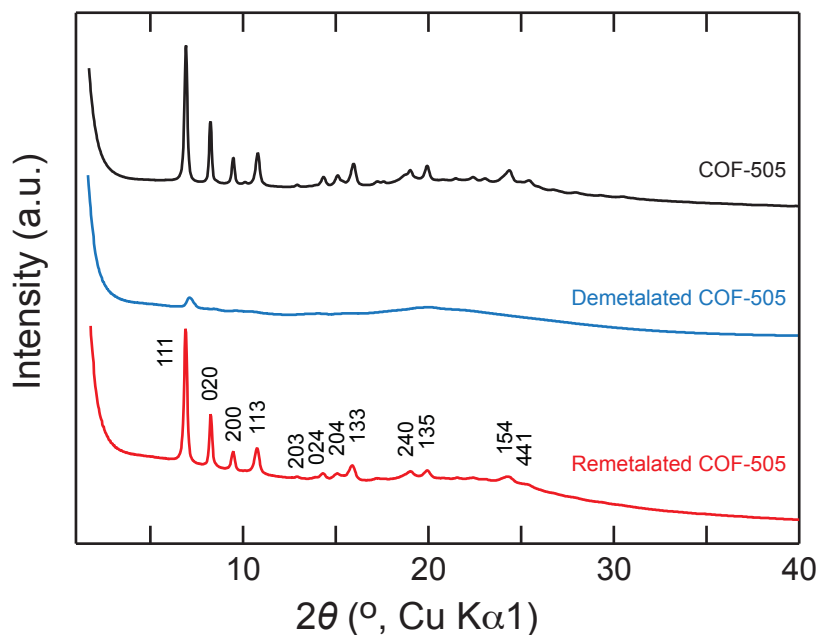
Figure 2.15. PXRD patterns of as-synthesized COF-505, the demetalated and remetalated materials. The crystallinity of COF-505 decreases upon demetalation and can be fully restored after remetalation with copper(I) ions.
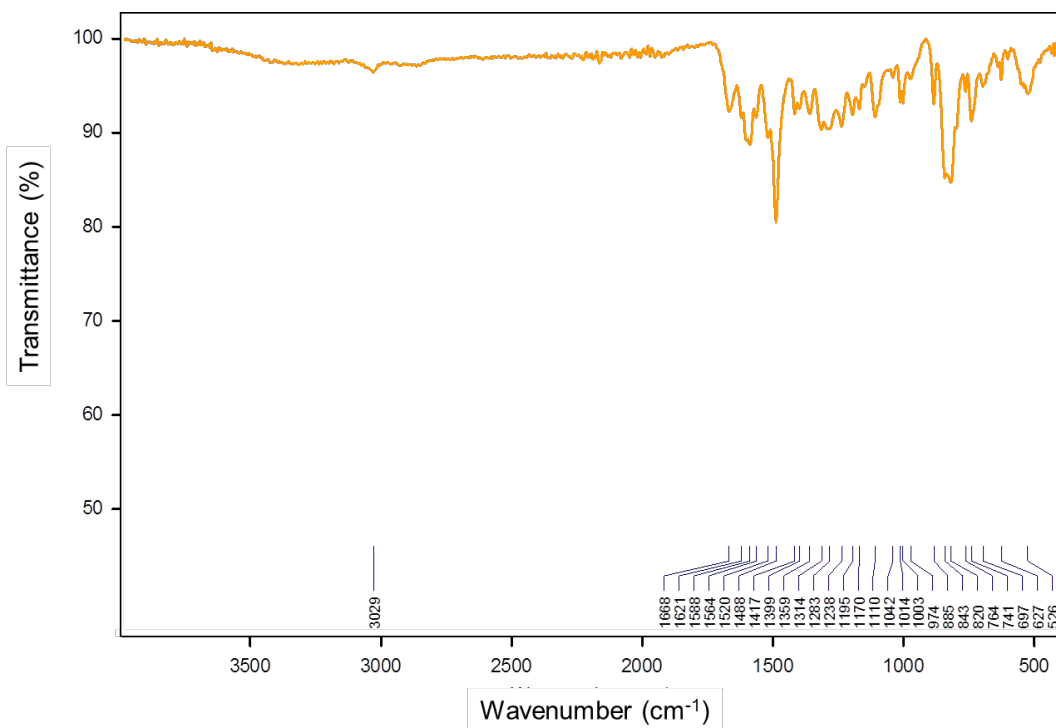
Figure 2.16. FT-IR spectrum of the demetalated COF-505.
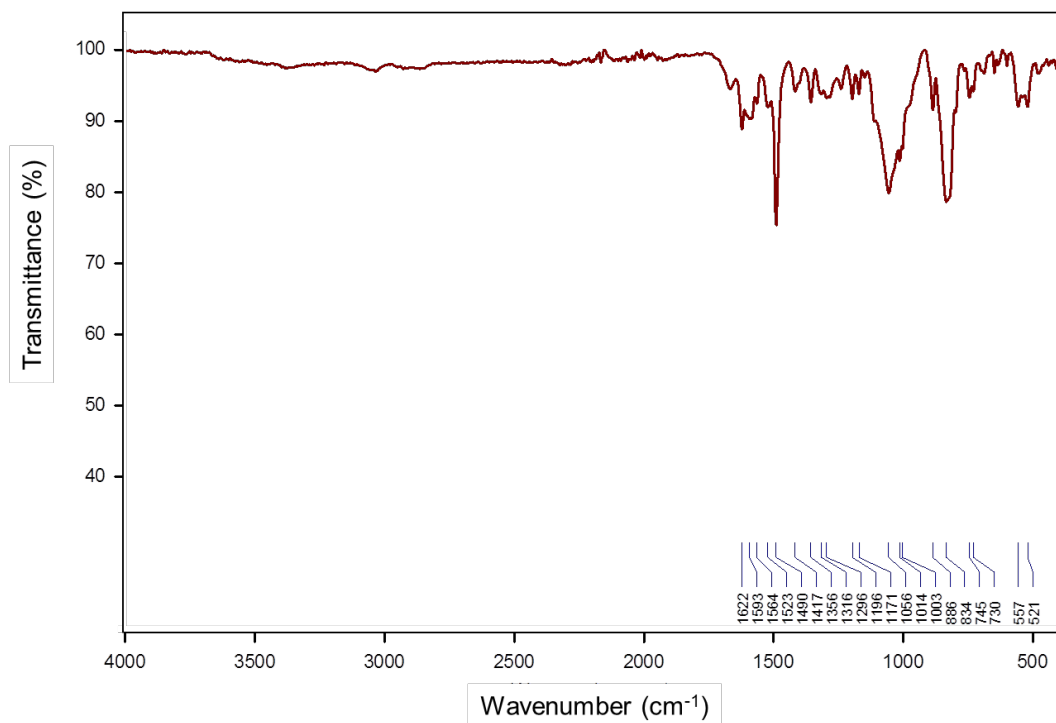
Figure 2.17. FT-IR spectrum of recovered COF-505 after remetalation.
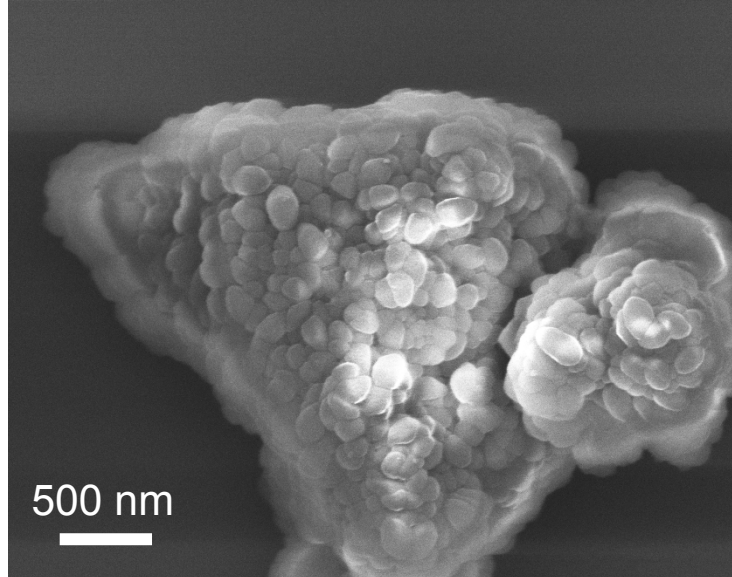
Figure 2.18. SEM image of the demetalated material, which shows similar morphology to COF-505.

2.2.9 Inductively coupled plasma atomic emission spectroscopy

Inductively coupled plasma atomic emission spectroscopy (ICP-AES) was used to determine the copper component in these materials. Samples were dissolved in OPTIMA grade nitric acid. The stock solutions were then diluted to 1:10 (*v/v*) with H_2O, which were analyzed on an Agilent 7500ce ICP-AES using helium collision gas mode. The copper content in COF-505 ($C_{76}H_{48}BCuF_4N_8 \cdot 4H_2O$) is calculated to be 4.9% and measured to be 4.8%, while in the demetalated material, it was determined to be in the range of 0.15% to 0.38%, approximately 3-8% of the original Cu concentration. After remetalation, the Cu content was determined to be 3.9% to 4.2%, which is 82-88% of COF-505.

2.2.10 Atomic force microscopy

Nano-indentation based on AFM (Nanoscope Dimension 3100) was employed to measure Young's modulus of COF-505 and the demetalated material[14]. AFM images of the particles were first acquired under non-contact mode (Figure 2.19 A and B), followed by indentation at the summit of the aggregate which is relatively flat.

Following the standard procedure of nano-indentation, the Young's modulus is related to the indentation curve by Eq. (1):

$$S = \frac{dP}{dh} = \beta \frac{2}{\pi} E_{eff} \sqrt{A} \qquad (1)$$

Where $\dfrac{1}{E_{eff}} = \dfrac{1-v^2}{E} + \dfrac{1-v_i^2}{E_i}$ is the effective elastic modulus of the system, E_{eff}, reflecting both the mechanical response of the sample, E, and the indenter, E_i, and v is Poisson's ratio.

For COF-505, the indentation curve is observed to be close to pure elastic deformation at small depth described by Hertz theory, as shown in Figure 2.19. Its Young's modulus is calculated to be 12.5 GPa using a tip radius of 15 nm, and Poisson's ratio of $v = 0.3$. This value lies within the typical range of MOFs.[15] The measured Young's moduli of other COF-505 particles and remetalated COF-505 are within 30% deviation. On the contrary, the demetalated material is very soft and shows significant plastic deformation under moderate force (Figure 2.19 C and D). Applying Eq. (1) its Young's modulus was obtained to be around 1.3 GPa, assuming a tip radius of 15 nm and a tip angle of 30°.
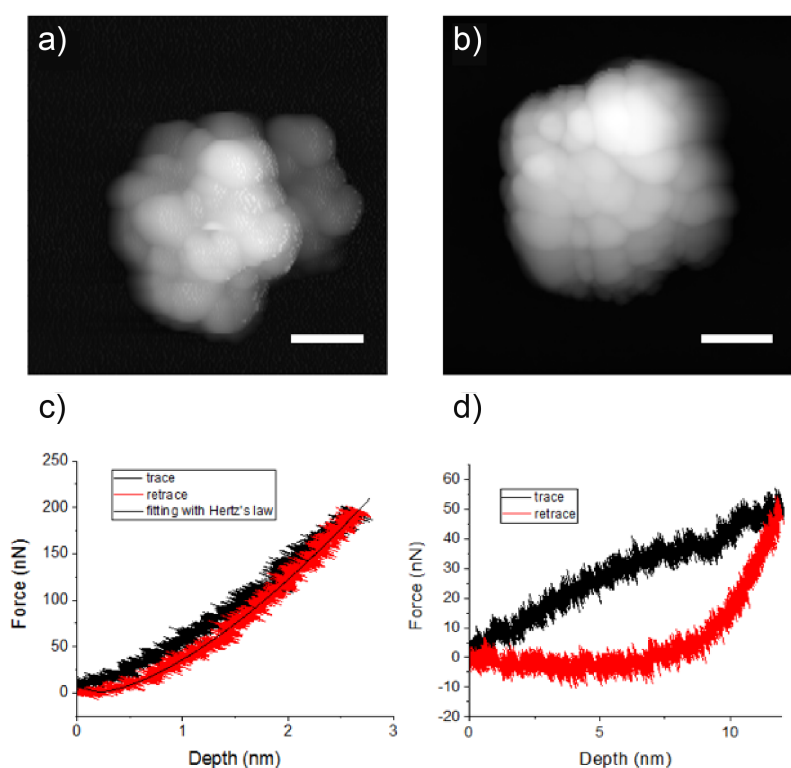
Figure 2.19. AFM images of the COF particles (**a**) before and (**b**) after demetalation. Scale bar: 200 nm. (**c**) The load of indentation P for COF particles before and (**d**) after demetalation as a function of elastic displacement Δh.

2.3 Results and discussion

The synthetic strategy is shown in Figure 2.20, where the aldehyde functionalized derivative of the well-known complex salt Cu(I)-bis[4,4'-(1,10-phenanthroline-2,9-diyl)dibenzaldehyde] tetrafluoroborate, Cu(PDB)$_2$(BF$_4$) was first synthesized (Figure 2.20a). The position of the aldehyde groups approximates a tetrahedral geometry and can be used in reticular synthesis as a building block to be linked with benzidine (BZ) and make imine-bonded PDB-BZ

threads weaving arrangement with the tetrafluoroborate anions occupying the pores (Figure 2.20b). The orientation of the PDB units in a mutually interlacing fashion ensures that the threads produced from linking of the building units are entirely independent, with the Cu(I) ions serving as templates (points-of-registry) to bring those threads together in a precise manner at well-defined intervals. Because the PDB-BZ threads are topologically independent of the Cu(I) ions, the resulting woven structure is formally a COF (termed COF-505). The overall tetrahedral geometry of the aldehyde units ensures the assembly of the threads into a 3D framework (Figure 2.20b). The topology of this framework is that of diamond as expected from the principles of reticular chemistry[1]. Even after the Cu(I) ions are removed, the structure and its topology remain intact regardless of how the threads deviate from their points-of-registry, and upon remetalating the overall structure is reversibly restored. A ten-fold increase in elasticity was observed when going from the metalated to the demetalated forms of the material.

The copper(I)-bisphenanthroline core of the Cu(PDB)$_2$ (without the aldehyde functionality) has been studied extensively as a discrete molecule for the formation of supramolecular complexes;[16–18] however, as yet it has not been used to make extended structures especially of the type discussed here. The tolerance for robust reaction conditions makes this complex suitable for imine COF synthesis, especially in weak acidic conditions. Thus, the tetrahedral building unit, Cu(PDB)$_2$, was designed bearing aldehyde groups in the *para* positions of the two phenyl substituents (Figure 2.20a). The synthesis of Cu(PDB)$_2$(BF$_4$) molecular complex was carried out by air-free Cu(I) complexation of 4,4'-(1,10-phenanthroline-2,9-diyl)dibenzaldehyde according to a previously reported procedure.[19] The single-crystal structure of this complex revealed a distorted tetrahedral geometry around the Cu(I) center, with a dihedral angle of 57° between the two phenanthroline planes. This distortion likely arises from the π-π interaction between the phenanthroline and neighboring phenyl planes.[20]

COF-505 was successfully synthesized via imine condensation reactions by combining a mixture of Cu(PDB)$_2$(BF$_4$) and BZ under solvothermal conditions to yield a dark brown crystalline solid (COF-505), which was insoluble in common polar and nonpolar organic solvents. Fourier-transform infrared spectroscopy (FT-IR) and solid-state nuclear magnetic resonance (NMR) spectroscopy studies were performed on COF-505 to confirm the formation of imine linkages. A molecular analog of COF-505 fragment, Cu(I)-bis[(1,10-phenanthroline-2,9-diyl)bis(phenylene)bis(biphenyl)methanimine]] tetrafluoroborate, Cu(PBM)$_2$(BF$_4$), was used as a model compound and synthesized by condensation of Cu(PDB)$_2$(BF$_4$) and 4-aminobiphenyl (Figures 2.3-2.7). The FT-IR spectrum of COF-505 shows peaks at 1621 and 1196 cm^{-1} [1622 and 1197 cm^{-1} for Cu(PBM)$_2$(BF$_4$)], which are characteristic C=N stretching modes for imine bonds.[21,22] Furthermore, the ^{13}C cross-polarization with magic-angle spinning (CPMAS) solid-state NMR spectrum acquired for COF-505 displays a series of peaks from 140 to 160 ppm, similar in shape and occurring at chemical shifts characteristic of those expected for C=N double bonds. In order to differentiate imine bonds from C=N double bonds of the phenanthroline unit, a cross-polarization and polarization inversion (CPPI) technique was applied, which leaves the signal for quaternary ^{13}C groups unchanged, while the residual tertiary ^{13}CH signal should approach zero.[20] The decreased intensity of the ^{13}CH signal under these conditions confirmed the existence of imine CH=N double bond. Overall, these observations served as initial confirmation of having covalently linked imine extended threads in COF-505.
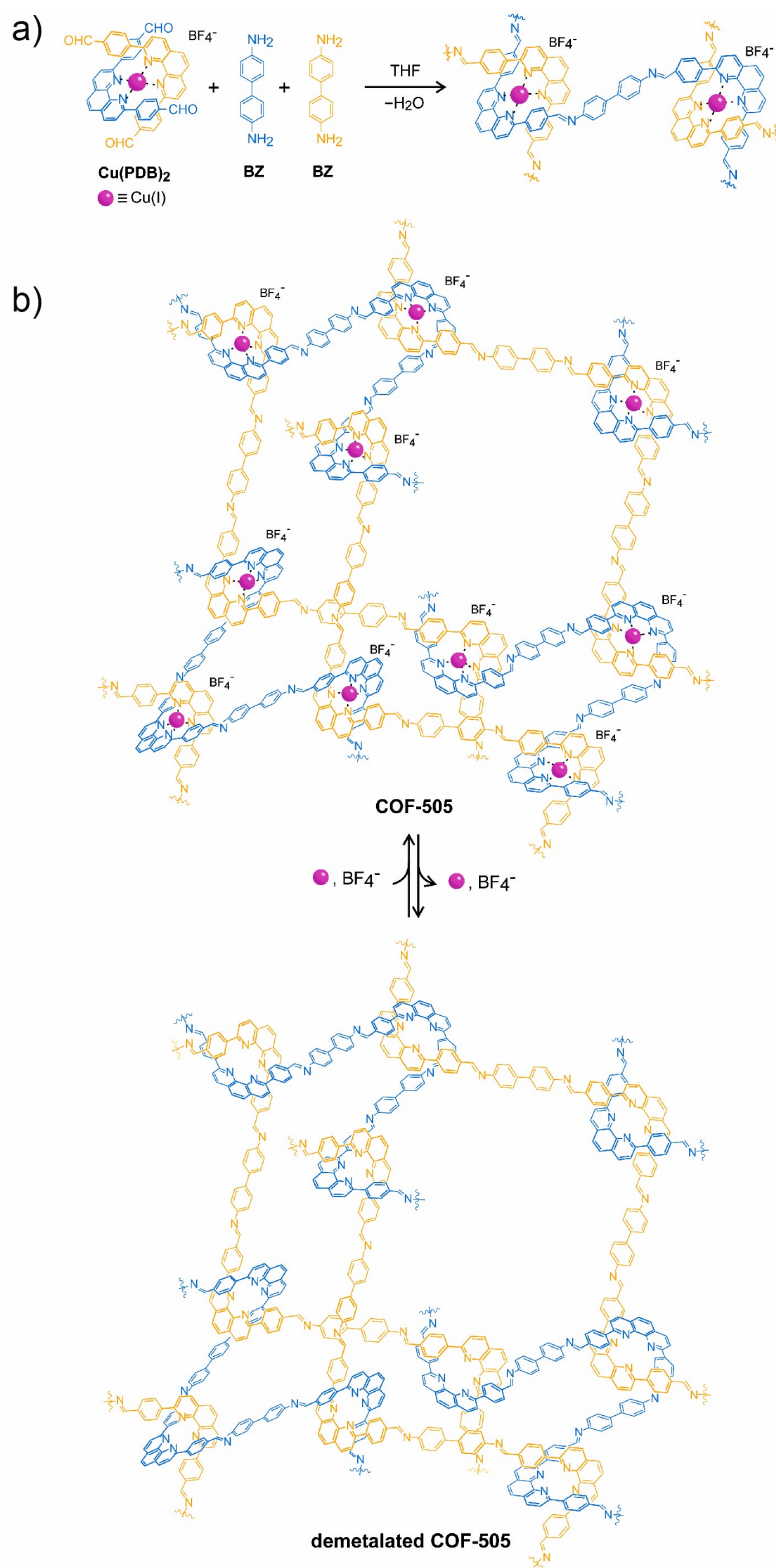
Figure 2.20. A general strategy for the design and synthesis of weaving structures. COF-505 was constructed from organic threads using copper(I) as a template (**a**) to make an extended weaving structure (**b**), which can be subsequently demetalated and remetalated.

Prior to determining the single crystal structure of COF-505, scanning electron microscopy (SEM) was used to examine the morphology and purity of the as-synthesized material. Crystallites of ~200 nm are found to aggregate into spheres of 2 μm in diameter (Figure 2.21a), which possibly arises from weak interactions of the synthesized material with the solvent, THF. No other phase was observed from SEM images taken throughout the material (Figure 2.10).
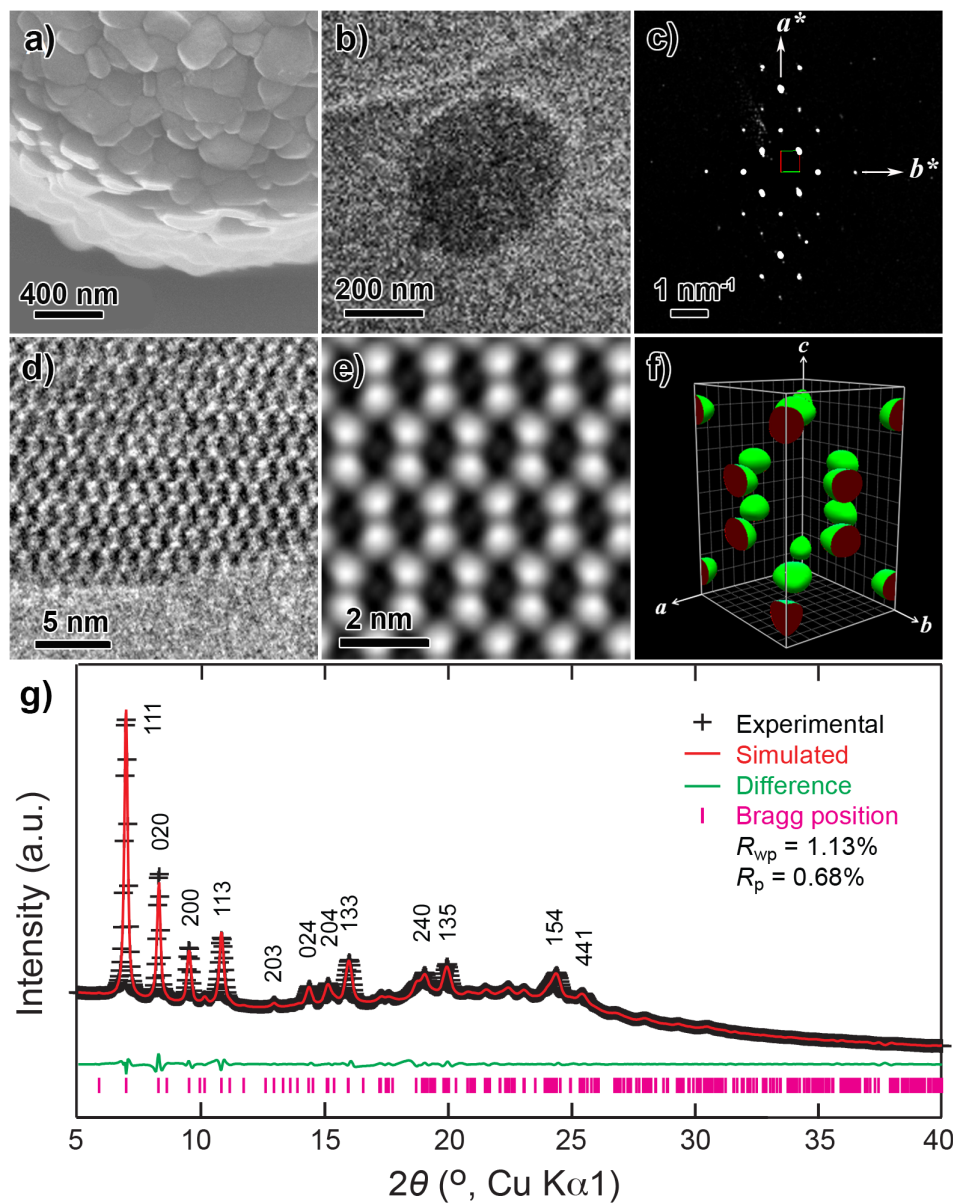
Figure 2.21. Morphology and electron microscopy studies of COF-505. (**a**) Crystallites aggregated on a crystalline sphere observed by SEM. (**b**) TEM image of a single sub-μm crystal used for 3D-EDT. (**c**) 2D projection of the reconstructed reciprocal lattice of COF-505 obtained at 298 K from a set of 3D-EDT data. (**d**) HRTEM image of COF-505 taken with the [1-10] incidence. (**e**) 2D projected potential map obtained by imposing *pgg* plane group. (**f**) Reconstructed 3D electrostatic potential map (threshold: 0.8). (**g**) Indexed PXRD pattern of the activated sample of COF-505 (black) and the Pawley fitting (red) from the modeled structure.

A single submicrometer-sized crystal (Figure 2.21b) from this sample was studied by 3D electron diffraction tomography (3D-EDT).[12,23,24] One EDT data set was collected from the COF-505 (Figure 2.21c) by combining specimen tilt and electron-beam tilt in the range of –41.3° to +69.1° with a beam-tilt step of 0.2°. From the acquired data set, 3D reciprocal lattice of COF-505 was constructed that was identified as a C-centered orthorhombic Bravais lattice. The unit cell parameters were a = 18.9 Å, b = 21.3 Å, c = 30.8 Å and V = 12399 Å^3, which were used to index reflections observed in both powder x-ray diffraction (PXRD) pattern and Fourier diffractograms of high-resolution TEM images (Figure 2.21d to f). The unit cell parameters were further refined to be a = 18.6 Å, b = 21.4 Å, c = 30.2 Å, V = 12021 Å^3 by Pawley refinement of PXRD pattern (Figure 2.21g). The observed reflection conditions were summarized as hkl: $h+k = 2n$; $hk0$: $h,k = 2n$; $h0l$: $h = 2n$; $0kl$: $k = 2n$, suggesting five possible space groups, $Cm2a$ (No. 39), $Cmma$ (No. 67), $Cmca$ (No. 64), $Cc2a$ (No. 41) and $Ccca$ (No. 68). Three of them, $Cm2a$, $Cmma$, and $Ccca$, were excluded, as their projected symmetries along [1-10] did not coincide with that of HRTEM image, pgg (Figure 2.21e).

Furthermore, by performing Fourier analysis of the HRTEM images and imposing symmetry to the reflections, Cu(I) positions were determined from the reconstructed 3D potential map (Figure 2.21f). The structure of COF-505 was built in Materials Studio by putting Cu(PDB)$_2$ units at copper positions and connecting them through biphenyl (reacted BZ) molecules. The chemical compositions were determined by elemental analysis, therefore once the number of copper atoms in one unit cell was obtained, the numbers of other elements in one unit cell were also determined, which indicates that the unit-cell framework is constructed by 8 Cu(PDB)$_2$ and 16 biphenyl units. However, symmetry operations of the space group $Cmca$ requires two PDB units connected to one copper onto a mirror plane perpendicular to a axis, which is not energetically favorable geometry. The final space group determined, $Cc2a$, was used to build and optimize a structure model. The PXRD pattern calculated from this model is consistent with the experimental pattern of activated COF-505 (Figure 2.12).

According to the refined model, COF-505 crystallizes in a diamond (**dia**) network with the distorted tetrahedral building units Cu(PDB)$_2$ and biphenyl linkers BZ linked through *trans* imine bonds. As a result, covalently linked adamantane-like cages 19 Å by 21 Å by 64 Å are obtained and elongated along the *c*-axis (dimensions are calculated based on Cu-to-Cu distances). This size allows two diamond networks of identically weaving frameworks to form the crystal. In other words, these two frameworks are mutually woven in COF-505 crystals along the *c* direction, where the two frameworks are related by a C$_2$ rotation along the *b*-axis, leaving sufficient space for BF$_4^-$ counter-ions. The use of 'interpenetrating frameworks' in this structure is not accurate because there is no interlocking of rings even in the presence of Cu centers (Figure 2.1c and d).[13]

Fundamentally, each of the threads making up the framework is a helix (Figure 2.22a). For clarity, only a fragment of one weaving framework is shown. The helices are entirely made of covalently linked organic threads. As expected, they are weaving and being held by Cu(I) ions at their points-of-registry (Figure 2.22b). These threads are propagating in two different directions along [110] and [-110]. Although the helices are chemically identical, they have opposite chirality giving rise to an overall racemic weaving framework (Figure 2.22c and d) of the same topology as in Figure 2.1b. In the context of reticular chemistry, the points-of-registry play an important role

in crystallizing otherwise difficult to crystallize threads and to do so into two- or three-dimensional frameworks. This arrangement is in stark contrast to the parallel manner in which such one-dimensional objects commonly pack in the solid-state.
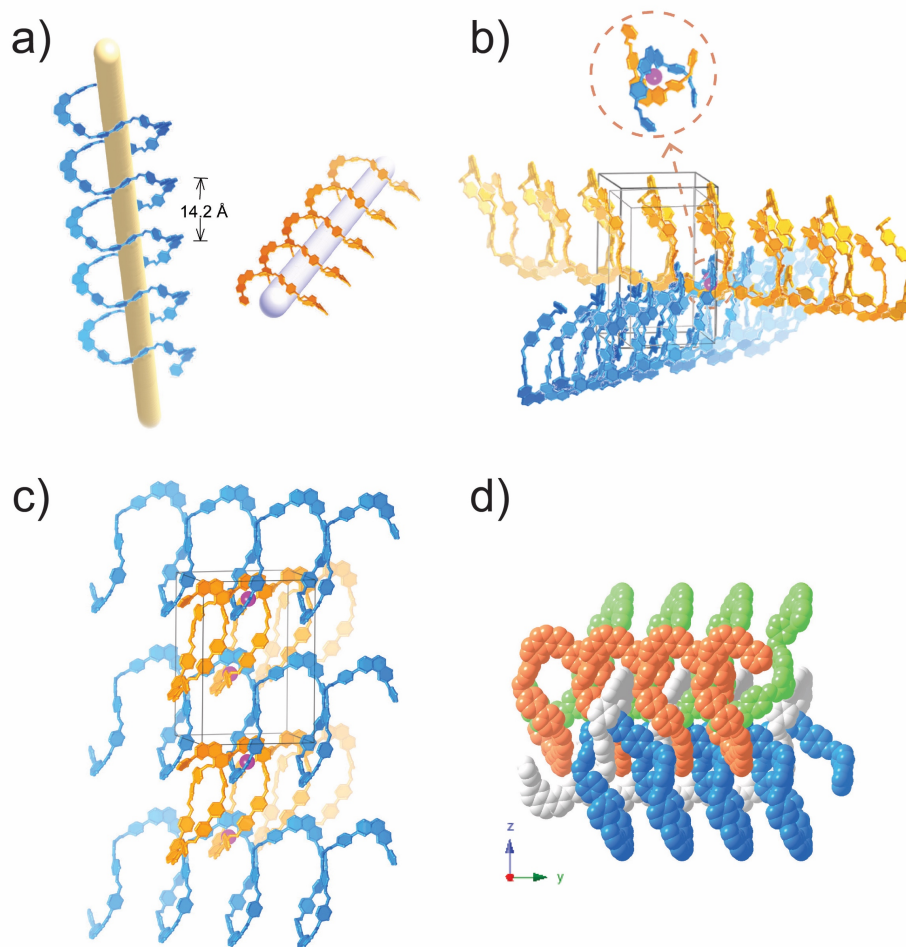
Figure 2.22. Crystal structure of COF-505. The weaving structure of COF-505 consists of chemically identical helices (marked in blue and orange as they are of opposite chirality) with the pitch of 14.2 Å (**a**). The orange helices propagate in the [1-10] direction, while the blue helices propagate in the [110] direction with copper (I) ions as the points-of-registry (**b**). Neighboring blue helices are weaved with the orange helices to form the overall framework (**c**). Blue and orange helices and their C_2 symmetry related green and grey copies are mutually weaved (**d**). Additional parallel helices in (**c**) and (**d**) are omitted for clarity.

The COF-505 structure is a woven fabric of helices, so I sought to remove the Cu centers and examine the properties of the material before and after demetalation. Heating COF-505 in a KCN methanol-water solution[25] yielded a demetalated material. Using inductively coupled plasma (ICP) analysis, it was found tht 92-97% of the Cu(I) copper ions had been removed (§2.2.8). The dark brown color of COF-505 [from the copper-phenanthroline metal-to-ligand charge transfer (MLCT)[26]] changed to pale-yellow as demetalation proceeded (Figure 2.14). Although the crystallinity of demetalated material decreased compared to COF-505, SEM images show similar

morphology before and after demetalation (Figure 2.18). Additionally, the imine linkages were also maintained; the FT-IR peaks at 1621 and 1195 cm^{-1} (Figure 2.16) are consistent with those of COF-505 (1621 and 1196 cm^{-1}). Furthermore, the material could be remetalated with Cu(I) ions by stirring in a CH$_3$CN/CH$_3$OH solution of Cu(CH$_3$CN)$_4$(BF$_4$) to give back crystalline COF-505. This remetalated COF-505 has identical crystallinity to the original as-synthesized COF-505 as evidenced by the full retention of the intensity and positions of the peaks in the PXRD. In the FT-IR spectrum, the peak representing imine C=N stretch was retained (Figure 2.17), indicating that the framework is chemically stable and robust under such reaction conditions.

Given the facility with which demetalation can be carried out and the full retention of the structure upon remetalation can be achieved, the elastic behavior of the metalated and demetalated COF-505 was examined. A single particle of each of these two samples was indented by a conical tip of an atomic force microscope and the load-displacement curves were recorded for both loading and unloading process.[14] The effective Young's moduli (neglecting the anisotropy of the elasticity) of the two COF-505 materials was ~12.5 GPa and 1.3 GPa for the metalated and demetalated particles, respectively (Figure 2.19). Remarkably, this ten-fold ratio in elasticity upon demetalation of COF-505 is similar to the elasticity ratio for porous MOFs to polyethylene.[15] The distinct increase of elasticity could be attributed to the loose interaction between the threads upon removal of copper. Moreover, the elasticity of the original COF-505 could be fully recovered after the process of demetalation and remetalation, being facilitated by the structure of weaving helical threads that easily 'zip' and 'unzip' at their points-of-registry. The large difference in elasticity modulus is caused by loss of Cu(I) ions, which in total only represent a minute mole percentage (0.67 mol%) of the COF-505 structure.

2.4 Conclusion and outlook

A three-dimensional covalent organic framework (COF-505) constructed from helical organic threads, designed to be mutually weaving at regular intervals, has been synthesized by imine condensation reactions of aldehyde functionalized copper(I)-bisphenanthroline tetrafluoroborate, Cu(PDB)$_2$(BF$_4$), and benzidine (BZ). The copper centers are topologically independent of the weaving within the COF structure and serve as templates for bringing the threads into a woven pattern rather than the more commonly observed parallel arrangement. The copper(I) ions can be reversibly removed and added without loss of the COF structure, for which a ten-fold increase in elasticity accompanies its demetalation. The threads in COF-505 have many degrees of freedom for enormous deviations to take place between them, throughout the material, without undoing the weaving of the overall structure.

The weaving strategy reported here is potentially applicable to the conversion of other network topologies to weaving structures as illustrated in Figure 2.23. In addition to the **dia** net of COF-505, a variety of other two- and three-dimensional topologies can also be achieved by weaving of threads (variously colored) using metal ions as points-of-registry. Tetrahedrally coordinated metal complexes with two ligands can be employed as tetratopic building units in reticular synthesis to construct weaving structures of corresponding topologies (*e.g.* **pnf**, **qtz** and **sod**). Metal ions with an octahedral coordination geometry, which provides another type of points-of-registry by coordinating three ligands, can also be used to synthesize weaving structures (*e.g.*

kgm and **pcu**). The reported strategy of weaving organic threads and its successful implementation is the first step in the development of a large area of synthetic chemistry of materials with unique mechanical properties.
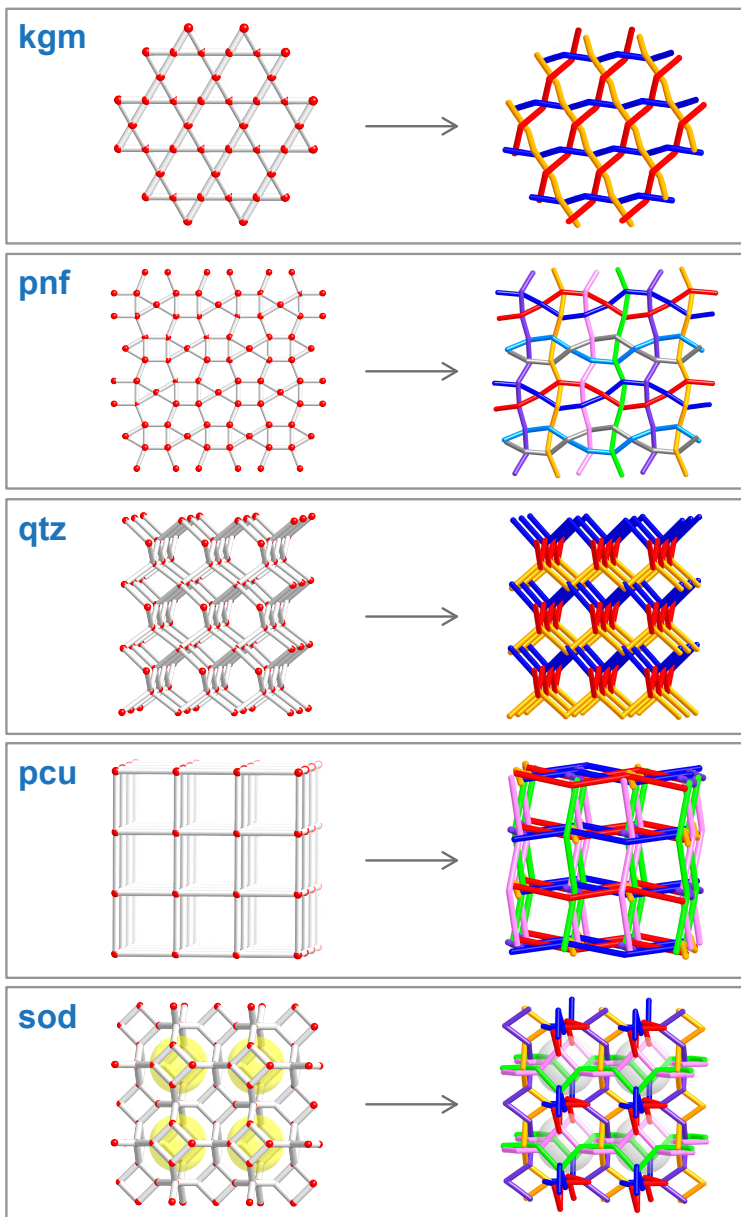
Figure 2.23. The same type weaving of threads observed in COF-505 could be used to make many other COFs based on common net topologies (**kgm**, **pnf**, **qtz**, **pcu**, and **sod**).

References

(1)   Yaghi, O.; O'Keeffe, M.; Ockwig, N. *Nature* **2003**, *423*, 705.

(2)   Carlucci, L.; Ciani, G.; Proserpio, D. M. *Coord. Chem. Rev.* **2003**, *246*, 247.

(3)   Chen, B.; Eddaoudi, M.; Hyde, S. T.; O 'keeffe, M.; Yaghi, O. M. *Science* **2001**, *291*, 1021.

(4)   Blatov, V. A.; Carlucci, L.; Ciani, G.; Proserpio, D. M. *CrystEngComm* **2004**, *6*, 377.

(5)   Batten, S. R.; Robson, R. *Angew. Chemie Int. Ed.* **1998**, *37*, 1460.

(6)   Maji, T. K.; Matsuda, R.; Kitagawa, S. *Nat. Mater.* **2007**, *6*, 142.

(7)   Guo, H. C.; Zheng, R. H.; Jiang, H. J. *Org. Prep. Proced. Int.* **2012**, *44*, 392.

(8)   Ishi-I, T.; Hirashima, R.; Tsutsumi, N.; Amemori, S.; Matsuki, S.; Teshima, Y.; Kuwahara, R.; Mataka, S. *J. Org. Chem* **2010**, *75*, 6858.

(9)   Dietrich-Buchecker, C.; Sauvage, J.-P. *Tetrahedron* **1990**, *46*, 503.

(10)   Morcombe, C. R.; Zilm, K. W. *J. Magn. Reson.* **2003**, *162*, 479.

(11)   Wu, X.; Zilm, K. W. *J. Mag. Reson.* **1993**, *102*, 205.

(12)   Gemmi, M.; Oleynikov, P. *Z. Krist.* **2013**, *228*, 51.

(13)   Alexandrov, E. V.; Blatov, V. A.; Proserpio, D. M. *Acta Crystallogr. Sect. A Found. Crystallogr.* **2012**, *68*, 484.

(14)   Oliver, W. C.; Pharr, G. M. *J. Mater. Res.* **2004**, *19*, 3.

(15)   Tan, J. C.; Cheetham, A. K. *Chem. Soc. Rev.* **2011**, *40*, 1059.

(16)   Dietrich-Buchecker, C. O.; Sauvage, J. -P. *Angew. Chem. Int. Ed.* **1989**, *28*, 189.

(17)   Dietrich-Buchecker, C. O.; Sauvage, J. P.; Kintzinger, J. P. *Tetrahedron Lett.* **1983**, *24*, 5095.

(18)   Jiménez, M. C.; Dietrich-buchecker, C.; Sauvage, J. *Angew. Chem. Int. Ed. Engl.* **2000**, *1*, 3284.

(19)   Dietrich-Buchecker, C. O.; Sauvage, J.-P. *Chem. Rev.* **1987**, *87*, 795.

(20)   Miller, M. T.; Gantzel, P. K.; Karpishin, T. B. *Inorg. Chem.* **1998**, *37*, 2285.

(21)   Zhang, Y. B.; Su, J.; Furukawa, H.; Yun, Y.; Gándara, F.; Duong, A.; Zou, X.; Yaghi, O. M. *J. Am. Chem. Soc.* **2013**, *135*, 16336.

(22)   Uribe-Romo, F. J.; Hunt, J. R.; Furukawa, H.; Klöck, C.; O'Keeffe, M.; Yaghi, O. M. *J. Am. Chem. Soc.* **2009**, *131*, 4570.

(23)   Mugnaioli, E.; Andrusenko, I.; Schüler, T.; Loges, N.; Dinnebier, R. E.; Panthöfer, M.; Tremel, W.; Kolb, U. *Angew. Chem. Int. Ed.* **2012**, *51*, 7041.

(24)   Sun, Q.; Ma, Y.; Wang, N.; Li, X.; Xi, D.; Xu, J.; Deng, F.; Yoon, K. B.; Oleynikov, P.; Terasaki, O.; et al. *J. Mater. Chem. A* **2014**, *2*, 17828.

(25)   Dietrich-Buchecker, C.; Sauvage, J.-P. *J. Am. Chem. Soc.* **1984**, *106*, 3043.

(26)   Scaltrito, D. V; Thompson, D. W.; O'Callaghan, J. A.; Meyer, G. J. *Coord. Chem. Rev.* **2000**, *208*, 243.

Chapter III

Reticular Tuning of Pore Size and Mode of Interpenetration In

Woven Covalent Organic Frameworks

3.1 Introduction

Woven covalent organic frameworks (COFs) are constructed by mechanical entanglement of 1D organic threads that cross at regular intervals.[1–3] The constituent threads in the resulting frameworks experience large degrees of freedom to move away from and back to the crossing points of the woven pattern (i.e. points of registry) within the constraints imposed by the internal accessible void space of the structure. This endows these materials with the prospect for dynamic motion in the solid-state without the need for flexing or breaking of chemical bonds – an important consideration in the context of resilience and longevity. The first generation of woven COFs, reported recently, were found to be dense structures with little internal guest-accessible void space (COF-505).[1] Evidently, this has posed an intrinsic limitation to the material's dynamic behavior. Here, an isoreticular series[4–7] of COFs (COF-504, COF-505, and COF-506) that differ in pore size and/or degree of framework interpenetration are reported and their structures and porosity are investigated.

Scheme 3.1. Aldehyde-functionalized Cu(PDB)$_2$ complexes with tetrafluoroborate (BF$_4^-$) or diphenylphosphinate anions are linked with organic linkers of different length (PDA or BZ) to yield COF-504 and COF-506, isoreticular analogues to the previously reported COF-505.
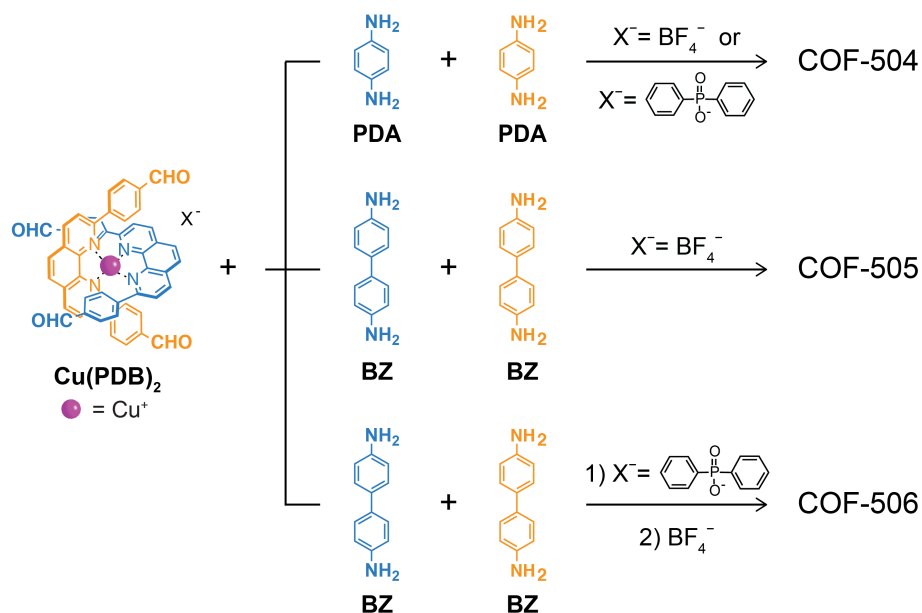
Two strategies are described to enhance the porosity within the frameworks both of which relate to the prevention of framework interpenetration: (i) Isoreticular contraction of the structure yields COF-504, and (ii) the use of bulky anions of the template that can be exchanged post-

synthetically yields COF-506. The structure of the two new frameworks of this series, COF-504 and COF-506, were elucidated by a combined transmission electron microscopy, 3D electron diffraction tomography, and powder X-ray diffraction approach. Subsequently, vapor and dye adsorption studies were performed to probe the porosity of the resulting frameworks. In this context, the importance of modulating the pore size of woven COFs is highlighted by the member of this isoreticular series that features the largest accessible internal surface, COF-506. Upon dematalation the framework was found to take up guest molecules that exceed the size of the material's pores thus corroborating the presence of dynamic motion in the structure in the absence of the copper(I) templates. This study highlights the power of reticular synthesis[8] in the context of the design of woven framework materials and lends credence to the notion of mechanical entanglements being a viable strategy for the introduction of dynamics[9,10] into the realm of extended structures.

3.2 Experimental Methods

All starting materials and solvents, unless otherwise specified, were obtained from Aldrich Chemical Co. and used without further purification. Tetrahydrofuran (HPLC grade, Aldrich) was passed through a PureSolv MD 7 Solvent Purification System before use. All reactions were performed at ambient laboratory conditions, and no precautions taken to exclude atmospheric moisture, unless otherwise specified. Pyrex glass tube charged with reagents and flash frozen with liquid N_2 were evacuated using a Schlenk line by fitting the open end of the tube inside a short length of standard rubber hose that was further affixed to a ground glass tap which could be close to insolate this assembly from dynamic vacuum when the desired internal pressure was reached. Tubes were sealed under the desired static vacuum using an oxygen propane torch. Elemental microanalyses were performed at the University of California, Berkeley, College of Chemistry. Solution ^{1}H nuclear magnetic resonance (NMR) spectra were recorded on a Bruker AVQ-400 (400 MHz) spectrometer operating with an Avance electronics console. Utraviolet-visual (UV-Vis) spectrophotometry measurements were performed on a Shimadzu UV1800 using 1 cm Hellma quartz optical cells.

3.2.1 Synthesis

Synthesis of Cu(I)-bis[4,4'-(1,10-phenanthroline-2,9-diyl)dibenzaldehyde] diphenylphosphinate [Cu(PDB)$_2$P]: Copper(I) diphenylphosphinate (199 mg, 0.71 mmol) was added to a solution of 4,4'-(1,10-phenanthroline-2,9-diyl)dibenzaldehyde (500 mg, 1.29 mmol) in CHCl$_3$ (15 mL) and CH$_3$CN (10 mL) in the glovebox, affording a dark red solution, which was stirred at room temperature for 30 min. The solution was then concentrated under vacuum and further purified by column chromatography with a gradient of solvent from 1:100 to 1:10 MeOH: DCM. Recrystallization from acetone afforded the analytically pure compound as red crystals (489.9 mg, 72%). ^{1}H NMR (400 MHz, dmso-d$_6$) δ 9.68 (s, 4H), 8.83 (d, ^3J = 7.9 Hz, 4H), 8.19 (d, ^3J = 7.9 Hz, 4H), 8.15 (s, 4H), 7.72 (m, 4H), 7.62 (d, ^3J = 8.0 Hz, 8H), 7.43 (m, 6H), 7.07 (d, ^3J = 8.0 Hz, 8H). ESI-MS for [C$_{52}$H$_{32}$CuN$_4$O$_4$]$^+$ (Calcd. 839.17): m/z =839.17 ([M]$^+$, 100%).

Scheme 3.2. Synthetic route to complexation to afford Cu(PBD)$_2$-P.

PBD

72%
Cu(PBD)$_2$P
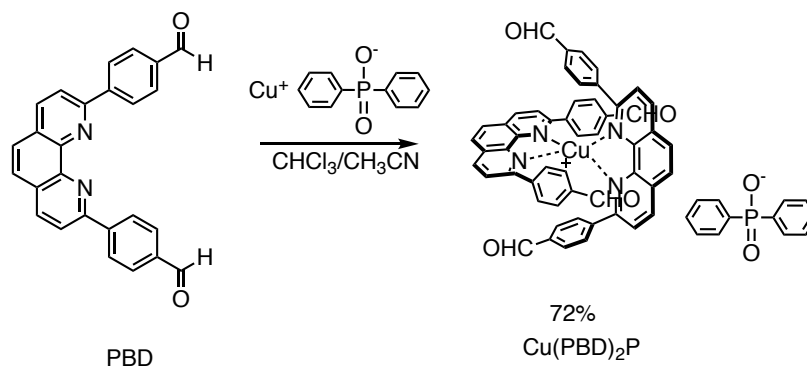
Synthesis and activation of COF-504: A Pyrex tube measuring 10 × 8 mm (o.d. × i.d.) was charged with Cu(PDB)$_2$BF$_4$ (15.0 mg, 0.016 mmol), *p*-phenylenediamine (3.4 mg, 0.032 mmol), 1 mL of anhydrous THF, and 0.1 mL of 6 M aqueous acetic acid. The tube was flash frozen at 77 K (liquid N$_2$ bath), evacuated to an internal pressure of 50 mTorr, and flame sealed. Upon sealing, the length of the tube was reduced to 18-20 cm. The reaction was heated at 120 °C for 72 h yielding a brown solid at the bottom of the tube which was isolated by centrifugation and subsequently washed with THF in a Soxhlet extractor for 24 h. The sample was activated at 75 °C under dynamic vacuum (50 mTorr) for 12 h. This material is insoluble in water and common organic solvents such as hexanes, methanol, acetone, tetrahydrofuran, *N,N*-dimethylformamide, and dimethyl sulfoxide, indicating the formation of an extended structure. Yield: 15.2 mg, 88.8% based on Cu(PDB)$_2$BF$_4$. Elemental analysis: for C$_{64}$H$_{40}$BCuF$_4$N$_8$·2H$_2$O: Calcd. C, 69.41; H, 4.00; N, 10.12%. Found: C, 69.95; H, 4.18; N, 10.24%.

Synthesis and activation of COF-504-P: A Pyrex tube measuring 10 × 8 mm (o.d × i.d) was charged with Cu(PBD)$_2$P (17.6 mg, 0.016 mmol), *p*-phenylenediamine (3.4 mg, 0.032 mmol), 1 mL of anhydrous 1,4-dioxane and 0.1 mL of 6 M aqueous acetic acid solution. The tube was flash frozen at 77 K (liquid N$_2$ bath), evacuated to an internal pressure of 50 mTorr and flame sealed. Upon sealing, the length of the tube was reduced to 18-20 cm. The reaction was heated at 120 °C for 72 h yielding a brown solid at the bottom of the tube which was isolated by centrifugation and washed with THF in a Soxhlet extractor for 24 h. The sample was activated at 75 °C under 50 mTorr for 12 h. This material is insoluble in water and common organic solvents such as hexanes, methanol, acetone, tetrahydrofuran, *N,N*-dimethylformamide, and dimethyl sulfoxide, indicating the formation of an extended structure. Yield: 10.1 mg, 56.6% based on Cu(PBD)$_2$P. Elemental analysis: for C$_{64}$H$_{40}$CuN$_8$·0.7(C$_2$H$_4$O$_2$)·0.3(C$_{12}$H$_{10}$O$_2$P)·5H$_2$O: Calcd. C, 68.82; H, 4.67; N, 9.30%. Found: C, 69.06; H, 4.99; N, 8.80%.

Synthesis and activation of COF-506: A Pyrex tube measuring 10 × 8 mm (o.d. × i.d.) was charged with Cu(PDB)$_2$-P (17.6 mg, 0.016 mmol), benzidene (6 mg, 0.032 mmol), anhydrous 1,4-dioxane (0.7 mL), mesitylene (0.3 mL), and 0.1 mL of 6 M aqueous acetic acid. The tube was flash frozen at 77 K (liquid N$_2$ bath), evacuated under dynamic vacuum to an internal pressure of 50 mTorr, and flame sealed. Upon sealing, the length of the tube was reduced to 18-20 cm. The reaction was heated at 120 °C for 72 h yielding a brown solid at the bottom of the tube which was isolated by centrifugation and washed with THF in a Soxhlet extractor for 24 h to give COF-506-P. This material is insoluble in water and common organic solvents such as hexanes, methanol,

acetone, tetrahydrofuran, *N,N*-dimethylformamide, and dimethyl sulfoxide, indicating the formation of an extended structure. Yield: 18.4 mg, 81.7% based on Cu(PDB)$_2$P. Elemental analysis: for C$_{88}$H$_{56}$CuN$_8$O$_2$P·6H$_2$O: Calcd. C, 72.39; H, 4.69; N, 7.67%. Found: C, 72.11; H, 4.20; N, 7.86%. The solid was then immersed in a 1 M NaBF$_4$ in CH$_3$CN solution for 12 h and then washed in a Soxhlet extractor with THF for 24 h to yield COF-506.

3.2.2 Single-crystal X-ray diffraction

Single-crystals of the complex Cu(PBD)$_2$P were crystallized in acetone. A red block-shaped crystal (1.0 × 1.0 × 0.50 mm) was mounted on a Bruker D8 Venture diffractometer equipped with a fine-focus Cu target X-ray tube operated at 40 W power (40 kV, 1 mA) and a PHOTON 100 CMOS detector. The specimen was cooled to -123 °C using an Oxford Cryosystem chilled by liquid nitrogen. Bruker APEX2 software package was used for data collection; SAINT software package was used for data reduction; SADABS was used for absorption correction; no correction was made for extinction or decay. The structure was solved by direct methods in a triclinic space group *P*-1 with the SHELXTL software package and further refined with least squares method. All non-hydrogen atoms were refined anisotropically, all hydrogens were generated geometrically. The details of crystallography data are shown in Table 3.1 and 3.2.
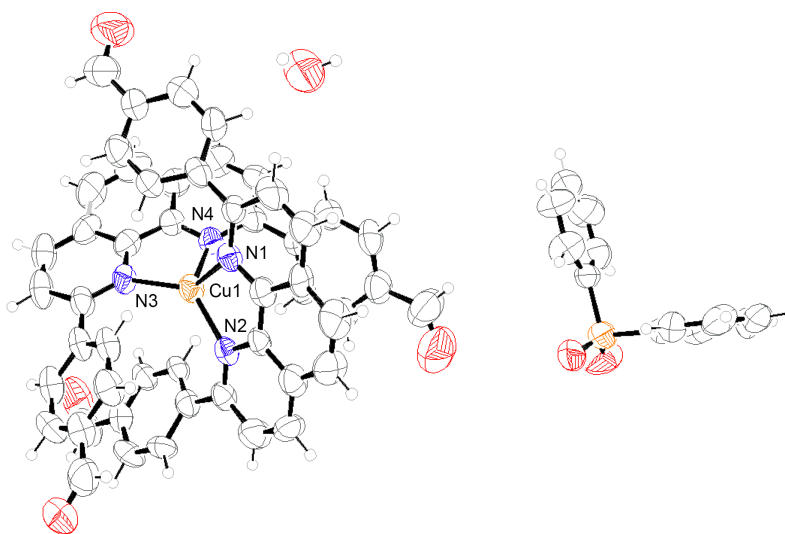
Figure 3.1. ORTEP drawing of the crystal structure of Cu(PBD)$_2$P. Thermal ellipsoids are shown with 50% probability.

Table 3.1. Crystal data and structure refinement Cu(PBD)$_2$P.

Empirical formula	C$_{64}$H$_{42}$CuN$_2$O$_9$P
Formula weight	1077.50
Crystal system	Triclinic
Space group	*P*-1
a/Å	13.784(2)
b/Å	14.350(2)
c/Å	15.994(3)
α/°	76.054(10)
β/°	70.967(10)
γ/°	61.640(10)
Volume/Å^3	2617.5(8)
Z	2
ρ$_{calc}$g/cm^3	1.367
μ/mm^{-1}	1.392
F(000)	1112.0
Radiation	CuKα (λ = 1.54178)
2Θ range for data collection/°	5.876 to 101.45
Index ranges	-13 ≤ h ≤ 13, -14 ≤ k ≤ 14, -15 ≤ l ≤ 16
Reflections collected	10151
Independent reflections	4984 [R$_{int}$ = 0.0839, R$_{sigma}$ = 0.1126]
Data/restraints/parameters	4984/0/694
Goodness-of-fit on F^2	1.041
Final R indexes [I>=2σ (I)]	R$_1$ = 0.0845, wR$_2$ = 0.2338
Final R indexes [all data]	R$_1$ = 0.1497, wR$_2$ = 0.2898
Largest diff. peak/hole / e Å^{-3}	1.03/-0.35

Table 3.2 Selected Structural Data for Complex Cu(PBD)$_2$P.

	Distances / Å
N(1)-Cu(1)	2.098(7)
N(2)-Cu(1)	2.047(8)
N(3)-Cu(1)	2.072(8)
N(4)-Cu(1)	2.060(7)
	Angles / °
N(2)-Cu(1)-N(1)	83.0(3)
N(2)-Cu(1)-N(3)	128.5(3)
N(2)-Cu(1)-N(4)	130.2(3)
N(3)-Cu(1)-N(1)	100.0(3)
N(4)-Cu(1)-N(1)	135.5(3)
N(4)-Cu(1)-N(3)	81.8(3)

3.2.3 Fourier transform infrared spectroscopy

The FT-IR spectra of starting materials, molecular analogue, and activated COFs were collected on a Bruker ALPHA FT-IR Spectrometer equipped with ALPHA's Platinum ATR single reflection diamond ATR module, which can collect IR spectra on neat samples. The signals are given in wavenumbers (cm^{-1}).
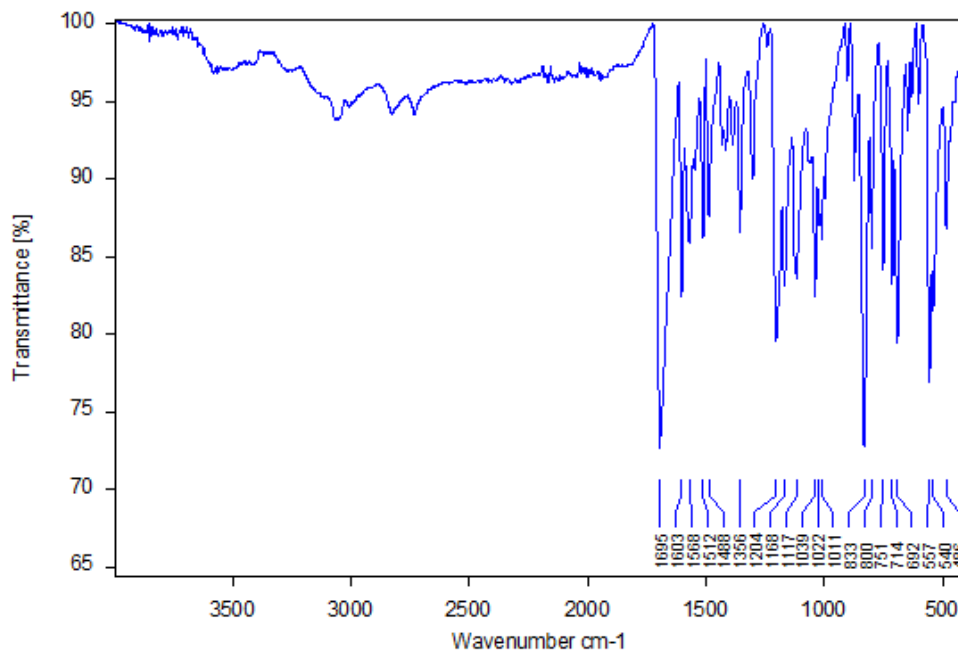
Figure 3.2. FT-IR spectrum of Cu(PBD)$_2$P.
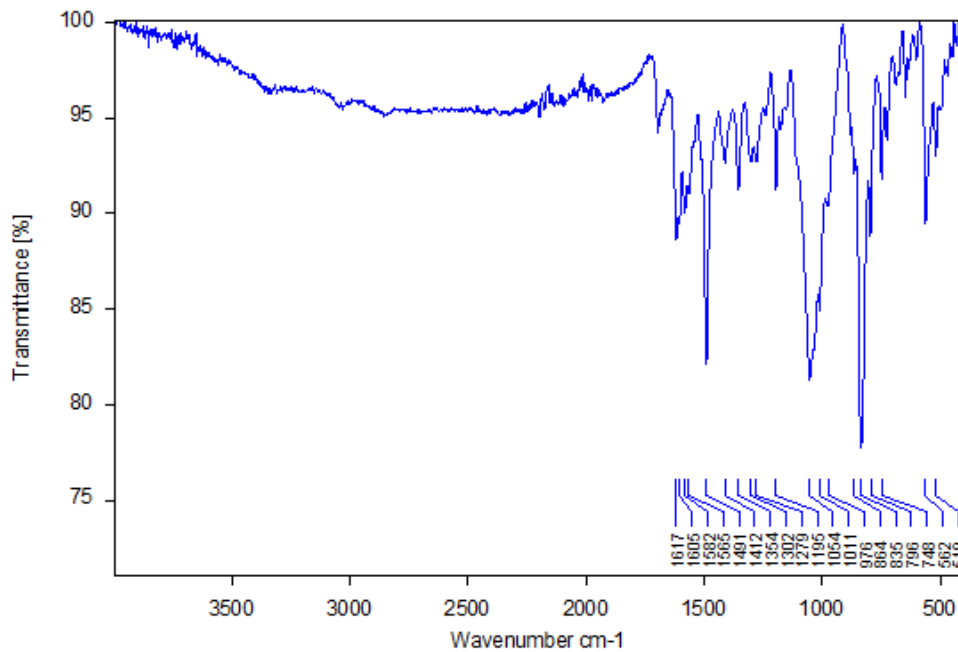
Figure 3.3. FT-IR spectrum of activated COF-504.
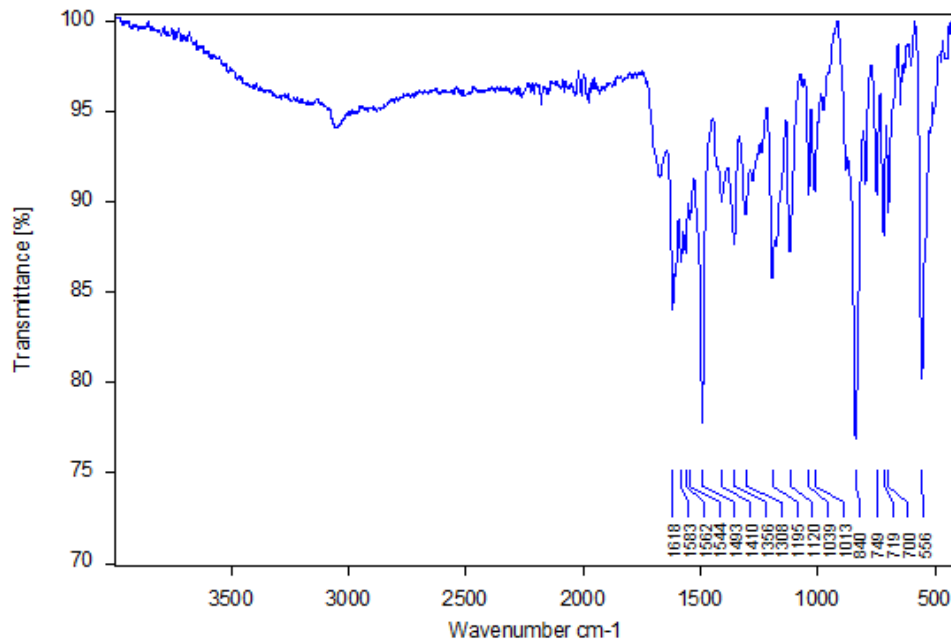
Figure 3.4. FT-IR spectrum of activated COF-504P.
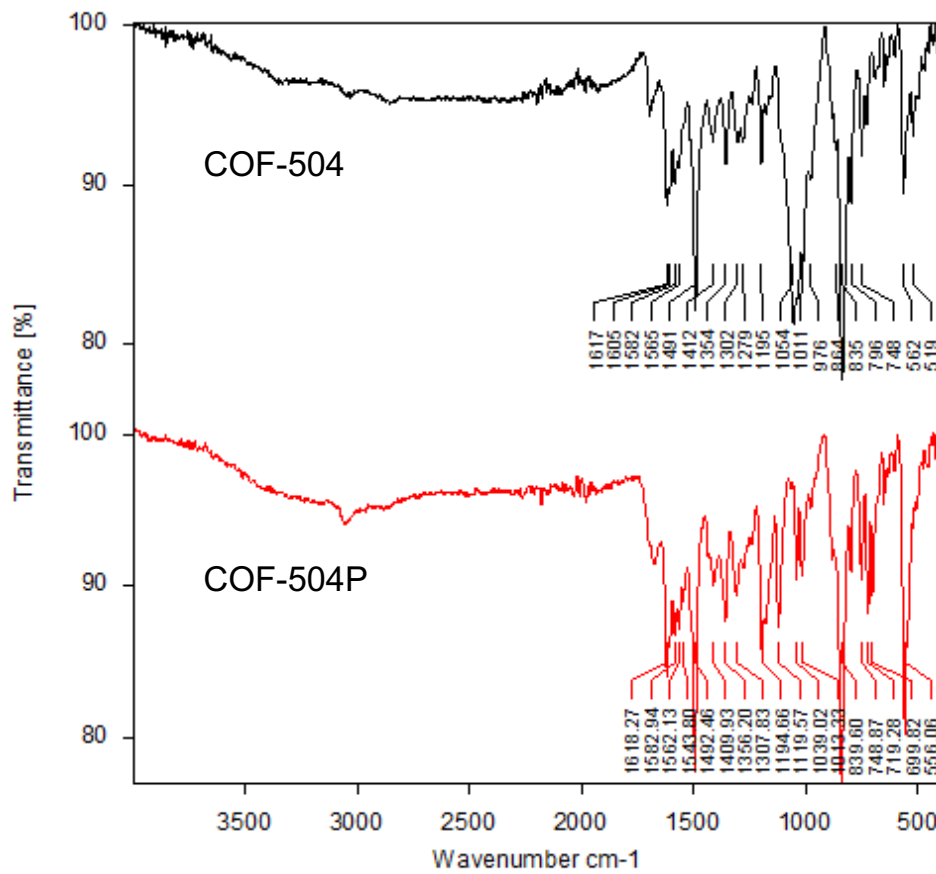
Figure 3.5. Stacked FT-IR spectrum comparison of activated COF-504 (black) and 504-P (red).
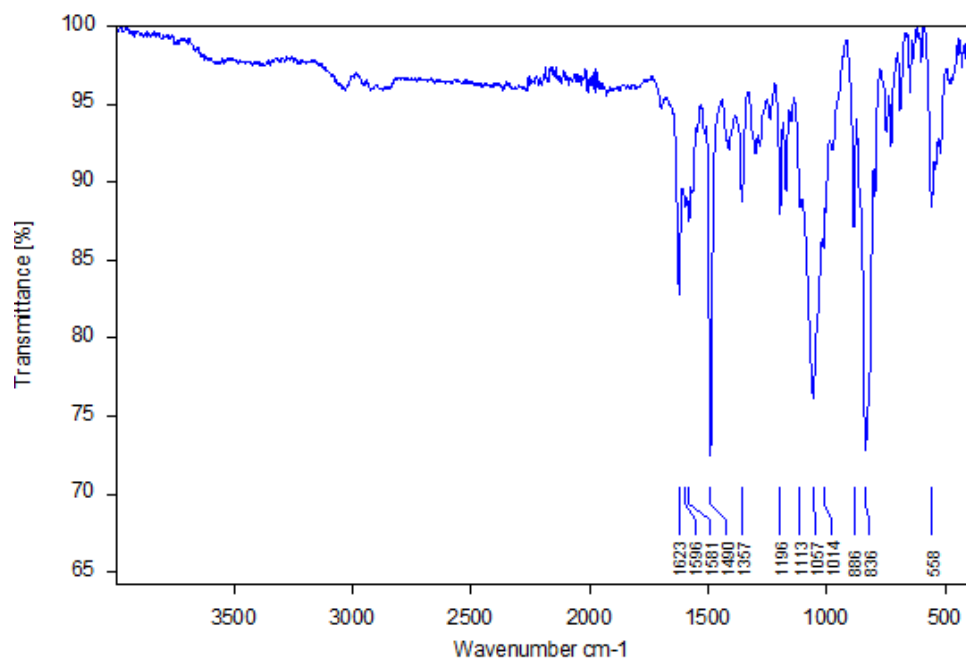
Figure 3.6. FT-IR spectrum of activated COF-506.
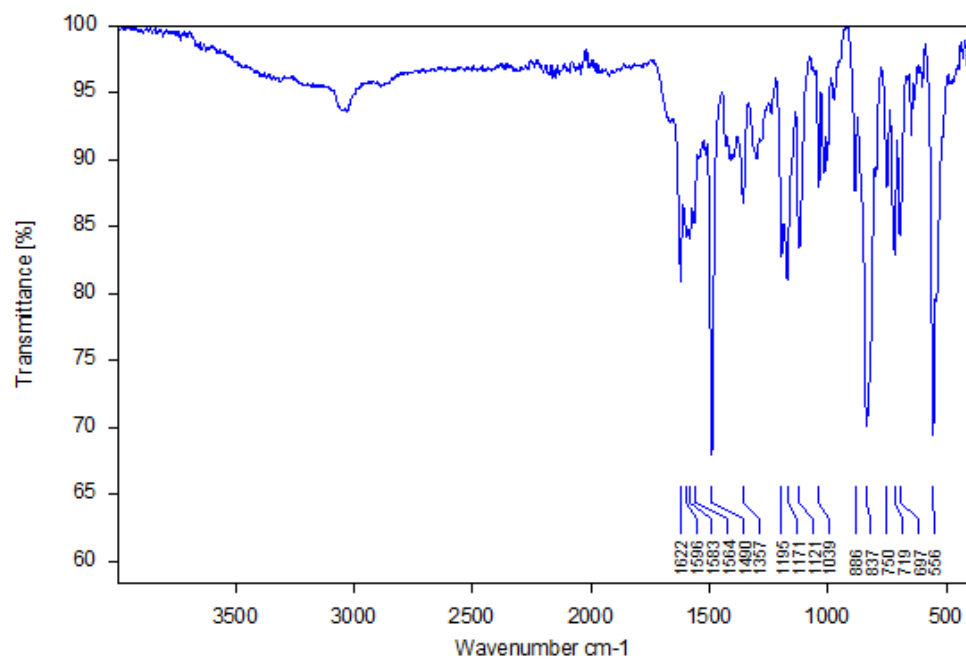
Figure 3.7. FT-IR spectrum of activated COF-506-P.
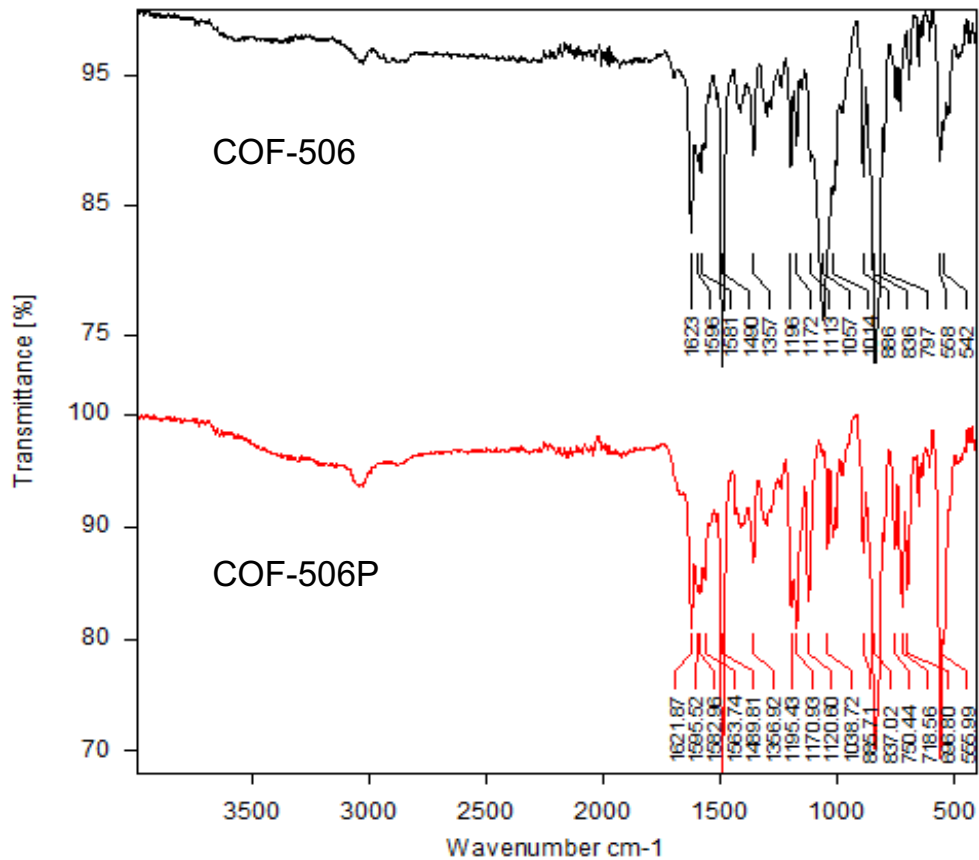
Figure 3.8. Stacked FT-IR spectrum comparison of activated COF-506 (black) and 506-P (red).

3.2.4 Scanning electron microscopy

Samples of COF-504, 504-P and 506 for SEM study were prepared by dropcasting the material in a THF suspension onto a 1 cm^2 silicon wafer. SEM images were recorded on a Quanta™ 3D FEG scanning electron microscope with accelerating voltage of 5 kV with a working distance of 10 mm. In COF-504, primary crystallites of size of 0.1×0.1 μm were aggregated into spheres with diameter of approximately 1.5 μm. In COF-504-P and COF-506, micron-sized plate-shaped and rod-shaped crystals were observed, respectively. No other forms were observed in the individual surveyed samples, and from morphology of primary crystallites, it can be concluded that they are phase pure.
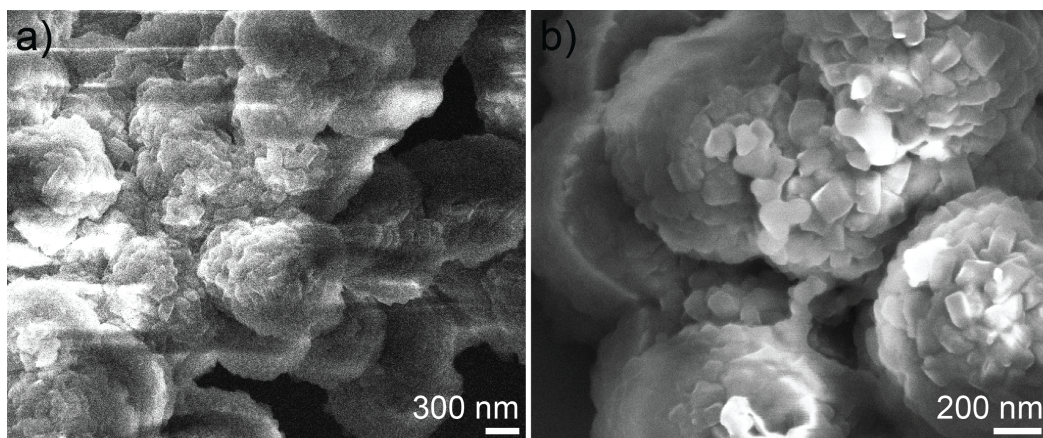
Figure 3.9. Morphology of COF-504 by SEM. (a) Crystalline spheres from aggregated crystallites. (b) Crystal plates on the surface of a sphere.
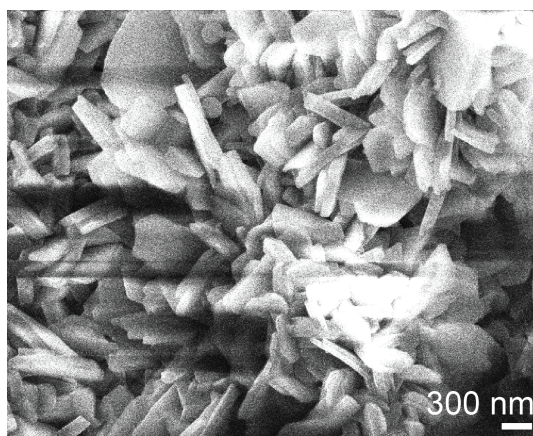
Figure 3.10. Plate morphology of COF-504-P by SEM.
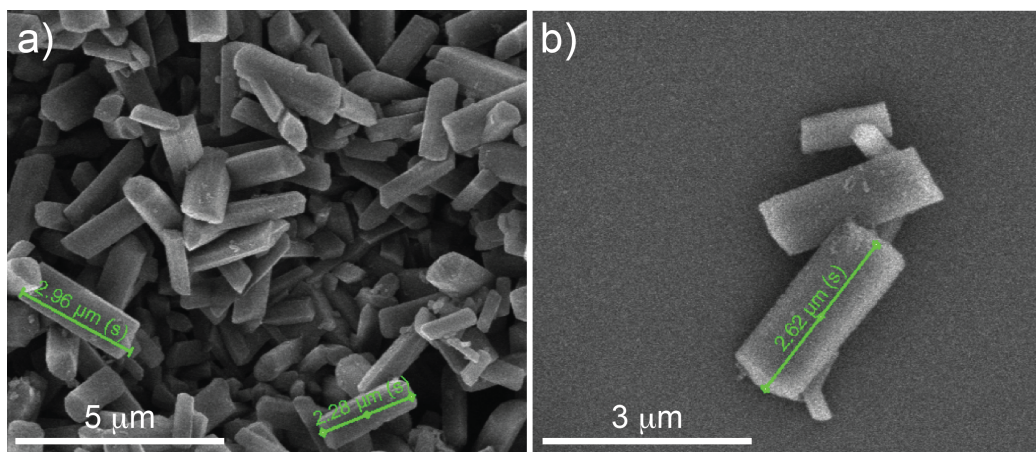
Figure 3.11. Morphology of COF-506 by SEM. (a) Rod-shaped crystallites. (b) Isolated single crystals after sonication in ethanol.

3.2.5 Structural determination by electron diffraction and powder X-ray diffraction studies

Electron diffraction analyses by transmission electron microscopy. A cold field emission JEM-2100F equipped with a DELTA C_s corrector operated at 60 kV was used for HRTEM imaging. Since COF materials are electron beam sensitive, the electron beam damage to the specimen was minimized as much as possible (in this study, the beam density during the observations was less than 500 electrons/(nm^2·s)). A Gatan 894 CCD camera was used for digital recording of the HRTEM images. A single HRTEM image with an exposure time of 2 seconds or a sequence of images (up to 20 frames) was recorded, with a 1 or 2 seconds exposure time for each. After drift compensation, some frames can be superimposed to increase the signal-to-noise (SN) ratio for display. HRTEM images are filtered by a commercial software named HREM-Filters Pro (HREM Research Inc. Japan).

COF-506 crystals were dispersed into ethanol by ultrasonic oscillation and dropped on a carbon film supported TEM grid. 3D electron diffraction tomography (3D-EDT) data were collected on a JEOL JEM-2100, with LaB6 filament and the control of EDT-collect program[11]. The data was further processed by EDT-process program.[11]

Powder X-ray diffraction analysis. PXRD of COFs were obtained by microdiffraction beamline 12.3.2 at the Advanced Light Source, Lawrence Berkeley National Laboratory (λ = 2.06643Å). Area detector (DECTRIS Pilatus 1M) was placed at angle of 39 degrees with respect to incident beam, distance of about 157 mm from sample. Data were azimuthally integrated between 2θ = 4 and 2θ = 40 deg using the XMAS software.

Table 3.3. Atom coordinates of COF-504 structural model

COF-504				
Tetragonal, $P\bar{4}$				
$a = b$ = 20.9133 Å, c = 21.8751 Å				
Atom	x	y	z	Occupancy
C1	0.86467	0.91381	-0.00386	1.0
C2	0.80285	0.93953	0.99842	1.0
C3	0.89192	0.89886	0.93939	1.0
C4	0.85962	0.91446	0.88527	1.0
C5	0.80025	0.94575	0.88778	1.0
C6	0.77091	0.95543	0.94478	1.0
C7	0.90509	0.09542	0.83672	1.0
C8	0.95169	0.04731	0.83407	1.0
N9	0.95453	0.04599	0.94376	1.0
C10	0.97589	0.02336	0.88923	1.0
C11	0.91438	0.09696	0.94767	1.0
C12	0.88734	0.1213	0.89346	1.0
C13	0.02419	0.97658	0.77855	1.0
C14	0.13916	0.35045	0.2982	1.0

C15	0.08165	0.32128	0.3155	1.0
C16	0.15431	0.35572	0.23585	1.0
C17	0.24254	0.37926	0.34041	1.0
N18	0.18077	0.37437	0.34498	1.0
H19	0.06889	0.31808	0.36338	1.0
H20	0.19723	0.38003	0.22097	1.0
H21	0.26723	0.36193	0.30015	1.0
H22	0.78114	0.95182	0.04184	1.0
H23	0.93927	0.87817	0.93702	1.0
H24	0.88291	0.90613	0.84176	1.0
H25	0.7247	0.97855	0.94816	1.0
H26	0.885	0.11516	0.79517	1.0
H27	0.8555	0.16211	0.89489	1.0
H28	0.04222	0.95872	0.73539	1.0
C29	0.35002	0.4302	0.49951	1.0
C30	0.2864	0.45052	0.49322	1.0
C31	0.37935	0.39718	0.45139	1.0
C32	0.34505	0.38331	0.39812	1.0
C33	0.28048	0.4009	0.39317	1.0
C34	0.25178	0.43572	0.44066	1.0
C35	0.43664	0.61838	0.33086	1.0
C36	0.4677	0.55915	0.32946	1.0
N37	0.46748	0.55789	0.43932	1.0
C38	0.48336	0.52948	0.38522	1.0
C39	0.43957	0.6167	0.44187	1.0
C40	0.42309	0.64748	0.38689	1.0
C41	0.51601	0.47057	0.27408	1.0
C42	0.29798	0.94248	0.79076	1.0
C43	0.32986	0.88651	0.8081	1.0
C44	0.29459	0.95884	0.7285	1.0
C45	0.22751	0.02554	0.83226	1.0
N46	0.27	0.98065	0.83809	1.0
H47	0.33372	0.874	0.856	1.0
H48	0.27209	1.00268	0.71361	1.0
H49	0.20724	0.03711	0.78813	1.0
H50	0.26303	0.47659	0.52972	1.0
H51	0.42741	0.37915	0.45635	1.0
H52	0.368	0.35616	0.3621	1.0
H53	0.20224	0.45051	0.43767	1.0

H54	0.42392	0.64263	0.28882	1.0
H55	0.4003	0.69398	0.38735	1.0
H56	0.52791	0.44828	0.23085	1.0
F267	0.37443	0.10258	0.77682	0.5
B268	0.43075	0.06468	0.77787	0.5
F269	0.42942	0.02383	0.82968	0.5
F270	0.48526	0.10503	0.78113	0.5
F271	0.43388	0.02723	0.72383	0.5
Cu57	0	0	0	1.0
Cu58	0.5	0.5	0.5	1.0

Table 3.4. Atom coordinates of COF-506 structural model

COF-506

Monoclinic, $P2_1$
$a = 26.8667$ Å, $b = 23.0617$ Å, $c = 34.3422$ Å
$\beta = 108.2392°$

Atom	x	y	z
Cu1	-0.16709	0.15652	0.71395
Cu2	0.67858	1.2767	0.28203
N3	-0.25352	1.29002	0.32621
N4	-0.35754	1.27762	0.31089
C5	-0.32686	1.28872	0.35006
C6	-0.20208	1.29728	0.33039
C7	-0.44042	1.24744	0.25985
C8	-0.40954	1.26592	0.30136
C9	-0.18526	1.29353	0.294
C10	-0.49879	1.17718	0.21567
C11	-0.51012	1.21624	0.1826
C12	-0.46511	1.19318	0.25414
C13	-0.17746	1.34432	0.2744
C14	-0.23954	1.30831	0.39742
C15	-0.27277	1.29544	0.35796
C16	-0.3484	1.29237	0.38214
C17	-0.17218	1.34158	0.23529
C18	-0.44859	1.28505	0.22638
C19	-0.18468	1.23967	0.27546
C20	-0.40236	1.28269	0.37297
C21	-0.48369	1.26993	0.18804
C22	-0.16705	1.31093	0.36924
C23	-0.18598	1.31651	0.40285
C24	-0.17487	1.28787	0.21532
C25	-0.17916	1.23667	0.23651
C26	-0.26102	1.3129	0.42968
C27	-0.31522	1.30461	0.4221
C28	-0.43288	1.26863	0.3327
H29	-0.51819	1.13539	0.21242
H30	-0.45922	1.16371	0.27975
H31	-0.17836	1.38614	0.28841
H32	-0.16855	1.3817	0.21998
H33	-0.42984	1.3271	0.23038
H34	-0.19104	1.20015	0.29027
H35	-0.42064	1.2849	0.39685
H36	-0.49076	1.3007	0.16304
H37	-0.12582	1.317	0.37334
H38	-0.15925	1.32769	0.43269
H39	-0.18127	1.19444	0.22222
H40	-0.23602	1.3224	0.46057
H41	-0.33105	1.30753	0.44735
H42	-0.4743	1.25968	0.32605
N43	0.22141	0.62098	0.31708
N44	0.12043	0.65206	0.30476
C45	0.14895	0.62982	0.34193
C46	0.27034	0.60271	0.31934
C47	0.04081	0.69904	0.25818
C48	0.07102	0.67315	0.29781
C49	0.28797	0.60756	0.28325
C50	-0.00638	0.68665	0.18562
C51	-0.03447	0.73834	0.18555
C52	0.03106	0.66733	0.22174
C53	0.29294	0.66222	0.26722
C54	0.23107	0.58745	0.38506
C55	0.20106	0.61299	0.34807
C56	0.12745	0.62481	0.37401
C57	0.30086	0.66699	0.22911
C58	0.01517	0.75221	0.25749
C59	0.29497	0.55751	0.26245
C60	0.07647	0.64522	0.36748
C61	-0.02171	0.77194	0.22147
C62	0.30149	0.57545	0.35548
C63	0.2818	0.56828	0.38848
C64	0.30406	0.61685	0.20657
C65	0.30326	0.56212	0.22443
C66	0.20917	0.58116	0.41694
C67	0.15776	0.60038	0.41159
C68	0.04838	0.66975	0.32958
H69	-0.01494	0.65969	0.15848
H70	0.04959	0.62576	0.22188

58

H71	0.28849	0.7012	0.28341	H110	0.26389	0.90556	0.67715
H72	0.30219	0.70996	0.2167	H111	0.38655	0.58839	0.72661
H73	0.02195	0.77723	0.28537	H112	0.40894	0.56629	0.66463
H74	0.29135	0.51494	0.27462	H113	0.41924	0.94498	0.75674
H75	0.0586	0.64274	0.3916	H114	0.24856	0.67993	0.65406
H76	-0.04231	0.81209	0.22237	H115	0.33533	0.9037	0.85443
H77	0.34035	0.55965	0.35797	H116	0.44244	0.98271	0.69829
H78	0.30547	0.54685	0.41614	H117	0.30681	0.57256	0.75997
H79	0.30611	0.52277	0.208	H118	0.30535	0.61225	0.82659
H80	0.23177	0.56183	0.4459	H119	0.27093	0.65843	0.5916
H81	0.14173	0.59601	0.43664	H120	0.31187	0.69982	0.87257
H82	0.00902	0.68564	0.32501	H121	0.32314	0.80562	0.88265
N83	0.30834	0.71502	0.73957	H122	0.34412	0.96235	0.7966
N84	0.31958	0.83192	0.75036	N123	1.16986	-0.26926	0.25515
C85	0.31662	0.79839	0.78211	N124	1.14225	-0.37782	0.2271
C86	0.30806	0.65709	0.73267	C125	1.15258	-0.3383	0.20132
C87	0.34019	0.92133	0.72082	C126	1.17682	-0.21438	0.27023
C88	0.3296	0.88977	0.75434	C127	1.10423	-0.46916	0.24093
C89	0.31603	0.63596	0.69478	C128	1.12425	-0.43206	0.21446
C90	0.31598	0.94347	0.64822	C129	1.16595	-0.20131	0.3085
C91	0.36644	0.96511	0.65361	C130	1.03019	-0.5161	0.25372
C92	0.30296	0.92194	0.68171	C131	1.06025	-0.52559	0.29485
C93	0.36044	0.60256	0.69714	C132	1.05193	-0.4879	0.22706
C94	0.30958	0.70185	0.80901	C133	1.19321	-0.22955	0.34513
C95	0.3108	0.73798	0.77654	C134	1.17488	-0.2387	0.18982
C96	0.32169	0.82322	0.82042	C135	1.16656	-0.28177	0.21582
C97	0.37345	0.59055	0.66176	C136	1.14733	-0.35277	0.16061
C98	0.38989	0.94527	0.72667	C137	1.17692	-0.22347	0.37975
C99	0.28331	0.65472	0.65639	C138	1.13532	-0.48182	0.28109
C100	0.33058	0.88316	0.82516	C139	1.12372	-0.165	0.30717
C101	0.40311	0.96659	0.69325	C140	1.13107	-0.40914	0.14715
C102	0.30677	0.61907	0.76437	C141	1.11349	-0.5091	0.30815
C103	0.30639	0.64167	0.80229	C142	1.18558	-0.16962	0.24529
C104	0.34189	0.61137	0.6234	C143	1.18573	-0.18218	0.20532
C105	0.296	0.64225	0.62086	C144	1.13292	-0.18929	0.37799
C106	0.31306	0.72687	0.84712	C145	1.10718	-0.15911	0.34148
C107	0.3193	0.78724	0.85283	C146	1.17066	-0.2533	0.14915
C108	0.33536	0.91649	0.79233	C147	1.15712	-0.31015	0.13464
H109	0.2869	0.94219	0.61803	C148	1.11867	-0.4486	0.17382

H149	0.98919	-0.52851	0.24251	C188	0.70568	0.14181	-0.07667
H150	1.02723	-0.47844	0.19607	C189	0.72128	0.15359	-0.03464
H151	1.22625	-0.25727	0.34661	C190	0.73685	0.20982	-0.01978
H152	1.19776	-0.24695	0.40747	C191	0.73404	0.25457	-0.04821
H153	1.1763	-0.47015	0.29154	C192	0.71747	0.24302	-0.09026
H154	1.10191	-0.14331	0.27893	C193	0.70457	0.18654	-0.10493
H155	1.12639	-0.42205	0.11589	C194	0.78542	0.1791	0.05257
H156	1.13815	-0.5164	0.33948	C195	0.80237	0.18925	0.0948
H157	1.1908	-0.12528	0.25628	C196	0.79199	0.24219	0.11045
H158	1.19219	-0.14754	0.18618	C197	0.76395	0.28513	0.08322
H159	1.07338	-0.13197	0.33889	C198	0.74629	0.27481	0.04101
H160	1.17692	-0.22069	0.12851	C199	0.75652	0.22147	0.02511
H161	1.1535	-0.32044	0.10311	N200	0.80451	0.24816	0.154
H162	1.10397	-0.49126	0.16269	C201	0.81163	0.2969	0.17396
C163	0.48069	0.5727	0.56689	H202	0.69519	0.09765	-0.08625
C164	0.50389	0.56345	0.53638	H203	0.7213	0.1184	-0.01378
C165	0.47278	0.55843	0.49506	H204	0.74613	0.2983	-0.03804
C166	0.41806	0.56328	0.48501	H205	0.71674	0.27801	-0.11149
C167	0.39482	0.57264	0.51552	H206	0.79493	0.13792	0.04153
C168	0.4262	0.57764	0.55685	H207	0.82318	0.15548	0.11552
C169	0.53945	0.50773	0.47018	H208	0.75335	0.32551	0.09448
C170	0.56162	0.49523	0.43951	H209	0.72318	0.30801	0.02103
C171	0.54193	0.52154	0.40071	H210	0.81229	0.33731	0.15808
C172	0.49932	0.55955	0.39296	N211	0.69472	0.17705	-0.14573
C173	0.47727	0.57235	0.4237	C212	0.68573	0.12556	-0.16588
C174	0.49708	0.54651	0.46268	C213	-0.07617	0.31527	0.51064
N175	0.56174	0.5075	0.36777	C214	-0.05261	0.3264	0.48056
C176	0.60866	0.48849	0.37204	C215	-0.0123	0.36756	0.48747
H177	0.5053	0.57623	0.59859	C216	0.0053	0.39627	0.52534
H178	0.54621	0.56053	0.54511	C217	-0.01829	0.38525	0.55538
H179	0.39321	0.55837	0.4536	C218	-0.0597	0.34561	0.54813
H180	0.35252	0.57456	0.50659	C219	-0.02494	0.39804	0.41559
H181	0.55453	0.48574	0.49941	C220	-0.00527	0.41457	0.3843
H182	0.59294	0.46362	0.44591	C221	0.04928	0.4157	0.39123
H183	0.48321	0.57931	0.36298	C222	0.08334	0.40097	0.4301
H184	0.44482	0.60259	0.41697	C223	0.06356	0.38468	0.46152
N185	0.40466	0.5861	0.58966	C224	0.00922	0.38285	0.45435
C186	0.35742	0.60317	0.58632	N225	0.07157	0.435	0.36062
H187	0.32996	0.61493	0.55683	C226	0.04652	0.44035	0.32166

H227	-0.10713	0.28334	0.50403	H266	0.63757	0.48474	0.40217
H228	-0.06607	0.30319	0.4517	P267	0.33898	0.11312	0.75718
H229	0.03615	0.42847	0.53117	O268	0.32517	0.18058	0.76177
H230	-0.005	0.40862	0.58419	O269	0.35501	0.09244	0.8045
H231	-0.06687	0.39898	0.41	C270	0.27717	0.07662	0.7291
H232	-0.03309	0.42792	0.35546	C271	0.39826	0.11111	0.74121
H233	0.12537	0.40245	0.43609	C272	0.24093	0.06231	0.7493
H234	0.09056	0.37346	0.49136	C273	0.19379	0.03478	0.72794
N235	-0.08362	0.33817	0.57964	C274	0.18222	0.02247	0.68616
C236	-0.12542	0.30841	0.57767	C275	0.21792	0.03739	0.66582
H237	-0.14686	0.28546	0.54998	C276	0.26538	0.06427	0.68725
C238	1.13811	0.19595	-0.05224	C277	0.39653	0.13211	0.70252
C239	1.18529	0.19829	-0.01987	C278	0.44169	0.13136	0.69059
C240	1.22555	0.23633	-0.02138	C279	0.48884	0.11005	0.71739
C241	1.21745	0.27187	-0.05605	C280	0.49084	0.08929	0.75609
C242	1.17005	0.27007	-0.0882	C281	0.44567	0.08974	0.76798
C243	1.1297	0.23188	-0.08658	H282	0.24903	0.07268	0.78143
C244	1.29742	0.18934	0.03531	H283	0.16609	0.02333	0.74368
C245	1.34257	0.19273	0.06944	H284	0.14567	0.00134	0.66958
C246	1.36706	0.24671	0.08229	H285	0.20915	0.02744	0.63354
C247	1.34646	0.29629	0.05925	H286	0.29294	0.07499	0.67129
C248	1.30092	0.29298	0.0254	H287	0.36043	0.14933	0.68174
C249	1.27544	0.23953	0.01336	H288	0.44017	0.14735	0.66061
N250	1.40871	0.25338	0.11705	H289	0.52378	0.10958	0.70818
C251	1.42953	0.21252	0.14611	H290	0.52736	0.07284	0.77683
H252	1.10777	0.16614	-0.0504	H291	0.44778	0.07343	0.79798
H253	1.18986	0.17082	0.00659	P292	0.664	0.60129	0.08905
H254	1.24811	0.30053	-0.05872	O293	0.65823	0.6408	0.04893
H255	1.16646	0.29758	-0.11437	O294	0.6928	0.64597	0.1256
H256	1.27976	0.14724	0.02611	C295	0.59817	0.58688	0.09212
H257	1.35767	0.15274	0.08509	C296	0.70978	0.54147	0.09083
H258	1.3646	0.33821	0.06853	C297	0.56448	0.63316	0.09226
H259	1.28481	0.33266	0.0095	C298	0.51512	0.62247	0.09625
N260	1.08376	0.22622	-0.11788	C299	0.49931	0.56555	0.10012
C261	1.06681	0.25994	-0.15192	C300	0.53284	0.51925	0.09993
H262	0.09724	0.29682	0.83524	C301	0.58215	0.52983	0.0958
H263	0.00575	0.42776	0.3093	C302	0.73137	0.53348	0.05905
H264	0.68429	0.08789	0.83904	C303	0.76612	0.48763	0.06088
H265	0.56619	0.66707	0.84577	C304	0.77931	0.4497	0.09438

C305	0.75757	0.45745	0.12597		H311	0.60784	0.49372	0.09581
C306	0.72298	0.5033	0.12424		H312	0.72138	0.56251	0.03295
H307	0.57661	0.67739	0.0896		H313	0.78284	0.48151	0.03637
H308	0.48923	0.65832	0.0965		H314	0.8063	0.41433	0.09577
H309	0.46119	0.55738	0.1034		H315	0.7672	0.42792	0.15172
H310	0.52067	0.4752	0.10307		H316	0.70609	0.50875	0.1487

3.2.6 Thermogravimetric analysis

Samples were run on a TA Instruments Q-500 series thermal gravimetric analyzer with samples held in a platinum pan under nitrogen atmosphere. A ramp rate of 5 °C/min was used.
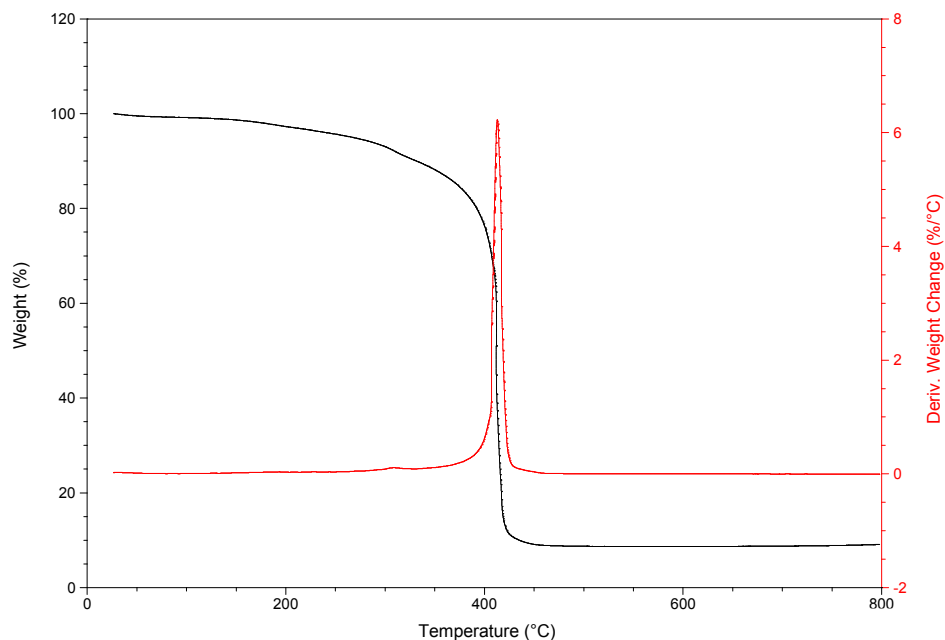

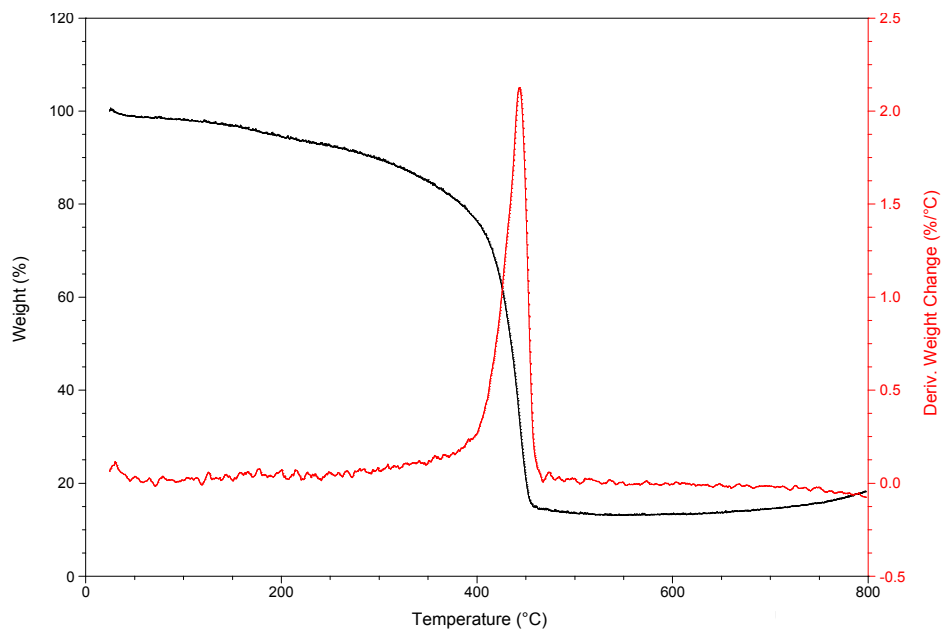**Figure 3.12.** TGA trace for activated COF-504 (black) and derivative of weight change (red).

Figure 3.13. TGA trace for activated COF-504P (black) and derivative of weight change (red).
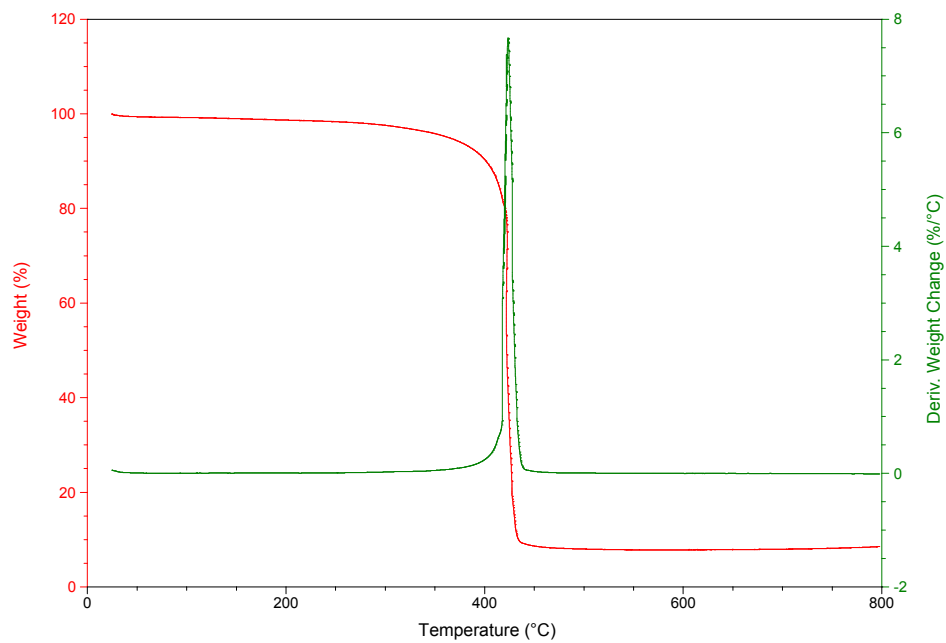
Figure 3.14. TGA trace for activated COF-506 (red) and derivative of weight change (green).
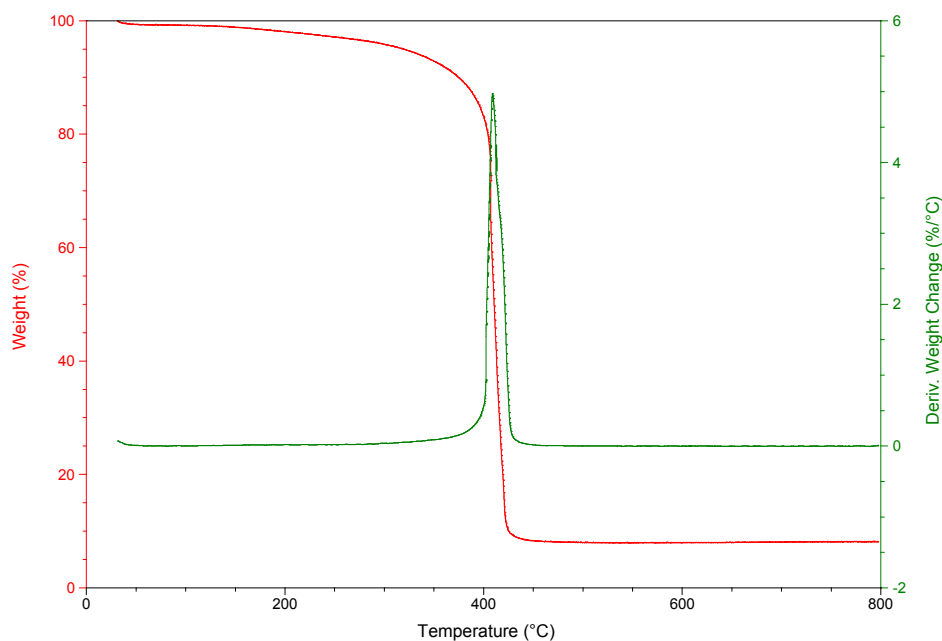
Figure 3.15. TGA trace for activated COF-506P (red) and derivative of weight change (green).

3.2.7 Digestion studies by ^{1}H NMR

The activated COF sample (2 mg) was transferred to a 4 mL vial. Deuterated dimethyl sulfoxide (dmso-d$_6$, 400 µL) was add to the vial followed by the addition of 30 µL of dCl (20 wt. % in D$_2$O). The vial was capped and the mixture was placed in a preheated 85 °C oven for 1-4 h to completely digest the COFs. The final clear solution was used for the ^{1}H NMR experiment.

Figure 3.16. ^{1}H NMR data of digested COF-504 in dmso-d$_6$.

Figure 3.17. ^{1}H NMR data of digested COF-504P in dmso-d$_6$. *PDA was easily oxidized during the acid-assisted digestion.
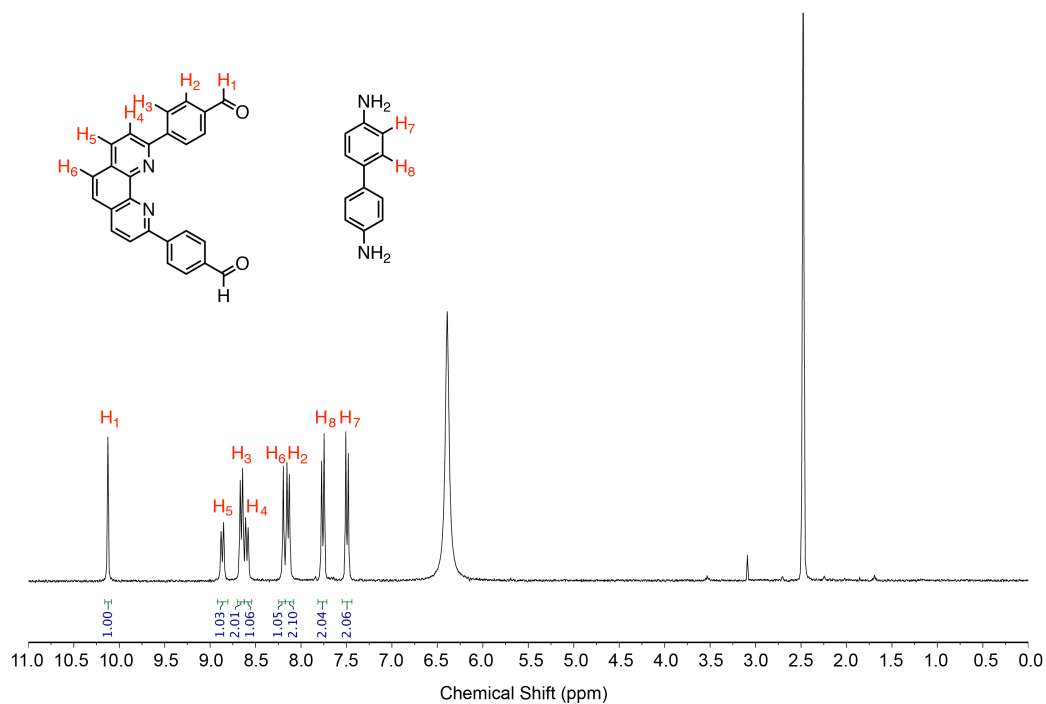
Figure 3.18. ^{1}H NMR data of digested COF-506 in dmso-d$_6$.
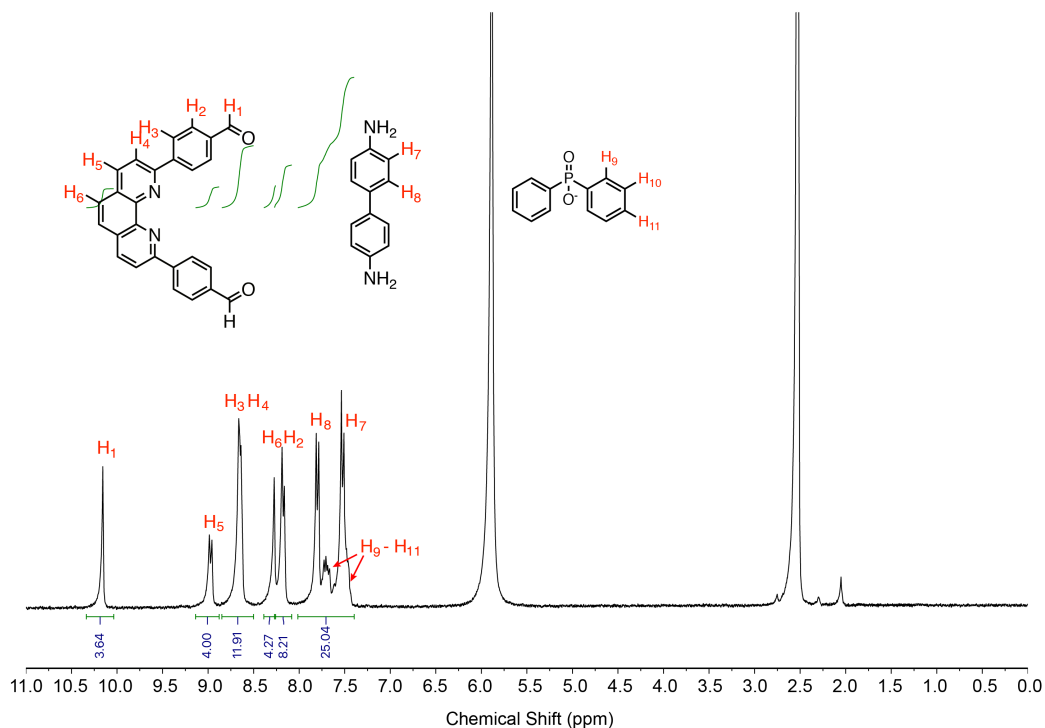
Figure 3.19. ^{1}H NMR data of digested COF-506 in dmso-d$_6$.

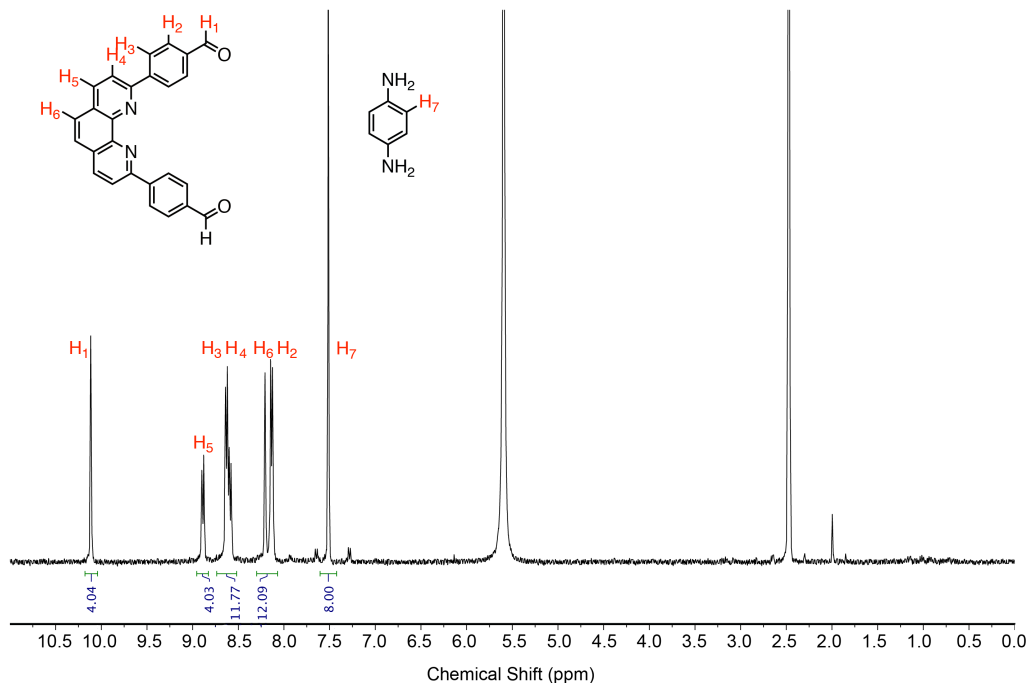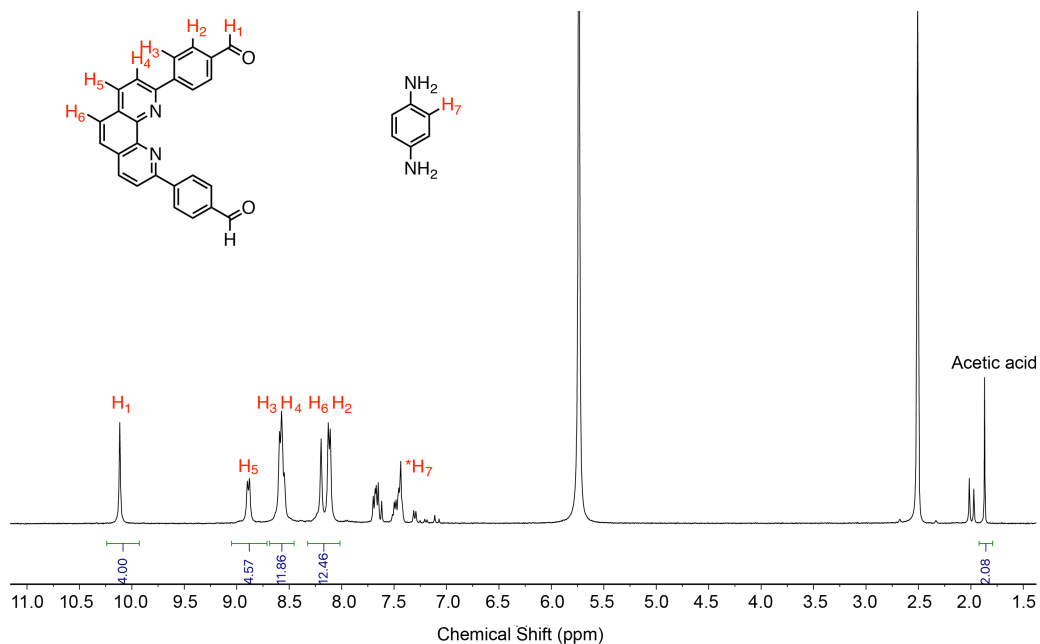### 3.2.8 Procedure for demetalation and remetaltion

To a suspension of COF-506 powder was added a 0.5 M MeOH KCN solution heated at 75 °C. The solution was replaced by a fresh solution of KCN every 24 h and this procedure was repeated two times. Subsequently, both samples were washed with anhydrous CH$_3$OH and dried at 75 °C under 50 mTorr for 12 h. The demetalated material was observed to be pale-yellow in color, in contrast to the dark brown color of COF-506. The demetalation process was unsuccessful with COF-504 and 505 under the same conditions, presumably due to more dense structures and resulting steric hinderance.

The remetalation process was carried out in similar conditions with the complexation reaction to yield complex Cu(PBD)$_2$BF$_4$. Dried powder of the demetalated material was immersed in anhydrous CHCl$_3$, to which was added a 0.1 M Cu(CH$_3$CN)BF$_4$ solution in CH$_3$CN under N$_2$ atmosphere. This mixture was stirred for 12 h under N$_2$ at room temperature and dark brown color was recovered.
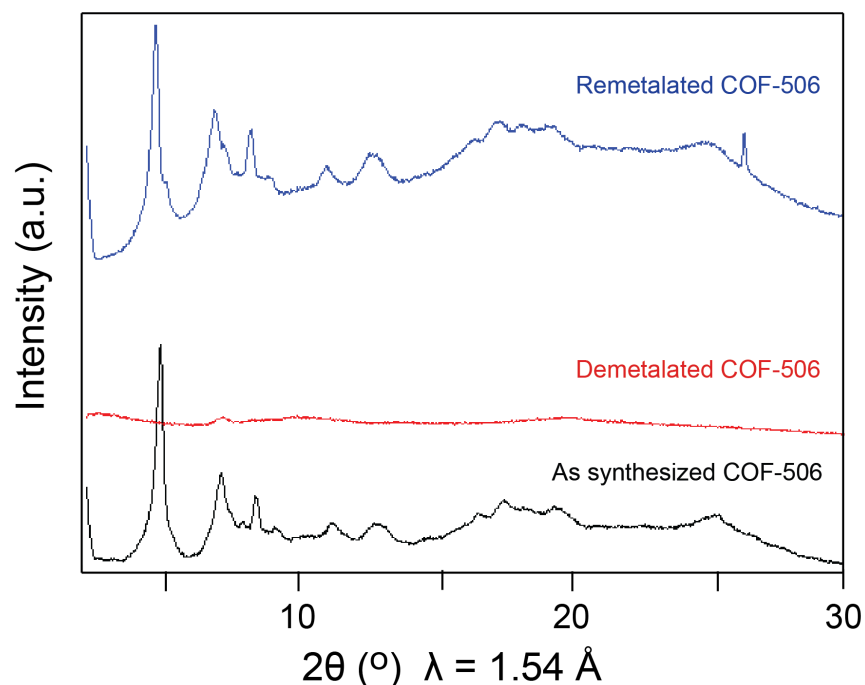
Figure 3.20. PXRD patterns of as-synthesized COF-506, the demetalated and remetalated materials. The crystallinity of COF-506 decreases upon demetalation and is fully restored after remetalation with copper(I) ions.

3.2.9 Inductively coupled plasma atomic emission spectroscopy

Inductively coupled plasma atomic emission spectroscopy (ICP-AES) was used to determine the copper component in these materials. Samples were dissolved in OPTIMA grade nitric acid. 5 mg of each activated COF was dissolved in 1 mL of nitric acid, which was then diluted to 1:20 (*v/v*) with DI H$_2$O, and analyzed on an Agilent 7500ce ICP-AES using helium collision gas mode.

Table 3.3. Calculated and measured copper content in COFs

Copper content	COF-504	COF-504P	COF-506	COF-506-P
Calculated	5.74%	5.77%	4.90%	4.69%
Measured	5.6%	5.7%	4.8%	4.8%

In the demetalated COF-506, copper content was determined to be less than 0.04%, which is less than 1% of the original Cu concentration. After remetalation, the Cu content was determined to be 4.4% to 4.5%, which is 92-94% of COF-506.

3.2.10 Low pressure THF vapor adsorption experiments

THF vapor adsorption isotherms were collected at 283 K using a Microtrac BELSorp-Aqua3 adsorption apparatus with a water circulator bath. The water bath with circulator was used for the temperature control at 283 K. Anhydrous and degassed THF was used for vapor adsorption. The COF samples were activated under dynamic vacuum at 75 °C for 12 h before the measurement.

3.2.11 Inclusion studies of fluorescent dye molecules

100 ppm stock solutions of methyl blue (MB), hydroxy naphthol blue disodium salt (HN) and methyl orange (MO) were prepared by dissolving 100 mg of dye in 1 L of methanol. 5 mg of activated COF samples were added to 10 mL of the dye solution. The mixture was stirred at room temperature and kept in the dark for 3 h. Aliquots of supernatant solution were collected after 5 min, 10 min, 30 min, 1 h, 3 h and diluted by ten-fold with methanol. UV-vis spectra were recorded on a Shimadzu UV-1800 spectrophotometer. The absorbance at 432nm (MO), 540 nm (HN), and 606 nm (MB) were recorded at various time points and plotted as a function of time; the decrease in absorbance is attributed to the inclusion of dye molecules into the COFs.
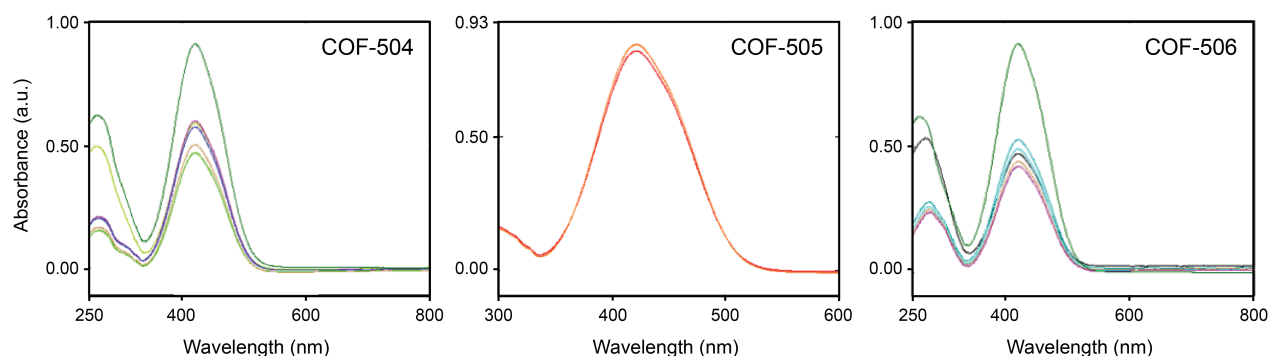

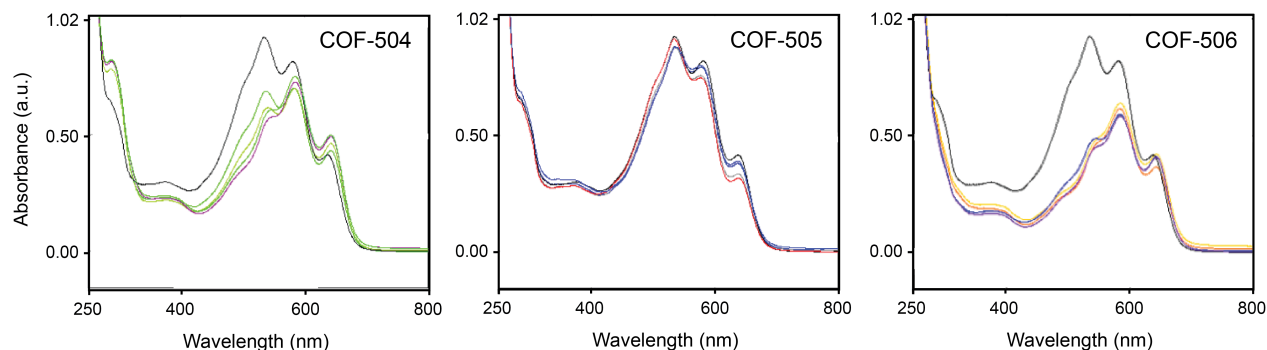**Figure 3.21.** UV-vis spectra of supernatant MO solution during incubation with COF samples.

Figure 3.22. UV-vis spectra of supernatant HN solution during incubation with COF samples.
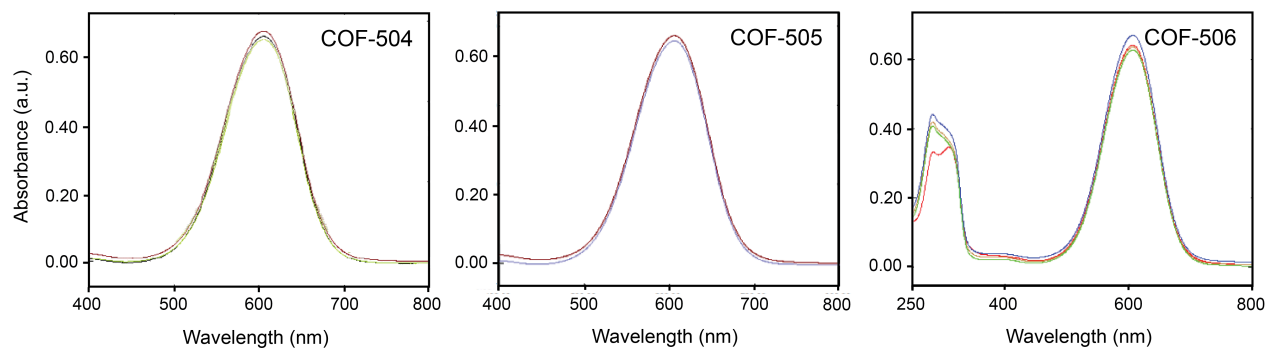
Figure 3.23. UV-vis spectra of supernatant MB solution during incubation with COF samples.
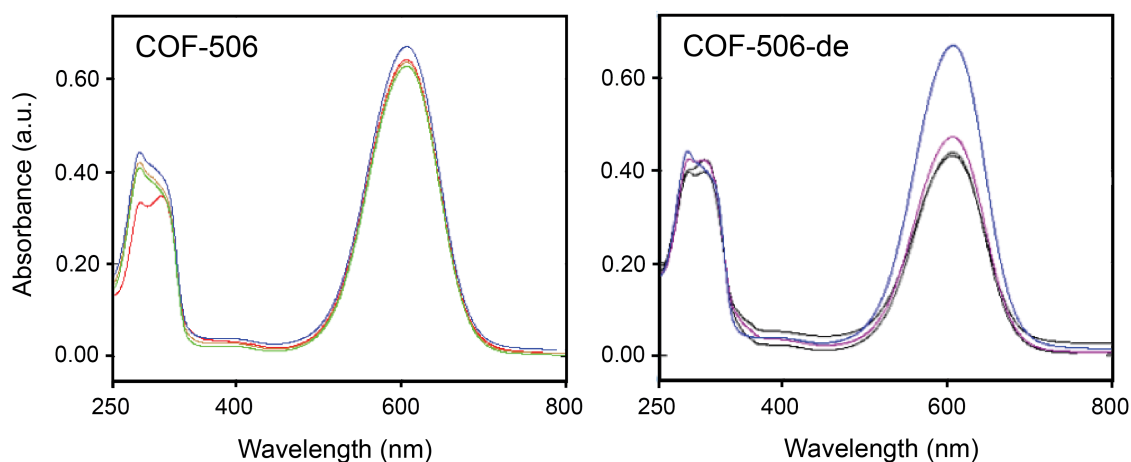
Figure 3.24. UV-vis spectra of supernatant MB solution in the presence of COF-506 and demetalated COF-506.

3.3 Results and Discussion
3.3.1 Designed synthesis and characterization of COF-504 and COF-506

The design and synthesis of the first woven framework, COF-505, have been previously reported by using an aldehyde-functionalized Cu(PDB)$_2$BF$_4$ complex as the tetrahedral building block, which was reticulated with a linear ditopic benzidine linker to yield a 2-fold interpenetrated 3D framework with an underlying **dia** topology. **dia** nets are self-dual and as such prone to self-interpenetration.[12] In the case of COF-505 this limits the available internal space and restricts the potential movement of the woven threads. To avoid interpenetration and maximize the guest accessible void space and thus the potential for dynamics in woven structures, *p*-phenylenediamine (PDA), which is one phenyl ring shorter than the benzidine linkers in COF-505, was employed as the linear linker in COF-504 (Scheme 3.3a). Here, a second net cannot fit within the structure due to the limited distance between each pair of neighboring complexes. This results in the non-interpenetrated structure COF-504. Alternatively, in COF-506, while benzidine is still employed as the linker, a bulky anion (diphenylphosphinate) is used to occupy the internal voids thus preventing interpenetration during framework formation. The anions are then post-synthetically

exchanged with tetrafluoroborate (BF$_4^-$) to obtain the non-interpenentrated structure COF-506 (Scheme 3.3b). Fundamentally, COF-506 is the result of an isoreticular expansion of COF-504.

Scheme 3.3. Synthetic strategies to make non-interpenetrated isoreticular COFs, by (a) employing short organic linkers (PDA) to make COF-504 or (b) including a bulky anion, diphenylphosphinate, during the synthesis which is subsequently exchanged with the smaller BF$_4^-$ to yield COF-506.
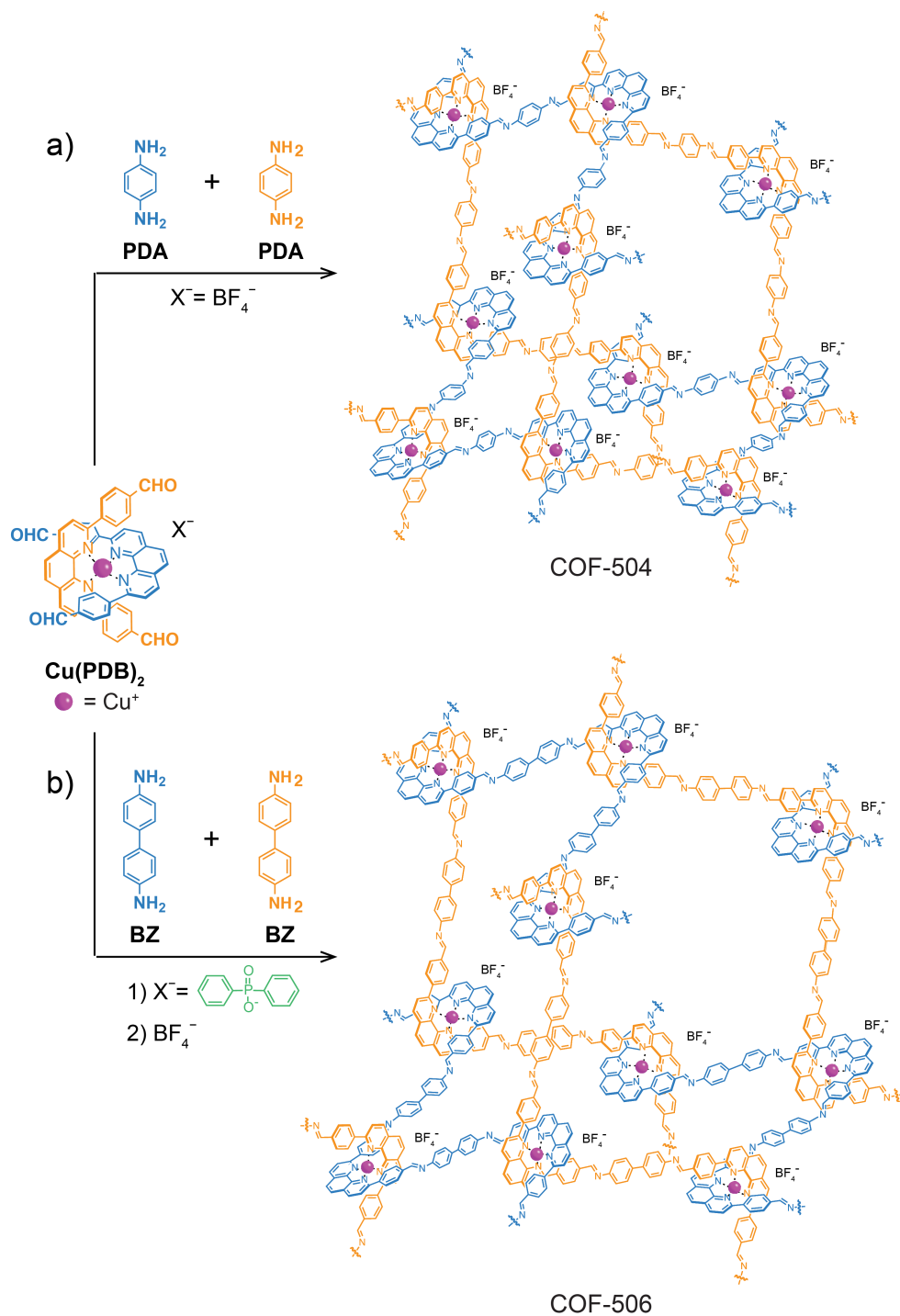
Both COFs were synthesized by combining a mixture of Cu(PDB)$_2$ (with BF$_4^-$ or diphenylphosphinate as the anion), PDA or BZ in suitable solvents, and aqueous acetic acid (6 mol/L, 100 μL). The reaction mixture was sealed in a Pyrex tube and heated at 120 °C for 3 days. The resulting precipitates were collected by centrifugation and washed with anhydrous THF to yield dark brown crystalline solids, which were found to be insoluble in common organic solvents or water.

Fourier-transform infrared spectroscopy (FT-IR) studies were performed on the COFs to confirm the formation of imine linkages. The FT-IR spectra of COF-504 and COF-506 show peaks at 1617 and 1623 cm^{-1} (1622 cm^{-1} for COF-505), which are assigned to the characteristic C=N stretching mode of their imine bonds. The anion exchange of COF-506 was also monitored by FT-IR where, after ion exchange, the presence of a prominent band at 1057 cm^{-1} was assigned to the asymmetric stretching mode of BF$_4^-$. The identical FT-IR spectra of COF-505 and COF-506 indicate the same chemical composition of both structures. Furthermore, ^{1}H NMR spectra of acid-digested materials show an equimolar ratio of the starting materials incorporated into the two materials, confirming completion of the COF-forming imine condensation reaction. It should be noted that attempts to link Cu(PDB)$_2$-P by PDA to yield COF-504-P were unsuccessful. Upon digestion of COF-504-P approximately 70% of acetate instead of the diphenylphosphinate anion was found to be included into the framework. This is attributed to spatial confinement in COF-504 which prohibits complete inclusion of bulky diphenylphosphinate anions (pKa of acetic acid = 4.75, pKa of diphenylphosphinic acid = 2.30).

3.3.2 Electron microscopy studies and structural determination of the COFs

The morphology and purity of the as-synthesized material were examined by Scanning electron microscopy (SEM). In COF-504 block-shaped crystallites of ~200 nm are aggregated into spheres of 2 μm in diameter (Figure 3.25a). No other phase was observed from SEM images taken throughout the material. Transmission electron microscopy (TEM) micrographs confirm the single-crystallinity of these crystallites, and the lattice fringes match well with the d spacings of the reflections observed by powder X-ray diffraction (PXRD). A structure model of COF-504 was constructed in Materials Studio 8.0[13] in the tetragonal space group $P\bar{4}$. The calculated PXRD pattern of the modeled structure was found to be in good agreement with the experimental pattern of activated COF-504.
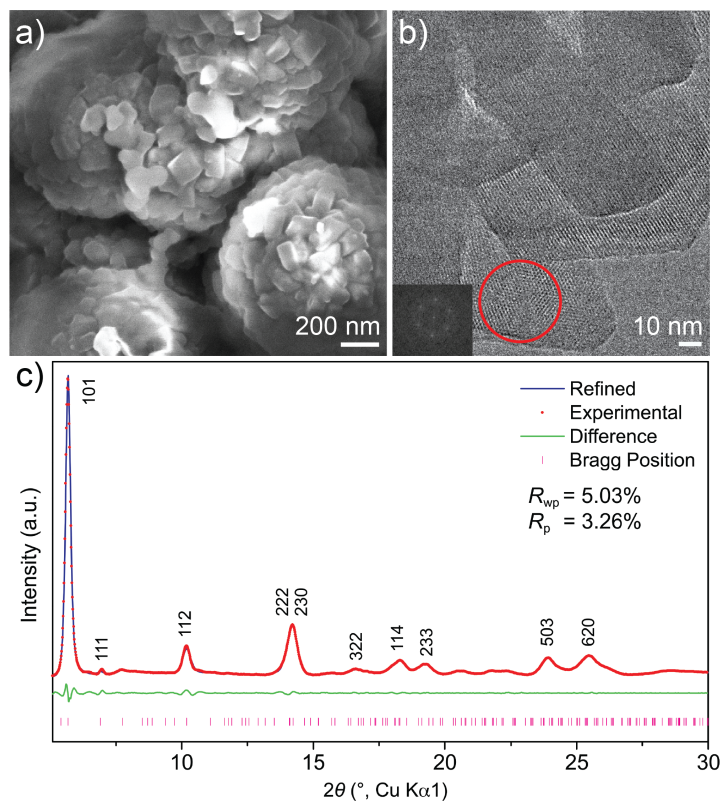
Figure 3.25. Electron microscopy and PXRD studies of COF-504. (**a**) Individual crystallites aggregated into spherical particles are observed by SEM. (**b**) TEM micrograph showing lattice fringes. Inset, fast Fourier transform (FFT) of the marked area in the red circle. (**c**) Indexed PXRD pattern of the activated sample of COF-504 (red) and the Pawley fitting (blue) from the modeled structure.

To elucidate the structure of COF-506, a single crystal (Figure 3.26b inset) of the sample was studied by 3D electron diffraction tomography (3D-EDT).[14] One EDT data set was collected (Figure 3.26b) by combining specimen tilt and electron-beam tilt in the range of –30.2° to +41.2° with a beam-tilt step of 0.2°. From the acquired data set, the 3D reciprocal lattice of COF-506 was constructed and identified as a monoclinic Bravais lattice. The unit-cell parameters were found to be $a = 27.7$ Å, $b = 21.9$ Å, $c = 33.8$ Å, $\beta = 104°$ and $V = 19895$ Å^3. The unit-cell parameters were further refined to be $a = 27.0$ Å, $b = 23.1$ Å, $c = 34.6$ Å, $\beta = 108°$ and $V = 20533$ Å^3 by Pawley refinement of the PXRD pattern. High-resolution TEM images viewed from the [010] and [001] directions show ordered lattice fringes and the resultant FFT matches well with the experimental dataset of the 3D-EDT (Figure 3.26c and d). The reflection condition was found to be $0k0$: $k = 2n$, which suggests a 2_1 screw axis along the crystallographic b direction. According to these parameters, a structure model of COF-506 in the monoclinic space group $P2_1$ was constructed in Materials Studio 8.0. The calculated PXRD pattern of the modeled structure was found to be in good agreement with the experimental pattern of activated COF-506 (Figure 3.27).
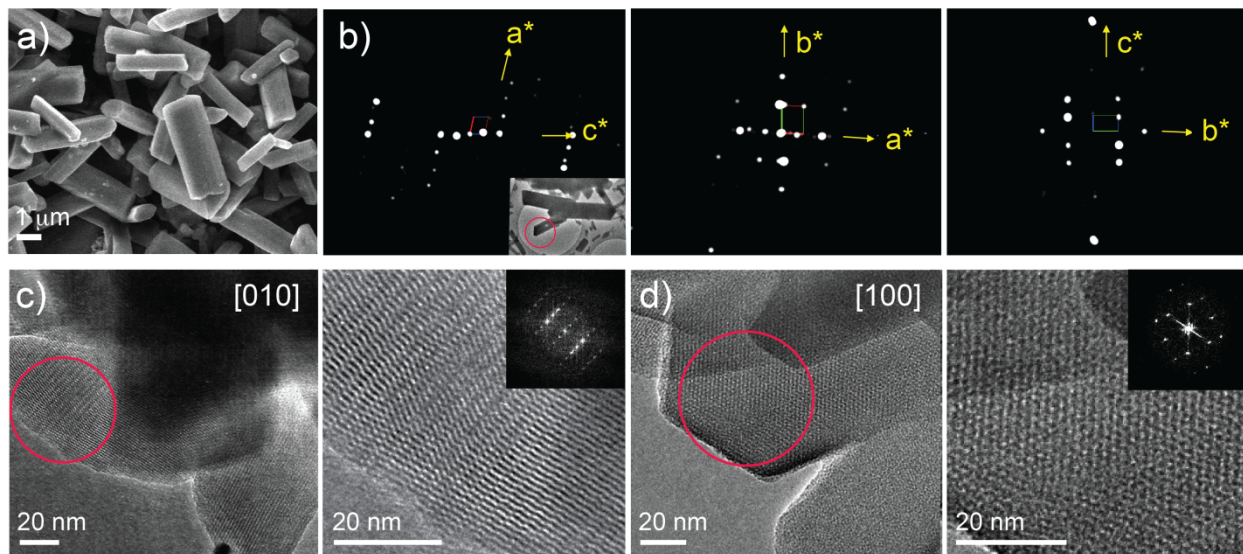
Figure 3.26. Electron microscopy studies of COF-506. **(a)** Rod-shaped single crystals of COF-506 are observed by SEM. **(b)** 2D projection of the reconstructed reciprocal lattice of COF-506 obtained at 298 K from a set of 3D-EDT data. Inset, TEM image of a single crystal used for 3D-EDT. (**c** and **d**) HRTEM images of COF-506 taken with [010] and [100] incidence, respectively, and magnified views onto the circled areas of the single crystal with FFT in the inset which shows a good agreement with the experimental measurements in (**b**).
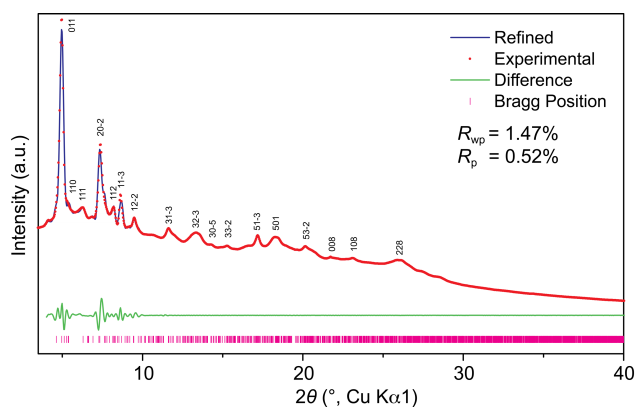
Figure 3.27. Indexed PXRD pattern of the activated sample of COF-506-P (red) and the Pawley refinement (blue) of the modeled structure. The pattern does not change upon anion exchange to COF-506. The difference plot and calculated Bragg positions are highlighted in green and pink, respectively.

3.3.3 THF vapor adsorption and dye inclusion studies for assessment of guest-accessible void space in COFs

The design principles of reticular chemistry have been applied towards the synthesis of non-interpenetrated COF-504 and COF-506. The available internal void space was first examined by THF vapor adsorption (Figure 3.28a). COF-504 and COF-505 show a minimal amount of THF

73

inclusion, which could be due to the relatively small pores that are occupied by solvated BF_4^- anions. COF-506, the non-interpenetrated version of COF-505, exhibits a Type I isotherm with a major uptake step at low partial pressure indicative of a microporous material. The first step in the isotherm is reached at $P/P_0 = 0.2$ with 39.6 cm^3g^{-1} and the maximum uptake reached 56.6 cm^3g^{-1} at P/P_0 is 0.98.
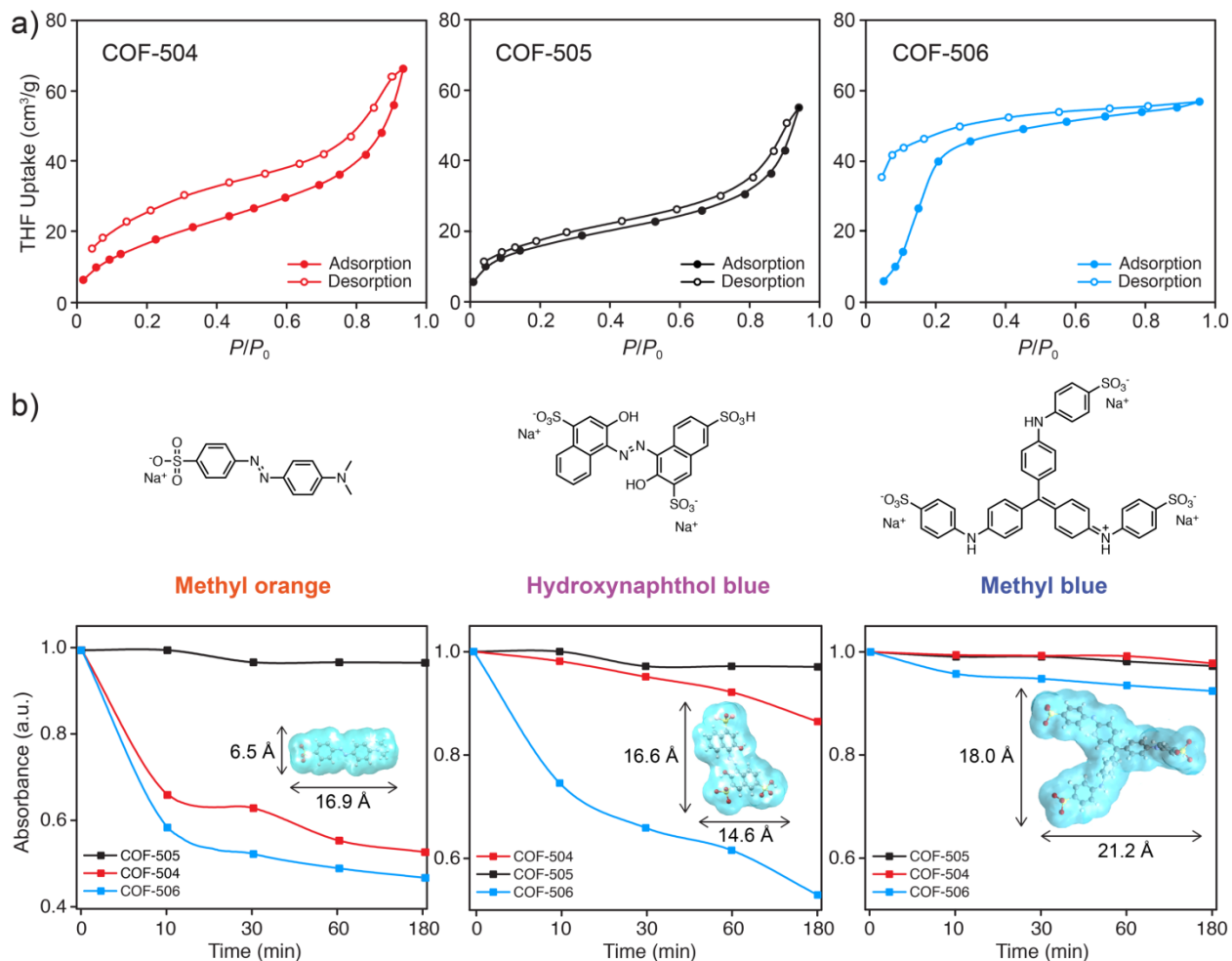
Figure 3.27. THF vapor sorption and dye inclusion studies of COF-504 (red), COF-505 (black) and COF-506 (blue). (**a**) THF isotherms show COF-504 and COF-505 with minimal porosity, while COF-506 exhibits a type I isotherm. (**b**) Inclusion study of large anionic dye molecules: Methyl orange, hyroxynaphthol blue, and methyl blue. The process was monitored through the decrease in absorbance at a selected wavelength as a function of contact time. For each measurement, the initial absorbance was normalized to 1.0.

Furthermore, anionic fluorescent dye inclusion studies[15–17] with dyes of increasing sizes [methyl orange (MO) < hydroxynaphthol blue disodium salt (HN) < methyl blue (MB)] were employed as probes for measurement of guest accessibility. 5 mg of each activated COF was immersed in a 100 ppm methanol solution containing the particular guest compound to be included. The amount of guest molecules in the supernatant was measured with ultraviolet-visible (UV-Vis)

spectrophotometry, and the characteristic absorbance at 432 nm (MO), 540 nm (HN), 606 nm (MB) was monitored over a period of 3 hours. Owing to the positively charged framework backbone, the uptake of the anionic dyes can be attributed to a combination of adsorption and anion exchange. Nevertheless, it provides insight into the accessible pore dimensions of the COFs. The results are plotted in Figure 3.28b, which clearly shows a continuous decrease of the amount of MO in the supernatant in the presence of COF-504 and COF-506, while a negligible amount of inclusion was observed with COF-505. As the size of the dye increases, the inclusion of HN in COF-504 became minimal, while a significant amount of the dye was adsorbed by COF-506. Finally, when MB was used as the guest molecule, all frameworks became saturated and did not display any major uptake. In summary, the pore dimensions increase in the order of COF-505, COF-504, and COF-506.

3.3.4 Demetalation of COF-506 and dye sorption to show structural flexibility of the demetalated material

The copper templates in COF-506, the structure with the largest guest accessible voids, were removed to investigate the resultant dynamics of the woven material. This was affected by heating COF-506 in a 1M KCN methanol solution at 75°C to yield the demetalated material. It is worth noting that under the same condition, COF-504 and COF-505 could not be demetalated possibly due to limited accessibility of the internal surface. Inductively coupled plasma atomic emission spectroscopy (ICP-AES) analysis revealed that 99% of the copper ions were removed in the process. Upon demetalation, the drastically decreased crystallinity of COF-506, together with disappearance of the lattice fringes in TEM micrographs (Figure 3.28), indicate spatial rearrangement of the structure and loss of long-range periodicity. Nevertheless, the morphology of the crystals remained unaffected. In addition, the chemical stability and the overall integrity of the structure was maintained; the FT-IR imine stretching vibration at 1623 cm^{-1} in dematalated COF-506 is identical with the one found for its metalated progenitor.
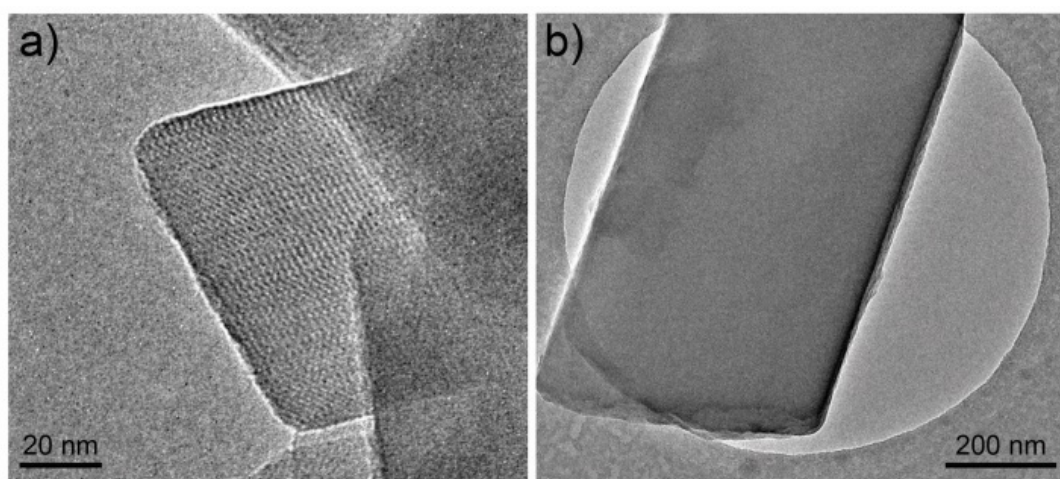

Figure 3.28. TEM images of (**a**) COF-506 and (**b**) demetalated COF-506. Upon demetalation the lattice fringes indicative of the material's crystalline nature disappeared while the morphology of the single crystal was retained.

The inclusion of MB dye was carried out with the demetalated COF-506 and shows a major uptake that is 11.6 fold higher than that of its metalated progenitor (Figure 3.29a). Upon demetalation, the absence of the copper(I) templates allows for spatial deviation of the threads to move about the points of registry and to accommodate the inclusion of dye molecules that do not fit within its metalated analogue. It should be noted that the higher uptake cannot only be rationalized by the absence of counterions in the pores since these would be exchanged by the anionic dye. As such, structural rearrangements of the structure are necessary to open up the framework and accommodate the dye.
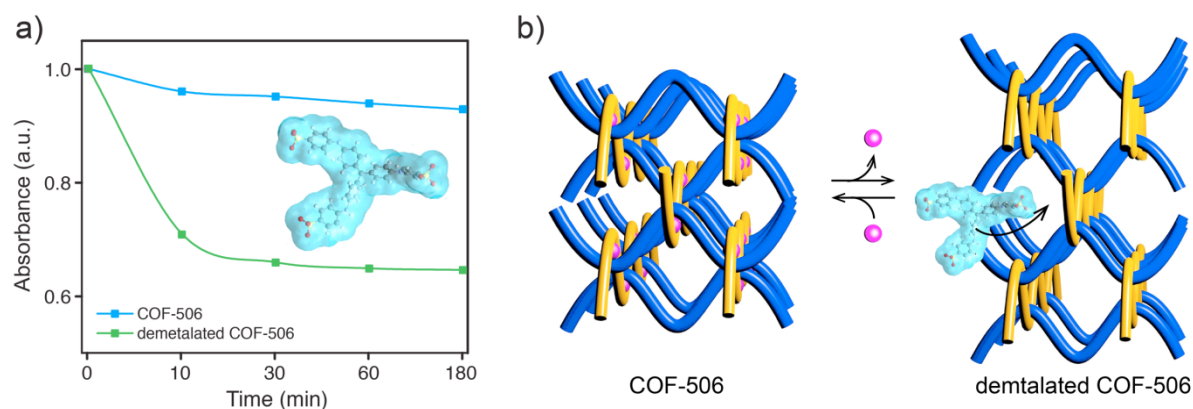
Figure 3.29. (**a**) Inclusion study of methyl blue in the metalated and demetalated COF-506. (**b**) Illustrative scheme of possible structural change during the reversible demetalation and remetalation process.

3.4 Conclusion and outlook

The findings of this study illustrate the promise of reticular chemistry for the tuning of dynamic properties in woven framework materials. In particular, the isoreticular principle was applied to modulate the pore size and aperture of woven COFs. Two approaches, isoreticular contraction and pore templation by bulky anions, were employed to prohibit framework interpenetration. A combination of electron microscopy, electron diffraction, and PXRD was employed to solve the structures of the resulting materials. The porosity of the frameworks was investigated by vapor and dye adsorption and confirmed the guest accessibility of their interior. In COF-506, the member of the series with the largest guest accessible void space, demetalation was found to render the material dynamic. Enormous spatial deviations within the structure allow for uptake of dye molecules that exceed the pore size of its metalated progenitor. The fact that the pore size of woven frameworks is proportional to its dynamic properties serves as a guide for the design of future generations of related structures. In this context, we anticipate the modularity of reticular synthesis of COFs to guide the design of woven frameworks of different structure types and metrics.

3.5 References

(1)   Liu, Y.; Ma, Y.; Zhao, Y.; Sun, X.; Gandara, F.; Furukawa, H.; Liu, Z.; Zhu, H.; Zhu, C.; Suenaga, K.; et al. *Science* **2016**, *351*, 365–369.

(2)   Zhao, Y.; Guo, L.; Gándara, F.; Ma, Y.; Liu, Z.; Zhu, C.; Lyu, H.; Trickett, C. A.; Kapustin, E. A.; Terasaki, O.; et al. *J. Am. Chem. Soc.* **2017**, *139*, 13166–13172.

(3)   Liu, Y.; O 'keeffe, M.; Treacy, M. M. J.; Yaghi, O. M. *Chem. Soc. Rev.* **2018**.

(4)   Spitler, E. L.; Koo, B. T.; Novotney, J. L.; Colson, J. W.; Uribe-Romo, F. J.; Gutierrez, G. D.; Clancy, P.; Dichtel, W. R. *J. Am. Chem. Soc* **2011**, *133*, 19416–19421.

(5)   Ascherl, L.; Sick, T.; Margraf, J. T.; Lapidus, S. H.; Calik, M.; Hettstedt, C.; Karaghiosoff, K.; Döblinger, M.; Clark, T.; Chapman, K. W.; et al. *Nat. Chem.* **2016**, *8*, 310–316.

(6)   Huang, N.; Wang, P.; Jiang, D. *Nat. Rev. Mater.* **2016**, *1*, 1–19.

(7)   Ding, S.-Y.; Wang, W. *Chem. Soc. Rev.* **2013**, *42*, 548–568.

(8)   Yaghi, O. M.; M, O. K.; Ockwig, N. W.; Chae, H. K.; Eddaoudi, M.; Kim, J. *Nature* **2003**, *423*, 705–714.

(9)   Dietrich-Buchecker, C. O.; Sauvage, J. P.; Kintzinger, J. P. *Tetrahedron Lett.* **1983**, *24*, 5095–5098.

(10)   Sauvage, J.-P. *Acc. Chem. Res.* **1998**, *31*, 611–619.

(11)   Gemmi, M.; Oleynikov, P. *Z. Krist.* **2013**, *228*, 51–58.

(12)   Friedrichs, O. D.; O'Keeffe, M.; Yaghi, O. M. *Solid State Sci.* **2003**, *5*, 73–78.

(13)   Dassault Systèmes BIOVIA, Materials Studio 8.0, San Diego: Dassault Systèmes (2014).

(14)   Gemmi, M.; Oleynikov, P. *Zeitschrift fur Krist.* **2013**, *228*, 51–58.

(15)   Ning, G. H.; Chen, Z.; Gao, Q.; Tang, W.; Chen, Z.; Liu, C.; Tian, B.; Li, X.; Loh, K. P. *J. Am. Chem. Soc.* **2017**, *139*, 8897–8904.

(16)   Fang, Q.; Zhuang, Z.; Gu, S.; Kaspar, R. B.; Zheng, J.; Wang, J.; Qiu, S.; Yan, Y. *Nat. Commun.* **2014**, *5*.

(17)   Haque, E.; Jun, J. W.; Jhung, S. H. *J. Hazard. Mater.* **2011**, *185*, 507–511.

Development of Anthracene Dimerization as A Linkage in Woven COFs
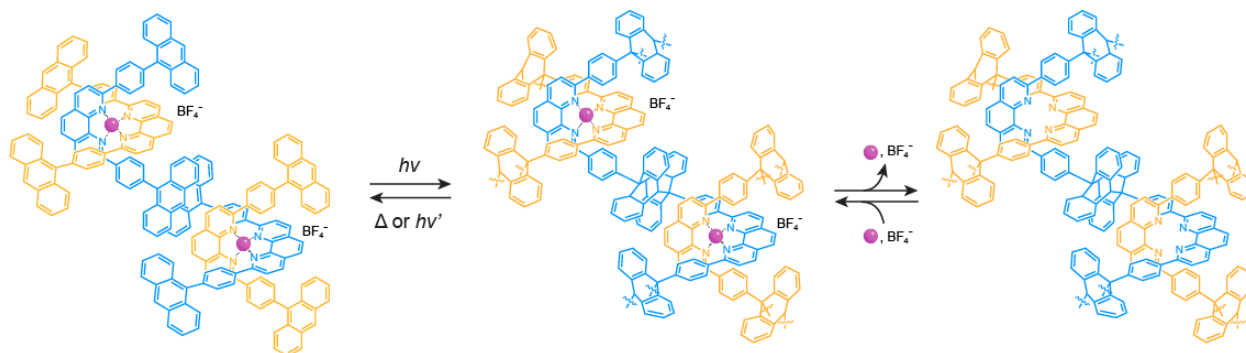
4.1 Introduction

Despite the increasingly rapid progress in COF synthesis, only a limited number of linkages are known as one needs to overcome the "crystallization problem"[1,2] when synthesizing a new framework. The crystallization process of COFs relies on the reversibility of the bond formation and suitable synthetic condition must be found such that the reaction is sufficiently reversible to allow for dynamic error correction in order to obtain crystalline periodic structures. When developing each new linkage, even for the ones that applies established chemical linkages to different building blocks, empirical guesswork for synthetic conditions, rather than rational experimental design, is usually involved. Discovery is therefore reduced to an exhaustive search of the ideal combination of appropriate solvent systems, starting material concentrations, temperature, and reaction time.

Scheme 4.1. photochemical dimerization of anthracenes and their thermally or photochemically activated back reaction.
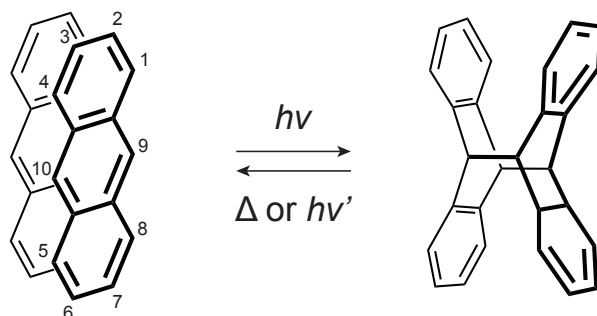
Solid-state photoreactions in single crystals have become well-established for single crystal to single crystal transformations of organic molecules[3] as well as the synthesis of polymers with high molecular mass[4]. The key feature of this strategy is to pre-organize photoreactive monomers in the form of single crystals, which allows exclusively lateral [4 + 4] cycloaddition by the means of lattice control in a predetermined manner. Recently, periodic two-dimensional polymers have been reported based on photopolymerization of anthracene moiety after the facile crystallization of monomeric small molecules.[5,6] Additionally, the C-C single bond formed during the photoreaction has outstanding chemical stability compared to the common linkages reported in COFs. In the reported structures, the anthracene units constitute the backbone of the monomeric species, which significantly restricts the substrate scope of this reaction and the concomitant framework variety. Towards this end, a tetratopic linker with a Cu(DPP)$_2$ core functionalized with anthracene units as points of extension were designed and synthesized as building blocks for COF synthesis, as well as their crystallization and photodimerization were explored.

Scheme 4.2. Synthetic strategy of woven materials based on the anthracene dimerization. Pre-alignment of the monomeric anthracene functionalized Cu(DPP)₂ complexes achieved by proper crystallization conditions would assist the photoreaction of anthracenes. The copper(I) templates can be removed and added back in a reversible manner.


4.2 Experimental Methods

All starting materials and solvents, unless otherwise specified, were obtained from Aldrich Chemical Co. and used without further purification. Tetrahydrofuran (HPLC grade, Aldrich) was passed through a PureSolv MD 7 Solvent Purification System before use. All reactions were performed at ambient laboratory conditions, and no precautions taken to exclude atmospheric moisture, unless otherwise specified. Pyrex glass tube charged with reagents and flash frozen with liquid N_2 were evacuated using a Schlenk line by fitting the open end of the tube inside a short length of standard rubber hose that was further affixed to a ground glass tap which could be close to insolate this assembly from dynamic vacuum when the desired internal pressure was reached. Tubes were sealed under the desired static vacuum using an oxygen propane torch. Elemental microanalyses were performed at the University of California, Berkeley, College of Chemistry. Solution ^{1}H nuclear magnetic resonance (NMR) spectra were recorded on a Bruker AVQ-400 (400 MHz) spectrometer operating with an Avance electronics console. Single-crystal X-ray diffraction (SXRD) data was collected using synchrotron radiation in beamline 11.3.1 of the Advanced Light Source, Lawrence Berkeley National Laboratory (LBNL), and a Bruker D8-Venture diffractometer. Beamline 11.3.1. is equipped with a PHOTO100 CMOS detector operating in shutterless mode equipped, and the radiation is monochromated using silicon (111). The Bruker D8-Venture diffractometer is equipped with a PHOTON100 CMOS detector and a micro-focus X-ray tube with a Cu/Mo target (λ = 1.54178 Å for Cu and 0.71073 Å for Mo), operated at 40 W power (40 kV, 1 mA).

4.2.1 Synthesis

Scheme 4.2. Synthetic route for copper(I) **complex 1**.
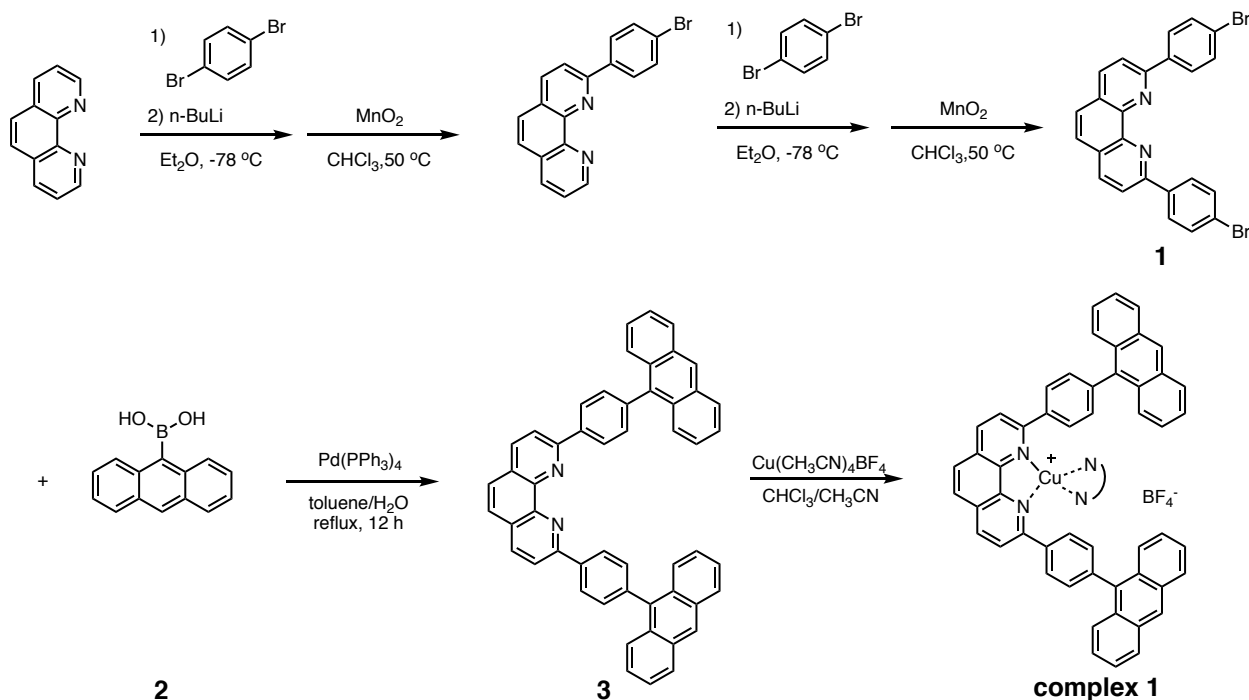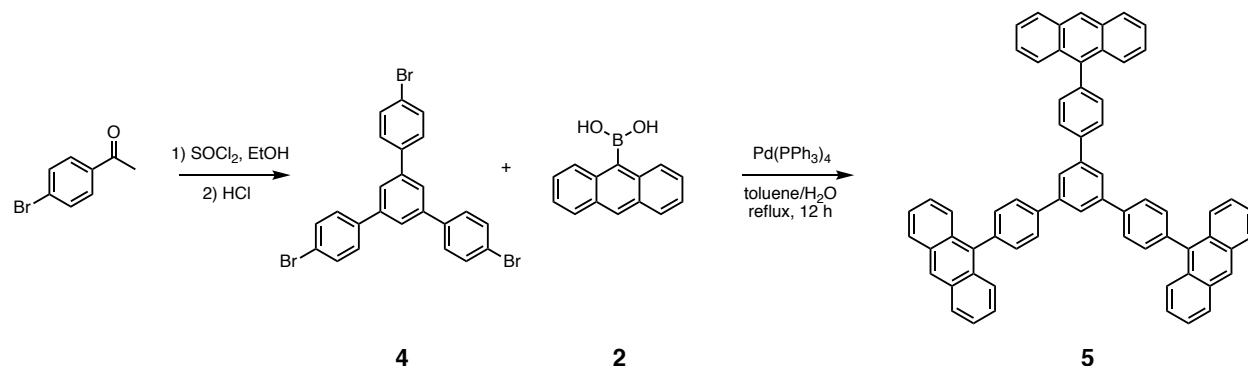

Synthesis of 2,9-bis(4-(anthracen-9-yl)phenyl)-1,10-phenanthroline (3): In a 500 mL round bottom flask, 2,9-bis(4-bromophenyl)-1,10-phenanthroline (**1**, 1.35 g, 2.76 mmol), which was synthesized according to literature,[7] and anthracen-9-ylboronic acid (**2**, 1.53 g, 6.89 mmol) were suspended in a mixture of toluene (100 mL), 2M Na_2CO_3 aqueous solution (50 mL) and EtOH (50 mL), which was purged with nitrogen for 15 min before $Pd(PPh_3)_4$ (158 mg, 0.13 mmol) was added. The resulting mixture was transferred to an oil bath preheated to 110 °C and stirred vigorously until completion of the reaction (progress periodically checked by TLC). After cooled down to room temperature, the organic layer was isolated and the aqueous layer was extracted with CH_2Cl_2 (2 × 60 mL). The organic layers were combined, dried over Na_2SO_4, filtered, and evaporated in vacuo to provide a brown solid. The product was further purified by flash silica gel chromatography with hexanes:DCM 1:1 to DCM. Evaporation solvent in vacuo afforded **3** as an off-white powder (402 mg, 52%). ^{1}H NMR (400 MHz, $CDCl_3$) δ 8.70 (d, [3]J = 7.9 Hz, 4 H), 8.52 (s, 2 H), 8.46 (d, [3]J = 7.6 Hz, 2 H), 8.31 (d, [3]J = 7.6 Hz, 2 H), 8.04 (d, [3]J = 7.9 Hz, 4 H), 7.90 (s, 2 H) 7.77 (d, [3]J = 7.6 Hz, 4 H), 7.68 (d, [3]J = 7.7 Hz, 4 H), 7.45 (dd, [3]J = 7.6 Hz, 6.3 Hz 4 H), 7.35 (dd, [3]J = 7.5 Hz, 6.3 Hz 4 H).

Synthesis of Cu(I)-[bis-2,9-bis(4-(anthracen-9-yl)phenyl)-1,10-phenanthroline] tetrafluoroborate (complex 1): [$Cu(CH_3CN)_4$]BF_4 (136 mg, 0.43 mmol) was dissolved in anhydrous CH_3CN (10 mL) under a N_2 atmosphere and added to a solution of 4,4'-(1,10-phenanthroline-2,9-diyl)dibenzaldehyde (537 mg, 0.78 mmol) in $CHCl_3$ (20 mL), affording a dark red solution, which was stirred at room temperature for 1 hr. The solution was then concentrated under vacuum to afforded an analytically pure compound as a red solid (596 mg, quantitative).

Recrystallization of **complex 1** was conducted in various solvent combinations to yield crystal structures shown in the next section.

Scheme 4.3. The synthesis of the tripotic molecule **5**.

Synthesis of 9,9'-(5'-(4-(anthracen-9-yl)phenyl)-[1,1':3',1''-terphenyl]-4,4''-diyl)dianthracene (5): In a 250 mL round bottom flask, 4,4''-dibromo-5'-(4-bromophenyl)-1,1':3',1''-terphenyl (**4**, 500 mg, 0.92 mmol), which was synthesized according to literature,[8] and anthracen-9-ylboronic acid (**2**, 1.20 g, 4.6 mmol) were suspended in a mixture of toluene (55 mL), 2M Na_2CO_3 aqueous solution (8 mL) and EtOH (8 mL), which was purged with nitrogen for 15 min before $Pd(PPh_3)_4$ (106 mg, 0.092 mmol) was added. The resulting mixture was transferred to an oil bath preheated to 110 °C and stirred vigorously until completion of the reaction (progress periodically checked by TLC). After cooled down to room temperature, the organic layer was isolated and the aqueous layer was extracted with CH_2Cl_2 (2 × 30 mL). The organic layers were combined, dried over Na_2SO_4, filtered, and evaporated in vacuo to provide a brown solid. The product was further purified washing with DCM to afford **3** as an off-white powder (402 mg, 52%). ^{1}H NMR (400 MHz, DMSO-d_6) δ 8.73 (s, 3 H), 8.38 (s, 3 H), 8.32 (d, $^3J = 8.3$ Hz, 6 H), 8.20 (d, $^3J = 8.4$ Hz, 6 H), 7.71 (d, $^3J = 7.6$ Hz, 6 H), 7.62 (d, $^3J = 7.7$ Hz, 6 H), 7.56 (dd, $^3J = 7.6$ Hz, 6.9 Hz, 6 H), 7.51 (dd, $^3J = 7.5$ Hz, 6.9 Hz, 6 H).

Scheme 4.4. 5-step synthesis to yield 9-bromo-1,2,3,4-tetrafluoroanthracene (**8**).
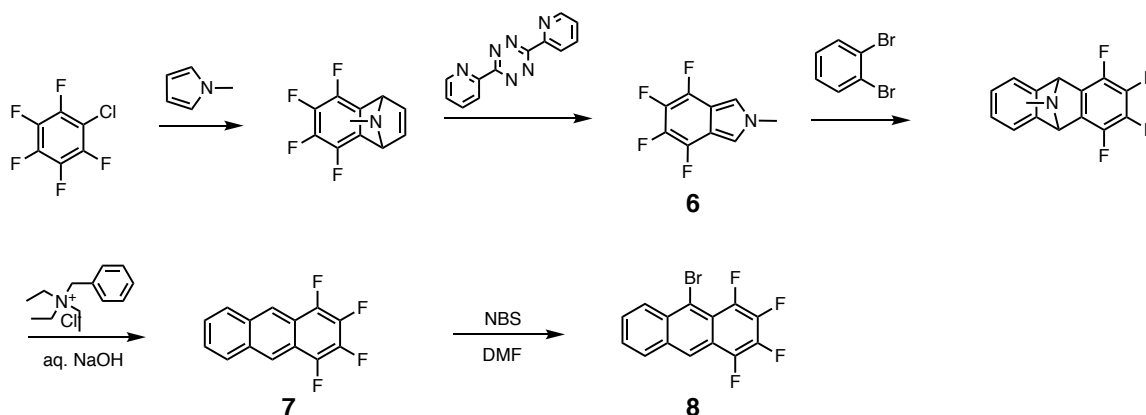
Synthesis of 1,2,3,4-tetrafluoroanthracene (7): 4,5,6,7-tetrafluoro-2-methyl-2*H*-isoindole (**6**) was synthesized according reported procedure;[6] synthesis of 1,2,3,4-tetrafluoroanthracene was carried out based on a modified procedure.[9] ^{1}H NMR (400 MHz, CDCl$_3$) δ 8.55 (s, 2H), 8.01 (dd, ^3J = 6.9, 6.5 Hz, 2H), 7.56 (dd, ^3J = 6.9, 6.6 Hz, 2H).

Synthesis of 9-bromo-1,2,3,4-tetrafluoroanthracene (8): A oven-dried 10 mL round bottom flask was charged with **7** (320 mg, 1.28 mmol), NBS (274 mg, 154 mmol), and 5 mL of DMF. The mixture was heated at 50 °C for 18 hr. After cooling down to room temperature, the reaction mixture was quench with 3 mL of water, which was subsequently extracted with hexanes (2 x 5 mL). The organic phase was collected, combined, and dried over Na$_2$SO$_4$. The solvent was removed in vacuo, and the product was further purified by column chromatography with hexanes to yield 250 mg of yellow solid (60% yield). ^{1}H NMR (400 MHz, CDCl$_3$) δ 8.59 (s, 1H), 8.57 (d, ^3J = 6.5 Hz, 1H), 7.98 (d, ^3J = 6.5 Hz, 1H), 7.65 (dd, ^3J = 6.5 Hz, 1H), 7.56 (dd, ^3J = 6.6 Hz, 2H).

Scheme 4.5. Synthetic scheme to yield the fluorinated **complex 2**.
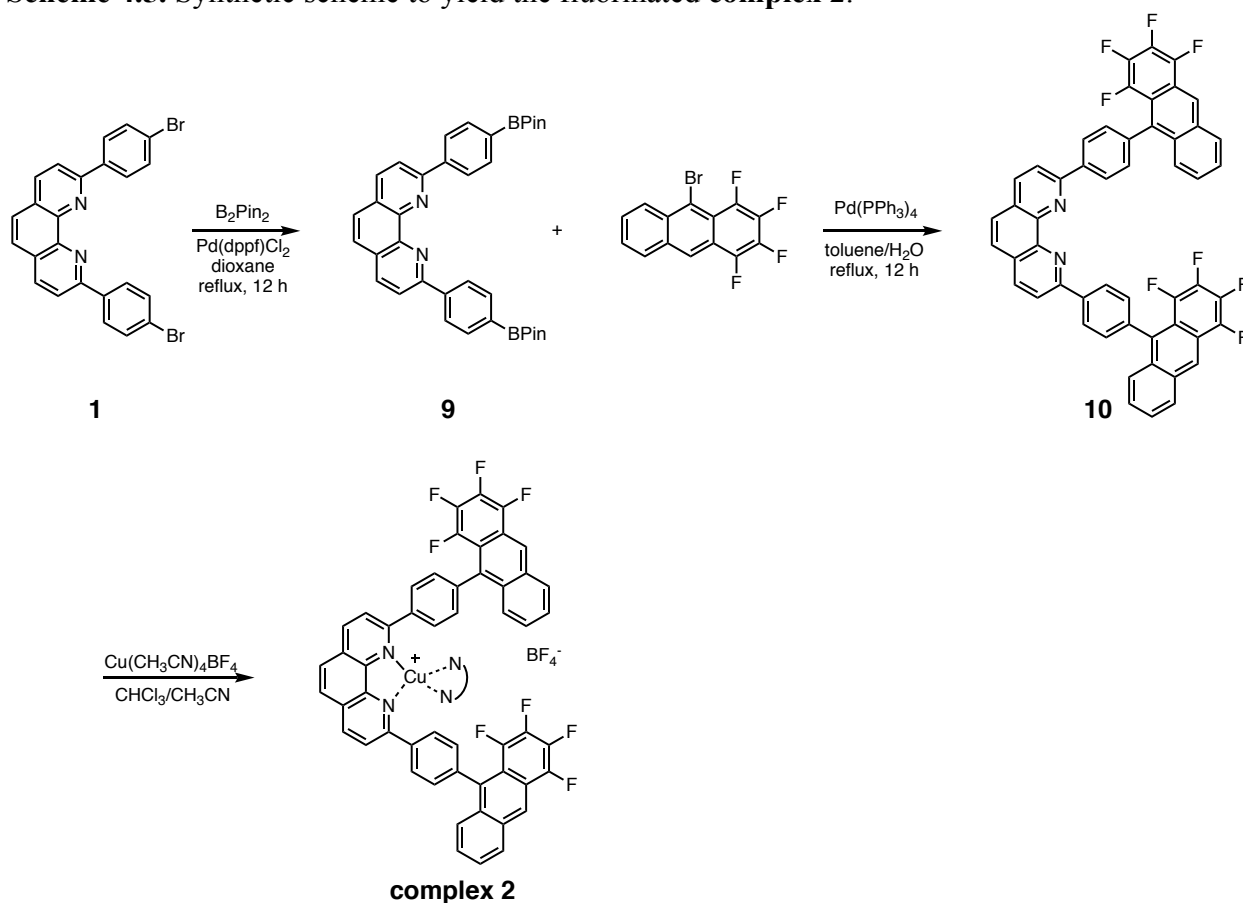
Synthesis of 2,9-bis(4-(5,5-dimethyl-1,3,2-dioxaborinan-2-yl)phenyl)-1,10-phenanthroline (9): Dioxane (80 mL) was added to a flask containing **1** (4.0 g, 8.2 mmol), bis(pinacolato)diboron (4.6 g, 18.0 mmol), KOAc (2.41 g, 24.6 mmol), and Pd(dppf)Cl$_2$ (669 mg, 0.82 mmol). The resulting suspension was deoxygenated by nitrogen bubbling at room temperature for 15 min, then immersed in oil bath preheated to 120 °C, and stirred at reflux for 16 h. After cooled down to room temperature, the mixture was filtered to remove the insoluble material using AcOEt to rinse the

filter cake. The filtrate was evaporated to give brown oil which solidified slowly at room temperature. The crude product was purified by flash silica gel column chromatography (DCM) followed by recrystallization from hot hexanes to provide compound 2 as colorless crystals (4.2 g, 92%). ^{1}H NMR (400 MHz, CDCl$_3$) δ 8.54 (d, ^3J = 8.3 Hz, 4 H), 8.34 (d, ^3J = 8.4 Hz, 2 H), 8.21 (d, ^3J = 8.4 Hz, 2 H), 8.07 (d, ^3J = 8.3 Hz, 4 H), 7.81 (s, 2 H), 3.74 (s, 8 H), 1.44 (s, 12 H).

Synthesis of 2,9-bis(4-(1,2,3,4-tetrafluoroanthracen-9-yl)phenyl)-1,10-phenanthroline (10): In a 100 mL round bottom flask, 4,4"-dibromo-5'-(4-bromophenyl)-1,1':3',1"-terphenyl (9, 462 mg, 0.79 mmol), which was synthesized according to literature,[8] and 8 (1.20 g, 4.6 mmol) were suspended in a mixture of toluene (10 mL), 2M Na$_2$CO$_3$ aqueous solution (10 mL) and EtOH (10 mL), which was purged with nitrogen for 15 min before Pd(PPh$_3$)$_4$ (106 mg, 0.092 mmol) was added. The resulting mixture was transferred to an oil bath preheated to 110 °C and stirred vigorously until completion of the reaction. The purification procedure is similar to the synthesis of 3 to afford 10 as an off-white powder (753 mg, 65%). ^{1}H NMR (400 MHz, CDCl$_3$) δ 8.72 (s, 2 H), 8.62 (d, ^3J = 7.9 Hz, 4 H), 8.46 (d, ^3J = 7.6 Hz, 2 H), 8.29 (d, ^3J = 7.6 Hz, 2 H), 8.05 (d, ^3J = 7.6 Hz, 2 H), 7.90 (s, 2 H), 7.66 (d, ^3J = 7.7 Hz, 2 H), 7.57 (d, ^3J = 7.9 Hz, 4 H), 7.52 (dd, ^3J = 7.5 Hz, 6.9 Hz, 2 H), 7.42 (dd, ^3J = 7.5 Hz, 6.9 Hz, 2 H).

Synthesis of Cu(I)-[bis-2,9-bis(4-(1,2,3,4-tetrafluoroanthracen-9-yl)phenyl)-1,10-phenanthroline] tetrafluoroborate (complex 2): The synthesis of **complex 2** was carried out with the procedure for **compelx 1** with quantitative yield.

Scheme 4.6. Synthesis of **11** as a molecular analogue for the photodimerization reaction.

11
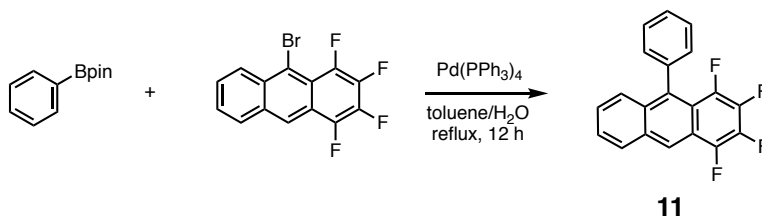
Synthesis of 9,9'-(5'-(4-(anthracen-9-yl)phenyl)-[1,1':3',1"-terphenyl]-4,4"-diyl)dianthracene (11): similar reaction conditions for **10** were used to synthesize **11** as a white powder (402 mg, 52%). ^{1}H NMR (400 MHz, CDCl$_3$) δ 8.80 (s, 1 H), 8.32 (dd, ^3J = 8.3 Hz, 1 H), 8.03 (d, ^3J = 8.3 Hz, 2 H), 7.71 (d, ^3J = 7.6 Hz, 1 H), 7.62 (d, ^3J = 7.7 Hz, 1 H), 7.59 (dd, ^3J = 8.3 Hz, 2 H), 7.56 (dd, ^3J = 7.6 Hz, 6.9 Hz, 1 H), 7.51 (dd, ^3J = 7.5 Hz, 6.9 Hz, 1 H).

General procedure for crystallization: Block-shaped crystals of the multitopic molecules (**5**, **complexs 1** and **2**) were obtained by cooling down a boiling solution of the complexes in aromatic solvents with high boiling points (*e.g.* nitrobenzene, dichlorobenzene, etc.) to room temperature in a hot oil bath over 1 hour (conc. ca. 5 mg/ml). The rod-shaped crystals of 1,2,3,4-tetrafluoroanthracene (**7**) and 9-phenyl-1,2,3,4-tetrafluoroanthracene (**11**) were obtained by slow evaporation of their hexane solution.

General procedure for photo-dimerization: In bulk reactions, crystals of monomeric species were collected in a 4 mL scintillation vial, immersed in LV CryoOil® and subsequently exposed

to 350 nm UV source from a RPR-200 photochemical reactor. Alternatively, single-crystalline samples were mounted on MiTeGen® kapton loops in LV CryoOil® for single-crystal X-ray diffraction measurements. The crystals, while covered by CryoOil®, were directly exposed to 400 nm UV light source for microscope ring light lamp illuminator (5 W, diameter: 60mm) overnight (Figure 4.x.) to avoid the possibility of melting and recrystallization in bulk samples.
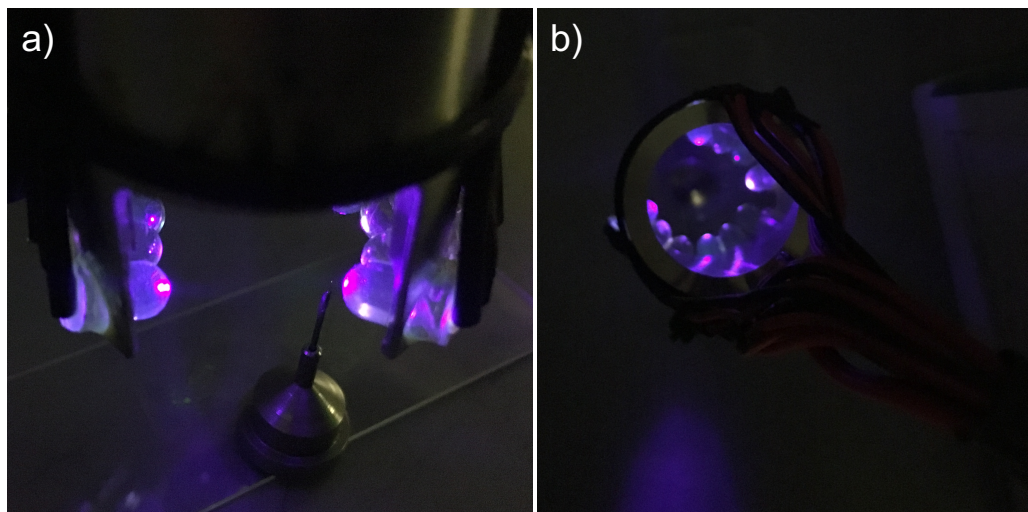

Figure 4.1. The experimental set-up for the photo-dimerization with the ring light lamp illuminator from a) side-view and b) top view.

Synthesis of 7 photodimer: The photoreaction condition for bulk material was used to quantitatively convert **7** to its photodimer. ^{1}H NMR (400 MHz, CDCl$_3$) δ 7.14 (d, ^3J = 8.3 Hz, 4H), 7.09 (m, 4 H), 4.97 (s, 4 H).

4.2.2 Single-crystal X-ray diffraction

Single crystals were mounted on the diffractometer equipped with a fine-focus target X-ray tube and a PHOTON 100 CMOS detector. The specimen was cooled to -123 °C using an Oxford Cryosystem chilled by liquid nitrogen. In case of measurements with synchrotron radiation, the wavelength is not CuK$_\alpha$. Bruker APEX2 software package was used for data collection; SAINT software package was used for data reduction; SADABS was used for absorption correction; no correction was made for extinction or decay. The structure was solved by direct methods with the SHELXTL software package and further refined with least squares method. All non-hydrogen atoms were refined anisotropically, all hydrogens were generated geometrically. The details of crystallography data are shown in the Tables 4.1 - 4.8 and Figures 4.2 - 4.9. The parameters in the table are derived in the following eq.

1) $R_1 = \Sigma||Fo| - |Fc||/\Sigma|Fo|$
2) $wR_2 = [\Sigma w(F_o^2 - F_c^2)^2/\Sigma w(F_o^2)^2]^{1/2}$
3) Goodness-of-fit on F^2 (GOOF) = $[\Sigma w(F_o^2 - F_c^2)^2/(N_{ref} - N_{par})]^{1/2}$

Figure 4.2. ORTEP drawing of the first crystal structure of **complex 1**-1. Thermal ellipsoids are shown with 50% probability.

Table 4.1. Crystal data and structure refinement of **complex 1**-1.

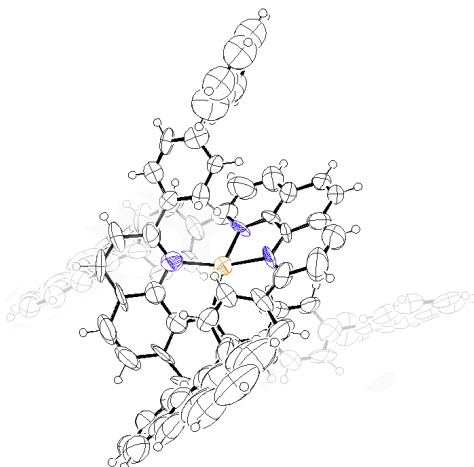|	
Empirical formula	$C_{52}H_{33}Cu_{0.5}N_2$
Formula weight	717.57
Wavelength	0.71073 Å
Crystal system	Monoclinic
Space group	$C2/c$
Unit cell dimensions	$a = 13.0503(11)$ Å $\quad \alpha = 90°$
	$b = 25.8486(19)$ Å $\quad \beta = 101.129(4)°$
	$c = 25.536(2)$ Å $\quad \gamma = 90°$
Volume	8452.0(12) Å^3
Z	8
Absorption coefficient	0.307
F(000)	2988.0
2 theta Min-Max	4.152 to 35.296°
Reflections collected	58245
Independent reflections	2714 [R(int) = 0.0916]
Goodness-of-fit on F^2	2.665
Final R indices [$I > 2\sigma(I)$]	$R_1 = 0.1856$, $wR_2 = 0.4977$
R indices (all data)	$R_1 = 0.2140$, $wR_2 = 0.5296$
Largest diff. peak and hole	1.39 and -0.72 e.Å^{-3}

Figure 4.3. ORTEP drawing of the first crystal structure of **complex 1**-2. Thermal ellipsoids are shown with 50% probability.

Table 4.2. Crystal data and structure refinement of **complex 1**-2.

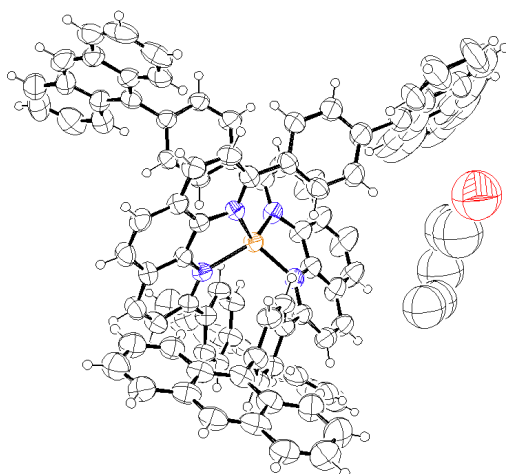|	
Empirical formula	$C_{130}H_{64}CuN_5O_3$
Formula weight	1807.40
Wavelength	0.7749 Å
Crystal system	Monoclinic
Space group	$P2_1/n$
Unit cell dimensions	$a = 25.3831(7)$ Å $\quad \alpha = 90°$
	$b = 16.0487(5)$ Å $\quad \beta = 97.229(2)°$
	$c = 25.7077(7)$ Å $\quad \gamma = 90°$
Volume	10389.2(5) $Å^3$
Z	4
Absorption coefficient	0.331
F(000)	3728.0
2 theta Min-Max	4.448 to 51.136°
Reflections collected	33646
Independent reflections	14851 [R(int) = 0.0442]
Goodness-of-fit on F^2	1.306
Final R indices [$I > 2\sigma(I)$]	$R_1 = 0.1029$, $wR_2 = 0.3125$
R indices (all data)	$R_1 = 0.1373$, $wR_2 = 0.3458$
Largest diff. peak and hole	1.19 and -0.45 e.$Å^{-3}$
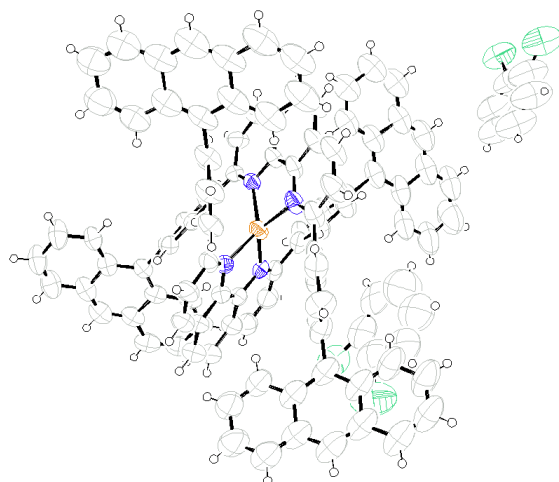
Figure 4.4. ORTEP drawing of the first crystal structure of **complex 1**-3. Thermal ellipsoids are shown with 50% probability.

Table 4.3. Crystal data and structure refinement of **complex 1**-3.

|	
Empirical formula	$C_{116}H_{72}Cl_4CuN_4$
Formula weight	1727.1
Wavelength	1.0333 Å
Crystal system	Triclinic
Space group	*P*-1
Unit cell dimensions	$a = 15.1879(8)$ Å$\quad\alpha = 88.169(3)°$ $b = 15.3944(8)$ Å$\quad\beta = 82.927(3)°$ $c = 25.3326(14)$ Å$\quad\gamma = 62.429(3)°$
Volume	$5208.3(5)$ Å^3
Z	2
Absorption coefficient	1.323
F(000)	1786.0
2 theta Min-Max	4.432 to 59.044°
Reflections collected	24478
Independent reflections	8998 [R(int) = 0.0476]
Goodness-of-fit on F^2	1.051
Final R indices [$I > 2\sigma(I)$]	$R_1 = 0.1355$, $wR_2 = 0.3527$
R indices (all data)	$R_1 = 0.1551$, $wR_2 = 0.3683$
Largest diff. peak and hole	0.94 and -0.74 e.Å^{-3}
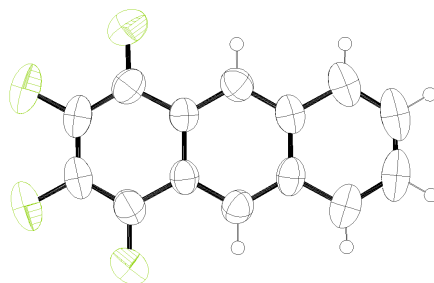
Figure 4.6 ORTEP drawing of the crystal structure of **7**. Thermal ellipsoids are shown with 50% probability.

Table 4.4. Crystal data and structure refinement of **7**.

|	
Empirical formula	$C_{14}H_6F_4$
Formula weight	250.19
Wavelength	1.54178 Å
Crystal system	Triclinic
Space group	*P*-1
Unit cell dimensions	$a = 7.4191(4)$ Å $\alpha = 101.348(5)°$
	$b = 7.8353(6)$ Å $\beta = 98.952(5)°$
	$c = 10.4030(8)$ Å $\gamma = 113.206(4)°$
Volume	526.39(7) Å^3
Z	2
Absorption coefficient	1.237
F(000)	252.0
2 theta Min-Max	8.976 to 127.266°
Reflections collected	6872
Independent reflections	1704 [*R*(int) = 0.0476]
Goodness-of-fit on F^2	1.074
Final *R* indices [$I > 2\sigma(I)$]	$R_1 = 0.0506$, $wR_2 = 0.1385$
R indices (all data)	$R_1 = 0.0594$, $wR_2 = 0.1508$
Largest diff. peak and hole	0.18 and -0.19 e.Å^{-3}
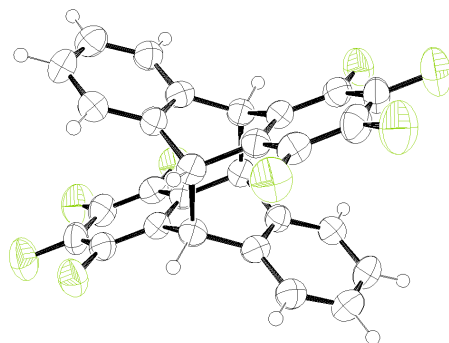
Figure 4.6. ORTEP drawing of the crystal structure of **7**-dimer after photoreaction. Thermal ellipsoids are shown with 50% probability.

Table 4.5. Crystal data and structure refinement of **7**-dimer.

|	
Empirical formula	$C_{14}H_6F_4$
Formula weight	250.19
Wavelength	1.54178 Å
Crystal system	Monoclinic
Space group	$P2_1/c$
Unit cell dimensions	$a = 11.1032(10)$ Å $\alpha = 90°$
	$b = 10.8606(11)$ Å $\beta = 113.936(7)°$
	$c = 9.5753(9)$ Å $\gamma = 90°$
Volume	1055.36(18) Å^3
Z	4
Absorption coefficient	1.233
F(000)	504.0
2 theta Min-Max	8.714 to 98.182°
Reflections collected	9538
Independent reflections	1038 [R(int) = 0.1141]
Goodness-of-fit on F^2	1.022
Final R indices [$I > 2\sigma(I)$]	$R_1 = 0.0387$, $wR_2 = 0.0863$
R indices (all data)	$R_1 = 0.0666$, $wR_2 = 0.0992$
Largest diff. peak and hole	0.15 and -0.16 e.Å^{-3}
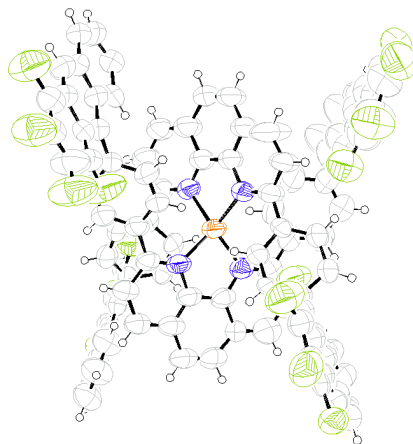
Figure 4.7. ORTEP drawing of the crystal structure of **complex 2** after photoreaction. Thermal ellipsoids are shown with 50% probability.

Table 4.6. Crystal data and structure refinement of **complex 2**.

|	
Empirical formula	$C_{104}H_{48}CuF_{16}N_4$
Formula weight	1719.99
Wavelength	1.2399 Å
Crystal system	Monoclinic
Space group	$P2_1/n$
Unit cell dimensions	$a = 16.3809(7)$ Å $\quad \alpha = 90°$
	$b = 26.3880(10)$ Å $\quad \beta = 104.284(2)°$
	$c = 22.8732(9)$ Å $\quad \gamma = 90°$
Volume	9581.5(7) Å^3
Z	4
Absorption coefficient	1.346
F(000)	3488.0
2 theta Min-Max	4.186 to 81.726°
Reflections collected	35669
Independent reflections	10637 [R(int) = 0.1406]
Goodness-of-fit on F^2	1.587
Final R indices [$I > 2\sigma(I)$]	$R_1 = 0.2245$, $wR_2 = 0.5018$
R indices (all data)	$R_1 = 0.3121$, $wR_2 = 0.5405$
Largest diff. peak and hole	0.56 and -0.55 e.Å^{-3}
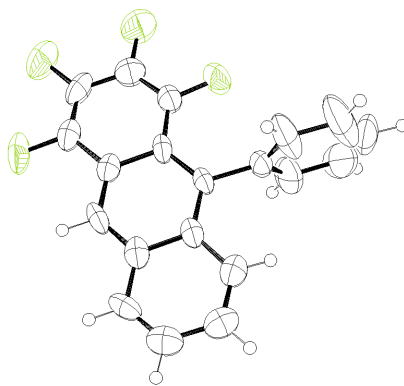
Figure 4.8. ORTEP drawing of the crystal structure of **11**. Thermal ellipsoids are shown with 50% probability.

Table 4.7. Crystal data and structure refinement of **11**.

|	
Empirical formula	$C_{10}H_5F_2$
Formula weight	163.14
Wavelength	0.71073 Å
Crystal system	Monoclinic
Space group	$P2_1/m$
Unit cell dimensions	$a = 9.664(3)$ Å $\quad \alpha = 90°$
	$b = 6.843(2)$ Å $\quad \beta = 111.534(8)°$
	$c = 11.950(4)$ Å $\quad \gamma = 90°$
Volume	735.1(4) Å^3
Z	4
Absorption coefficient	0.120
F(000)	332.0
2 theta Min-Max	4.53 to 40.74°
Reflections collected	4632
Independent reflections	808 [R(int) = 0.1098]
Goodness-of-fit on F^2	1.108
Final R indices [$I > 2\sigma(I)$]	$R_1 = 0.0565$, $wR_2 = 0.1531$
R indices (all data)	$R_1 = 0.1227$, $wR_2 = 0.2376$
Largest diff. peak and hole	0.22 and -0.30 e.Å^{-3}
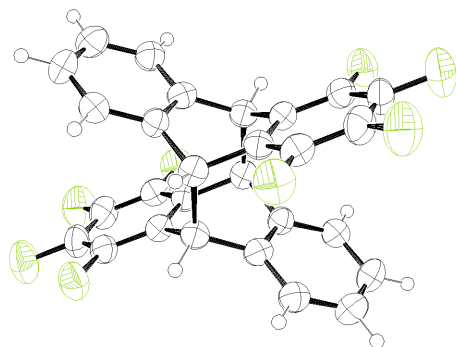
Figure 4.9. ORTEP drawing of the crystal structure of **11** photodimer. Thermal ellipsoids are shown with 50% probability.

Table 4.8. Crystal data and structure refinement of **11** photodimer.

Empirical formula	$C_{20}H_{10}F_4$
Formula weight	326.28
Wavelength	1.54178 Å
Crystal system	Monoclinic
Space group	$P2_1/c$
Unit cell dimensions	$a = 7.459(4)$ Å $\quad \alpha = 90°$
	$b = 19.775(12)$ Å $\quad \beta = 97.643(15)°$
	$c = 9.424(5)$ Å $\quad \gamma = 90°$
Volume	$1377.8(14)$ Å^3
Z	4
Absorption coefficient	1.102
F(000)	664.0
2 theta Min-Max	8.944 to 80.272°
Reflections collected	2967
Independent reflections	835 [R(int) = 0.1565]
Goodness-of-fit on F^2	1.072
Final R indices [$I > 2\sigma(I)$]	$R_1 = 0.0808$, $wR_2 = 0.1720$
R indices (all data)	$R_1 = 0.1720$, $wR_2 = 0.2166$
Largest diff. peak and hole	0.34 and -0.32 e.Å^{-3}

4.2.3 Fourier transform infrared spectroscopy

The FT-IR spectra of starting materials, molecular analogue, and activated COFs were collected on a Bruker ALPHA FT-IR Spectrometer equipped with ALPHA's Platinum ATR single reflection diamond ATR module, which can collect IR spectra on neat samples. The signals are given in wavenumbers (cm^{-1}).

4.3 Results and discussion
4.3.1 Synthesis and crystallization of anthracene-functionalized Cu(I) complex (1)

Anthracene moiety is known to dimerize upon UV excitation at 350 nm. The rigid aromatic system also provides the prerequisite for pre-assembly of the monomers through π-π interaction in the crystal structures. The tetrahedrally-shaped copper(I)-bisphenthanroline building block for woven COF synthesis are functionalized with these photoactive units as points of extension and by pre-alignment of face-to-face π-π packed anthracenes between neighboring complexes in the molecular single crystals, any undesired molecular motions should be suppressed and UV treatment would lead to exclusively the photo-polymerization of the monomeric species into an 3D extended framework in **dia** topology through C-C bond formation with exceptional chemical stability.

The anthracene-containing complex **1** was synthesized in similar steps with complexes reported in the previous chapters by first functionalization of 2 and 9 positions of the phenanthroline molecule with bromophenyl moieties for the subsequent Suzuki coupling to yield the di-anthracene ligand **3**. The air-free reaction of **3** with Cu(CH$_3$CN)$_4$BF$_4$ salt lead to the quantitative complexation of complex **1**.
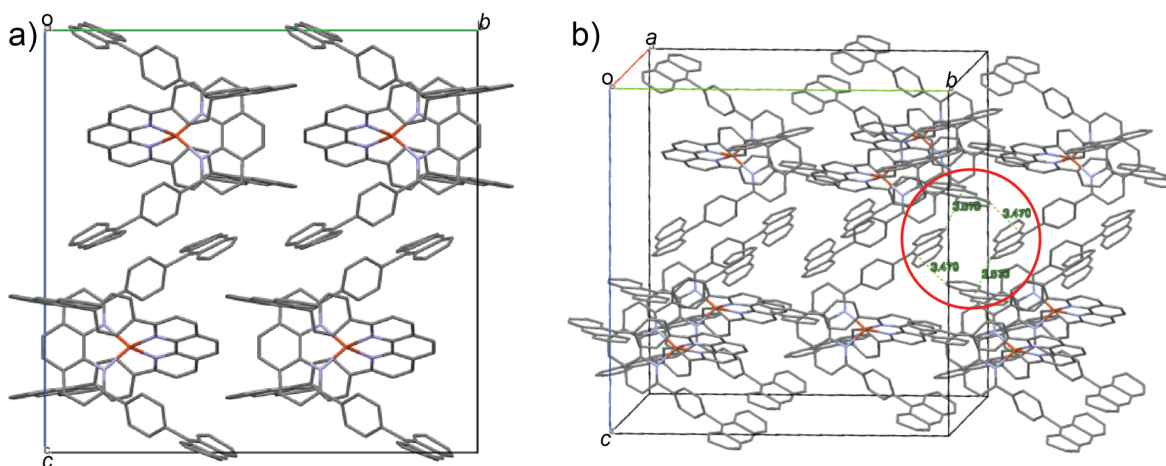
Figure 4.10. Crystal structure of complex **1** obtained by slow evaporation of a dichloromethane solution of the complex. (**a**) complex molecules pack in opposite directions along the *b* axis and (**b**) neighboring anthracenes form a four-fold propeller arrangement though face-to-edge π-π interaction highlighted in the red circle. Nitrogen atoms are depicted in purple, copper atoms in red, and carbon atoms in grey. Hydrogen atoms are not shown for clarity.

The crystals of complex **1** were obtained by various crystallization methods including recrystallization, slow evaporation, diffusion, and layering in combination with different organic solvents, which leads to three distinctly packed crystal structures that are reported in this section. Figure 4.10 shows the first structure which was obtained by slow evaporation of a 0.015 mM dichloromethane solution of complex **1**, which crystallized in a monoclinic space group, $C2/c$, with eight complexes in one unit cell. The cell parameters are $a = 13.0503(11)$ Å, $b = 19.775(12)$ Å, $c = 25.8486(19)$ Å and $\beta = 101.129(4)°$. Close examination of the structure shows that layers of complexes are arranged in the crystallographic ab planes, with opposite packing directions of the complexes in the alternating layers above and below in c direction (Figure 4.10a). It was also observed that four anthracene units from different ligands are positioned in a propeller shape by face-to-edge π-π interaction. In solid state, indeed, unfunctionalized anthracene molecules are commonly seen to pack in a face-to-edge fashion.[10] Therefore, polar aromatic solvents were then engaged to assist the desirable packing mode of anthracene.

2-cyanopyridine (CPY) was previously used in the reported crystallization of anthracene-containing photoactive molecules to enable the face-to-face stacking of the anthracene units.[5] In the report, CPY, together with two anthracene molecules, form a sandwich arrangement; in addition, the CPY molecules can achieve proper space filling to facilitate crystallization. Therefore, CPY was first used to crystallize complex **1**, however yielded no crystals as the complex is very well soluble. Nitrobenzene, a similar polar aromatic solvent, was utilized towards another attempt to crystalize complex **1**. Dark red crystals were obtained by slow diffusion of hexane into a 0.015 mM complex **1** in a nitrobenzene solution. The complexes crystallized in a $P2_1/n$ space group with cell parameters of $a = 25.3831(7)$ Å, $b = 16.0487(5)$ Å, $c = 25.7077(7)$ Å, and $\beta = 97.229(2)°$. However, the crystal structure revealed that nitrobenzene molecules did not participate in the packing of anthracene during crystallization as expected (Figure 4.11) and no obvious π-π interaction was noticed in this crystals structure.
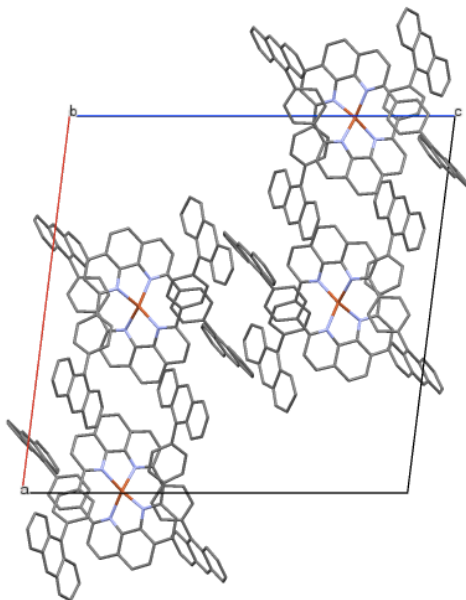

Figure 4.11. Packing of complex **1** in the crystal structure obtained from slow diffusion of hexane into a nitrobenzene solution of the complex. Nitrogen atoms are depicted in purple, copper atoms in red, and carbon atoms in grey. Hydrogen atoms are not shown for clarity.

Although the stacking modes in the previous two crystals are not suitable for the photoreaction, it was obvious that the crystallization solvent had an impact on the packing of complex **1**. Another crystallization attempt was carried out with dichlorobenzene which is also a polar aromatic solvent. A different crystal structure was obtained with space group $P\bar{1}$, and cell parameters of a = 15.1879(8) Å, b = 15.3944(8) Å, c = 25.3326(14) Å, α = 88.169(3)°, β = 82.927(3)°, and γ = 62.429(3)°. Unfortunately, dichlorobenzene molecules again were not engaged in the packing of anthracene during crystallization (Figure 4.12) and no obvious π-π interaction was observed in this crystals structure (Figure 4.12a). When viewed from b axis, two anthracene units are seemingly overlaid, but the distance between them is 9.4 Å thus prevents efficient photodimerization (Figure 4.12b).
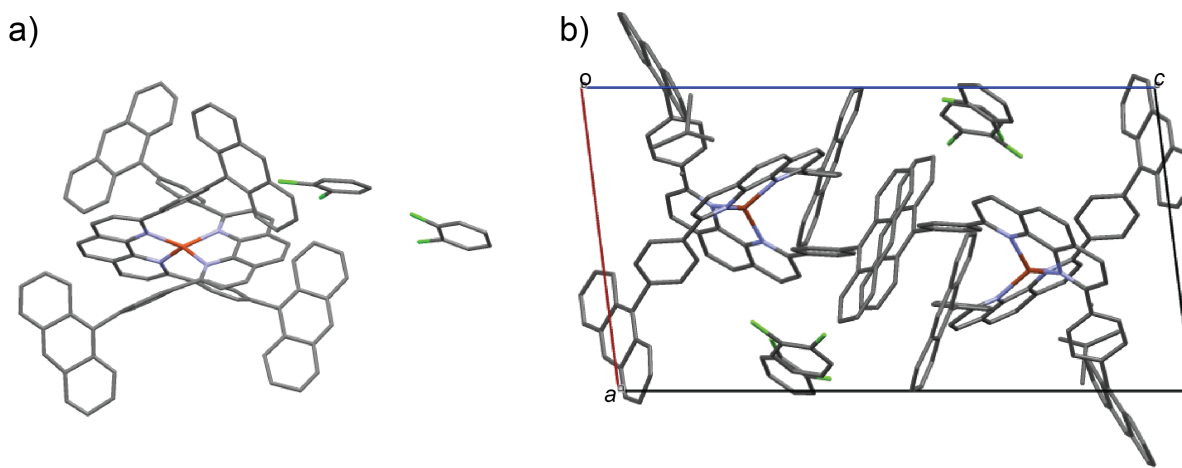
a) b)

Figure 4.12. Crystal structure of complex **1** obtained by slow diffusion of hexane into a dichlorobenzene (DCB) solution. (**a**) DCB molecules did not engage in the stacking of anthracene units as expected which leads to (**b**) undesirable packing of complex **1** in the crystal structure. Chlorine atoms are in green, nitrogen atoms in purple, copper atoms in red, and carbon atoms in grey. Hydrogen atoms are not shown for clarity.

4.3.2 Synthesis and crystallization of 1,2,3,4-tetrafluoroanthracene-containing Cu(I) complex (2)

Fluorinated organic molecules offer a manifold supramolecular chemistry due to the strong electron-withdrawing nature of fluorine and accordingly a significantly polarized C-F bond.[11] The electronic structure of a molecule can be changed drastically and therefore arrangements with a strong interaction between fluorinated and non-fluorinated rings can be designed.[12] Fluorine atoms at the half side of the anthracene were therefore introduced to take advantage of the co-facial, antiparallel packing motif that is often observed in end-fluorinated acenes.[13,14]

The organic synthesis of 1,2,3,4-tetrafluoanthracene (**7**) was performed based on a modified procedure.[6] The subsequent bromination of the 9-position was carried out with *N*-bromosuccinimide while other reaction attempts with other reagents including Br$_2$, HBr/H$_2$O$_2$, or CuBr$_2$ did not proceed, possibly due to steric hindrance. Suzuki coupling with the 2,9-bis(4-(4,4,5,5-tetramethyl-1,3,2-dioxaborolan-2-yl)phenyl)-1,10-phenanthroline (**9**) leads to the

constrcution of the fluorinated phenathroline ligand, **10**. With a similar complexation reaction with $Cu(CH_3CN)_4BF_4$, the successful synthesis of complex **2** was achieved.

Before conducting the further investigation of the complex **2**, the crystallization and photodimerization reaction of 1,2,3,4-tetrafluoanthracene (**7**) were first examined as there is no previous literature on the photo-reactivity of the fluorinated molecule. By slow evaporation of a dichloromethane solution of **7**, needle-shaped pale yellow crystals were obtained in a triclinic space group, $P\bar{1}$, and cell parameters of $a = 7.4191(4)$ Å, $b = 7.8353(6)$ Å, $c = 10.4030(8)$ Å, $\alpha = 101.348(5)°$, $\beta = 98.952(5)°$, and $\gamma = 113.206(4)°$. The crystal structure confirms the packing of **7** in a co-facial manner through arene-tetrafluoroarene stacking (Figure 4.13a and b). The distance between two layers is 3.708 Å, which is less than 4.2 Å and thus, is suitable for the following dimerization reaction[3]. Upon exposure to a UV source at 350 nm, the solid state single-crystal-to-single-crystal dimerization reaction was complete within 30 min. The completion of the bulk reaction was confirmed by solution ^1H NMR, and the resultant single crystal after the reaction was examined by X-ray single crystal diffraction studies.

The obtained crystal after the UV exposure transforms from a triclinic space group into a monoclinic one, $P2_1/c$ with unit cell parameters of $a = 11.1032(10)$ Å, $b = 10.8606(11)$ Å, $c = 9.5753(9)$ Å and $\beta = 113.936(7)°$, which has a cell volume that is twice of the original monomer crystal and four asymmetric units instead of two. The distance between C9 and C10 is now 1.6 Å (3.7 Å in monomer), where the carbons deviate spatially to form a C-C single bond. Interestingly, every other pair of the dimers experience a 90° change of orientation during the photoreaction (Figure 4.13b). The dimerization can also be monitored by Fourier-transform infrared spectroscopy (FT-IR, Figure 4.14). The disappearance of the peak at 1667 cm^{-1} in the dimer suggests the sp^2 C9 and C10 are now converted to sp^3 carbons.
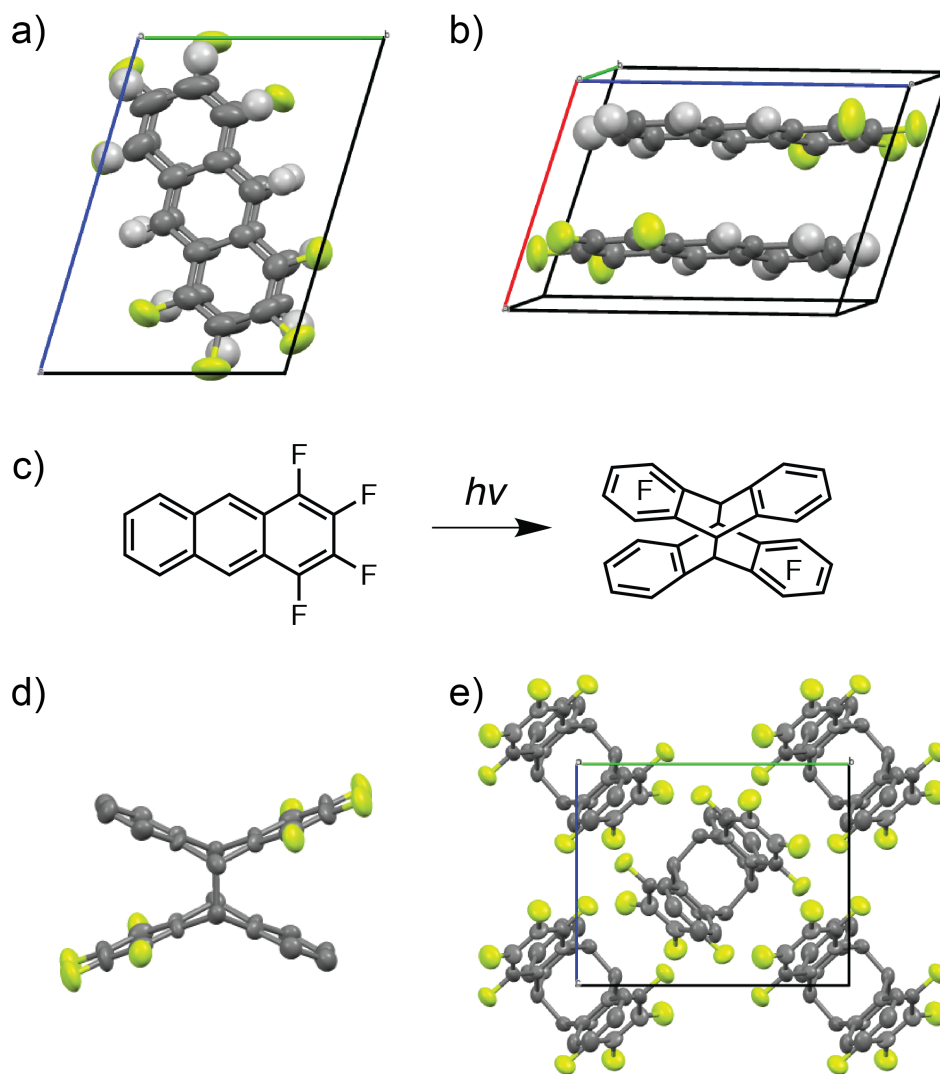
Figure 4.13. Crystal structure of 1,2,3,4-tetrafluoroanthracene viewed along (**a**) *a* and (**b**) *b* directions which displays a face-to-face stacking of the functionalized anthracene molecules. (**c**) The crystal was then subjected to UV treatment at 350 nm which resulted in dimerization. The structure is shown in (**d**) and stacking arrangement in (**e**). Fluorine atoms are depicted in green and carbon atoms in grey. Thermal ellipsoids are shown with 50% probability.
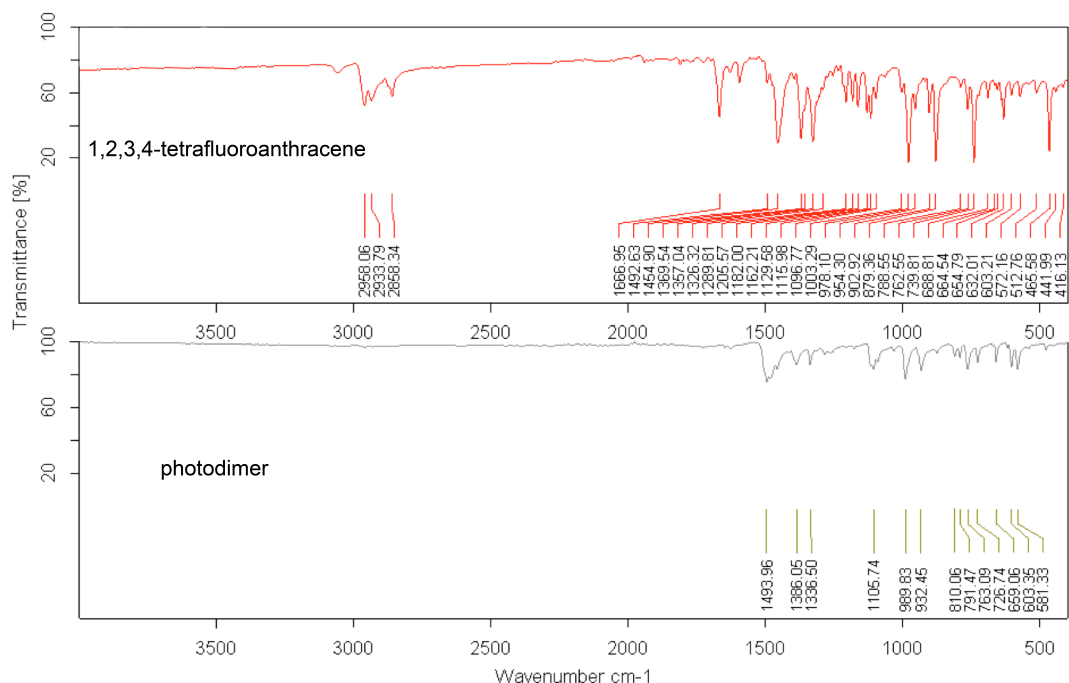
Figure 4.14. FT-IR spectra of **11** and its photodimer.

Since the photoreactivity of the fluorinated anthracene was confirmed, the same crystallization and UV treatment were carried out on the fluorinated complex **2**. Dark red block-shaped crystals of complex **2** were obtained by slow diffusion of hexane into a 0.015 mM solution of DCB solution. It crystallized in a monoclinic space group $P2_1/n$, with cell parameters of $a = 16.3809(7)$ Å, $b = 26.3880(10)$ Å, $c = 22.8732(9)$ Å, $\beta = 104.284(2)°$. Figure 4.14a shows the crystal structure of complex **2** with the four anthracene units numbered for clarity (1,2 correspond to two anthracenes on one of the phenanthroline ligands, and 3,4 on the other). Anthracene units 2, 3 and 4 have relatively small ellipsoids, indicating small magnitudes and directions of the thermal vibration of atoms in the crystal structure. This can be explained by the face-to-face stacking of these anthracene units from the next complexes as expected (Figure 4.13b to d). Anthracene unit 1, which does not engage in any π-π interaction, has large thermal ellipsoids. On a fundamentally level, the packing of the complex **2** in the crystal structure leads to the proper face-to-face stacking of anthracene units 3 and 4, which constitute one complete thread of the woven structure and therefore, this crystal was subjected to UV excitation at 350 nm. However, no conversion was observed with solution ^{1}H NMR or FT-IR.
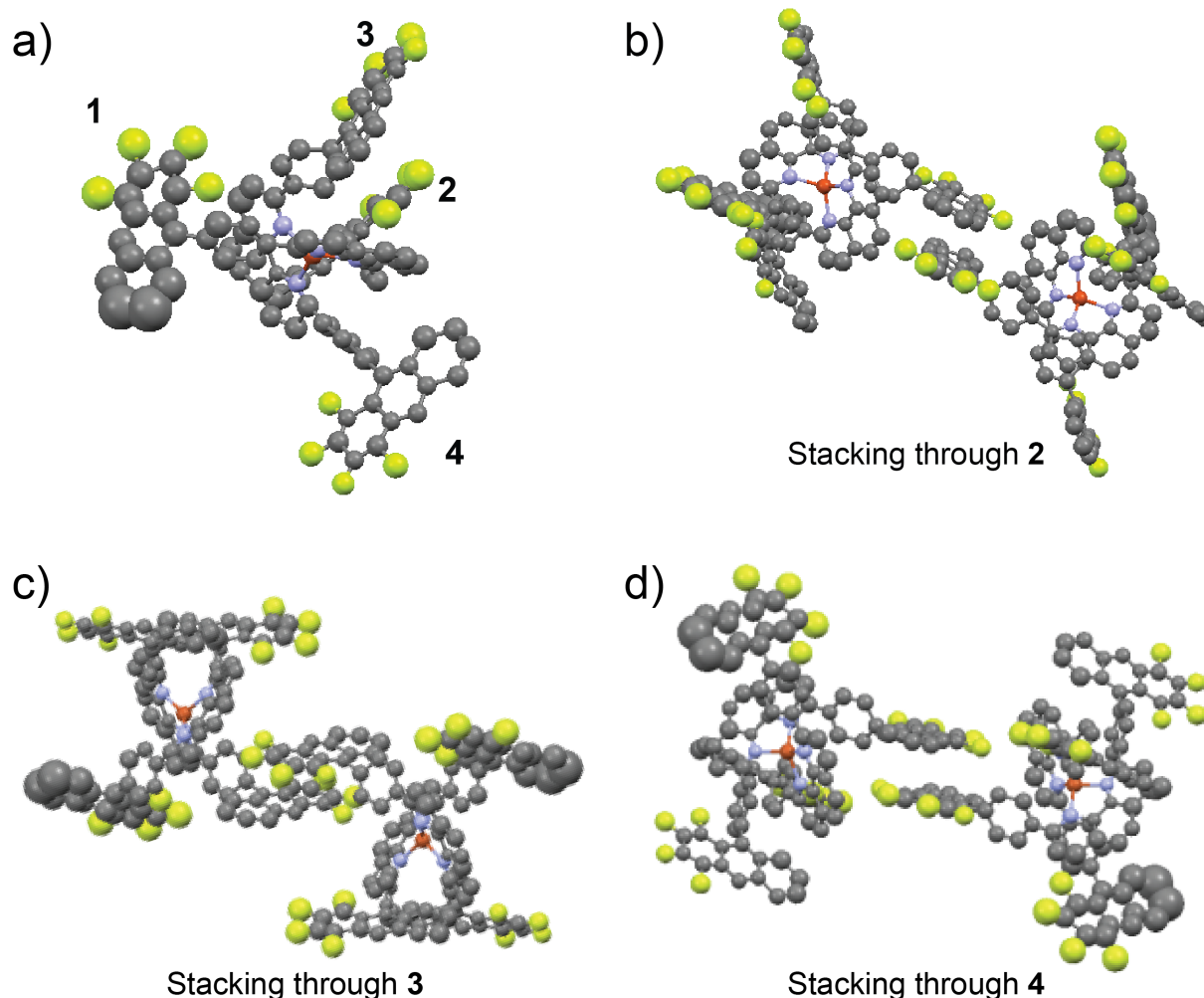
Figure 4.15. (**a**) Crystal structure of complex **2**. Packing of the complex in the crystal structure through (**b**) anthracene unit 2, (**c**) anthracene unit 3, and (**d**) anthracene unit 4. Fluorine atoms are depicted in green, nitrogen atoms in purple, copper atoms in red, and carbon atoms in grey. Thermal ellipsoids are shown with 50% probability. Hydrogen atoms are omitted for clarity.

4.3.3 Synthesis and crystallization of 9-functionalized molecular analogue

A molecular analogue, 1,2,3,4-tetrafluoro-9-phenylanthracene (**11**), was synthesized to provide insights into the photodimerization of the anthracene moiety with phenyl-functionalized 9 position as no relevant literature was reported. **11** crystalized in a $P2_1/m$ space group, with cell parameters of $a = 9.664(3)$ Å, $b = 6.843(2)$ Å, $c = 11.950(4)$ Å, and $\beta = 111.534(8)°$. Neighboring anthracene units were shown to stack in a head-to-tail co-facial fashion and the attached phenyl ring is orthogonal to the anthracene plane. The distance between the anthracene pair is 3.77 Å which is within the limits for dimerization[3]. Exposure to UV, however, did not yield any conversion to the dimer in the solid state. Therefore, **11** was dissolved in dichloromethane (0.1 M) and solution was subject to UV treatment at 350 nm. The conversion was complete within 30 min,

confirmed by solution NMR, and pale yellow crystals were obtained by slow evaporation of the dichloromethane solution. The dimer crystalized in a different space group, $P2_1/c$, with drastically different cell parameters: $a = 7.459(4)$ Å, $b = 19.775(12)$ Å, $c = 9.424(5)$ Å, and $\beta = 97.643(15)°$.
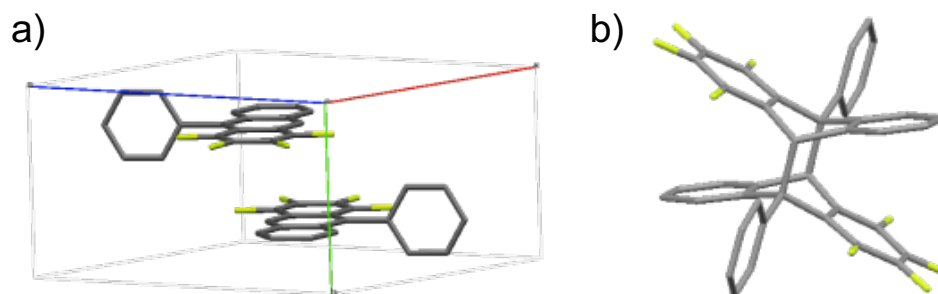

Figure 4.16. (**a**) Crystal structure of 1,2,3,4-tetrafluoro-9-phenylanthracene (**11**) which displays a head-to-tail stacking with the 9-phenyl group being perpendicular to the anthracene plane. This crystal was then subjected to UV treatment at 350 nm which resulted in dimerization and the crystal structure is shown in (**b**). Fluorine atoms are depicted in green and carbon atoms in grey. Hydrogen atoms are omitted for clarity.

The crystal structure of the **11**-dimer indicates that the phenyl substituent experiences a 22.7° rotation upon photodimerization (calculated based on the C_{phenyl}-C9-C10 angle). The large energy penalty needed for rotation and spatial deviation of the phenyl group in the solid state might contribute to the unsuccessful single-crystal-to-single crystal dimerization.

4.4 Conclusion and outlook

Solid-state photopolymerization based on anthracene dimerization could potentially provide a solution to COFs' "crystallization problem". By employing anthracene moieties as the points of extension into building block design and their pre-assembly into desirable orientation in the solid state, single-crystal-to-single-crystal photoreactions would lead to single crystalline extended frameworks through C-C bond formation. In this chapter, anthracene functionalized Cu(DPP)$_2$ complex **1** was synthesized; however, preferable co-facial stacking in the crystal structures was not observed. Fluorine atoms were therefore installed on half of the anthracene rim to enhance face-to-face π-π interaction in complex **2**. Three anthracene units of complex **2** were properly stacked, but showed no photoreactivity in the solid state. In order to offer mechanistic elucidation towards the unsuccessful dimerization of complex **2**, a molecular analogue, 1,2,3,4-tetrafluoro-9-phenylanthracene (**11**) was synthesized. Similarly, **11** was not photoreactive in the solid state, although the interlayer distance is suitable; however, it can be dimerized in the solution, which indicates that a phenyl group appended at the 9 position of anthracene could potentially impede its photodimerization possibly due to a high cost in energy penalty to spatially move the phenyl groups to form the C9-C10 bond.

Future work can be expanded towards the functionalization of the 2-position of tetra-fluoroanthracene, which is remote from the reaction site, and less steric hindered than the 3-position and thus easier to be chemically modified. By properly aligning of these anthracene

functionalities in the molecular crystal, polymerization can be performed to construct extended frameworks in one simple step of photoreaction.

4.5 References

(1)   Waller, P. J.; Lyle, S. J.; Osborn Popp, T. M.; Diercks, C. S.; Reimer, J. A.; Yaghi, O. M. *J. Am. Chem. Soc.* **2016**, *138*, 15519.

(2)   Deblase, C. R.; Silberstein, K. E.; Truong, T. T.; Abruña, H. D.; Dichtel, W. R. *J. Am. Chem. Soc.* **2013**, *135*, 16821.

(3)   Schmidt, G. M. J. *Pure Appl. Chem.* **1971**, *27*.

(4)   Wegner, G. *Macromol. Chem. Phys.* **1972**, *154*, 35.

(5)   Kory, M. J.; Wörle, M.; Weber, T.; Payamyar, P.; Van De Poll, S. W.; Dshemuchadse, J.; Trapp, N.; Schlüter, A. D. *Nat. Chem.* **2014**, *6*, 779.

(6)   Kissel, P.; Murray, D. J.; Wulftange, W. J.; Catalano, V. J.; King, B. T. *Nat. Chem.* **2014**, *6*, 774.

(7)   Dietrich-Buchecker, C.; Colasson, B.; Fujita, M.; Hori, A.; Geum, N.; Sakamoto, S.; Yamaguchi, K.; Sauvage, J. P. *J. Am. Chem. Soc.* **2003**, *125*, 5717.

(8)   Lange, R. Z.; Hofer, G.; Weber, T.; Dieter Schluter, A. *J. Am. Chem. Soc.* **2017**, *139*, 2053.

(9)   Müller, V.; Shao, F.; Baljozovic, M.; Moradi, M.; Zhang, Y.; Jung, T.; Thompson, W. B.; King, B. T.; Zenobi, R.; Schlüter, A. D. *Angew. Chem. Int. Ed.* **2017**, *56*, 15262.

(10)   Politov, A.; Chupakhin, A. P.; Tapilin, V. M.; Bulgakov, N. N.; Druganov, A. G.; Politov, A. A. *J. Struct. Chem.* **2010**, *51*, 1064.

(11)   O'Hagan, D. *Chem. Soc. Rev.* **2008**, *37*, 308.

(12)   Coates, G. W.; Dunn, A. R.; Henling, L. M.; Dougherty, D. A.; Grubbs, R. H. *Angew. Chem. Int. Ed.* **1997**, *36*, 248.

(13)   Cho, D. M.; Parkin, S. R.; Watson, M. D. *Org. Lett.* **2005**, *7*, 1067.

(14)   Cozzi, F.; Bacchi, S.; Filippini, G.; Pilati, T.; Gavezzotti, A. *Chem. - A Eur. J.* **2007**, *13*, 7177.

Chapter V

Crystalline Porous 1D Interlocking COF-500

5.1 Introduction

Mechanical entanglement has been utilized to link discrete molecules to impart them with unique dynamic properties[1–4]. Despite the utility of this approach its application to extended solids remains largely unexplored with natural occurrence of interpenetration remaining the only form of entanglement in 2D and 3D frameworks (*e.g.* metal organic frameworks, MOFs[5], and covalent organic frameworks, COFs[6]). In these structures the synthetic control over the degree of interpenetration is limited and dynamics are restricted by the fact that entire extended 2D or 3D lattices would need to be dislocated in a synchronized manner. Therefore, in the context of framework dynamics, elaboration of novel modes of entanglement based on constituents of lower dimensionality and their designed synthesis are highly sought after. In our recently embarked program on the synthesis of woven COFs[7,8], design strategies are devised for the targeted formation of such novel modes of entangled frameworks based on established principles of reticular chemistry[9] in conjunction with metal-template synthesis[10–12].

The reticular synthesis of woven materials was previously reported, which are constructed by mutual interlacing of 1D molecular threads[7]. These frameworks exemplify a novel mode of entanglement and display dynamics in extended solids. Woven structures are however fundamentally different from interlocking systems as no catenated rings are present. As such the realization of 1D interlocking motifs remains an outstanding synthetic target. In this chapter, the first example of a 3D framework, termed COF-500, is described, which is constructed by interlocking of 1D corner-sharing ladders. Pre-organization of building blocks by metal templation predispose the functionalized ligands of the resulting complex in the necessary geometry to serve as a building block for reticulation into crystalline interlocked frameworks. Upon framework formation and subsequent removal of the metal templates, the structure is composed entirely of interlocking 1D ladders. These ladders experience high degrees of motional freedom due to facile movement of the interlocked constituents without the need for flexing or breaking of chemical bonds while preserving the underlying COF structure.

5.2 Experimental Methods

All starting materials and solvents, unless otherwise specified, were obtained from Aldrich Chemical Co. and used without further purification. Tetrahydrofuran (HPLC grade, Aldrich) was passed through a PureSolv MD 7 Solvent Purification System before use. All reactions were performed at ambient laboratory conditions, and no precautions taken to exclude atmospheric moisture, unless otherwise specified. Pyrex glass tube charged with reagents and flash frozen with liquid N_2 were evacuated using a Schlenk line by fitting the open end of the tube inside a short length of standard rubber hose that was further affixed to a ground glass tap which could be close

to insolate this assembly from dynamic vacuum when the desired internal pressure was reached. Tubes were sealed under the desired static vacuum using an oxygen propane torch. Elemental microanalyses were performed at the University of California, Berkeley, College of Chemistry. Solution ^{1}H nuclear magnetic resonance (NMR) spectra were recorded on a Bruker AVQ-400 (400 MHz) spectrometer operating with an Avance electronics console. Utraviolet-visual (UV-Vis) spectrophotometry measurements were performed on a Shimadzu UV1800 using 1 cm Hellma quartz optical cells.
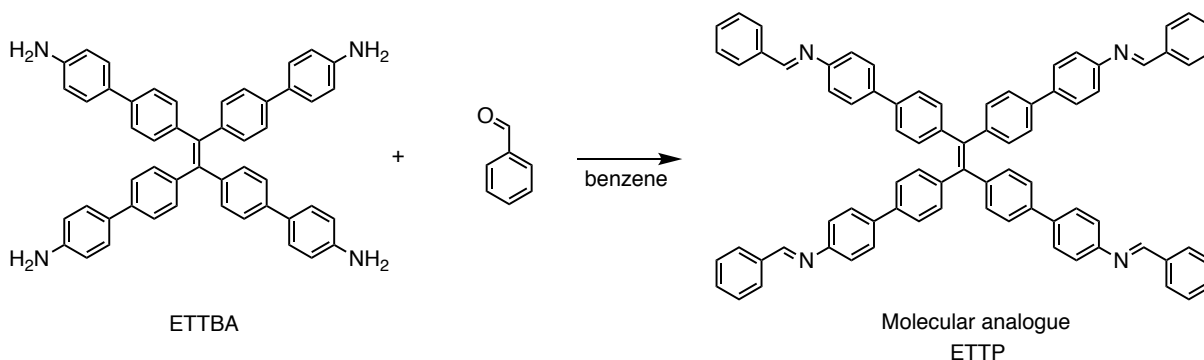
5.2.1 Synthesis

Scheme 5.2. Synthetic scheme of ETTBA linker.

1
quantitative

ETTBA
56%
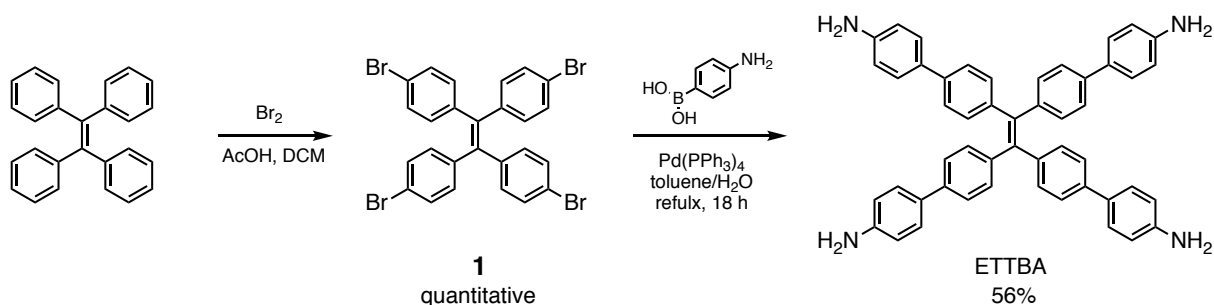
Synthesis of 4',4''',4''''',4'''''''-(ethene-1,1,2,2-tetrayl)tetrakis(([1,1'-biphenyl]-4-amine)) (TBPA): 1,1,2,2-tetrakis(4-bromophenyl)ethane (**1**) was synthesized based on reported procedure. In a 250 mL round bottom flask, **1** (1.0 g, 1.55 mmol) and (4-aminophenyl)boronic acid (2.4 g, 10.87 mmol) were suspended in a mixture of toluene (80 mL), 2M Na_2CO_3 aqueous solution (15 mL) and EtOH (15 mL), which was purged with nitrogen for 15 min before Pd(PPh$_3$)$_4$ (225 mg, 0.15 mmol) was added. The resulting mixture was transferred to an oil bath preheated to 110 °C and stirred vigorously for 18 h. After cooled down to room temperature, the organic layer was isolated and the aqueous layer was extracted with CH_2Cl_2 (2 × 40 mL). The organic layers were combined, dried over Na_2SO_4, filtered, and evaporated in vacuo to provide a brown solid. The product was further purified by flash silica gel chromatography with DCM to 1:100 MeOH:DCM. Evaporation solvent in vacuo afforded **1** as a bright yellow powder (606.1 mg, 56%). ^{1}H NMR (400 MHz, DMSO-d_6) δ 7.36 (d, [3]J = 8.2 Hz, 8 H), 7.33 (d, [3]J = 8.2 Hz, 8 H), 7.02 (d, [3]J = 8.1 Hz, 8 H), 6.58 (d, [3]J = 8.2 Hz, 8 H), 5.22 (s, 8 H).

Synthesis and activation of COF-500: A Pyrex tube measuring 10 × 8 mm (o.d × i.d) was charged with Cu(PBD)$_2$P (17.6 mg, 0.016 mmol), TBPA (12.0 mg, 0.016 mmol), 1 mL of 1: 1 dichlorobenzene:n-butanol mixture and 0.1 mL of 9 M aqueous acetic acid solution. The tube was flash frozen at 77 K (liquid N$_2$ bath), evacuated to an internal pressure of 50 mTorr and flame sealed. Upon sealing, the length of the tube was reduced to 18-20 cm. The reaction was heated at 180 °C for 72 h yielding a brown solid at the bottom of the tube which was isolated by centrifugation and washed by Soxhlet extractor with anhydrous THF for 12 h. The sample was activated at 85 °C under 50 mTorr for 12 h. Yield: 21.2 mg, 75.7% based on Cu(PBD)$_2$P. Elemental analysis: Calcd. for $C_{114}H_{74}CuN_8O_2P \cdot 6H_2O$: C, 76.47; H, 4.84; N, 6.25%. Found: C, 76.43; H, 5.26; N, 6.11%. ICP-AES of Cu content: Calcd.: 3.55%; Found: 3.5%

Scheme 5.3. Synthetic scheme of molecular analogue ETTP.

ETTBA

Molecular analogue
ETTP

Synthesis of the molecular analogue, (1E,1'E,1''E,1'''E)-N,N',N'',N'''-(ethene-1,1,2,2-tetrayltetrakis([1,1'-biphenyl]-4',4-diyl))tetrakis(1-phenylmethanimine), ETTP: A mixture of TBPA (70.0 mg, 0.10 mmol) and 4-phenyl-aniline (64.8 mg, 0.60 mmol) in anhydrous benzene (10 mL) was stirred at 75 °C overnight. A pale yellow solid precipitated during reaction and after cooling down the mixture to room temperature, the solid was collected by filtration, washed with DCM and dried under vacuum (105.0 mg, 100% yield). The molecule was not soluble in organic solvents, and was digested by using dimethyl sulfoxide (DMSO-d_6, 400 µL) and 30 µL of dCl (20 wt. % in D$_2$O) for NMR studies.^{1}H NMR (400 MHz, DMSO-d_6) δ 9.98 (s, 4 H), 7.83 (d, $^3J = 8.1$ Hz, 8 H), 7.71 (d, $^3J = 8.2$ Hz, 8 H), 7.68 (dd, $^3J = 7.8$ Hz, 4 H), 7.60 (dd, $^3J = 7.9$ Hz, 8H), 7.50 (d, $^3J = 7.5$ Hz, 8H), 7.39 (d, $^3J = 7.5$ Hz, 8H), 7.13 (d, $^3J = 7.7$ Hz, 8H). ESI-MS for [C$_{78}$H$_{57}$N$_4$]$^+$ (Calcd. 1049.46): m/z =1049.46 ([M]$^+$, 100%); Calcd. for C$_{78}$H$_{56}$N$_4$·H$_2$O: C, 87.77; H, 5.48; N, 5.25%. Found: C, 87.75; H, 5.67; N, 5.24%.

5.2.2 Fourier transform infrared spectroscopy

The FT-IR spectra of starting materials, molecular analogue, and activated COFs were collected on a Bruker ALPHA FT-IR Spectrometer equipped with ALPHA's Platinum ATR single reflection diamond ATR module, which can collect IR spectra on neat samples. The signals are given in wavenumbers (cm^{-1}).
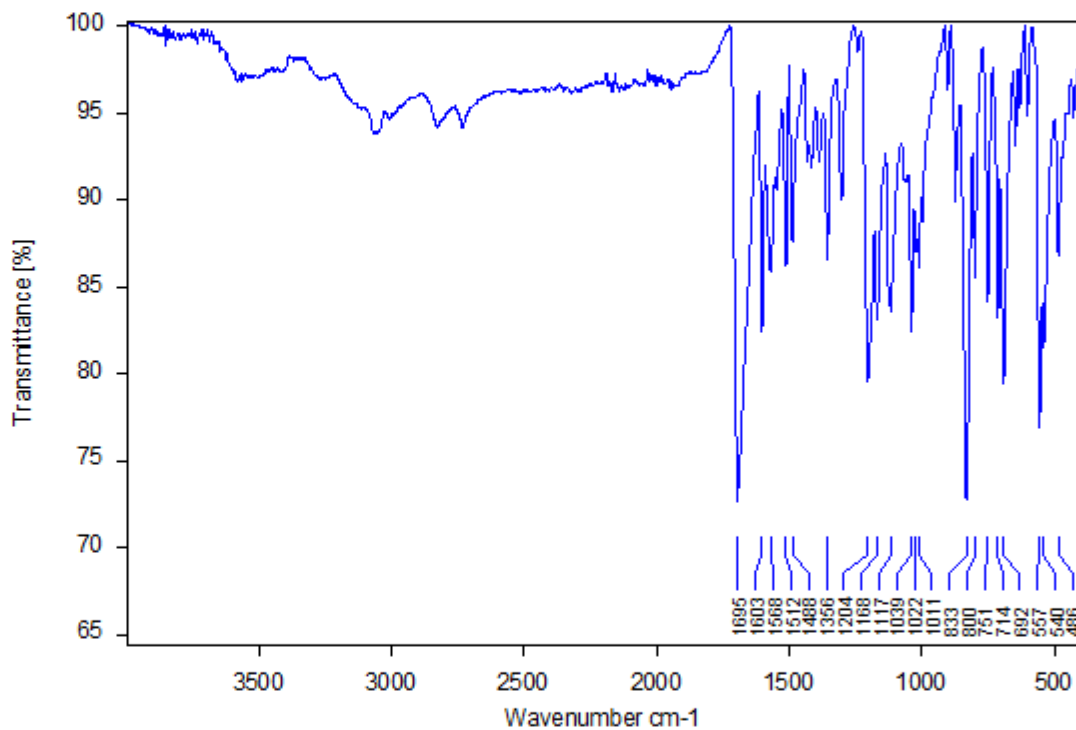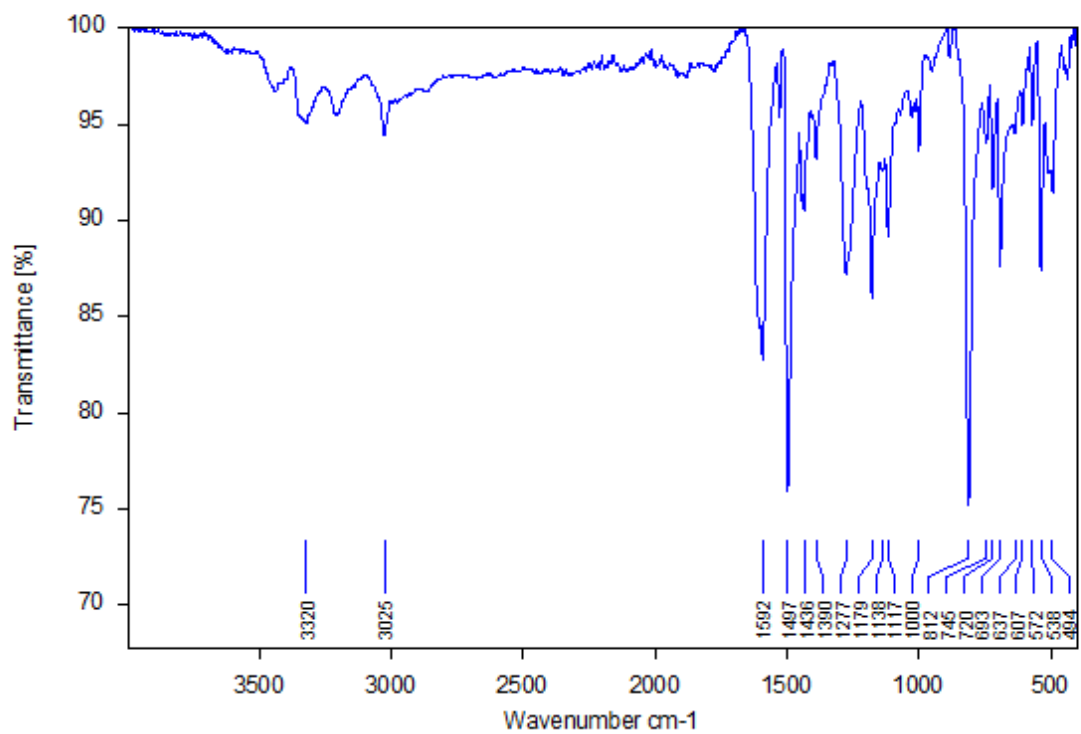

Figure 5.1. FT-IR spectrum of Cu(PDB)$_2$P.
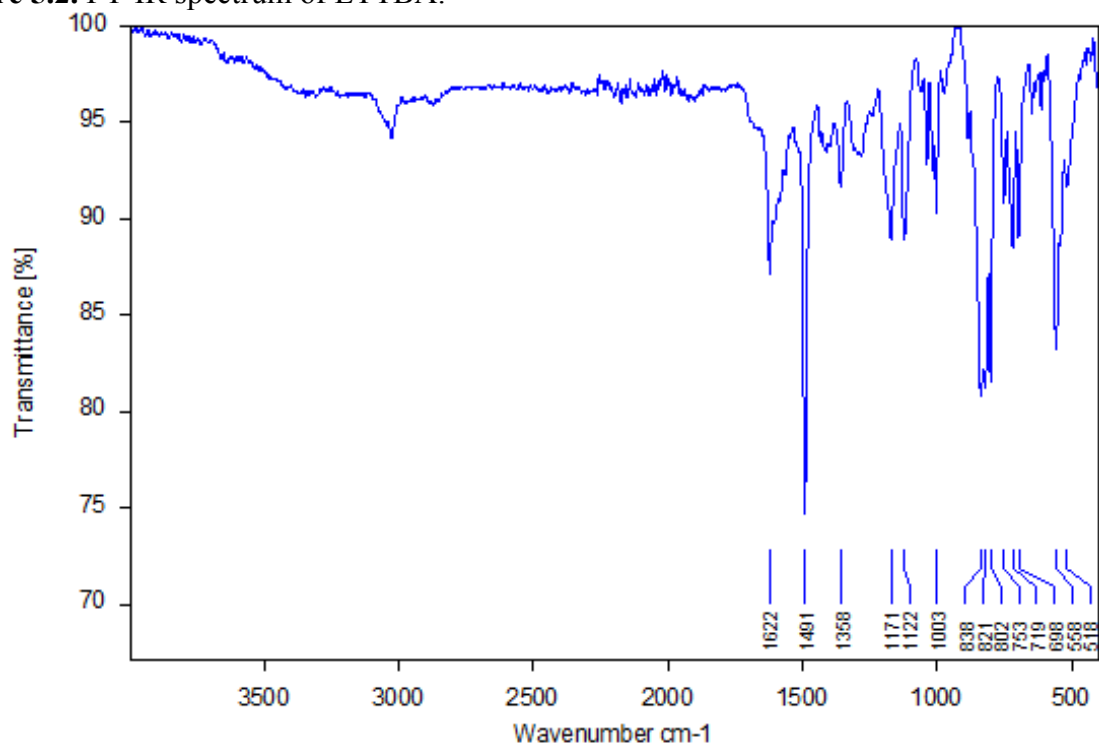
Figure 5.2. FT-IR spectrum of ETTBA.

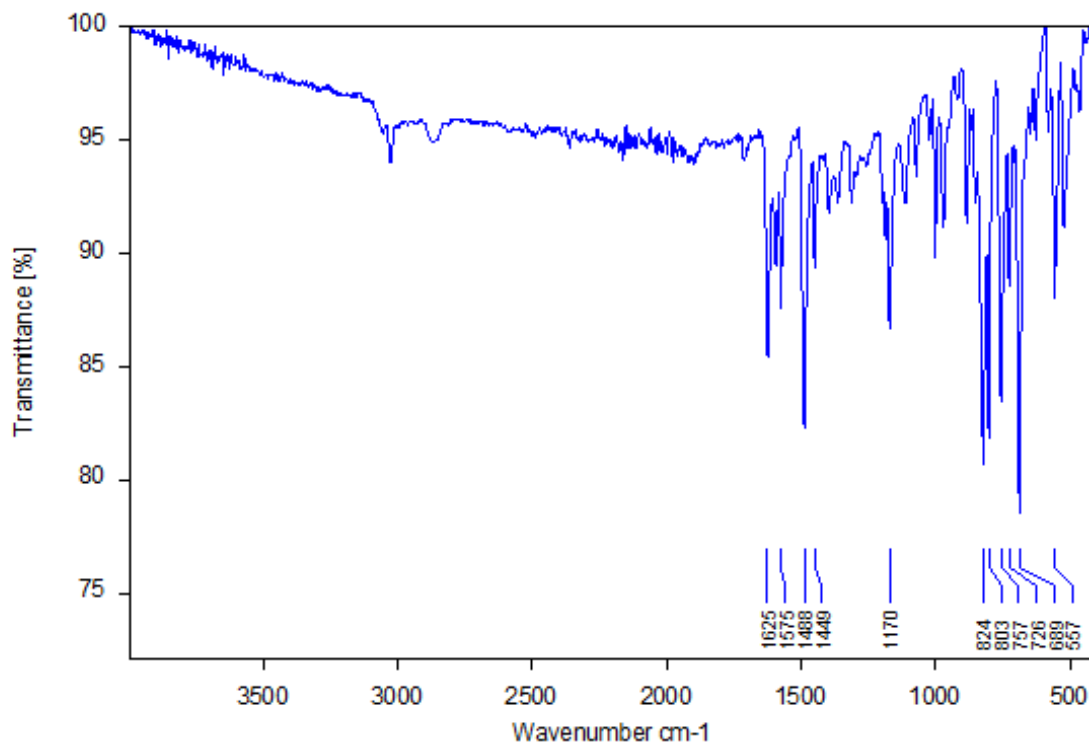**Figure 5.3.** FT-IR spectrum of activated COF-500.

Figure 5.4. FT-IR spectrum of COF-500 molecular analogue.

5.2.3 Scanning electron microscopy

Samples of COF-500 for SEM study were prepared by dropcasting the material suspended in THF onto a 1 cm^2 silicon wafer. SEM images were recorded on a Quanta™ 3D FEG scanning electron microscope with accelerating voltage of 5 kV with a working distance of 10 mm. SEM images of COF-500 show homogenous morphology of 1 × 0.5 μm spindle-shaped crystals.
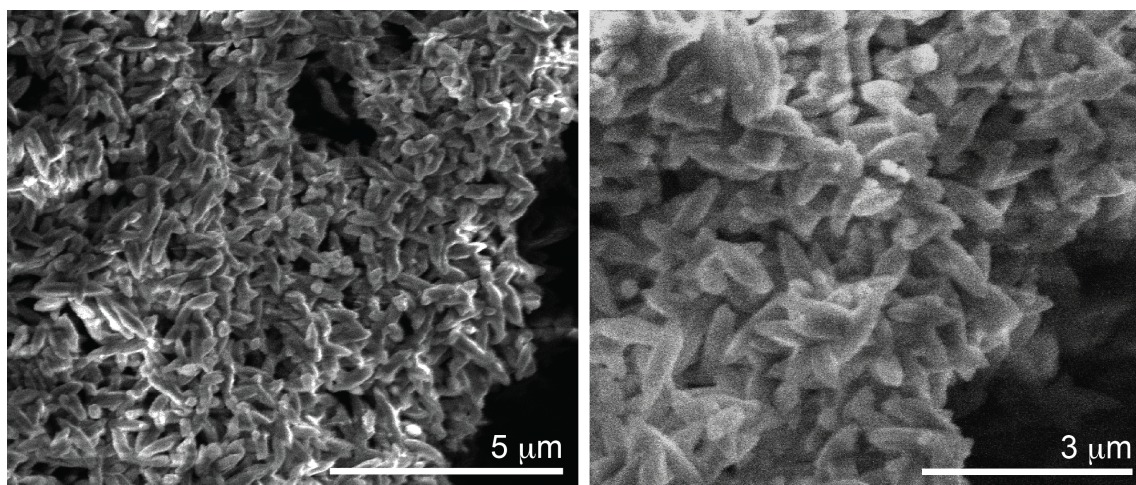

Figure 5.5. Rice-shaped crystals of COF-500 by SEM. No other forms were observed in the surveyed samples.

5.2.4 Structural determination

Electron diffraction analyses by transmission electron microscopy. A cold field emission JEM-2100F equipped with a DELTA Cs corrector operated at 60 kV was used for HRTEM imaging. Since COF materials are electron beam sensitive, the electron beam damage to the specimen was minimized as much as possible (in this study, the beam density during the observations was less than 500 electrons/(nm^2·s)). A Gatan 894 CCD camera was used for digital recording of the HRTEM images. A single HRTEM image with an exposure time of 2 seconds or a sequence of images (up to 20 frames) was recorded, with a 1 or 2 seconds exposure time for each. After drift compensation, some frames can be superimposed to increase the signal-to-noise (SN) ratio for display. HRTEM images are filtered by a commercial software named HREM-Filters Pro (HREM Research Inc. Japan).

COF-500 crystals were dispersed into ethanol by ultrasonic oscillation and dropped on a carbon film supported TEM grid. 3D electron diffraction tomography (3DEDT) data were collected on a JEOL JEM-2100, with LaB6 filament and the control of EDT-collect program. The data was further processed by EDT-process program.

Structural Modeling. Unit cell parameters and possible space groups were determined with the electron diffraction experiments. The unit cell parameters were refined against the PXRD pattern with a Pawley refinement (a = 20.0 Å, b = 20.0 Å, c = 51.9 Å, orthorhombic, space group C222). A crystal model was built accordingly with the use of Materials Studio v8.0, which was then optimized through a combination of energy and geometrical minimization and PXRD Pawley refinement. Different modes of interpenetration were included for structural construction. Non-interpenetrated form and four-fold interpenetration, which is maximal number of nets that is chemically reasonable, are not included for consideration, due to the unfitted pore size distribution compared to the experimental measurements. The model with two-fold interpenetration shows a better agreement with the PXRD, and therefore, this is a more reasonable model. Anions diphenylphosphinate - were finally introduced into the model to balance the charge of the Cu complexes, and to account for the missing electron density from electron diffraction studies. Since the position of the anions - anions does not affect the overall framework, the accurate positions of the anions are not claimed. The structure was further refined with the Pawley method (R_{wp} = 3.12%, R_p = 1.18%).
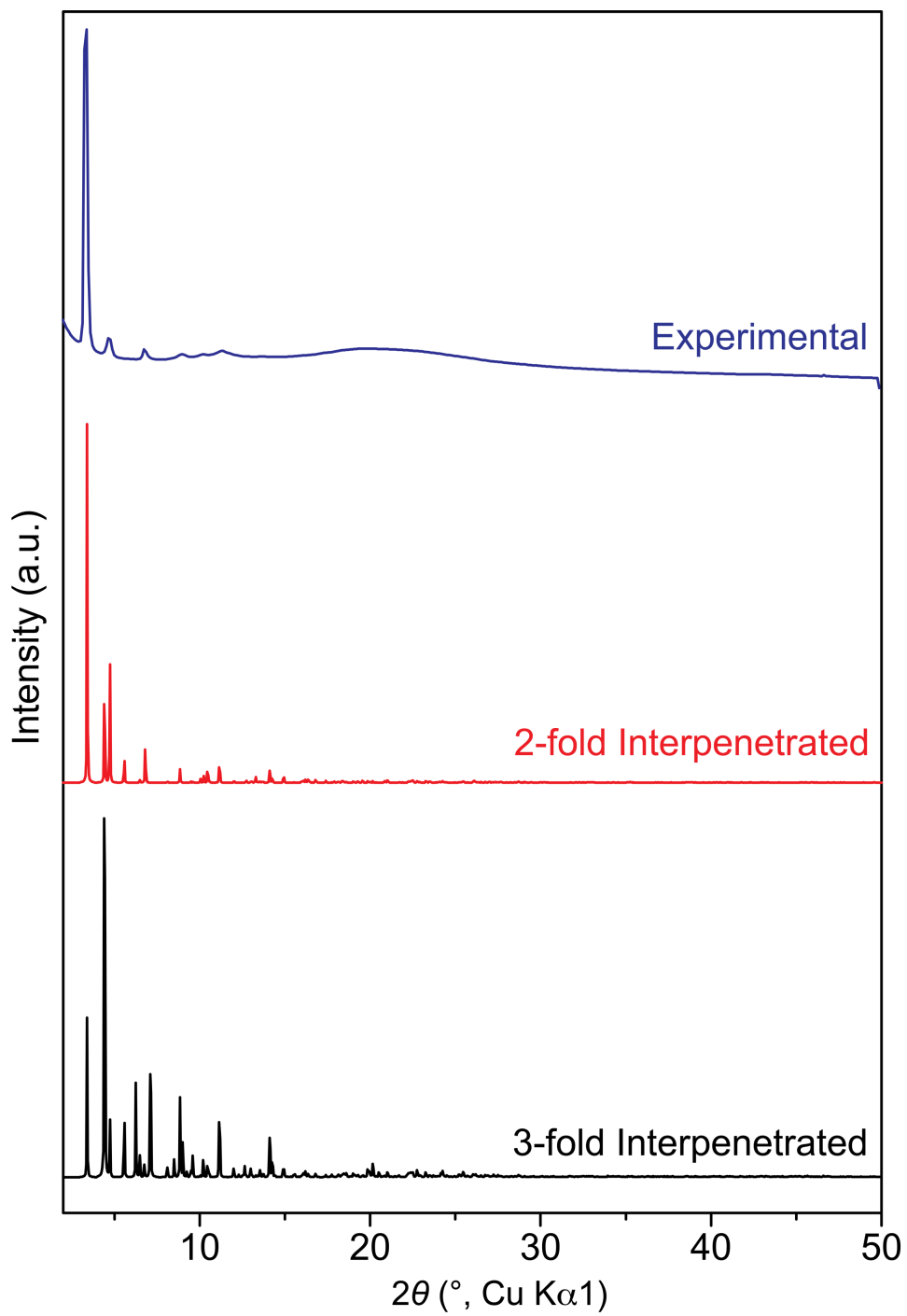
Figure 5.6. PXRD comparison for different modes of interpenetration of COF-500.

Table 5.1. Atom coordinates of COF-500 structural model.

COF-500				
Orthorhombic, *C*222				
a = 19.9819 Å, *b* = 51.8701 Å, *c* = 19.9839 Å				
Atom	*x*	*y*	*z*	Occupancy
C1	0.61488	0.06537	0.48282	1.0
C2	0.65432	0.06591	0.54124	1.0
C3	0.85363	0.30103	0.59326	1.0
C4	0.88393	0.27849	0.56921	1.0
C5	0.9408	0.32634	0.5389	1.0
C6	0.88243	0.32507	0.57804	1.0
C7	-0.09289	0.20578	0.35267	1.0
C8	-0.0717	0.22881	0.38287	1.0
C9	-0.03749	0.18151	0.4402	1.0
C10	-0.07538	0.18214	0.38126	1.0
C11	1.08722	0.41793	0.79532	1.0
C12	0.1423	0.37663	0.78232	1.0
C13	1.11181	0.37351	0.71951	1.0
N14	1.10674	0.34869	0.68957	1.0
C15	1.1438	0.32936	0.70648	1.0
C16	1.12622	0.30359	0.68372	1.0
C17	1.05906	0.29757	0.67047	1.0
C18	0.17485	0.28425	0.68133	1.0
C19	1.0413	0.27265	0.65288	1.0
C20	0.15683	0.25936	0.66185	1.0
C21	1.09023	0.25378	0.64533	1.0
C22	0.87046	0.39854	0.17985	1.0
C23	-0.07415	0.39361	0.30767	1.0
C24	0.573	0.97667	0.48661	1.0
C25	0.69727	0.91175	0.44371	1.0
C26	0.76848	0.87708	0.48212	1.0
C27	0.77075	0.86694	0.4168	1.0
C28	0.79922	0.82509	0.45211	1.0
C29	0.81894	0.79845	0.4419	1.0
C30	0.85194	0.74657	0.42854	1.0
C31	0.26791	0.89932	0.50465	1.0
C32	0.26003	0.88028	0.63548	1.0
C33	0.57484	0.04405	0.4686	1.0

C34	0.29718	0.90242	0.62215	1.0
H35	0.61474	0.08147	0.44839	1.0
H36	0.80787	0.30004	0.62202	1.0
H37	0.85889	0.34252	0.59585	1.0
H38	-0.12233	0.20611	0.30717	1.0
H39	-0.09154	0.16445	0.35751	1.0
H40	-0.03325	0.13998	0.44822	1.0
H41	0.17115	0.36123	0.8047	1.0
H42	1.02005	0.31194	0.67536	1.0
H43	0.22648	0.28853	0.69346	1.0
H44	0.98933	0.26787	0.64606	1.0
H45	0.85103	0.3993	0.12934	1.0
H46	1.03158	0.43085	0.7081	1.0
H47	0.61153	0.99222	0.39392	1.0
H48	0.79288	0.86732	0.52332	1.0
H49	0.26976	0.90652	0.45382	1.0
H50	0.25898	0.87256	0.6858	1.0
H51	0.32387	0.91155	0.6629	1.0
N52	0.94157	0.28025	0.53439	1.0
C53	0.97023	0.30314	0.51854	1.0
C54	0.97071	0.34976	0.51969	1.0
C55	1.06255	0.41587	0.72956	1.0
H56	0.94867	0.36794	0.53458	1.0
H57	-0.05031	0.39134	0.356	1.0
C58	0.65249	0.04494	0.58538	1.0
H59	0.6831	0.04464	0.63009	1.0
C60	0.61207	0.97614	0.42846	1.0
N61	-0.03508	0.22777	0.44027	1.0
C62	-0.01822	0.20497	0.46968	1.0
C63	-0.01886	0.15818	0.47042	1.0
H64	0.19465	0.24464	0.65729	1.0
H65	0.5456	0.04367	0.42297	1.0
C66	1.01849	0.47695	0.92832	1.0
C67	1.06416	0.4388	0.84013	1.0
H68	0.92559	0.47488	0.87328	1.0
C69	0.97579	0.4673	0.87885	1.0
C70	0.1066	0.44861	0.89012	1.0
H71	0.15799	0.44224	0.89437	1.0
C72	0.99812	0.4481	0.83562	1.0

H73	0.96349	0.44049	0.79896	1.0
C74	0.08363	0.46732	0.93433	1.0
H75	0.11766	0.4752	0.97125	1.0
N76	0.79572	0.84165	0.40411	1.0
C77	0.84352	0.78919	0.38051	1.0
C78	0.86062	0.76319	0.37406	1.0
H79	0.85075	0.80205	0.33848	1.0
H80	0.88284	0.75632	0.32798	1.0
C81	0.80945	0.21835	0.50461	1.0
C82	0.82588	0.24413	0.51141	1.0
H83	0.78963	0.21151	0.45735	1.0
H84	0.8199	0.2569	0.4692	1.0
Cu85	0	0.25392	0.5	1.00
C86	0	0.5	0.03354	1.00
C87	0.46628	0	0.5	1.00
P265	0.9137	0.23076	-0.18488	0.50
O266	0.90335	0.22969	-0.26516	0.50
O267	0.88376	0.20312	-0.16245	0.50
C268	0.8591	0.25586	-0.14982	0.50
C269	1.00401	0.23117	-0.16738	0.50
C270	0.81663	0.27022	-0.19134	0.50
C271	0.7753	0.28923	-0.16392	0.50
C272	0.77609	0.2939	-0.09504	0.50
C273	0.81814	0.27951	-0.05346	0.50
C274	0.85962	0.26051	-0.08078	0.50
C275	1.04259	0.25231	-0.1874	0.50
C276	1.11125	0.25284	-0.17388	0.50
C277	1.14153	0.23231	-0.14029	0.50
C278	1.10323	0.21114	-0.12046	0.50
C279	1.03458	0.21055	-0.1339	0.50
H280	0.81527	0.26672	-0.24468	0.50
H281	0.74243	0.30027	-0.19604	0.50
H282	0.74399	0.30859	-0.07389	0.50
H283	0.81865	0.28308	-0.00008	0.50
H284	0.89216	0.24949	-0.04827	0.50
H285	1.01968	0.26814	-0.21413	0.50
H286	1.14128	0.26893	-0.19049	0.50
H287	1.19475	0.23267	-0.13036	0.50
H288	1.1268	0.19514	-0.09492	0.50

H289	1.00552	0.19404	-0.11822	0.50

5.2.5 Procedure for demetalation and remetaltion

To a suspension of COF-500 powder was added a 0.5 M KCN methanol solution, and was heated at 80 °C. The solution was replaced by a fresh solution of KCN every 24 h and this procedure was repeated three times. Control experiment without KCN solution was also conducted under otherwise identical conditions. Subsequently, both samples were washed with anhydrous methanol and dried at 85 °C under 50 mTorr for 12 h. The demetalated material was observed to be pale-yellow in color, in contrast to the dark brown color of COF-500.

The remetalation process was carried out in similar conditions with the complexation reaction to yield complex $Cu(PBD)_2BF_4$. Dried powder of the demetalated material was immersed in anhydrous $CHCl_3$, to which was added a 0.01 M $Cu(CH_3CN)BF_4$ solution in CH_3CN. This mixture was stirred for 12 h under N_2 at room temperature and dark brown color was recovered.

In the demetalated COF-500, copper content was determined by ICP-AES to be less than 0.02%, which is less than 1% of the original Cu concentration. After remetalation, the Cu content was determined to be 3.5% which is 99% of COF-500.
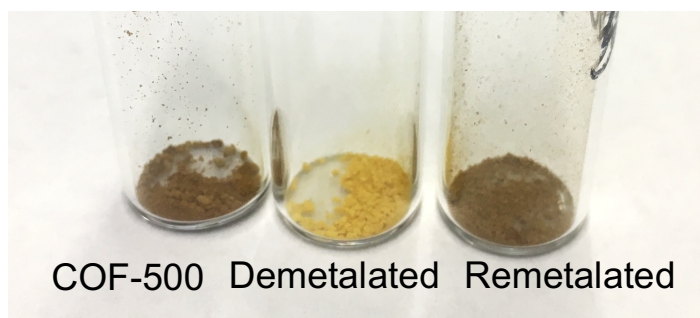
Figure 5.7. Powder of COF-500 (left), demetalated COF-500 (middle), and remetalated COF-500 (right). The sample changed color from dark brown to yellow as it was demetalated and after remetalation, the dark color was recovered.
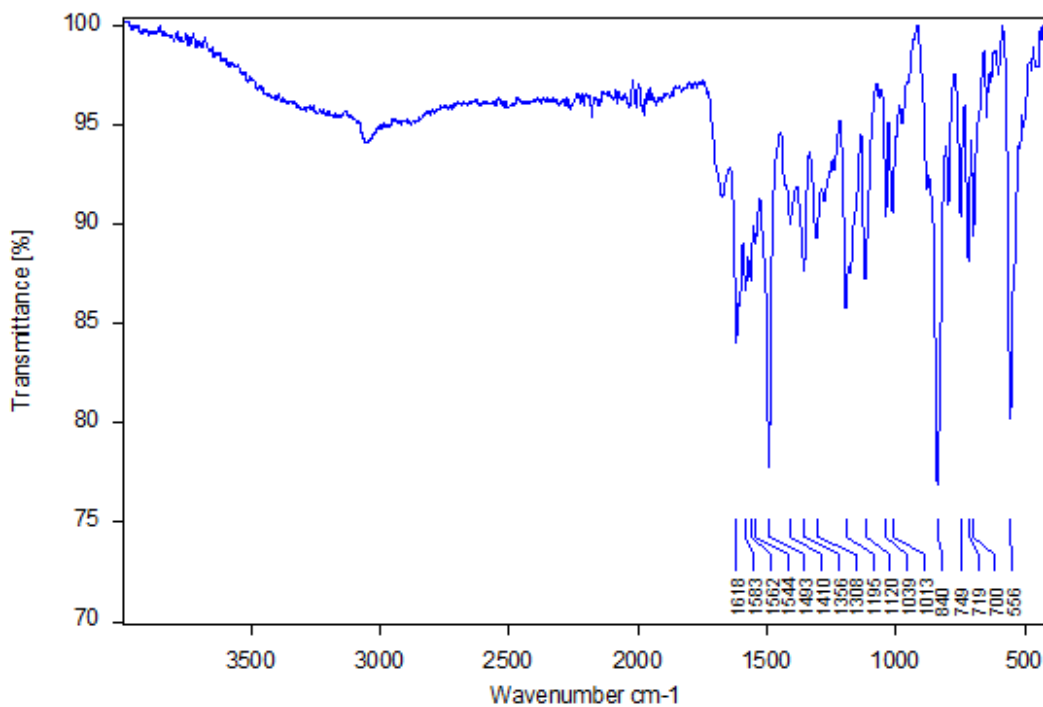
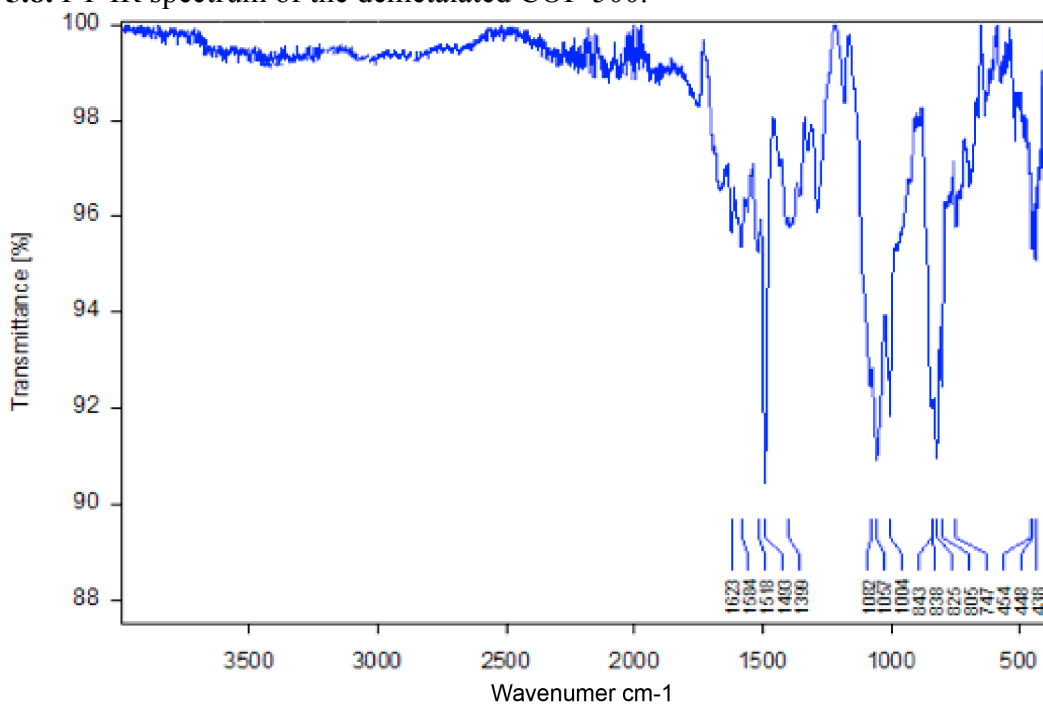**Figure 5.8.** FT-IR spectrum of the demetalated COF-500.

Figure 5.9. FT-IR spectrum of the remetalated COF-500, where the characteristic peak for BF_4^- at 1057 cm^{-1} confirms the remetalation with $Cu(CH_3CN)BF_4$.
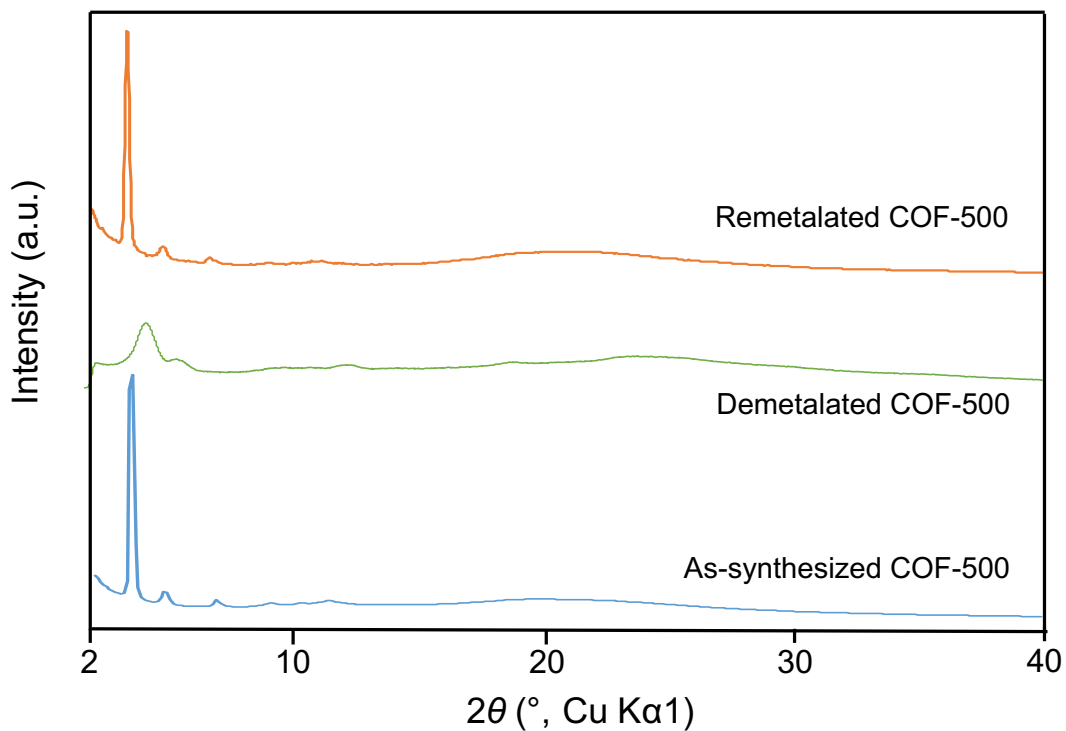
Figure 5.10. PXRD patterns of as-synthesized COF-500, the demetalated and remetalated materials. The crystallinity of COF-500 decreases upon demetalation and can be fully restored after remetalation with copper(I) ions.
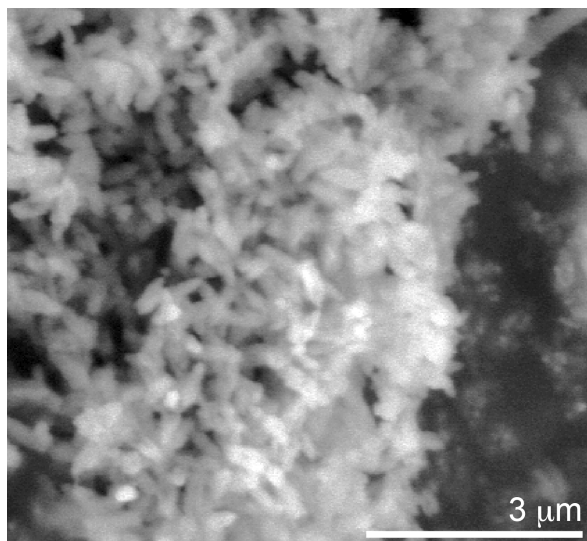

Figure 5.11. SEM image of the demetalated sample, which shows similar rice-shaped morphology to COF-500.

5.2.6 Low pressure gas adsorption experiments

Low-pressure gas (0-110 kPa) adsorption isotherms were measured volumetrically using Quadrasorb-SI. Liquid nitrogen bath was used for the temperature control of 77 K. Water bath with circulator were used for the temperature control at 283 K. The THF vapor adsorption isotherms were collected at 283 K using a Microtrac BELSorp-Aqua3 adsorption apparatus with a water circulator bath. Ultrahigh grade (purity >99.999%) of N_2, were used through all the experiments. Anhydrous THF was used for vapor adsorption, which was degassed at least three times before isotherm collection.

The sample was outgassed at 75 °C for 12 h before the measurement. Surface areas were calculated from the adsorption data using Brunauer-Emmett-Teller (BET) and Langmuir methods, respectively. Pore size distribution was assessed by slit-pore NLDFT equilibrium method at 77 K.
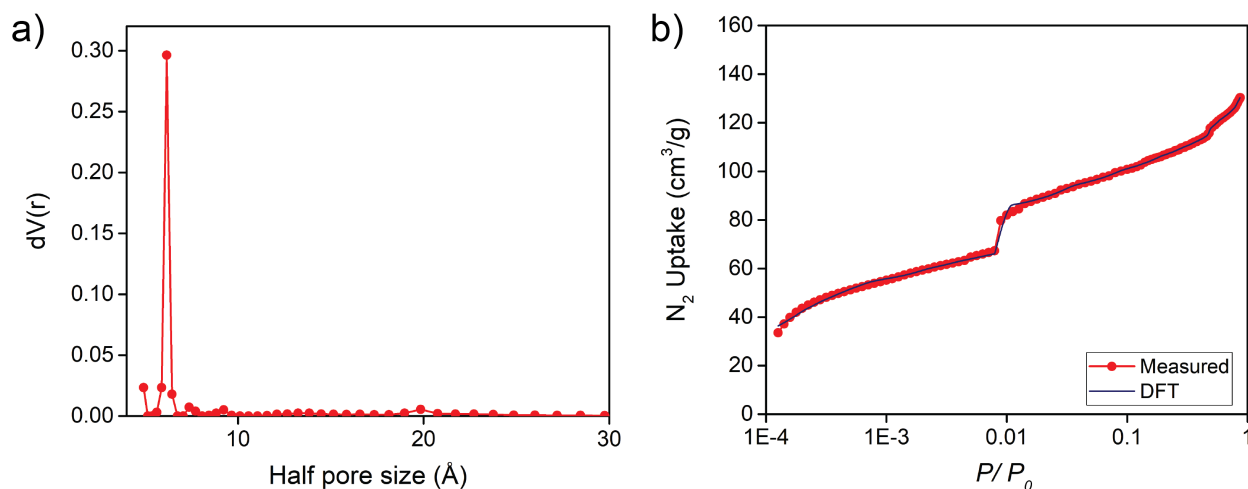

Figure 5.12. (a) Pore size distribution histogram of COF-500 calculated from DFT/Monte-Carlo fitting[13] of the adsorption branch of the N_2 adsorption isotherm at 77 K (b) with the fitting error of 0.682% using slit pore NSDFT equilibrium model for carbon at 77 K.
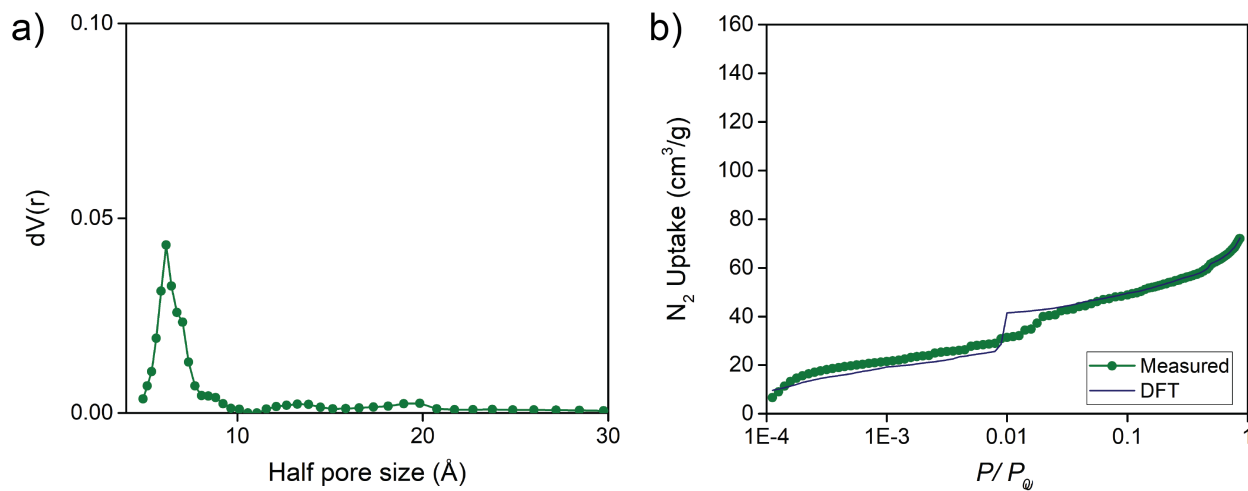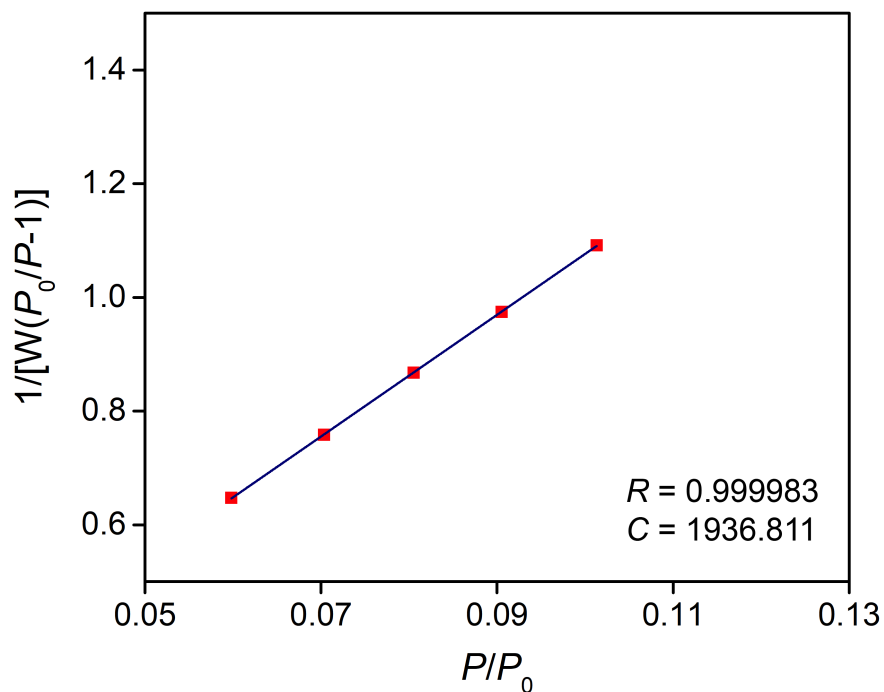
Figure 5.13. (a) Pore size distribution histogram of demetalated COF-500 calculated from DFT/Monte-Carlo fitting of the adsorption branch of the N_2 adsorption isotherm at 77 K (b) with the fitting error of 4.386% using slit pore NSDFT equilibrium model for carbon at 77 K.

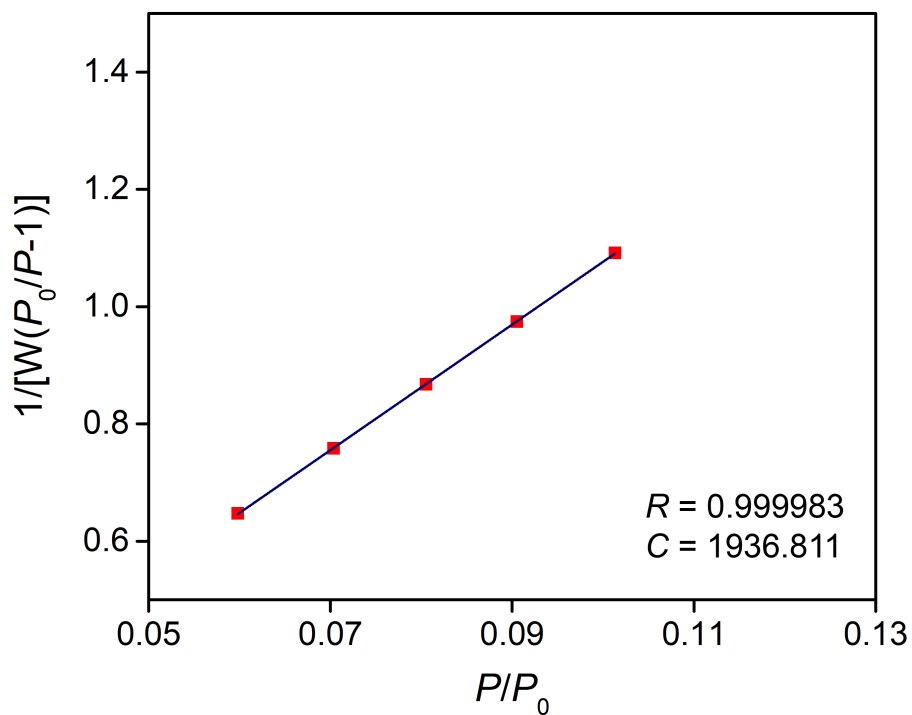**Figure 5.14.** Multiple point BET[14] plot of COF-500 giving a specific surface area of 325 m^2/g.

Figure 5.15. Multiple point BET[14] plot of COF-500 giving a specific surface area of 325 m^2/g.

5.2.7 Solid state fluorescent emission measurement

PL measurements were conducted using a focused excitation from a 375 nm laser diode with emission collected on a Nikon ME600 optical microscope coupled to a multimode fiber. The laser power was decreased to 1 mW with neutral density filters and an integration time of 5 seconds was used per sample. The spectra were acquired using a liquid-nitrogen-cooled CCD. The samples were prepared on a glass slide, and spectra were acquired at the same location for serial measurements.
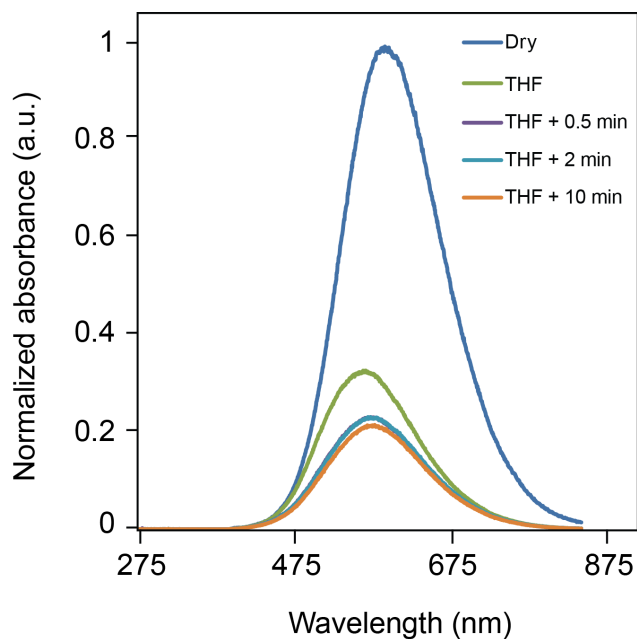

Figure 5.16. Solid-state photoluminescence spectra of demetalated COF-500 and upon addition of THF with various incubation time.
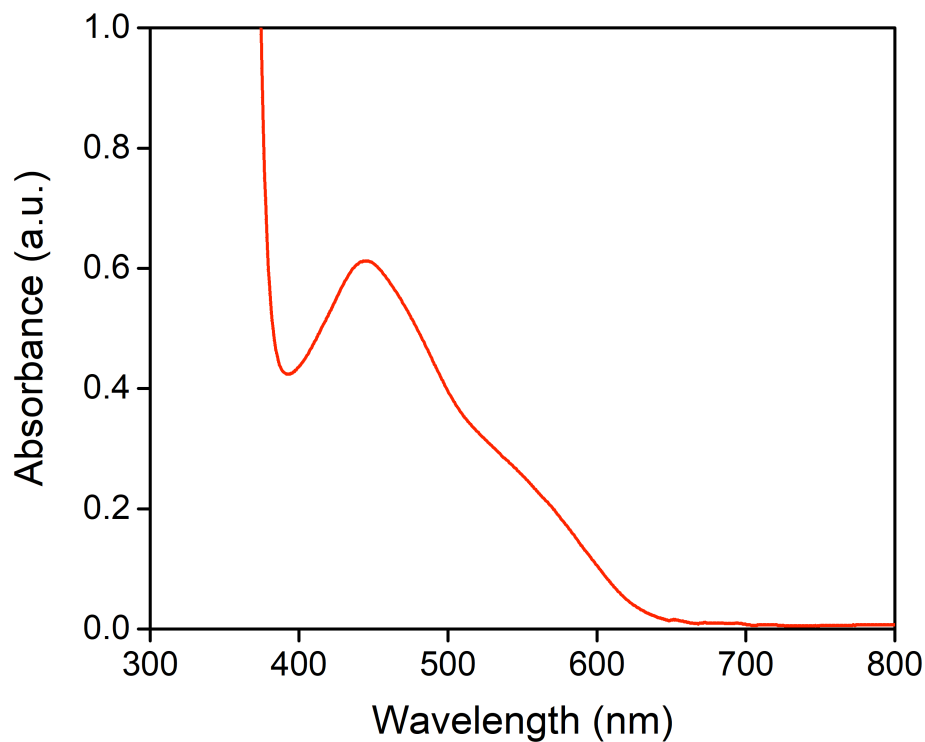
Figure 5.17. UV-Vis Absorption spectrum of Cu(PDB)$_2$P in DCM.

5.3 Results and discussion

The synthetic strategy of COF-500 is described in Figure 5.18. Tetrahedral tetratopic Cu(I)-bis[4,4'-(1,10-phenanthroline-2,9-diyl)dibenzaldehyde] diphenylphosphinate [Cu(PDB)$_2$P], an aldehyde functionalized copper(I)-bisphenanthroline complex salt, was linked with square planar tetratopic 4',4''',4''''',4'''''''-(ethene-1,1,2,2-tetrayl)tetrakis(([1,1'-biphenyl]-4-amine)) (ETTBA) through imine bond formation. In Cu(PDB)$_2$P, the copper centers pre-organize two PDB ligands such that their appended aldehyde functional groups approximate a tetrahedral geometry. The 60° angles between the two points of extension (*i.e.* aldehyde funtionalities) of each phenanthroline ligand are complementary to the 120° angles between the points of extension (*i.e.* amino functionalities) of ETTBA thus leading to the formation of 4-membered macrocycles (Figure 5.18a). These macrocycles are covalently linked through the double bonds of ETTBA to yield corner-sharing 1D ladders. In each individual ladder, the phenanthroline ligands comprising the corners of the macrocycles are linked to a second set of phenanthroline ligands by copper(I) ions in an embracing manner. This second set of phenanthroline ligands forms part of an adjacent interlocking ladder (blue and orange, Figure 5.18a). Due to the dihedral angle of the two phenanthroline ligands of the complex the entangled ladders are orthogonal to each other and construct a 3D framework with an underlying **pts** net, the default net for the linking of tetrahedral and square planar building units[9,15].
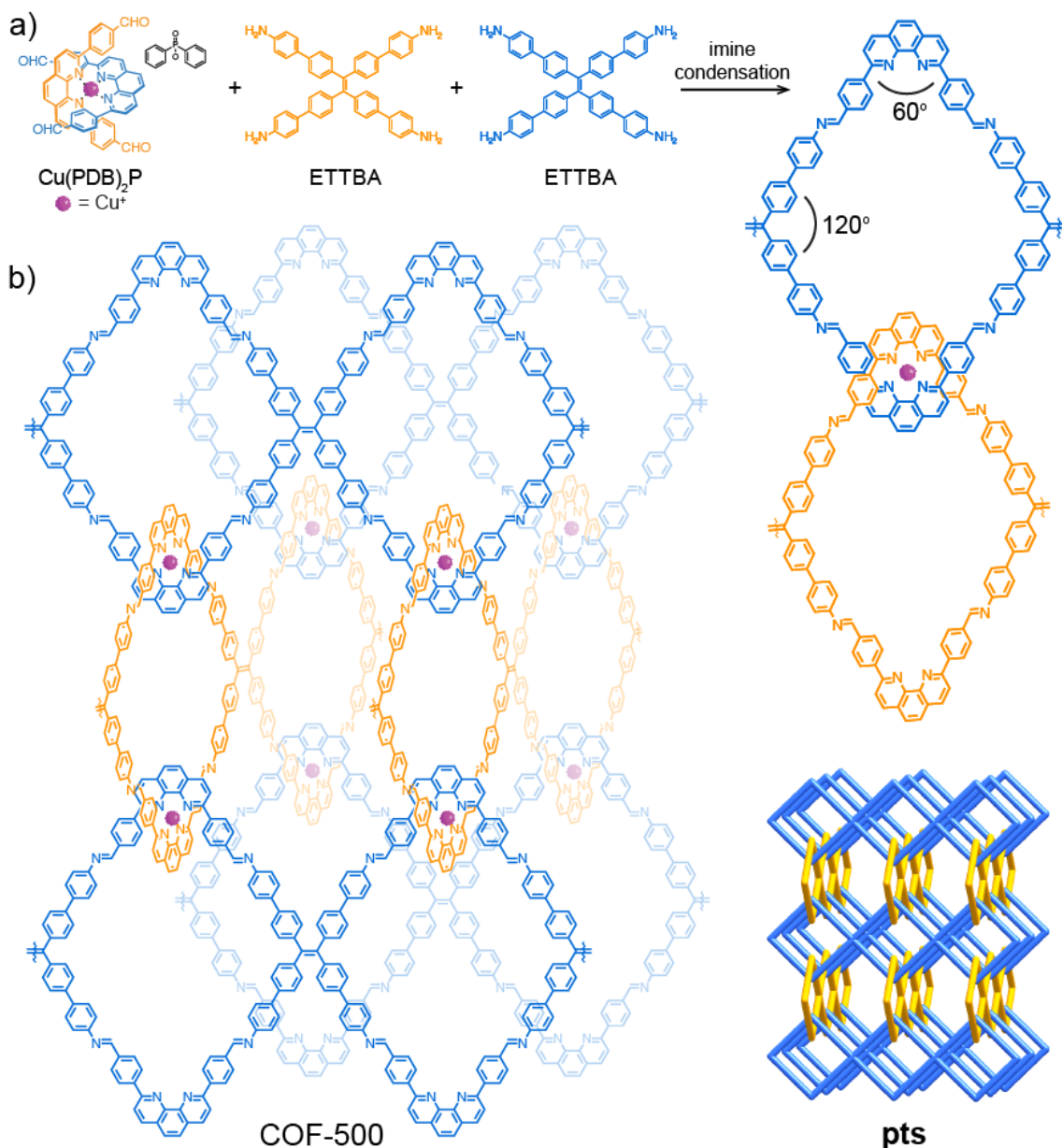
Figure 5.18. Synthetic strategy for the design and synthesis of interlocking 1D ladders. COF-500 was constructed from (**a**) Cu(PDB)$_2$P and ETTBA to yield interlocking corner-sharing ladders connected through the copper(I) ion templates to form (**b**) an extended 3D framework with **pts** topology.

The synthesis of COF-500 was carried out based on reversible imine bond formation; equimolar amounts of Cu(PDB)$_2$P and ETTBA where reacted in a 1:1 (*v/v*) mixture of 1,2-dicholorobenzene and 1-butanol in the presence of aqueous acetic acid as a catalyst. The reaction mixture was sealed in a Pyrex tube and heated at 180°C in order to increase solubility of the starting materials and enhance the reversibility of the reaction. After three days, the resulting precipitate was collected and washed by Soxhlet extraction with anhydrous THF to yield a dark brown crystalline solid, which was found to be insoluble in common organic solvents or water.

The formation of imine linkages in COF-500 was confirmed by Fourier-transform infrared spectroscopy (FT-IR) and ^{13}C cross-polarization magic angle spinning (CP-MAS) solid-state nuclear magnetic resonance (NMR) spectroscopy. A molecular analog of COF-500 with an tetraphenylethylene core, (1E,1'E,1''E,1'''E)-N,N',N'',N'''-(ethene-1,1,2,2-tetrayltetrakis([1,1'-biphenyl]-4',4-diyl))tetrakis(1-phenylmethanimine) (ETTP) was used as a model compound for data analysis and comparison. The disappearance of the C=O stretching vibration at 1695 cm^{-1} of the aldehyde functional groups in the FT-IR spectra, as well as the absence of peaks at a chemical shift above 200 ppm in the ^{13}C CP-MAS NMR solid-state NMR spectrum demonstrate full conversion of the Cu(PDB)$_2$P aldehyde starting material. Furthermore, the FT-IR spectrum of COF-500 features characteristic C=N stretching vibrations at 1622 and 1171 cm^{-1} (1625 and 1170 cm^{-1} for ETTP) corroborating the formation of imine bonds[7,16,17]. These observations support complete formation of imine bonds between the Cu(PDB)$_2$P and ETTBA building blocks and thus the construction of an extended framework.

Scanning electron microscopy (SEM) micrographs of as-synthesized COF-500 show a homogeneous morphology of rod-shaped crystals with dimension of approximately 1 μm x 0.2 μm x 0.2 μm (Figure 5.19a). After ultrasonic oscillation of the sample in ethanol, individual crystals of COF-500 were dispersed on a copper sample grid for transmission electron microscopy (TEM) studies. 3D electron diffraction tomography (3D-EDT)[18] data of COF-500 was collected by combining specimen tilt and electron-beam tilt in the range of −34.3° to +33.0° with a beam-tilt step of 0.3°. From the acquired data set the 3D reciprocal lattice of COF-500 was constructed and found to have unit-cell parameters of a = 21 Å, b = 52 Å, c = 21 Å, and V = 22932 Å^3, which were used to index reflections observed in both the powder X-ray diffraction (PXRD) pattern and Fourier diffractograms of high-resolution transmission electron microscopy (HRTEM) images (Figure 5.19b and c). The unit-cell parameters were further refined by Pawley refinement of the PXRD pattern to be a = 20.0 Å, b = 51.9 Å, c = 20.0 Å, and V = 20760 Å^3. A structure model of COF-500 was built in Materials Studio 8.0[19] in an orthorhombic space group *C*222. The calculated PXRD pattern of the modeled structure was found to be in good agreement with the experimental pattern of activated COF-500 (Figure 5.19d).
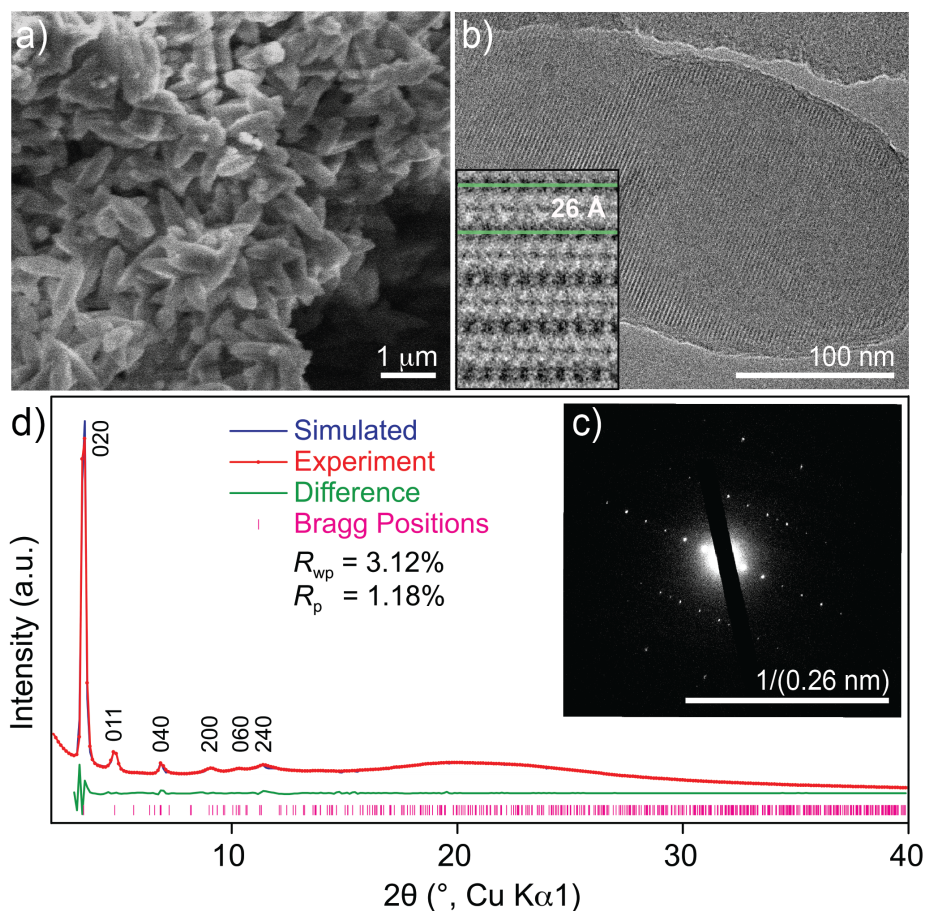
Figure 5.19. Electron microscopy and PXRD studies of COF-500. (a) One single phase of rod-shaped crystals is observed by SEM indicating the formation of COF-500 in pure phase. **(b)** HRTEM image of a single crystal of COF-500 showing lattice fringes with distances of 26 Å (highlighted in the inset). **(c)** Selected area electron diffraction pattern acquired from the crystal shown in **c** confirms the single-crystalline nature of the particles. **(d)** Indexed PXRD pattern of the activated sample of COF-500 (red) and Pawley refinement (navy) of the unit cell from the modeled structure. The refined model is in good agreement with the experimental data.
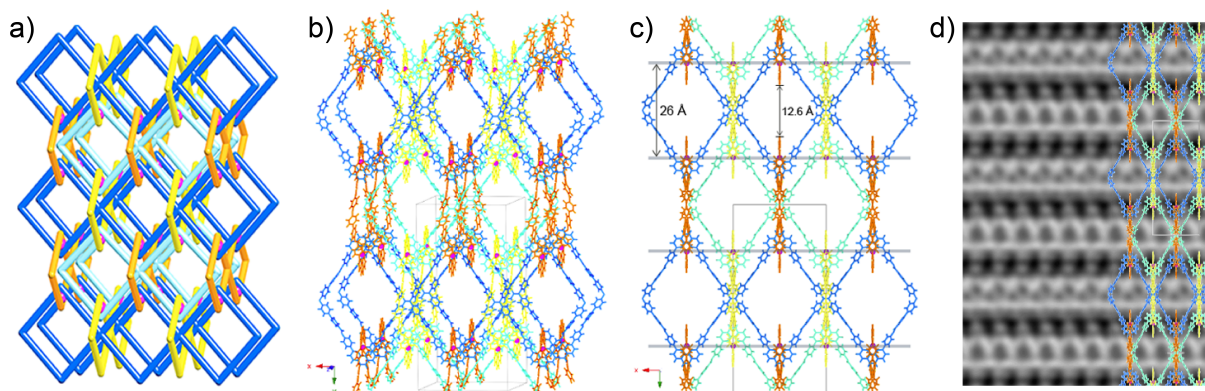

Figure 5.20. Structure elucidation of COF-500. (a) One net of the **pts** topology framework is constructed from interlocking blue and orange 1D ladders, which are in turn mutually interlocked with a second identical net comprised of 1D ladders highlighted in cyan and yellow. The

121

entanglement is templated by copper(I) ions represented as pink spheres. **(b)** Structural model of COF-500 with the same connectivity of **a**. **(c)** Representation of the structural model viewed along the crystallographic [001] direction reveals that the copper ions are aligned in the 0 ¼ 0 and 0 ¾ 0 lattice planes separated by 26 Å. **(d)** The structural model overlaid with a HRTEM image of COF-500 shows good agreement. Color code: Individual 1D-ladders are depicted in blue, orange, cyan, and yellow, respectively. Copper(I) ions are depicted in pink. All counterions are omitted for clarity.

According to the refined model, COF-500 crystallizes in a **pts** network with tetrahedral building units $Cu(PBD)_2P$ and square planar ETTBA connected through imine bonds. Covalently linked 1D ladders propagate along the crystallographic *a* (highlighted in blue and cyan) and *c* directions (orange and yellow) and are mechanically entangled along the crystallographic *b* axis (Figure 5.20). The **pts** net is self-dual[20] and as such prone to framework interpenetration. Indeed, the Cu-Cu distance within each macrocycle is half of the b parameter, 26 Å, which allows for another identical net to reside in the pore to form the overall COF-500 framework (Figure 5.19b and c, blue and orange, cyan and yellow represent two individual **pts** nets). These two sets of frameworks are also mutually interlocked in the COF-500 crystal along the *ac* plane (blue and yellow, cyan and orange, respectively) to form 2D interlocking sheets, where the tetraphenylethylene corners of blue ladders are encircled by the rings of yellow ladders, and *vice versa*. The 2D layers are further interlocked with neighboring layers along the *b* direction, templated by the entangled phenanthroline ligands with copper(I) ions serving as the points of registry, to yield a 3D interlocking framework. As the copper centers sit in the 0 ¼ 0 and 0 ¾ 0 lattice planes in the crystal structure, they are apart by 26 Å viewed along the *c* axis (Figure 5.20c and d), in good agreement with the striped pattern of the lattice fringes observed in the high-resolution TEM image shown in Figure 5.19b.

In order to obtain the truly catenated framework, the copper templates were removed to yield the demetalated material. This was affected by heating COF-500 in a 1M KCN methanol solution at 75°C[7,10]. Inductively coupled plasma (ICP) analysis revealed that more than 99% of the copper ions were removed upon demelation. The dark color of COF-500, which arises from the copper-phenanthroline metal-to-ligand charge transfer[21], disappeared and the demetalated material instead shows a pale yellow color. Upon demetalation, the crystallinity of COF-500 decreases drastically, indicating spatial rearrangement of the structure and concomitant loss of long-range periodicity. However, the covalent bonding within the individual ladders and the overall integrity of the structure was maintained during the process; the FT-IR imine stretching vibrations at 1623 and 1171 cm^{-1} are consistent with those of COF-500 (1622 and 1171 cm^{-1}, respectively). In the demetalated framework the 1D chains are held together by interlocking such that the overall structure remains unaltered. Indeed, upon remetalation of the material by stirring in a $CH_3CN/CHCl_3$ solution of $CuBF_4$ crystalline COF-500 can be recovered. This remetalated material has identical crystallinity and chemical composition to the original as-synthesized COF-500, as evidenced by the complete recovery of the intensity and positions of the reflections in the PXRD pattern as well as the presence of identical vibration bands in the FT-IR spectrum.
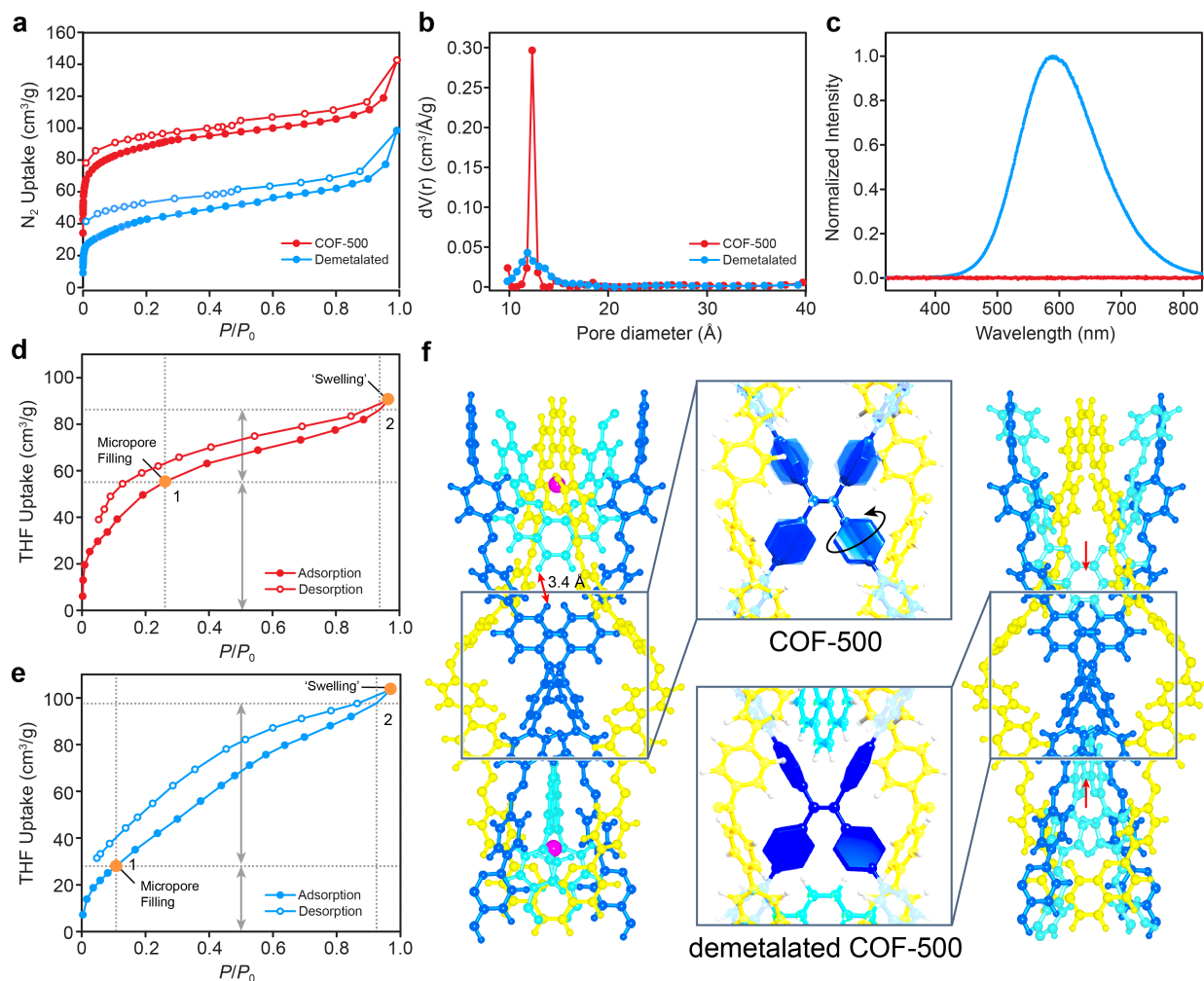
Figure 5.21. Adsorption and solid-state photoluminescence studies of COF-500 and the demetalated material. (a) Comparison of N_2 sorption isotherms of COF-500 before and after demetalation. Solid and open circles represent the adsorption and desorption branches, respectively. Data of COF-500 and the demetalated material in this figure are depicted in blue and red, respectively. **(b)** Pore size distribution calculated from the N_2 sorption isotherms using a NLDFT slit pore equilibrium model. **(c)** Upon excitation at 375 nm, the demetalated material exhibits an intense emission while metalated COF-500 is non-emissive. **(d** and **e)** THF vapor sorption isotherms of COF-500 and the demetalated material. **(f)** Within the boundary of each rigid covalently linked macrocycle, the phenanthroline corners (highlighted in cyan) are free to move towards the tetraphenylethylene core (blue) upon demelation. As a result, the motion of the phenyl rings of the tetraphenylethylene core is restricted thus causing aggregation induced emission.

The facile demetalation process indicates that the copper centers in COF-500 are readily accessible suggesting an open, guest accessible structure. N_2 gas adsorption isotherms of evacuated samples of both COF-500 and the demetalated compound were recorded to examine their porosity (Figure 5.21a). The nitrogen isotherm of COF-500 (at 77 K from 0 to 1 bar (1 bar = P_0)) shows a sharp uptake between $P/P_0 = 10^{-5}$ to 10^{-1}, a signature feature of microporous materials. The

Brunauer-Emmett-Teller (BET) model[14] was applied to the isotherm for P/P_0 between 0.05 and 0.1 to give an apparent surface area of $S_{BET} = 352$ m^{2}g^{-1}. In contrast, the demetalated material shows decreased porosity with a S_{BET} of only 155 m^{2}g^{-1}. Calculation of the pore size obtained from fitting of the two respective isotherms using a non-linear density functional theory (NLDFT) slit pore equilibrium model[13] yielded a definitive pore size of 12.66 Å for COF-500. In contrast a wider distribution of the pore size from 10-16 Å with a maximum at 12.30 Å was observed for the demetalated material indicating a less well-defined pore system (Figure 5.21b). This is attributed to the added degrees of freedom and concomitant motional dynamics of the 1D chains upon demetalation.

Additional structural information was obtained through fluorescence emission spectra of the ETTBA constituent in COF-500 before and after the demetalation. The tetraphenylethylene core of ETTBA is known to exhibit aggregation induced emission (AIE).[22–24] When rotation of the phenyl rings along the =C–Ar axes and torsional motions of the C=C bond are unrestricted, both can serve as non-radiative relaxation channels for decay of the excited state, thus rendering the molecule non-emissive. Once such molecular motion becomes restricted, photoluminescence activity is turned on.[22] Solid-state photoluminescence studies were performed on both COF-500 and the demetalated material. Upon excitation with a laser at 375 nm, COF-500 was found to be non-emissive, while an intense emission centered at 586 nm was observed for the demetalated compound (506 nm for ETTP, Figure 5.21c). Based on the crystal structure of COF-500 there is an ETTBA linker of an adjacent 1D chain located at the center of each macrocycle. Spatial segregation between this ETTBA linker and the phenanthroline corners of the surrounding macrocycle (3.4 Å for the closest H-H distance) allows for free rotation of the ETTBA's phenyl rings and thus for quenching of fluorescent emission. Upon demetalation, the phenanthroline corners of neighboring 1D chains are free to move about within the constraints of the rigid covalently linked macrocycle of the surrounding 1D chain. To maximize van der Waals interactions the 1D chains move closer to the central ETTBA linker thereby restricting the rotation of the phenyl rings and thus affecting aggregation induced emission. This implies that overall the 1D chains become more packed along the crystallographic c direction when the material is demetalated, which is consistent with the decrease in uptake observed in the N$_2$ absorption studies.

To test whether this observed structural rearrangement between adjacent 1D chains in the demetalated material is dynamic, tetrahydrofuran (THF) vapor adsorption studies were carried out. We envisioned that, in a manner akin to the process of swelling of long-chain polymers by organic solvents, favorable interactions with the framework can serve as a thermodynamic driving force for the diffusion of THF molecules between the 1D chains to re-open up the structure. THF vapor adsorption isotherms were collected for both COF-500 and the demetalated material at 283 K. COF-500 shows a type I isotherm with a major uptake step at low partial pressure indicative of a microporous material. The maximum uptake reached 90.5 cm^{3}g^{-1} at P/P_0 is 0.97.[25] For the demelated material, the first step in the isotherm is reached at $P/P_0 = 0.06$ with 21.9 cm^{3}g^{-1} (*vs.* $P/P_0 = 0.26$ with 55.3 cm^{3}g^{-1} for COF-500, Figure 5.21d). This is expected as this uptake corresponds to filling of the first accessible surface layer which is expected to be lower for the

demetalated material due to the proposed structural rearrangement. Subsequently the adsorption curve exhibits a linear shape, which suggests the filling of disordered pores, until it reaches 103.6 cm^3g^{-1} at $P/P_0 = 0.97$ (Figure 5.21e). By taking the density difference between the two materials (1680 and 1400 $gmol^{-1}$ for each repeating unit of COF-500 and demetalated material, respectively) into consideration, the THF adsorption per unit volume can be roughly compared. It can be concluded that in the presence of THF vapor, the demelatated framework opens up to possess 95.3% of accessible porosity of COF-500. The proposed dynamic structural rearrangement and reopening of the structure is further supported by solid-state photoluminescence studies. After careful dosing of the demetalated material with THF on a glass slide, the emission intensity was observed to decrease drastically to approximately 20% of the dry sample. While this result can only give qualitative data due to limitations in the experimental setup, the decreased intensity nonetheless gives credence to the notion that solvent molecules can diffuse into the less open framework, and "swell" the 1D chains apart so that they are far enough from each other to again allow for molecular motion of the phenyl rings of the tetraphenyl ethylene centers. Such low emission intensity was retained for at least 10 minutes even after surrounding THF evaporated, suggesting strong interactions of THF with the framework.

5.4 References

(1)   Livoreil, A.; Dietrich-Buchecker, C. O.; Sauvage, J. P. *J. Am. Chem. Soc.* **1994**, *116*, 9399.

(2)   Tock, C.; Frey, J.; Sauvage, J. P. In *Molecular Switches, Second Edition (eds B. L. Feringa and W. R. Browne)*; Wiley-VCH Verlag GmbH & Co. KGaA, Weinheim, Germany, 2011.

(3)   Jiménez, M. C.; Dietrich-buchecker, C.; Sauvage, J. *Angew. Chem. Int. Ed. Engl.* **2000**, *1*, 3284.

(4)   Bruns, C. J.; Stoddart, J. F. *The Nature of the Mechanical Bond : From Molecules to Machines*; John Wiley & Sons, 2016.

(5)   Furukawa, H.; Cordova, K. E.; O'Keeffe, M.; Yaghi, O. M. *Science* **2013**, *341*, 1230444.

(6)   Diercks, C. S.; Yaghi, O. M. *Science* **2017**, *355*, eaal1585.

(7)   Liu, Y.; Ma, Y.; Zhao, Y.; Sun, X.; Gandara, F.; Furukawa, H.; Liu, Z.; Zhu, H.; Zhu, C.; Suenaga, K.; et al. *Science* **2016**, *351*, 365.

(8)   Liu, Y.; O 'keeffe, M.; Treacy, M. M. J.; Yaghi, O. M. *Chem. Soc. Rev.* **2018**, DOI: 10.1039/C7CS00695K.

(9)   Yaghi, O. M.; M, O. K.; Ockwig, N. W.; Chae, H. K.; Eddaoudi, M.; Kim, J. *Nature* **2003**, *423*, 705.

(10)   Dietrich-Buchecker, C.; Sauvage, J.-P. *J. Am. Chem. Soc.* **1984**, *106*, 3043.

(11)   Chichak, K. S.; Cantrill, S. J.; Pease, A. R.; Chiu, S.-H.; Cave, G. W. V.; Atwood, J. L.; Stoddart, J. F. *Science* **2004**, *304*, 1308.

(12)   Ayme, J.-F.; Beves, J. E.; Leigh, D. A.; McBurney, R. T.; Rissanen, K.; Schultz, D. *Nat. Chem.* **2011**, *4*, 15.

(13)   Ravikovitch, P. I.; Neimark, A. V. *Langmuir* **2006**, *22*, 11171.

(14)   Walton, K. S.; Snurr, R. Q. *J. Am. Chem. Soc.* **2007**, *129*, 8552.

(15)   Delgado-Friedrichs, O.; O'Keeffe, M.; Yaghi, O. M. *Phys. Chem. Chem. Phys.* **2007**, *9*, 1035.

(16)   Uribe-Romo, F. J.; Hunt, J. R.; Furukawa, H.; Klöck, C.; O'Keeffe, M.; Yaghi, O. M. *J. Am. Chem. Soc.* **2009**, *131*, 4570.

(17)   Zhang, Y. B.; Su, J.; Furukawa, H.; Yun, Y.; Gándara, F.; Duong, A.; Zou, X.; Yaghi, O. M. *J. Am. Chem. Soc.* **2013**, *135*, 16336.

(18)   Gemmi, M.; Oleynikov, P. *Zeitschrift fur Krist.* **2013**, *228*, 51.

(19)   Dassault Systèmes BIOVIA, Materials Studio 8.0, San Diego: Dassault Systèmes (2014).

(20)   Friedrichs, O. D.; O'Keeffe, M.; Yaghi, O. M. *Solid State Sci.* **2003**, *5*, 73.

(21)   Scaltrito, D. V; Thompson, D. W.; O'Callaghan, J. A.; Meyer, G. J. *Coord. Chem. Rev.* **2000**, *208*, 243.

(22)   Hong, Y.; Lam, J. W. Y.; Tang, B. Z. *Chem. Soc. Rev.* **2011**, *40*, 5361.

(23)   Dalapati, S.; Jin, E.; Addicoat, M.; Heine, T.; Jiang, D. *J. Am. Chem. Soc.* **2016**, *138*, 5797.

(24)   Shustova, N. B.; McCarthy, B. D.; Dincă, M. *J. Am. Chem. Soc.* **2011**, *133*, 20126.

(25)   Sing, K. S. W.; Everett, D. H.; Haul, R. A. W.; Moscou, L.; Pierotti, R. S.; Rouquerol, J.; Siemieniewska, T. *Pure Appl. Chem.* **1985**, *57*, 603.

Chapter VI

The Geometry of Knots, Weaving and Polycatenanes: A Library for Reticular Chemistry

6.1 Introduction

The geometry of simple knots and catenanes can be described using the concept of linear line segments (sticks) joined at corners. This is extended to include woven linear threads as members of a broader family of knots. In this chapter, a unified method has been developed to describe the underlying structures of knots, polycatenanes and weavings. The basic units are identified as corners, sticks and rings or threads. The number of distinct kinds of these are denoted by a transitivity *p q r*. The analogy is made with structures such as polyhedra or plane tilings, where the transitivity refers to, respectively, the numbers of kinds of vertices, edges and faces. Just as transitivity 1 1 1 identifies regular polyhedra or tilings, polycatenanes and weavings with transitivity 1 1 1 are denoted as *regular*.

A database of 2- and 3-periodic regular polycatenanes, and weavings have been identified. For 2-periodic structures, there are two regular weavings (the plain biaxial and kagome triaxial) and, interestingly, no regular chain mail has been derived. In contrast, the 3-periodic case is rich in regular structures. While no claim on completeness of the library is being attempted, systematic enumeration of the most regular weaving constructs has been described here. The structures thus identified are the most plausible synthetic targets based on the mathematical calculations, further complemented by a general synthetic strategy to materialize these structures, which together serve as a database that synthetic chemists can refer to for the rational design of woven frameworks in the future.

6.1.1 knots, catenanes and weaving

If a knot is tied in a length of string and then the ends of the string are joined, one will have a knotted loop. This is what mathematicians consider as a knot. If a drawing is made of the knot it will be found that, at points, pieces of string cross. The minimal number of crossings in such a drawing is the *crossing number* of the knot. To make a knot in a single loop, one needs at least 3 crossings (*i.e.* crossing number = 3, Figure 6.1). Suppose now two loops are linked together so they cannot be separated without breaking the string – this also is a knot. The simplest such link (a *Hopf link*) has a crossing number of 2.
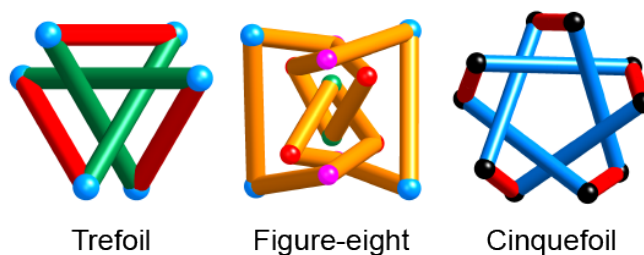

| Trefoil | Figure-eight | Cinquefoil |

Figure 6.1. The simplest knots shown as sticks and corners. In the trefoil and cinquefoil knots, symmetry-related sticks have the same color.

Knots are given a symbol n_k^m indicating that m loops form a knot with n crossings. k is an arbitrary serial number to distinguish knots with the same values of n and m. A comprehensive listing of knots can be found at the *Knot Atlas*.[1] A good introduction to knot theory for the non-mathematicians is the book by Adams.[2] In chemistry, linked molecular loops (rings) are known as *catenanes* and multiple linked rings are *polycatenanes*.[3,4]

In this chapter, an approach to this subject with an emphasis on periodic structures from the point of view of reticular chemistry[5] is presented. In reticular chemistry, atoms, or molecular groups of atoms (secondary building units, SBUs), are joined by links into symmetrical frameworks notably in materials such as metal-organic frameworks (MOFs)[6] and covalent organic frameworks (COFs)[7]. The geometry is abstracted as nodes joined by straight links. In application to knots and related structures the straight links are called *sticks*. They meet in pairs at two-coordinated vertices (termed *corners*). The loops of knots now become (generally non-planar) polygons.

In modern mathematics of, for example, periodic polyhedra (Grünbaum-Dress polyhedra)[8], faces (rings) are allowed to become infinite and take shapes such as zigzags and helices with linear segments. Accordingly, entanglement (*weaving*) of threads can be considered as part of the same structure family as knots and catenanes. In particular, from a crystallographic point of view, these threads are regarded to be also made up of corners and sticks. For many structures, a three-letter (lower case, bold) identifying symbol is given. In some cases, the symbols **abc-w** and **abc-y** are used for a weaving or a polycatenane, repectively, derived from a 3-periodic net **abc**, which can be found in the RCSR database.[9]

6.1.2 Transitivity, the minimal transitivity principle and regular structures

In the theory of graphs (nets) and tilings, vertices related by the intrinsic symmetry are said to be the same kind. If there are p kinds of vertex the graph is vertex p-transitive. For a net characterizing a crystal structure the transitivity $p\ q$ indicates that there are p kinds of vertex and q kinds of edge.

Of the more than six million distinct polyhedra with 12 vertices only the five vertex 1-transitive (often abbreviated to 'vertex transitive' when $p = 1$) are of special interest in chemistry. Similarly, of the essentially infinite number of periodic graphs (nets) the principle of *minimal transitivity* states that the net formed by linking SBUs is likely to have the minimal transitivity consistent with the starting materials.[10]

In tilings of the sphere (polyhedra) or 2-dimensional tilings, the transitivity $p\ q\ r$ indicates that there are p kinds of vertex, q kinds of edge and r kinds of face. The five regular polyhedra and three regular plane tilings are those with transitivity 1 1 1.[11] They are of special importance to structural chemistry.

For crystal nets, the algorithms of Systre can be used to determine the symmetry and transitivity.[12] However for knots and weavings, the symmetry can only analyzed by inspection, then construction of a model with sticks and corners and finally determination of the transitivity p $q\ r$ which now indicates the numbers of kinds of, respectively, corners, sticks and rings or threads.

Note that as different rings and threads do not share corners or sticks p and q must be $\geq r$. Structures with transitivity 1 1 1 are termed *regular*. 3-periodic catenanes and weavings are particularly rich in regular structures, which should be prime targets for future synthesis.

6.1.3 Symmetry and symmetry groups

All of the structures described in detail are 3-dimensional. The 3-periodic structures have symmetry that is one of the 230 space groups. The 2-periodic structures will have one of the 80 layer group symmetries.[13] It is one of the advantages of the Hermann-Mauguin system of symbols for symmetry groups that layer group symbols are interpreted exactly as space group symbols. The lattice is 2-dimensional and always defines the **ab** plane so there are no translational components of symmetry operations along **c**. Layer group symbols are distinguishable from space group symbols as the lattice symbol is always lower case (*p* or *c*). For 2-periodic weavings and polycatenanes, there is the further restriction that there cannot be a mirror normal to **c**. A mathematical account of weaving simply states that the symmetry must be one of the seventeen 2-dimensional 'wallpaper' groups, but no symmetries were given,[14] or in the literature.

1-periodic structures such as chains and braids are briefly mentioned. They have rod group symmetries. In one dimension, there is no crystallographic restriction of the order of rotations, but our examples have crystallographic symmetries recognizable as the lattice symbol is $\wp$ for the 1-periodic lattice.

6.2. 0- and 1-Periodic structures
6.2.1 Some simple knots

Knots are 3-dimensional and their symmetries are one of the point symmetry groups of Euclidean space. Figure 6.1 shows the three simplest single-loop knots with respectively crossing numbers 3, 4, and 5. These are the structures of almost all reported molecular knots,[39–41] although a molecular knot with 8 crossings has recently been reported.[42]

Knots can always be formed from straight sticks and the *stick number* is the minimal number of sticks required. Minimal stick configurations generally have less than maximum symmetry. Here, the maximum symmetry configurations are being examined and generally more edges are required. The trefoil knot, symmetry 32 (D_3) has transitivity 1 2 1 and can be formed from 6 sticks, so the stick number is 6. The cinquefoil knot, symmetry 52 (D_5), also has transitivity 1 2 1. In the symmetric conformation illustrated there are 10 sticks, but note that the stick number for this knot is 8. The figure-eight knot with crossing number 4 has only symmetry 222 (D_2) and transitivity 4 4 1 making it a much more challenging target for designed synthesis.[43]

6.2.2 Linked pairs of rings

The simplest pair of linked rings, the classical catenane, has crossing number 2 and is generally known as the *Hopf link*. It is shown in two ways in Figure 6.2 to emphasize that the link cannot always be associated with just two corners. In the most symmetrical conformation (shown)

the symmetry is $\bar{4}2m$ (D_{2d}) and the transitivity 2 2 1. For non-concentric linked rings, a *link point* as the barycenter (average of all corner vertices) of the two rings can be identified. An important step in synthetic chemistry was the introduction of a metal template at the link point to facilitate the formation of catenanes.[44–48]
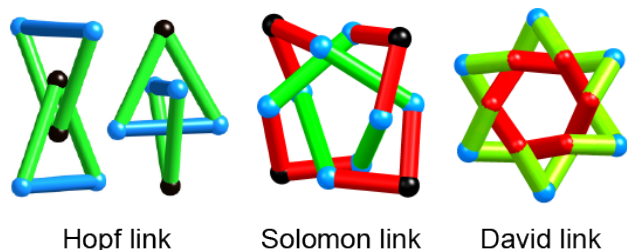

Hopf link   Solomon link   David link

Figure 6.2. The simplest links of pairs of rings. Sticks and corners of the same color are related by symmetry.

Also shown are the double link (4 crossings) known as the *Solomon link* and the triple link. The latter has 12 edges, but in its most symmetrical form, it has 18 edges (Figure 6.2) and has the shape of the star of David, so it is termed *David link* here. Both these knots have transitivity 2 2 1.

6.2.3 Polycatenanes

Polycatenanes have more than two linked rings. There are two ways to link three rings so that each is linked to the other two (Figure 6.3). There are six crossings and the knot symbols are 6_1^3 and 6_3^3. 6_2^3, in which no pair of rings is linked, will be discussed in the next section. The illustration of 6_1^3 (top right in the figure) clearly shows the six crossings and the symmetry 32 (D_3). Flipping one link (from over-under to under-over) converts 6_1^3 to 6_3^3 (top left in the figure) apparently destroying the symmetry. But surprisingly 6_3^3 also has an embedding with symmetry 32. A piecewise linear embedding of 6_3^3 made with three triangles is also shown, again with symmetry 32 and transitivity 2 2 1. In that embedding three corners are now about a central symmetry point in a conformation, which is referred to in the descriptions of 3-periodic weavings as a *triple crossing*. Directed syntheses of a 6_3^3 [3]catenane have recently been reported.[25,26]

Also shown in the figure is the simplest form of a linear chain. This has symmetry $4_2/mmc$ and transitivity 1 2 1. A chemical analogue has been reported recently.[27] This has transitivity 1 1 1 and thus, is the simplest *regular* knot (transitivity 1 1 1).
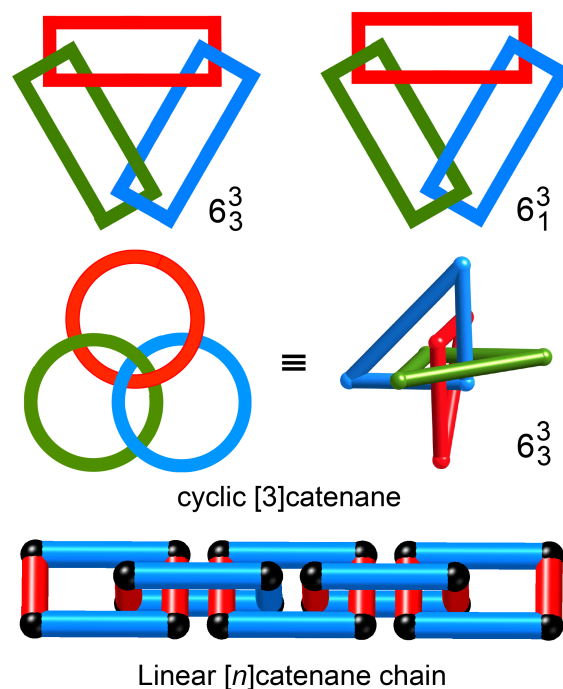
Figure 6.3. Simple polycatenanes with Hopf links. Top: a cyclic [3]catenanes showing on left 6_3^3 and on the right 6_1^3. Below that are shown alternative embeddings of 6_3^3 with 32 (D_3) symmetry. The linear chain is an infinite catenane. In the embedding shown there is one kind of corner and two kinds of stick (red and blue).

6.2.4 Borromean rings

The famous Borromean rings are another way of linking 3 rings, again with six crossings, knot symbol 6_2^3. Figure 6.4 shows the structure as interwoven circles. It can be seen that it may be derived from 6_3^3 (Figure 6.3) by reversing the three outer crossings. In a maximum-symmetry embedding the structure is cubic, symmetry $m\overline{3}$ (T_h). Two embeddings as sticks in that symmetry are shown in Figure 6.4: with one kind of corner, transitivity 1 2 1, and with one kind of stick, transitivity 2 1 1. This knot possesses the *Borromean property*: Although the rings are linked in the sense that no ring can be separated from the others without breaking sticks (links), no two rings are linked. Molecular Borromean rings have been achieved by directed assembly of eighteen components.[28]
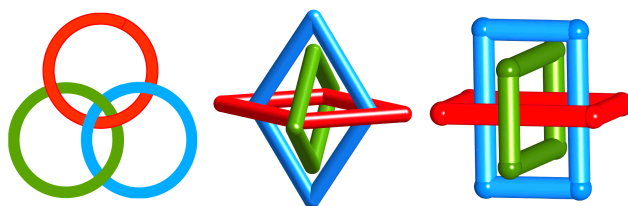
Figure 6.4. Left: Borromean rings (knot 6_2^3) as circular loops. Center (transitivity 2 1 1) and right (transitivity 1 2 1) with cubic symmetry. Note that no two rings are linked. In the drawing on the right the corners are at the vertices of a regular icosahedron.

6.2.5 Brunnian knots and braids

A Brunnian knot is composed of multiple rings and has the property that if one ring is removed the remaining rings are not linked. The Borromean rings are the simplest such Brunnian knot. Figure 6.5 shows the first two of a series of Brunnian knots with three loops and a multiple of six crossings.
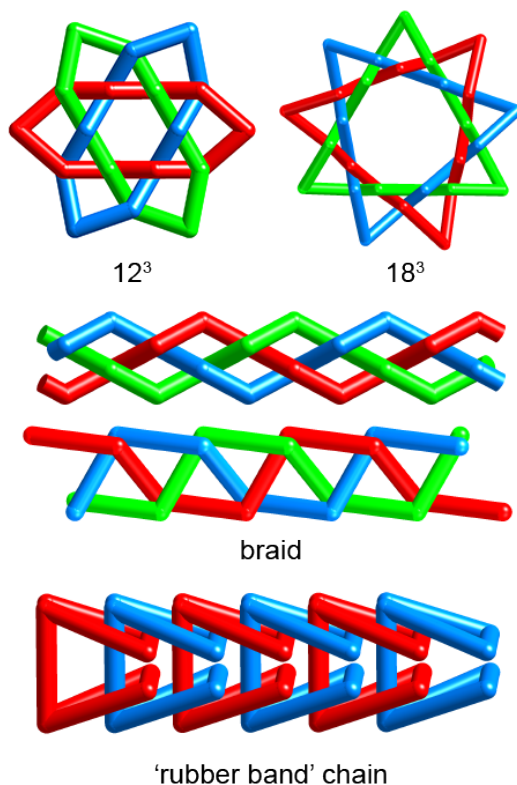
Figure 6.5. Examples of Brunnian knots. The top two have three finite rings and removing one ring leaves the other two unlinked. The braid is the corresponding structure with infinite rings (threads). In the upper embedding there are two kinds of corner and one kind of stick (transitivity 2 1 1). In the lower, one kind of corner and two kinds of stick (transitivity 1 2 1). Note that in each case red is above blue, blue above green and green above red. The rubber band chain also has the Brunnian property. In a finite chain, rings at the end can be removed by bending, but not by breaking, the sticks.

If the number of crossings is increased to infinity, the structure is that of a three-strand braid. The braid is intrinsically a rather simple structure, symmetry $_p2/c$. As made with flexible strings (or hair) the configuration is as shown in the top illustration with transitivity 2 2 1. Braids are well known in materials like MOFs.[29] It is interesting that some of these have a less-curved embedding, also shown in the figure, that has the same symmetry but transitivity 1 2 1. The adoption and recognition of this structure emphasizes the utility of the stick-and-corner description of molecular structures.

A characteristic of three-component Brunnian structures, say green, red, blue, is that the crossings are such that green is over red, red over blue and blue over green (Figure 6.5). Also shown in the figure is a Brunnian chain of what are known as 'rubber band' links. Pairs of loops are not linked topologically and can be separated if sticks are allowed to bend. But the whole chain is linked. The symmetry is $_{/\!/}\bar{4}m2$ and the transitivity is 1 2 1.

6.2.6 Regular polycatenanes

Seven regular finite polycatenanes with transitivity 1 1 1 (Figure 6.6) are identified. These structures have not been formally described elsewhere, or realized as molecules, although some are familiar to model builders. They can be considered as regular weavings on the sphere – on the sphere a thread becomes a ring – emphasizing again that polycatenanes and woven fabrics are part of the same structure family. Also shown in the figure (bottom right) is a well-known regular figure, symmetry 532 (*I*), composed of five catenated tetrahedra with vertices forming a regular rhombic dodecahedron.

| 12^4 | 24^6 | 30^6 | 24^8 |

| 60^{12} | 120^{12} | 60^{20} | Five Tetrahedra |
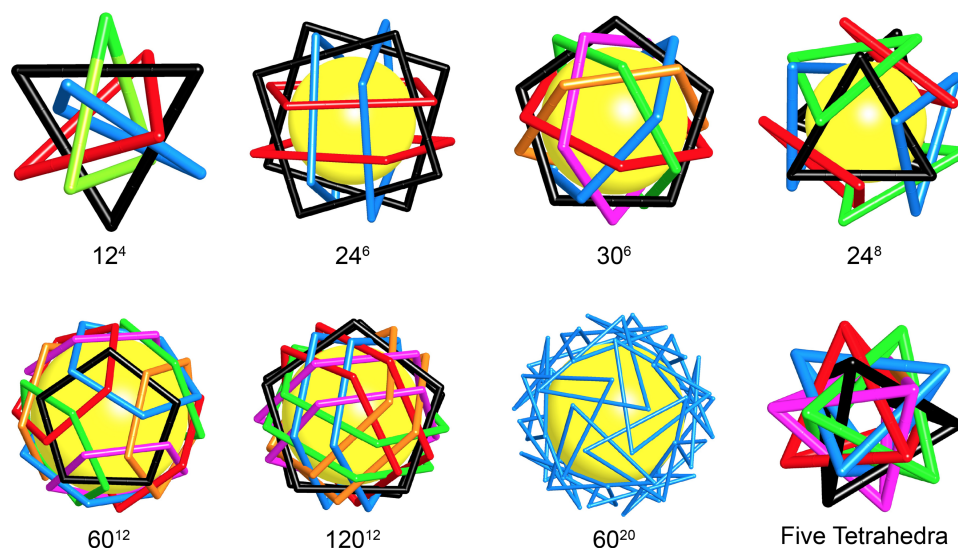
Figure 6.6. Some regular polycatenanes and a regular linkage of five tetrahedra. For the polycatenanes p^q indicates p crossings and q rings (loops).

The simplest regular polycatenane (knot) 12^4 is composed of four equilateral triangles, each linked to the other three, and has symmetry 432 (*O*). The vertices are at the positions of those of a regular cuboctahedron (3.4.3.4). The ring link points are at the vertices of a regular tetrahedron. The polycatenane 24^6, symmetry 432 (*O*), is made of six squares, each linked to four others. The corners form an Archimedean snub cube (3^4.4) and the link points form a cuboctahedron (3.4.3.4). The polycatenane 30^6, symmetry 532 (*I*), is formed from six concentric pentagons, each linked to the other five. The corners are at the vertices of an Archimedean icosidodecahedron (3.5.3.5). This structure is known as Makalu to origami enthusiasts. The polycatenane 24^8 is formed from eight triangles, each linked to three others. The corners are at the vertices of a snub cube and the link points form a cuboctahedron (as in 24^6 above). The polycatenane 60^{12}, symmetry 532 (*I*), is formed from 12 pentagons, each linked to five others. The corners are at the vertices of an Archimedean

snub dodecahedron ($3^4.5$). The polycatenane 120^{12}, symmetry 532 (*I*), is formed again from 12 pentagons, each now linked to ten others. The corners are again at the vertices of a snub dodecahedron. The polycatenane 60^{20}, symmetry 532 (*I*), is formed from 20 triangles each linked to three others. The corners are again at the vertices of a snub dodecahedron.

6.3 2-Periodic structures
6.3.1 The lattice plane

In 2-periodic structures there will be an underlying lattice either primitive, symbol *p* or centered rectangular, symbol *c*. The lattice vectors are always **a** and **b**. They define a plane, the *lattice plane* of the structure.

6.3.2 Biaxial weaving

The weaving of threads into *fabrics* is one of the oldest human crafts and 2-periodic weaving patterns are found in chemical structures, for example, in MOFs. The classical (*warp* and *woof*) weavings are of threads in two directions at right angles (*biaxial*). The literature on ornamental weaving is vast, but of little relevance to the purpose of this chapter, which is to identify structures of minimal transitivity.
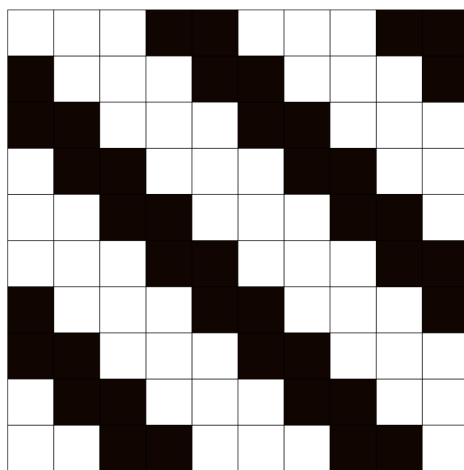
Figure 6.7. The design of a (3,2) twill. Horizontal and vertical rows have the sequence three white, two black squares.

The structures being described are restricted to have one kind of thread which have been termed *isonemal*.[14] Such threads are characterized by a sequence of integers (*p,q,...*) which states that at every crossing for a thread there are *p* over, followed by *q* under, followed by ... (*p,q*). With the exception of (2,2), for an isonemal weaving successive parallel rows must be displaced by one crossing. Such weaves are known as *twills*. Weaving patterns are often illustrated by *designs* that show the weaving patterns by sequences of black and white squares for under and over crossings. Figure 6.8. shows the design for a (3,2) twill. Note that the sequence of black and white is the same for every horizontal and vertical row as it must be for an isonemal weaving. If $p \neq q$ the fabric is not *balanced* - the two sides are not the same.
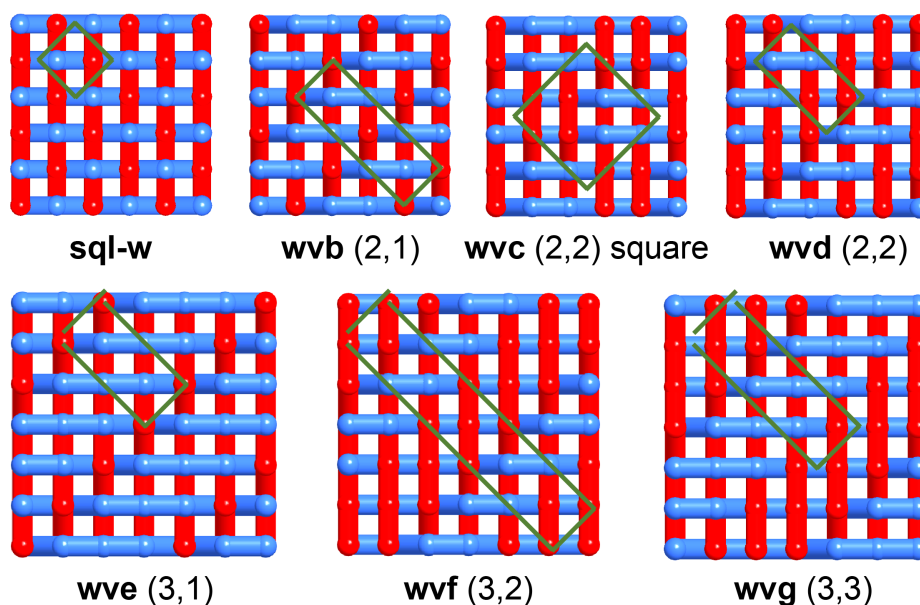
Figure 6.8. The simplest biaxial weavings. All but **wvc** are twills.

The first, and perhaps obvious, result is that there is just one regular biaxial weaving with transitivity 1 1 1 (Figure 6.8). This is generally known as plain weave but also known as *box* weave, *calico*, *tabby*, *taffeta*, etc. The symmetry *p4/nbm* indicates the presence of all possible glides (*a, b, n*) in the layer lattice plane. It is the presence of such glides that adds to the attractiveness of weaving patterns. Figure 6.8 also shows isonemal weavings (*p,q*) for $p \leq q \leq 3$. Clearly (*p,q*) is the same as (*q,p*) but viewed from the other side. Data for these structures are in Table 6.1.

Table 6.1. Geometric data for 2-periodic weavings. For fabric weaving (*p,q*) after the symbol means for each thread *p* over and *q* under crossings. The entries for stick(s) are the coordinates of corners linked to the corner with coordinates given in the 'corner' column to the left.

Symbol	Trans	Symmetry	Cell *a, b*	Corner	Stick(s)
wva (1,1)	1 1 1	*p4/nbm*	1.414, 1.414	¼, ¼, z	¾, ¾, -z
wvb (2,1)	2 2 1	*c222*	1.714, 4.247	0, 0, z	0.063, ½, -z
				0, 0.333, z	0.167, ½, z
wvc (2,2)	1 2 1	*p4/nbm*	2.828, 2.828	0, ¼, z	¼, 0, -z;
					-¼, 0, z
wvd (2,2)	1 2 1	*pbaa*	2.818, 1.414	0.375, ¼, z	0.625, ¾, -z;
					0.125, -¼, z
wve (3,1)	2 2 1	*p222*	1.414, 2.828	0, 0, z	0.25, ½, -z;
					0.75, -½, -z
				0.25, ½, -z	
wvf (3,2)	2 3 1	*c222*	1.414, 7.070	0, 0.2, z	- ½, 0.3, z;
					½, 0.1, -z
				0, 0.4, z	1, 0.6, z
wvg (3,3)	1 2 1	*pban*	4.247, 1.414	0.083, ¾, z	-0.083, ¼, -z;
					0.417, ¾, z
kgm-w (1,1)	1 1 1	*p622*	1.0, 1.0	0, ½, z	½, 0, -z
wvm (3,3)	1 2 1	*p622*	1.732, 1.732	0.167, 0.833, z	0.333, 1.167, -z;
					-0.167, 1.167, z
wvx	2 1 1	*c222*	1.4, 2.8	0.15, 0, 0	-0.25, 0.25, z
				-0.25, 0.25, z	
wvy	2 2 1	*pban*	1.4, 2.8	0.4, ¼, 0	¼, 0.35, z;
				¼, 0.35, z	¼, 0.15, -z
wvz	1 2 1	*pbam*	3.0, 4.0	0.35, 0.85, -z	1.15,0.85, -z
					0.65,0.15, z

The shape of the threads themselves is relevant to the design of crystals (Figure 6.9). (1,1) gives a zigzag with transitivity (corners, sticks) = 1 1. (*p,p*) gives a 'crankshaft' pattern of transitivity 1 2 whereas the general case ('gaptooth') (*p,q*) gives transitivity 2 2. Examples of woven coordination networks include plain weave[30–33] and a (2,2) twill[34].
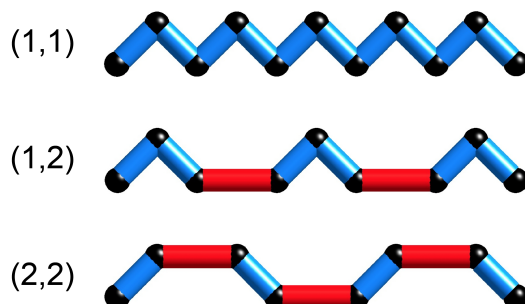

(1,1)

(1,2)

(2,2)

Figure 6.9. The shape of one thread in simple weavings. Red and blue sticks are not related by symmetry. (1,1) is 'zigzag' and (2,2) is 'crankshaft'.

6.3.3 Triaxial weave –kagome

In triaxial weave, three coplanar sets of threads at 120˚ to each other are woven. It should be clear that isonemal weavings must be balanced [e.g. threads (*p,p*)]. The simplest, and only regular, has (1,1) threads (*kagome*, Figure 6.10). This weave is in a sense analogous to the Borromean rings.[28] There are three sets of threads and no two sets are interwoven. It may be seen in the figure that red is over blue, blue over green, and green over red. A hydrogen bonded structure based on the kagome weave has been reported.[35]

kgm-w

wvm mad weave

wvn

mad weave
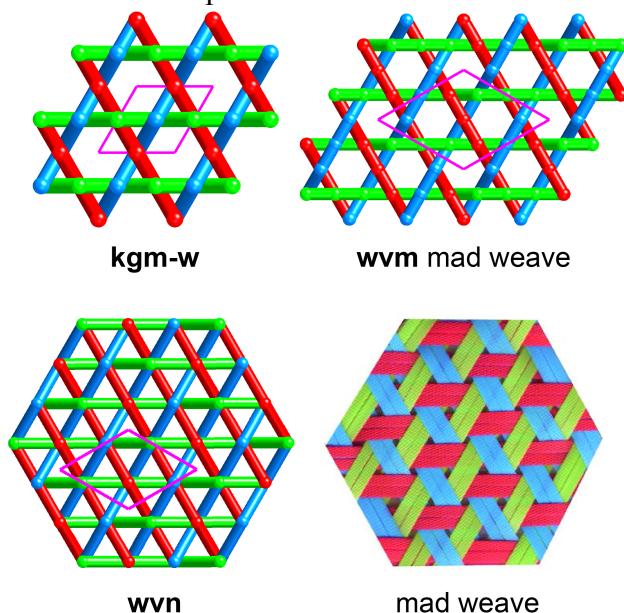
Figure 6.10. Simple triaxial weaves. The picture on the bottom right was reproduced from Ref. 25 with permission from Taylor and Francis copyright, 2017.

In kagome weave, commonly made with flat ribbons or wooden laths, the plane is not covered. Indeed, *kagome* is Japanese for 'basket eye'. The next simplest triaxial weave, symbol **wvm**, is (3,3) and now the plane can be covered as shown in Figure 6.10. This style is known as *mad weave*.[36,37] It has transitivity 1 2 1. In three-way weave, there could be triple crossings at which three threads meet.[14] Now at a crossing, a thread can be at the bottom (*A*), middle (*B*), or top (*C*). For an isonemal weave *A*, *B* and *C* must occur in equal numbers in a thread so the simplest sequence is *ABCABC...* and this is shown as **wvn** in the figure. It has transitivity 1 2 1.

6.3.4 Chain-link weave

In the 2-periodic weaves discussed so far, the *diagonals* between two corners at a crossing are normal to the lattice plane. By contrast in chain-link weaving the diagonals lie in the lattice plane. The two simplest isonemal examples are shown in Figure 6.11 and data (symmetry etc.) in Table 6.1. The one with symbol **wvx** is most nearly regular with transitivity 2 1 1. It is chiral and the underlying structure of chain-link fences which appear to be always made with right-handed helical threads as shown in the figure. It should be a good target for designed synthesis. Knitting patterns have the same kind of link. The simplest, **wvz**, also shown in Figure 6.11, is a variation of 'stockinette' knit. It has transitivity 1 2 1, and again should be a good target for synthesis.

2-periodic chain-link weaves have been reported in a MOF.[38] They are sometimes referred to as 'chicken wire' but in chicken wire the two-crossing link of chain link is replaced by multiple crossings, typically about 10.

WVX   **WVY**   **WVZ**
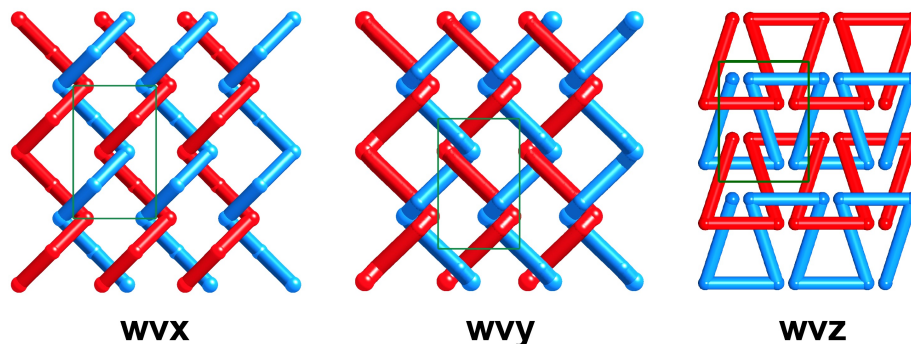
Figure 6.11. Left and center the two simplest patterns of chain link. **wvx** is used in fences. Right a stockinette knit, **wvz**.

6.3.5 Two-periodic polycatenanes

In polycatenanes, the first structures discussed have rings joined by double crossings (Hopf link) to any other ring and to those with just one kind of link point (all link points related by symmetry) and one kind of ring. These are the most likely targets for designed synthesis. In such structures the link points must be at the vertices of a uninodal (vertex transitive) 4-coordinated (4-c) planar net. There are just three of these: the net, **sql**, of the square lattice (4^4), the kagome net, **kgm** (3.6.3.6), and the 'hexagonal tungsten bronze' net, **htb** (3.4.6.4).
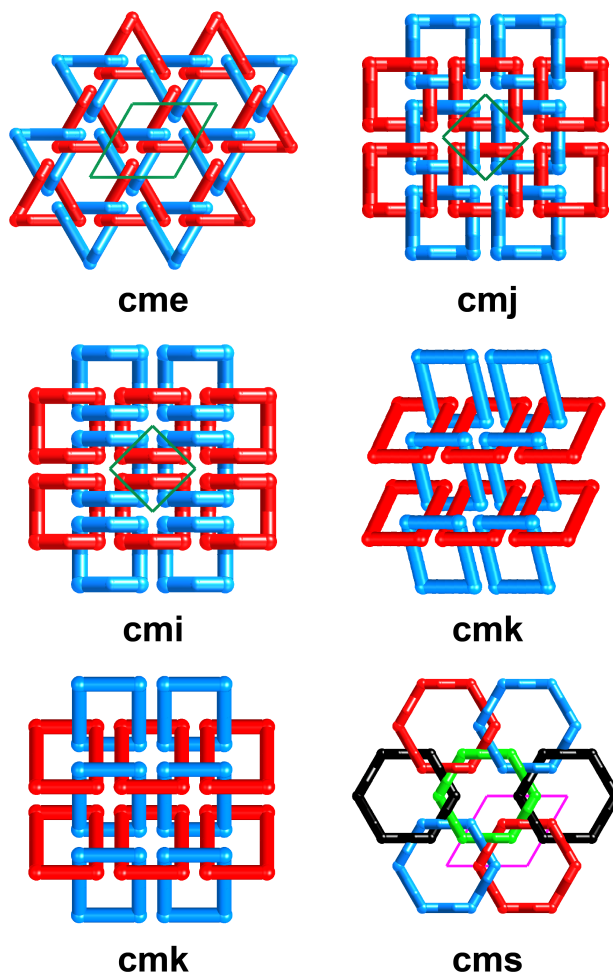
Figure 6.12. 2-periodic linked rings with symmetry related link points that form the **kgm** (3.6.3.6) or **sql** (4^4) nets. **cmk** ('European four-in-one chain mail') shown twice is the only one with an embedding with planar rings.

The structures have 3, 4, or 6 crossings per ring. Structural data are collected in Table 6.2. In the one (**cme**) with 3 crossings per ring, and shown as triangles in projection, the rings have six corners and are in fact nonplanar hexagons. Likewise the rings in the one (**cms**) with six crossings per ring, and derived from **kgm**, are really dodecagons.

There are three structures with 4 crossings per ring and one kind of link point derived from **sql**. The projections shown in Figure 6.12 are shown as quadrangles, but in **cmi** and **cmj** they are in fact nonplanar octagons. However, in **cmk** the rings can be planar rectangles. Indeed, this structure with transitivity 1 2 1 is the most nearly regular 2-periodic chainmail. It is the only one that can be made with one kind of planar ring. It is not surprising therefore that it was very commonly used in chainmail armor. In that context it is known as the 'European four-in-one' mail. All other chainmail armor designs use at least two kinds of ring (i.e. not all related by symmetry).

cmm　　**cmn**

cmt　　**cmu**
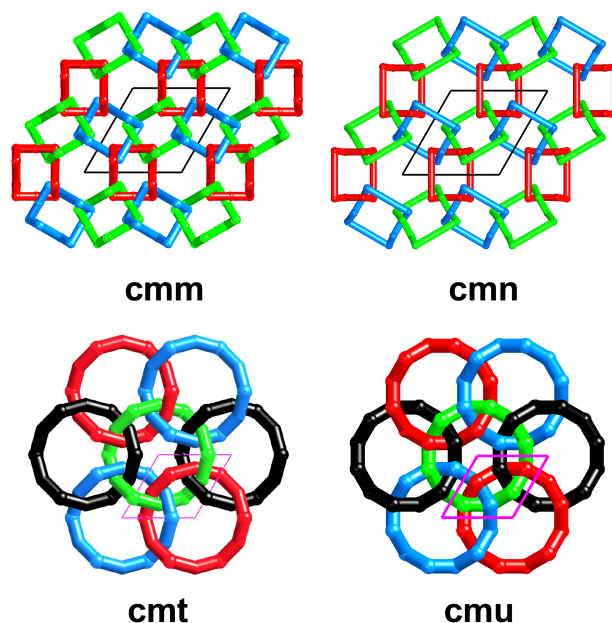
Figure 6.13. 2-periodic linked rings with symmetry related link points that form the **htb** (3.4.6.4) net. **cmt** has the Borromean property that no two rings are directly linked.

Shown in Figure 6.13 are the polycatenanes derived from **htb**. There are two (**cmm** and **cmn**) with four crossings per ring. The rings in the catenanes with 6 crossings per ring are all dodecagons. **cmt** (transitivity 2 1 1) is particularly interesting as it has the Borromean property that no two rings are linked (so the link points are referred to as 'virtual link points'). The rings cannot be made into (skew) hexagons without sticks intersecting. Interestingly it occurs in a MOF structure[39] in which the angles at one type of corner are very close to 180˚. However, intersections are avoided by reducing the symmetry so that there are now two kinds of ring. Those corners cannot be ignored as they correspond to 2-c metal atoms linking the organic components.

Table 6.2. Geometric data for 2-periodic polycatenanes. The entries under 'link point' are the nets with vertices at the link points. The entries for stick(s) are the coordinates of corners linked to the corner with coordinates given in the 'corner' column to the left.

Symbol	Link points	Trans	Sym	Corner	Stick(s)
cme	**kgm**	2 2 1	$p622$	0.583, 0.167, 0 0.583, 0, z	0.58, 0, z; 0.42, 0.42, -z
cmj	**sql**	2 2 1	$p422$	0, 0.3, 0 0.5, 0.8, z	-0.2, 0.5, z; 0.5, 0.8, z
cmi	**sql**	2 1 1	$p\overline{4}2m$	0.3, 0, 0 0.65, 0.35, z	0.65, 0.35, z
cmk	**sql**	1 2 1	$pbmn$	0.15, 0.15, z	0.85, 0.15, -z; 0.15, 0.85, z
cms	**kgm**	2 1 1	$p622$	0.4, 0, 0 0.6, 0.2, z	0.6, 0.2, z
cmt	**htb**	2 1 1	$p\overline{3}1m$	0.61, 0.39, 0 0.32, 0, z	0.32, 0, z
cmu	**htb**	1 2 1	$p622$	0.21, 0.79, z	0.58, 0.79, -z; -0.21, 0.58, -z

6.3.6 Some linked knots

Some simple examples of catenanes can be considered as linked knots (Figure 6.14). Data are listed in Table 6.2. **cka** is linked Solomon links but could also be considered as woven linear chains. **ckb** is linked trefoil knots. **ckc** is linked Borromean rings, but could also be considered as a three-way weave of linear chains. **ckd** is linked David links but could also be considered as three interwoven copies of the polycatenane **cme** (Figure 6.12).
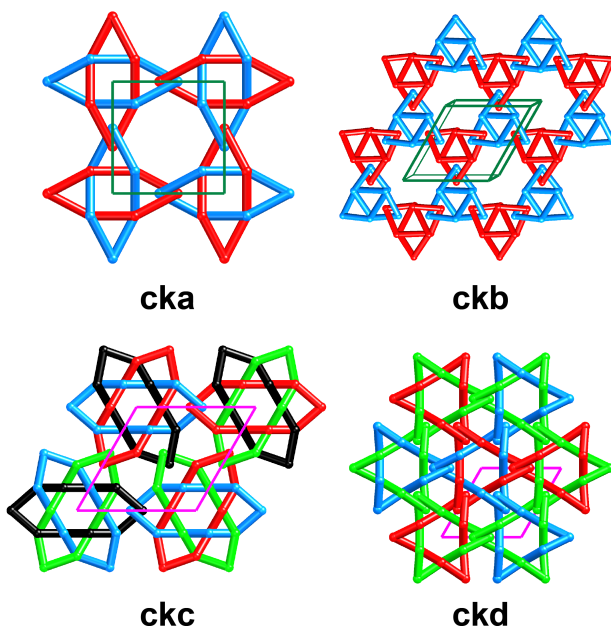

cka **ckb**

ckc **ckd**

Figure 6.14. Examples of linked knots. **cka** is linked Solomon links. **ckb** is linked trefoil knots. **ckc** is linked Borromean rings. **ckd** is linked David links and can also be described as an interpenetration of three **cme** layers (each shown with a different colour).

6.4 3-Periodic structures
6.4.1. Description and generation of 3-periodic weavings
6.4.1.1. Fabric and chain-link weaving and line sets

A weaving of threads can be recognized by the fact that the threads are interlacing in such a way that they cannot be simultaneously pulled straight without either intersecting or passing through others. A broader definition of "weaving" has been used to describe 3-periodic patterns of helices.[40] None of those structures appear as weavings in this paper. In the 2-periodic weavings of the last section, straightening the threads in fabric weaving leads to the threads intersecting in a vertex-and-edge-transitive 4-c net, either the square lattice net **sql**, or the kagome net **kgm** (Figure 6.15). This gives a hint of how to find regular 3-periodic weavings. Thread-weaving structures derived from connected nets, **abc**, are designated as **abc-w**. The nets from which the regular fabric weavings are derived will have edges forming straight lines in their symmetric embeddings. The

3-periodic invariant (all coordinates fixed by symmetry) nets formed by intersecting straight lines are listed in Table 6.3.[41]
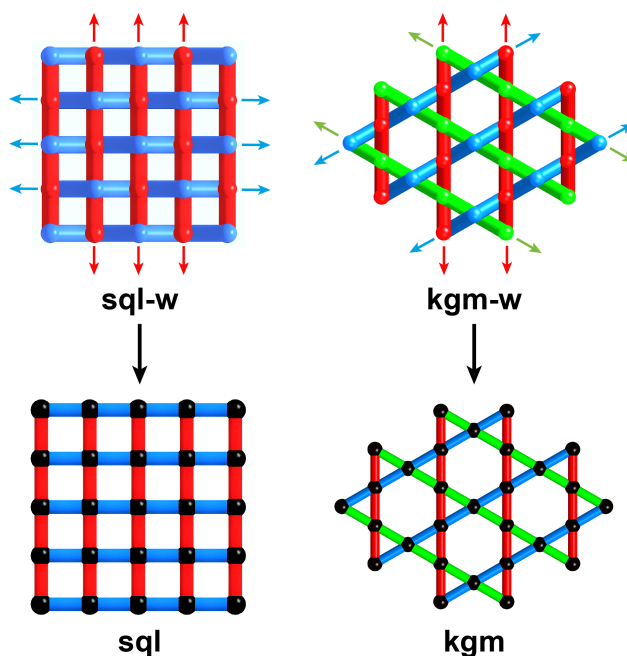
Figure 6.15. By pulling the interlacing threads straight in **sql-w** and **kgm-w**, they will collide and intersect to form **sql** and **kgm**, respectively.

Table 6.3. The 3-periodic invariant intersecting line sets. *pq* indicates that the lines run in *p* directions and *q* intersect at a point. The vertices are 2*q*-coordinated.

Type	pq	Symbol	Symmetry	Coordinates
tetragonal 4-way <101>	42	**lvt**	$I4_1/amd$	0, 0, 0
cubic 3-way <100>	32	**nbo**	$Im\bar{3}m$	½, 0, 0
	33	**pcu**	$Pm\bar{3}m$	0, 0, 0
cubic 4-way <111>	43	**bcs**	$Ia\bar{3}d$	0, 0, 0
	44	**bcu**	$Im\bar{3}m$	0, 0, 0
cubic 6-way <110>	63	**hxg**	$Pn\bar{3}m$	0, 0, 0
	63	**crs**	$Fd\bar{3}m$	0, 0, 0
	64	**reo**	$Pm\bar{3}m$	½, 0, 0
	66	**fcu**	$Fm\bar{3}m$	0, 0, 0

In the case of 2-periodic chain-link weaving, straightening threads would require that they pass through each other and form a simple non-intersecting layer pattern. For the regular 3-periodic chain-link weavings the axes of the threads will likewise form a 3-dimensional invariant non-intersecting line pattern. These are summarized in Table 6.4 and illustrated in Figure 6.16.[42] In most of the weavings described, the axes of the threads form one of these patterns. The idea of 3-periodic chain-link structures has been suggested earlier, and several illustrated, but no geometric or other data given.[43]

5 ϑ

6 Φ

7 Λ

8 Δ

9 Π

10 Π*

11 Σ

12 Γ

13 Ω

14 Σ*
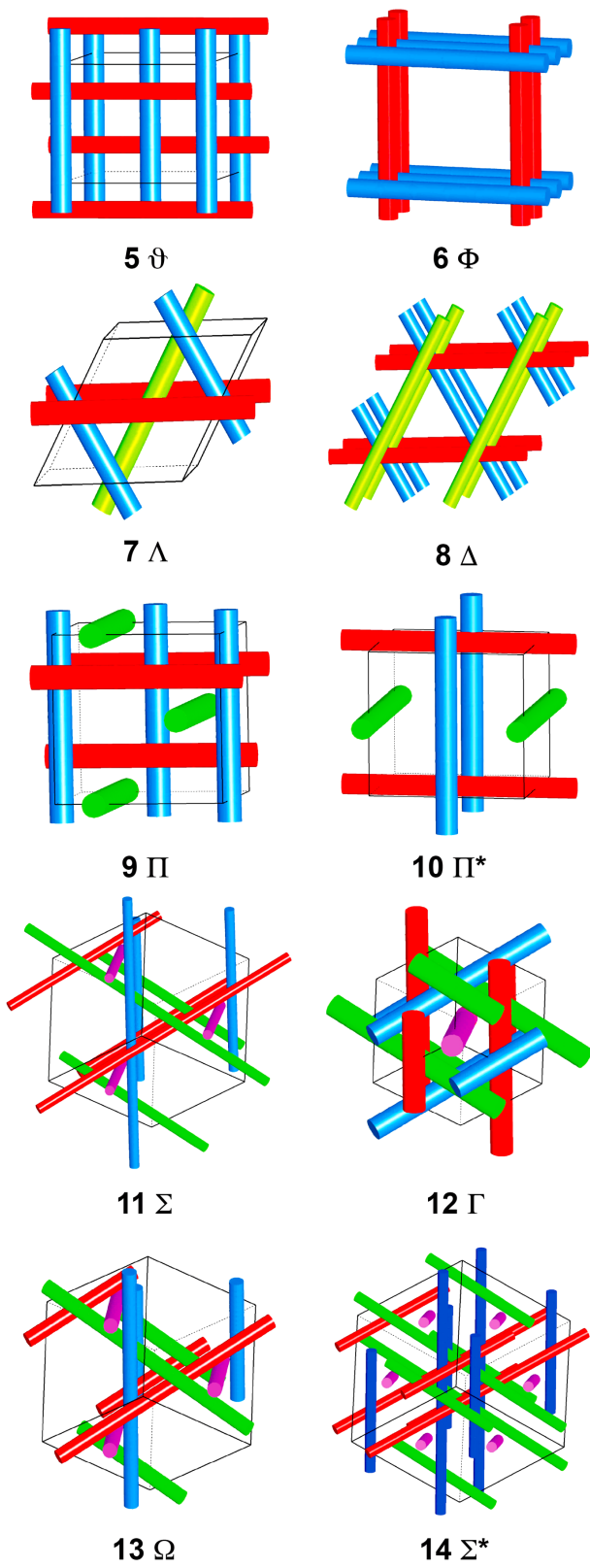
Figure 6.16. The invariant rod packings with the numbers and symbols of Table 6.4.

Table 6.4. The 3-periodic invariant non-intersecting line sets ('rod packings'). To generate the structure the symmetry operations act on the line in the direction given in the first column passing through a point with the coordinates given.

Type	Symbol	Symmetry	Coordinates
1-way <001>	1 **hcb**	*P6mm*	$\frac{1}{3}, \frac{2}{3}, 0$
	2 **hxl**	*P6mm*	$0, 0, 0$
	3 **kgm**	*P6mm*	$\frac{1}{2}, 0, 0$
	4 **pcu**	*P4mm*	$0, 0, 0$
2-way tetragonal <100>	5 ϑ	$I4_1/amd$	$0, 0, \frac{1}{4}$
	6 Φ	$P4_2/mmc$	$0, 0, 0$
3-way hexagonal <010>	7 Λ	$P6_222$	$\frac{1}{2}, 0, \frac{1}{6}$
3-way hexagonal <100>	8 Δ	$P6_222$	$0, \frac{1}{2}, 0$
3-way cubic <100>	9 Π	$I4_132$	$\frac{1}{4}, 0, 0$
	10 Π*	$Pm\bar{3}n$	$\frac{1}{2}, 0, 0$
4-way cubic <111>	11 Σ	$I4_132$	$\frac{1}{3}, \frac{2}{3}, 0$
	12 Γ	$Ia\bar{3}d$	$0, 0, 0$
	13 Ω	$I432$	$\frac{1}{3}, \frac{2}{3}, 0$
	14 Σ*	$Ia\bar{3}d$	$\frac{1}{3}, \frac{2}{3}, 0$

In contrast to the 2-periodic case, it is found now that there are many regular (transitivity 1 1 1) chain-link weavings, but only three regular fabric weavings were found.

6.4.1.2. Derivation of weavings

Shown in this section is how chain-link weavings are derived from uninodal 4-c nets. Such nets have six angles and the original node is split into 6 (Figure 6.17). Two of these, related by symmetry at opposite angles, can be selected to serve corners of a weaving with double crossings. Later an example of a weaving (**dia-w****) is adduced with sextuple crossings. For isogonal (one corner) weavings the original net must be uninodal and have symmetry at the vertex of order at least 2. The RCSR lists 67 such nets, and one net can provide more than one weaving, as now demonstrated, so the number of possibilities is large. Below is how the most symmetric vertex- and edge-transitive nets were derived.

a) $Fd\bar{3}m$ b) $I4_1/amd$ c) $I4_122$
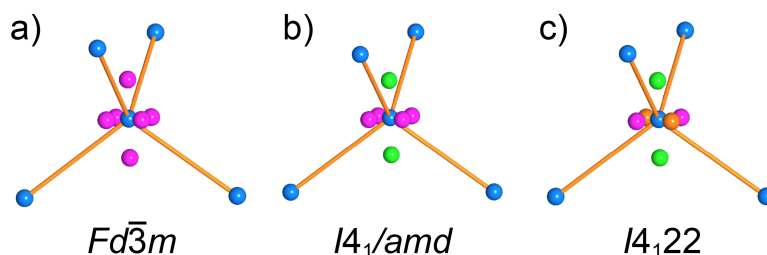
Figure 6.17. (a) Six symmetry-related points at a vertex of the diamond (**dia**) net with symmetry $Fd\bar{3}m$. (b) With symmetry $I4_1/amd$ the points are split into sets of 2 and 4 symmetry-related points. (c) With symmetry $I4_122$ the points are further split into 3 groups of 2.

The diamond net, **dia**, at full cubic symmetry ($Fd\bar{3}m$) has six equivalent angles. To remove some of the degeneracy one must go to trigonal or tetragonal symmetry. Trigonal will split into groups of 3, so, to make a weaving with double crossings, the new symmetry must be tetragonal

and the maximal tetragonal subgroup is $I4_1/amd$. This splits the 6 into $2 + 4$ as shown in the figure. Linking the 2 appropriately gives the regular weaving **dia-w**. The only maximal subgroup of $I4_1$/*amd* that splits the group of 4 is $I4_122$, which produces two pairs (Figure 6.17). Constructing weavings from these pairs gives an enantiomorphic pair of weavings **dia-w***. By contrast the quartz net, **qtz**, has maximum site symmetry 222 and the angles are already split into three pairs. Each of these leads to a regular weaving **qtz-w**, **qtz-w***, and **qtz-w****.

Table 6.5. Generation of regular chain-link weavings and catenanes. The original nets are 4-c except for **acs** (6-c). For **acs**, the symmetry of the net is shown first, then that of the weaving.

Parent	Symmetry	Angles	
dia	$Fd\bar{3}m$	(6)	-
	$I4_1/amd$	(4) + 2	**dia-w** zigzag
	$I4_122$	(2) + 2 +2	**dia-w*** 4_1 and 4_3 helices
qtz	$P6_222$	2 + (2 +2)	**qtz-w** zigzag
		(2) + 2 + (2)	**qtz-w*** 3_2 helices
		(2 + 2) + 2	**qtz-w**** 6_2 helices
sod	$Im\bar{3}m$	(4) + 2	catenated 4-rings
	$Pn\bar{3}$m	(2) + 2 + 2	catenated 6-rings
	$I432$	(2) + 3 + 3	**sod-w** 3_1 and 3_2 helices
lcs	$Ia\bar{3}d$	(4) + 2	**lcs-w** 4_1 and 4_3 helices
	$I4_132$	(2) + 2 + 2	**lcs-w*** two sticks
lcv	$I4_132$	2 + (2 +2)	catenated 3-rings
		(2) + 2 + 2	**lcv-w** 3_1 or 3_2 helices
ana	$Ia\bar{3}d$	(1 + 1 + 2) + 2	catenated 4-rings
		(1 + 1) + 2 (+ 2)	catenated 6-rimgs
acs	$P6_3/mmc$	$\rightarrow P6_322$	**acs-w** 6_1 or 6_5 helices

The sodalite net, **sod**, illustrates another feature. At full symmetry ($Im\bar{3}m$) the site symmetry is $\bar{4}2m$ and the angles are split into $4 + 2$. Linking corners corresponding to the unique pair give a regular polycatenane of linked squares, **sod-y**. Lowering the symmetry to $Pn\bar{3}m$ splits the four into two pairs, each of which gives the regular polycatenane **sod-y*** of linked hexagons. These results show the close relation between weavings and polycatenanes. However, a different maximal subgroup of $Im\bar{3}m$, namely $I432$, again splits the group of four into two pairs and these give enantiomorphs of a regular chiral weave **sod-w.** Nets with planar 4-coordination (e.g. **nbo**) are not amenable to this treatment but a regular fabric weave **nbo-w** has been found. In contrast to the 2-periodic case, regular 3-periodic weaves with triple crossings are possible. **pcu-w**, **pcu-w***, **crs-w**, **acs-w**, and **lcy-w** are all derived from vertex- and edge-transitive 6-c nets. Just one regular weaving with quadruple crossings has been found – **thp-w** derived from the 8-c net **thp**.

6.4.1.3 Optimal embedding and girth

Knot theorists determine an 'ideal' embedding of a finite knot as that which uses the shortest length of a rope of fixed width. The 'energy' that is minimized is the ratio of rope length to diameter.[44] A recent paper, which gives a comprehensive review, shows how such a procedure can be applied to periodic systems.[45]

In this section, a related procedure was used to find an *optimal embedding* for piecewise linear weavings. For weavings of threads containing just one kind of cylindrical stick, the width of the cylinder that brings a stick into contact with one or more neighbors was measured. The *girth* of a stick is then the ratio of that width to the stick length. The optimal embedding is the one that maximizes the girth of non-intersecting sticks.
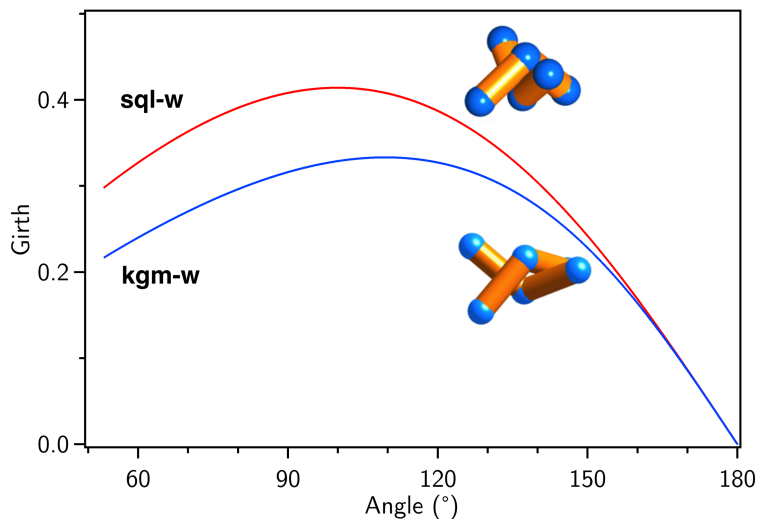

Figure 6.18. Girth as a function of the angle at a corner (*corner angle*) between two contiguous sticks for the regular 2-periodic weavings **sql-w** and **kgm-w**. The crossings shown are for maximum girth.

In Figure 6.18, notable is a broad maximum in each case. The maxima are at:

sql-w girth = 0.414 at 99.9˚ ($\sqrt{2}$-1, 2tan^{-1}2$^{1/4}$)

kgm-w girth = 0.333 at 109.5˚ [1/3, cos^{-1}(-1/3)]

The greater the maximum girth is, the more amenable to synthesis will be a weaving composed of polyatomic threads. The broad maximum, which is characteristic of the weavings that have been studied, indicates that the angle at a corner is not critical in determining a weaving. Optimal embeddings for the regular 3-periodic weavings and numerical data are reported in Table 6.6. For structures with transitivity other than 1 1 1, the reported embedding is not optimal, but adequate to specify the structure. However, such optimal embeddings could be found for all the structures in this chapter.

6.4.2 3-periodic fabric weaving

The nets of the invariant intersecting line set (Table 6.3) are identified as sources of fabric weaving. The two with 4-c vertices (**nbo** and **lvt**) give fabric weaves with one kind of crossing point. There are four of these nets with 6-c vertices. Two (**pcu** and **crs**) yield fabric weaves with triple crossing points. Geometric data for these weavings are given in Table 6.6.

nbo-w. The **nbo** net is the only one with full square symmetry (4/*mmm* = D_{4h}) at the vertex and the derived weave, **nbo-w** (Figure 6.19), and is the only regular (transitivity 1 1 1) fabric weave with two-way crossings. At the optimal embedding, girth = 0.619, corner angle = 139˚. The

threads are 4_1 and 4_3 helices and threads of one hand are directly linked only to threads of opposite hand. Interwoven helical SBUs based on this pattern have been identified in rod MOFs but in those materials the rods are linked by polytopic linkers so the structure is not a weaving.[41]

nbo   **nbo-w**
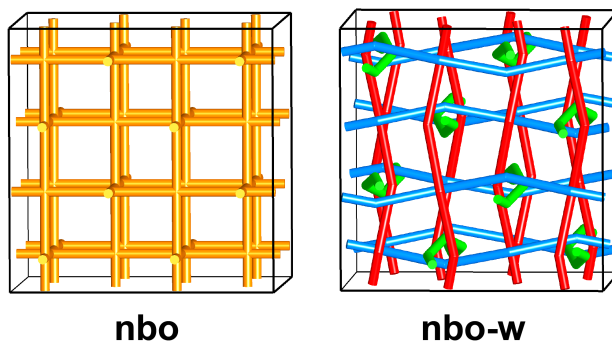
Figure 6.19. The **nbo-w** fabric weave. On the left is shown the structure of the intersecting thread axes.

cds-w. All other 4-c nets with embeddings in which all vertices are in square coordination are at least edge 2-transitive so cannot yield isonemal weavings. The simplest such net is **cds** and the corresponding weaving **cds-w** (Figure 6.20) which has symmetry $F4_12_12$ and transitivity 4 4 2 (each thread 2 2 1).

cds   **cds-w**
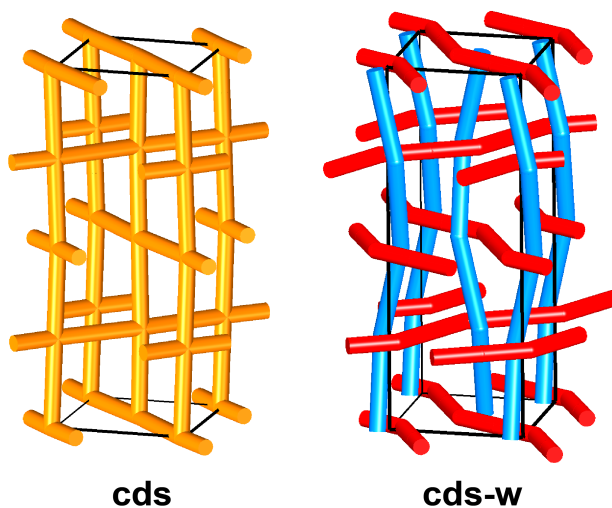
Figure 6.20. A weaving derived from the **cds** net shown on left.

lvt-w. The **lvt** net, the other invariant 4-c net formed from intersecting; it yields **lvt-w** (Figure 6.21) but the best embedding was found to have transitivity 1 2 1.

lvt   **lvt-w**
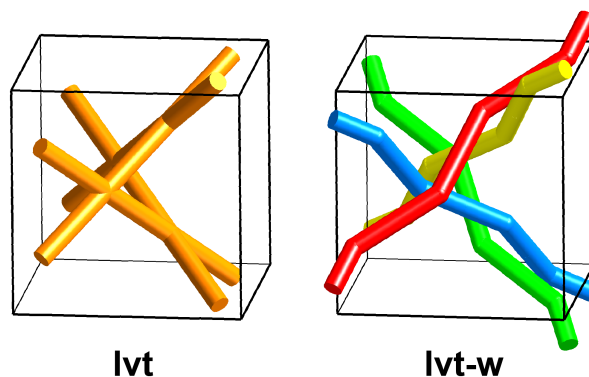
Figure 6.21. A fabric weave (right) derived from the **lvt** net (left).

      pcu-w. The 3-periodic analog of the simple regular 2-periodic two-way weaving has zigzag threads running in three perpendicular directions. This is the regular weaving **pcu-w** (Figure 6.22). Presumably there is a family of less-regular weavings just as in the 2-periodic case – which has not been explored. In the optimal embedding girth = 0.253, corner angle = 94.6˚

pcu   **pcu-w**
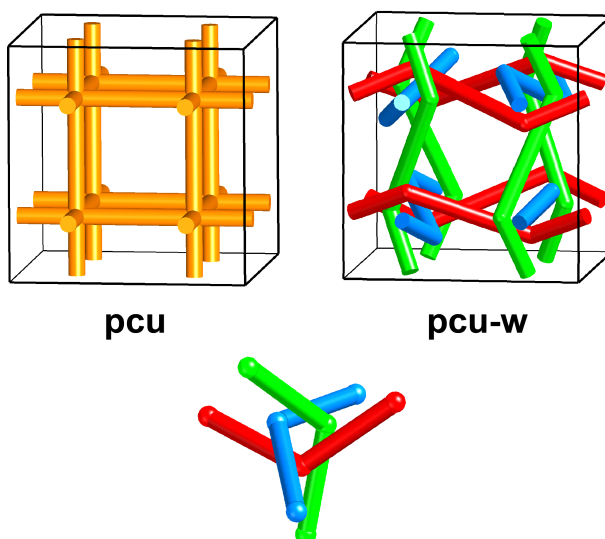
Figure 6.22. A fabric weave (top right) derived from the **pcu** net (top left). On the bottom is a detail in the vicinity of a triple crossing link point.

      crs-w. This (Figure 6.23), like **pcu-w**, is a chiral regular weaving with triple crossings and zigzag threads. It was suggested by examination of nets formed from linked helical ladders.[46] In the optimal embedding girth = 0.277, corner angle = 108.3˚.

crs   crs-w
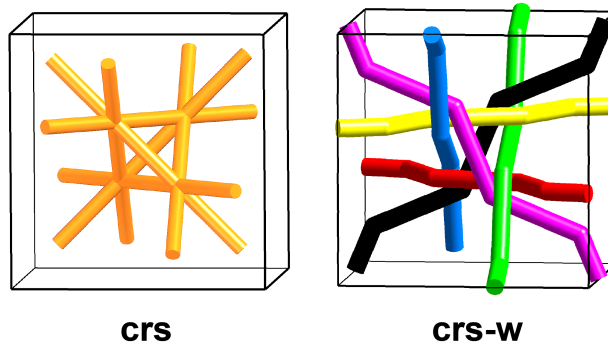
Figure 6.23. The **crs** net and the derived fabric weave with triple crossing link points.

Table 6.6 Geometric data for 3-periodic fabric weaving. In the 'stick' column, that vertex is linked to the one in the 'corner' column. All have transitivity 1 1 1 except **lvt-w** (1 2 1).

Symbol	Symmetry	Corner	Stick
nbo-w	$Fd\bar{3}c$	⅞, ⅞, -0.024	⅛, 0.774, ⅛
lvt-w	$I4_122$	0.5, 0.7, 0.68	0.2, 1.0, 0.83; 0.7, 0.5, 0.33
pcu-w	$I432$	¾, 0.413, 0.087	¼, 0.087, 0.413
crs-w	$F4_132$	0.29, 0.46, ⅝	0.71, 0.54, ⅝

6.4.3 3-periodic chain-link weaving

In contrast to the 2-periodic case, there are many different kinds of chain-link weaving. Accordingly, only regular isonemal weavings are examined.

6.4.3.1 Parallel helical threads

Described here are some isonemal and dinemal (two kinds of thread) with respectively transitivity 1 1 1 and 2 2 2. For isonemal weavings only chiral structures appear possible. Geometrical data are recorded in Table 6.7.

dia-w*. This (Figure 6.24) is one of two isonemal structures derivable from the diamond (**dia**) net with either linked 4_1 or 4_3 helices. The optimal embedding has a simple exact solution – the girth is $1/\sqrt{6} = 0.408$, the axial ratio c/a is $2\sqrt{2}$ and the corner angle is $\cos^{-1}(-1/3) = 109.5°$. The diamond net is particularly amenable to forming interpenetrating pairs and also shown is the structure **dia-w*-c** with two interpenetrating weavings.

149

dia-w*   **dia-w*-c**
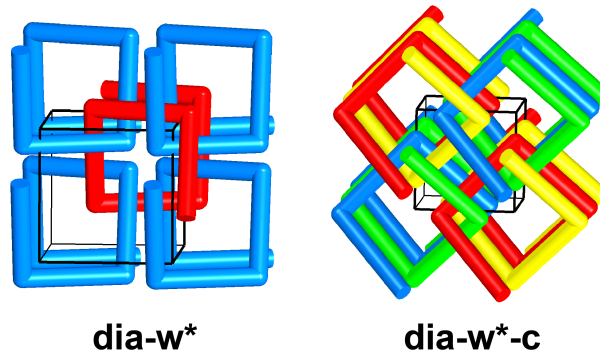
Figure 6.24. Left: a chain-link weaving of tetragonal helices derived from the diamond (**dia**) net. Right: two such interpenetrating weavings.

qtz-w*. This (Figure 6.25) is the corresponding weaving of 3_1 or 3_2 helices. In the optimal embedding, girth = 0.310, c/a = 1.88, corner angle = 78.5˚. Quartz nets of the same hand also readily interpenetrate, and also shown in the figure is the interpenetrating weaving.

qtz-w*   **qtz-w*-c**
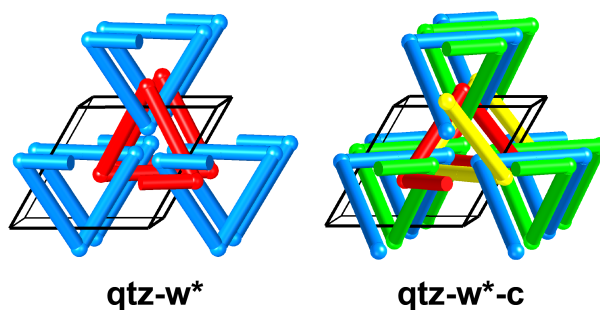
Figure 6.25. Left: a chain-link weaving of trigonal helices derived from the quartz (**qtz**) net. Right: two such interpenetrating weavings.

qtz-w**. This (Figure 6.26) is another of the three isonemal weaving derived from the quartz net. Now the threads are 6_1 or 6_5 helices. At the optimal embedding girth = 0.450, c/a = 1.41, corner angle = 129.6˚. Note that there are two separate coaxial helices that are not directly linked. With reference to the figure it may be seen that green and blue are coaxial, and that green is linked to black, black to yellow, and yellow to blue. Note that there is just one kind of helix – indeed there is just one helix per unit cell in the sense that all are related by translations.

qtz-w**
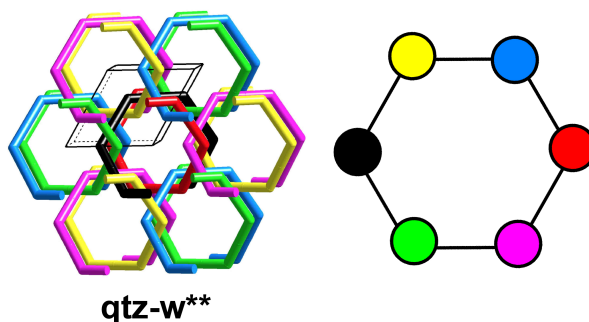
Figure 6.26. Left: a chain-link weaving of hexagonal helices derived from the quartz (**qtz**) net. The pattern on the right shows how the helices are linked. Helices are linked to those of neighboring colours; for example, blue is linked to red and yellow. Coaxial helices have colours on a diameter of the hexagon; for example, blue and green.

acs-w. This (Figure 6.27) is a nice example of a weaving with a triple crossing (see figure). At the optimal embedding girth = 0.315, c/a = 1.50, corner angle = 135.6˚. Now there are three coaxial 6_1 or 6_5 helical threads that are not directly linked. Each of the three is linked to two of the three in neighboring columns so the whole assembly forms just one weaving as the net of link points (**acs**) is a connected net. Again, there is just one helix per unit cell.

acs-w
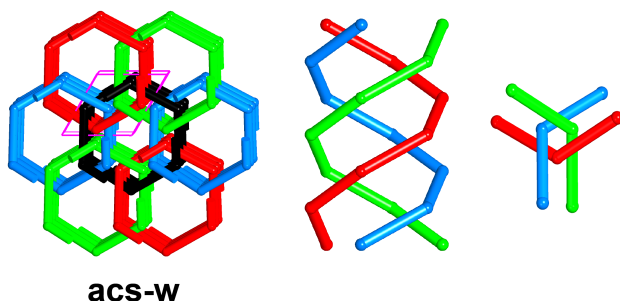
Figure 6.27 Left: a chain-link weaving derived from the 6-c **acs** net. As shown in the middle, each column is actually three coaxial helices. Right shows the vicinity of a triple crossing link point. Note that colours do not have the same significance in the different panels.

Shown in Figure 6.28 are some dinemal weaving of parallel helices. The transitivity in each case is 2 2 2 -the minimum for a dinemal weaving. Importantly, from the design point of view, in each case there is just one kind of link point. Zigzag threads can link trigonal helices of opposite (**unc-w**) or the same (**und-w**) hands. Likewise zigzags can link tetragonal helices of opposite (**unh-w**) or the same (**ung-w**) hands. It should be clear from the figure that zigzags can only link hexagonal helices of the same hand (**uni-w**). Finally in the figure is a linkage of trigonal and hexagonal helices (**unj-w**). In this chiral pattern 3_1 and 6_1 (or 3_2 and 6_5) helices are linked.
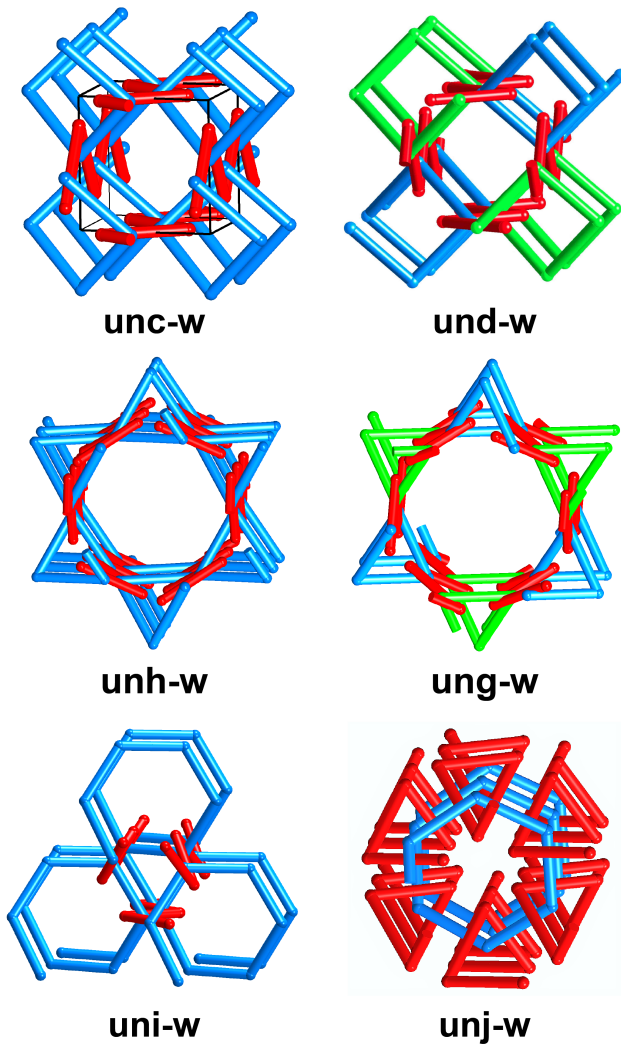
Figure 6.28. A series of weavings of two kinds of parallel threads and transitivity 2 2 2. Top four: zigzag + helix. Bottom two: two helices.

Table 6.7. Geometric data for 3-periodic chain-link weaving with parallel threads. In the 'stick' column, that vertex is linked to the one in the 'corner' column. The transitivity is 1 1 1 or 2 2 2; in the latter case, there are two rows per structure.

Symbol	Symmetry	Corner	Stick
dia-w*	$I4_122$	0.25, 0.25, 0	0.25, -0.75, ¼
dia-w*-c	$P4_222$	0.0, 0.3, 0.5	0.7, 1.0, 0.0
qtz-w*	$P6_222$	0.25, 1-x, ⅓	2x-1, x, ⅔
qtz-w*-c	$P6_222$	0.44, 0.88, 0	0.44, 1.16, ⅓
qtz-w**	$P6_222$	0.764, 0, 0	0.764, 0.764, ⅓
acs-w	$P6_322$	1, -0.505, ¼	1.01, 1.505, ¾
unc-w	$P4_122$	0.44, 0, ¾	0, 0.56, ½
		0, 0.22, 0	0, 0.78, ½
und-w	$I4_1/amd$	¾, 0.4, 0	¾, 0.1, ½
		¼, 0.28, ½	0.47, ½, ¼
unh-w	$P6_122$	0.48, 0.96, 0.25	0.48, 0.52, 0.92
		0.38, 0.76, 0.25	0.62, 0.25, 0.75
ung-w	$R\bar{3}c$	0, 0.47, ¼	0.14, ⅓, ⁷⁄₁₂
		0, 0.39, ¼	0, 0.61, ¾
uni-w	$P6_122$	0.46, 0, 0	0.46, 0.46, ⅙
		0.32, 0, 0	0.68, 0, ½
unj-w	$P6_122$	0.32, 0.16, ¹⁄₁₂	0.84, 0.16, ⁵⁄₁₂
		0.31, 0.62, ¼	0.62, 0.31, ¹⁄₁₂

6.4.3.2 Chain-linked zigzag threads in layers

qtz-w and **dia-w.** Two special structures with threads whose axes lie in parallel layers are recognized. They are derived from the quartz (**qtz**) and diamond (**dia**) nets by splitting the 4-c vertices as describer earlier (§6.4.1.2). **dia-w** is notable for the fact that the threads cross at right angles making them particularly favorable for designed synthesis of 3-periodic weaving with zigzag threads in crystals and indeed the structure of the 3-periodic weavings (COF-505[47] and COF-112[48]) reported to date are based on **dia-w**. At the optimal embedding for **dia-w** girth = 0.294, c/a = 0.52, corner angle = 95.4˚. For **qtz-w** girth = 0.293, c/a = 0.40, corner angle = 104.5˚. Data (symmetry, coordinates) are to be found in Table 6.8.

dia-w qtz-w
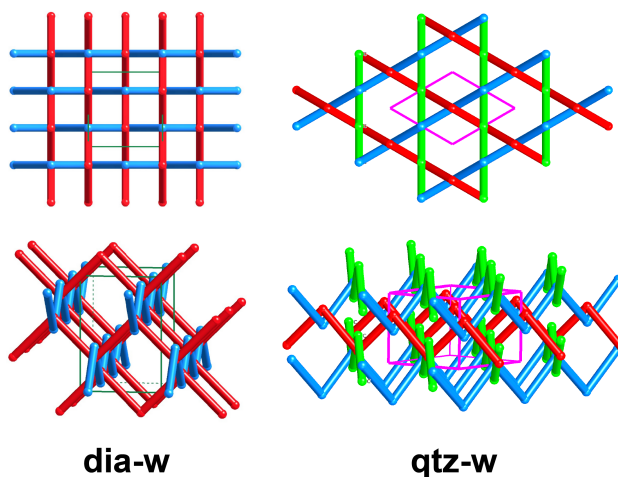
Figure 6.29. Left: two views of the **dia-w** chain-link weave derived from the diamond (**dia**) net. Right: two views of the **qtz-w** chain-link weave derived from the quartz (**qtz**) net.

The structures are illustrated in Figure 6.29, **dia-w** is particularly amenable into forming two interpenetrating structures **dia-w-c**. The symmetry goes from $I4_1/amd$ to $P4_2/nnm$. In both cases four link points per primitive cell. Of interest with respect to real materials is the symmetry of the zigzag threads, which are replaced by 4-fold helices. Then one gets a structure with interwoven 4_1 and 4_3 helices as shown in Figure 6.30. Finally, interpenetrating two such structures gives an idealization of the actual structure of COF-505. The symmetries are now $I\bar{4}2d$ and $P\bar{4}n2$ (interpenetrated pair), and COF-112 has the non-interpenetrated structure. COF-505 has the interpenetrated structure.
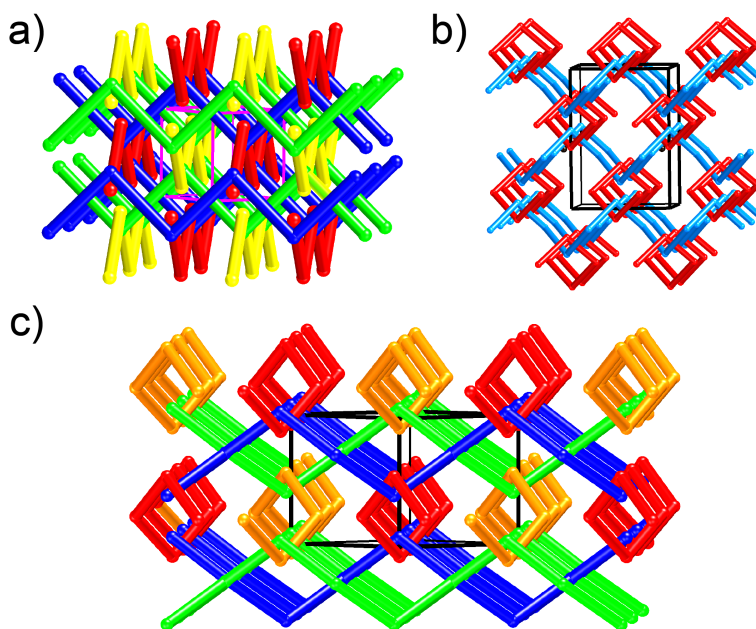
Figure 6.30. Variation on the **dia-w** weaving of Figure 6.29. (a) Two interpenetrating weavings. (b) The basic weaving with the zigzags replaced by helices. (c) Two interpenetrating copies of the structure in (b). Red and blue helices are linked together by the yellow and green ones. This is the underlying structure of COF-505.

Structures derived from the tetragonal net **pts**, the simplest structure with both planar and tetrahedral 4-c vertices, are also shown here. Splitting the tetrahedral vertices in chain-link fashion results in linked rods running normal to the tetragonal axis. Splitting also the planar vertices in fabric-weave fashion produces a weaving of threads (Figure 6.31). As shown in the figure, the structure can be considered a weaving (interpenetration) of four **dia-w** weaves.

pts-w
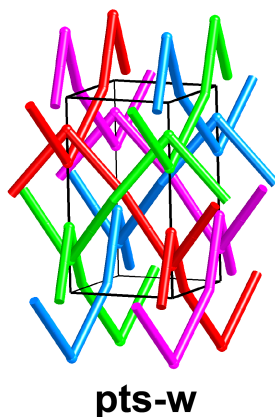
Figure 6.31. Decomposing the **pts** net into threads. Threads of one color constitute a **dia-w** weaving.

6.4.3.3 Cubic chain-link weaves

Here described are regular isonemal chain-link weavings with thread axes running in three directions (cubic <100>) or four directions (cubic <111>). For the most symmetrical, the pattern of axes is one of the invariant ones illustrated in Figure 6.16.

sod-w. This (Figure 6.32) structure is formed by 3_1 (or 3_2) helices with axes in the Ω pattern. Twelve threads combine to weave the cage (tile) shown. In the optimal embedding girth = 0.152, corner angle = 93.6˚.

sod-w   **sod** tile
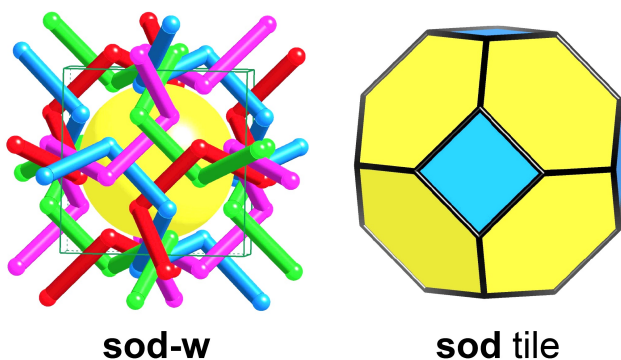
Figure 6.32. Left: **sod-w**. Parallel threads (trigonal helices) have the same colour. Twelve threads combine to make the space-filling cage shown.

lcs-w. In this structure (Figure 6.33), threads are 4_1 and 4_3 helices with axes forming the Π^* pattern with a doubled cell to allow ordering of the 4_1 and 4_3 helices as shown in the figure. As in **nbo-w**, direct links are only between helices of opposite hand. In the optimal embedding girth = 0.429, corner angle = 108.2˚.
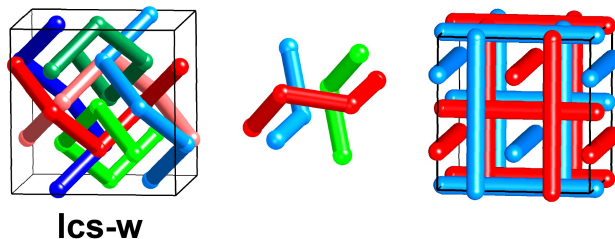
lcs-w

Figure 6.33. Aspects of the **lcs-w** chain-link weaving of tetragonal helices. Directly linked helices are of opposite hand. Middle: a close-up of the pattern of linking. Right: the pattern of helix axes. Red and blue rods correspond to helices of opposite hand and form a superstructure of the Π* packing (Figure 6.16).

lcv-w and **lcv-w*** (Figure 6.34). These are more chiral structures with two degrees of freedom. In **lcv-w** the corners in x, $x+\frac{1}{4}$, $\frac{1}{8}$ and the threads are 3_1 (or 3_2) helices in the Σ pattern. In **lcv-w*** the corners in x, 0, $\frac{1}{4}$ and the threads are 4_1 (or 4_3) helices in the Π pattern. This latter weaving accommodates only narrower threads. In the optimal embedding for **lcv-w** girth = 0.142, corner angle = 124.6°; for **lcv-w*** girth = 0.082, corner angle = 147.9°.

lcv-w

lcv-w*   **lcv** tile
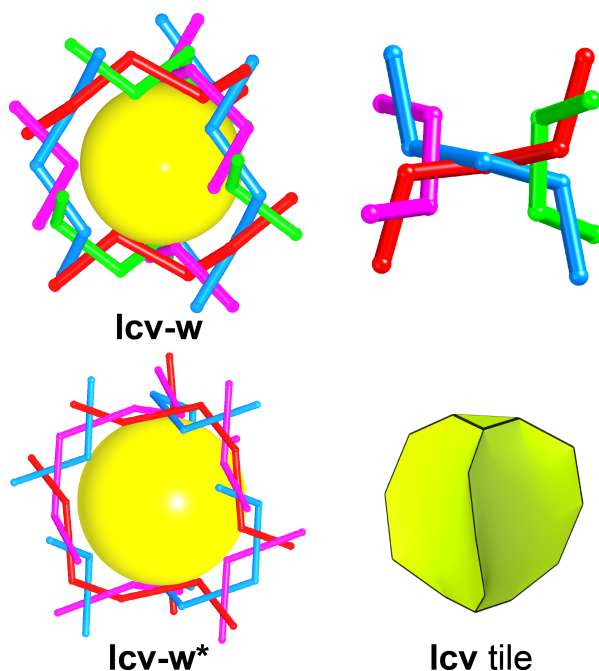
Figure 6.34. The **lcv-w** and **lcv-w*** weavings corresponding to a tile of the structure, shown on the lower right. Threads of the same color are parallel. In **lcv-w** they run along <111> and in **lcv-w*** they run along <100>.

lcy-w. **lcy** (Figure 6.35) is a 6-c net, so a triple-crossing link point (shown in the figure) is necessary. Again, the threads are 3_1 (or 3_2) helices in the Σ pattern. In the optimal embedding the girth = 0.252, corner angle = 108.3°.
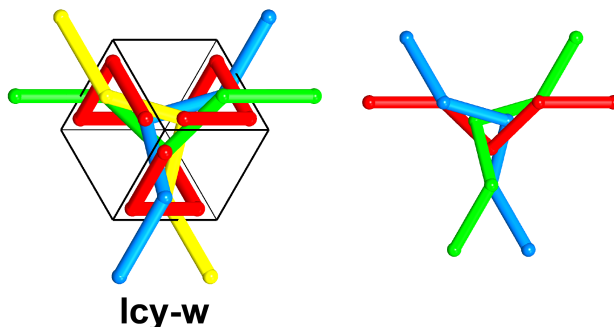
lcy-w

Figure 6.35. lcy-w. Chain-link weaving derived from the 6-c net **lcv**. Detail in the vicinity of a triple-crossing link point is shown on the right.

lcy-w*. The corners of **lcy-w** (Figure 6.36) can be connected differently to obtain a new weaving of zigzag threads. The threads run along <100> and their axes are arranged in a lower-symmetry version of the Π packing. In the optimal embedding girth = 0.104, corner angle = 68.8˚.
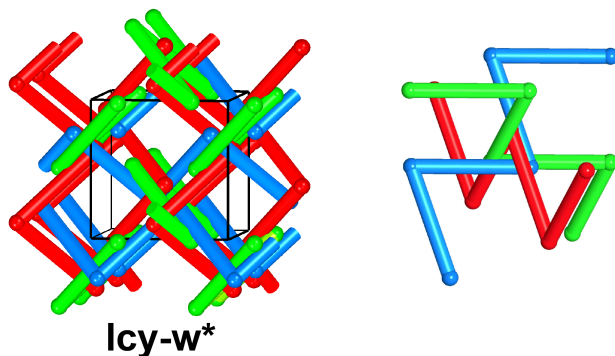
lcy-w*

Figure 6.36. lcy-w*. A secend chain-link weaving derived from **lcv** compared with **lcv-w** (Figure 6.34).

pcu-w* This structure (Figure 6.37) is another weaving with triple crossings and of interest in several ways. It is a chain-link weaving with link points at the vertices of a **pcu** net. – contrast with **pcu-w**, which is a triple-crossing fabric weave with the same pattern of link points. The threads are 3_1 (or 3_2) helices with axes forming the same pattern as in **sod-w**. In fact, all three weaves (**pcu-w**, **pcu-w*** and **sod-w**) have the same symmetry ($I432$) and corners in the same Wyckoff set (x, $x+\frac{1}{2}$, $\frac{1}{4}$), The difference between the three weavings is that the stick corners are different pairs of coordinates. For the optimal embedding of **pcu-w*** girth = 0.077, corner angle = 74.2˚.
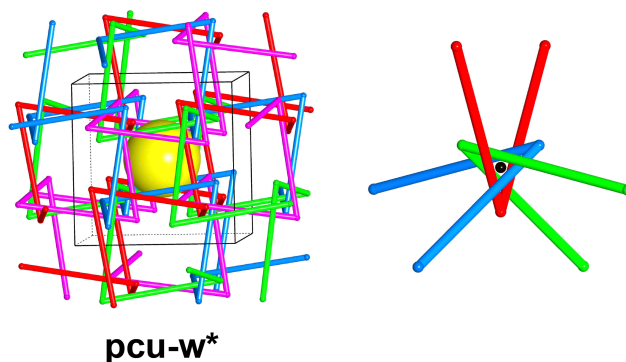
pcu-w*

Figure 6.37. The **pcu-w*** weaving. Parallel threads have the same colour. On the left are shown 12 helices enclosing the yellow sphere at the center – compare **sod-w** (Figure 6.32). On the right are shown three threads in the vicinity of a link point (black sphere).

thp-w. **thp** (Figure 6.38) is an 8-c net so the derived weaving has a quadruple-crossing link point as shown in the figure. The full structure is hard to depict clearly and only the proximity of a link point and the thread packing is shown. The threads are zigzags running along <111> and the pattern of their axes is a supercell (2×2×2) of the Γ packing in a lower-symmetry arrangement, as shown in the figure. For the optimal embedding, girth = 0.111, corner angle = 86.4°.
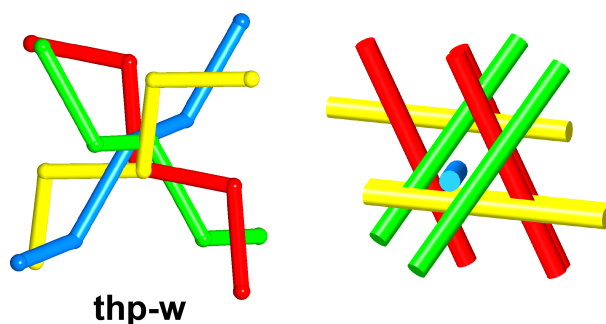
thp-w

Figure 6.38. thp-w. Left: a fragment of a chain-link weaving derived from the 8-c net **thp.** Right: the pattern of the helical thread axes.

dia-w** This weaving (Figure 6.39) is shown as an example of a weaving with sextuple crossings. The six symmetry-related points around a vertex in the **dia** (diamond) net are still related by symmetry in $F4_132$ and can be linked to make a weaving as shown in the figure. There it can be seen that each edge of the parent **dia** net is replaced by three sticks. The threads are 4_1 (or 4_3) helices with axes forming the Π* pattern with a doubled cell as in **lcs-w**, but now all helices of the same hand. As might be expected for a structure with a high number of crossings, the weaving is only possible with narrow threads. At the optimal embedding girth = 0.051, corner angle = 94.2°.

158
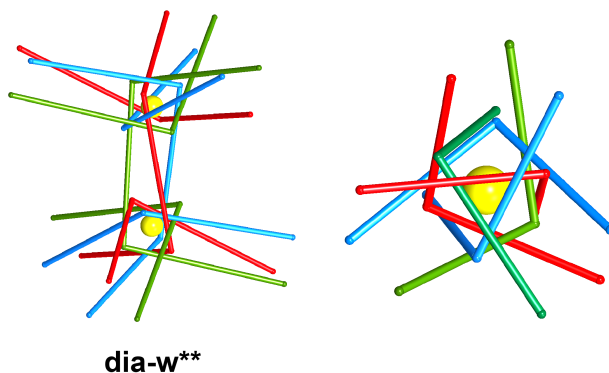
dia-w**

Figure 6.39. Two aspects of the **dia-w**** weaving. Left: showing how corners at two crossing points are linked by three sticks. Yellow balls are at the vertices of the parent **dia** net. Right: close-up of one sextuple crossing at the optimal embedding. Threads of the same color are parallel.

hbo-w. This (Figure 6.40) is an example of an isonemal weaving with crankshaft threads. Though not regular (the transitivity is 1 2 1) it should be a credible candidate for designed synthesis.
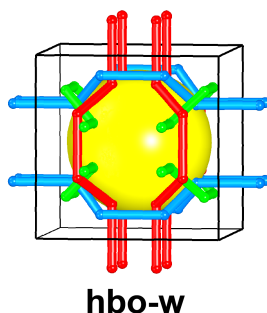
hbo-w

Figure 6.40. hbo-w. A chain-link weaving of crankshaft threads derived from the 4-c net **hbo** with transitivity 1 2 1. Twelve threads combine to form the cavity centered by the yellow ball.

Table 6.8. Geometric data for 3-periodic chain-link weaving with non-parallel threads. In the 'stick' column, that vertex is linked to the one in the 'corner' column. Under 'thread' is the shape (2_1 is zigzag) and the symbol for the packing (Figure 6.16). All have transitivity 1 1 1 except **pts-w** (2 1 1) and **hbo-w** (1 2 1).

Symbol	Symmetry	Corner	Stick	Thread
dia-w	$I4_1/amd$	0, ¾, 0.434	0, ¼, 0.434	2_1 Θ
dia-w-c	$P4_2/nnm$	¼, ¾, 0.85	-¼, ¼, 0.15	2_1 Φ
qtz-w	$P6_222$	½, ½, 0.008	0, ½, 0.992	2_1 Λ
pts-w	$P4_122$	0, 0, 0.17	-½, 0.12, ½	2_1 Φ
sod-w	$I432$	0.069, ¼, 0.431	-0.069, 0.569, ¾	3_1 Ω
lcs-w	$Ia\bar{3}d$	¾, 0.488, 0	¾, 0.512, -¼	$4_{1,3}$ Π*
lcv-w	$I4_132$	0.458, 0.708, ⅝	0.792, ⅝, 0.542	3_1 Σ
lcv-w*	$I4_132$	0.075, 0, ¼	¼, 0.175, 0	3_1 Σ
lcy-w	$P4_132$	⅜, 1.539, 0.211	0.461, 0.711, ⅛	3_1 Σ
lcy-w*	$P4_132$	⅞, -0.008, 0.742	⅜, 0.508, 0.242	2_1 Π
thp-w	$I\bar{4}3d$	0.80, 0.18, 0.03	0.32, 0.03, 0.20	3_1 Γ
dia-w**	$F4_132$	¼, ¼, 0.63	0.62, 0, 0	4_1 Π*
hbo-w	$Pm\bar{3}n$	0.62, 0.29, 0.83	0.32, 0.29, 1.17	-

6.4.4 Polycatenanes

Polycatenanes (linked rings) are readily derived from 4-c nets and a symbol **abc-y** is used for a polycatenane obtained from **abc**. There are many possibilities, so with one exception, only the regular structures are included. Geometrical data are in Table 6.9.

Linked triangles. The only regular structure formed from a 4-c net is **lcy-y** (Figure 6.41). However, there is at least one other with transitivity 1 1 1. This is obtained by taking the regular finite polycatenane formed from four triangles (12^4). The twelve vertices can be linked as in face-centered cubic to produce the polycatenane with symbol **lkv** (Figure 6.41). However, it is not considered as a new regular polycatenane as it may also be considered as four interwoven **lcy-y** polycatenanes.

lcv-y   **lkv**
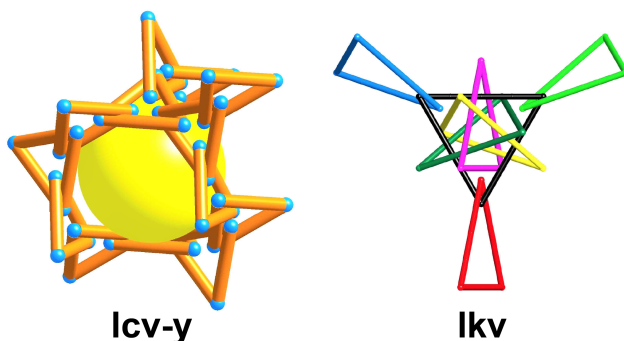
Figure 6.41. Left: The polycatenane **lcv-y**. Linked triangles derived from the 4-c net **lcv**. Right: a fragment of a structure with transitivity 1 1 1 with each triangle linked to six others as shown for the black triangle. This structure is four interpenetrating **lcv-y** polycatenanes.

Linked quadrangles. Two regular structures **sod-y** and **ana-y** (Figure 6.42) are identified. Note that although the quadrangles in **ana-y** are not planar they are regular with equal (symmetry-related) edges and angles.

sod-y   **ana-y**
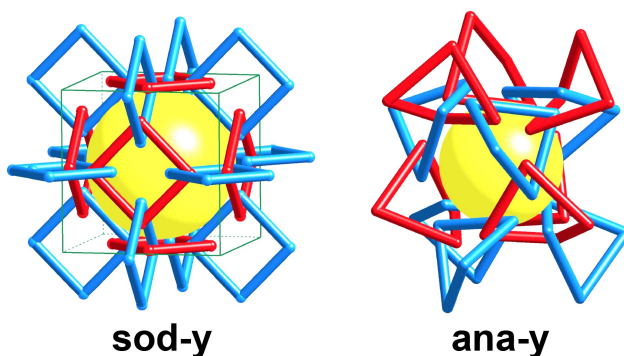
Figure 6.42. Regular polycatenanes of linked quadrangles.

lka (Figure 6.43) is less regular (transitivity 2 1 1). This is made by linking Borromean sets of three rings into a cubic network. The structure can be considered to be interpenetrating 1-periodic chains with the Borromean property that no two chains are directly linked.

lka
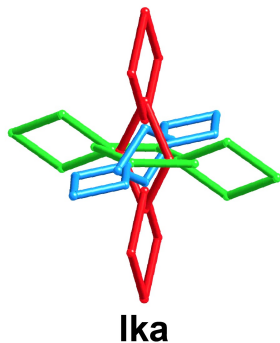
Figure 6.43. A polycatenane with transitivity 2 1 1 formed by linking Borromean rings into a cubic framework.

Linked hexagons. There are three regular structures (Figure 6.44) **sod-y***, **ana-y***, and **lcs-y**. The skew ('chair') hexagons in **ana-y*** and **lcs-y** are regular (all edges and all angles related by symmetry).
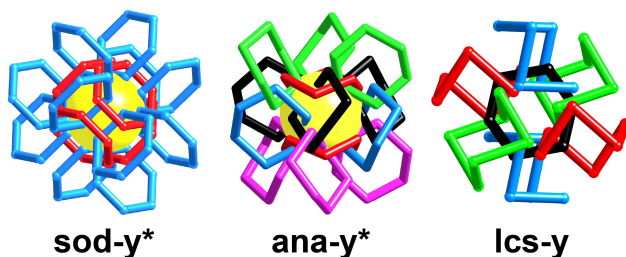

sod-y*   **ana-y***   **lcs-y**

Figure 6.44. Three regular polycatenanes formed by linking hexagons into a 3-periodic framework.

Linked quadrangles with triple crossings. One regular polycatenane derived from a 6-c net is found. This is **pcu-y** (Figure 6.45) in which each quadrangle is linked to 8 others.

pcu-y
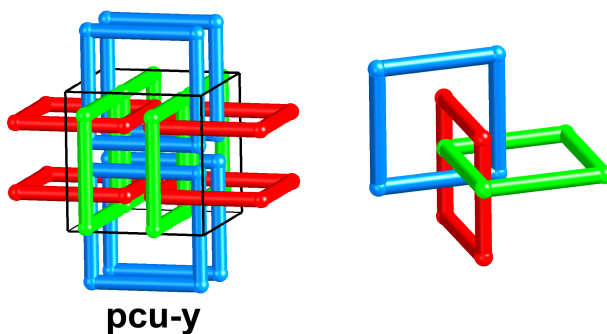
Figure 6.45. A regular polycatenane constructed by interlocking quadrangles in a 6-c net.

Table 6.9. Geometric data for 3-periodic polycatenanes. In the 'stick' column, that vertex is linked to the one in the 'corner' column. All have transitivity 1 1 1 except **lka** (2 1 1).

Symbol	Symmetry	Corner	Stick
lcv-y	$I4_132$	0.44, 0.19, $\frac{7}{8}$	0.81, $\frac{3}{8}$, 1.06
lkv	$F432$	0.3, 0, 0.7	0, 0.3, 1.3
sod-y	$Im\bar{3}m$	0.19, 0, $\frac{1}{2}$	$\frac{1}{2}$, 0, 0.19
ana-y	$Ia\bar{3}d$	0.89, 0.42, 0.81	0.83, 0.14, 0.94
lka	$Fm\bar{3}c$	$\frac{1}{2}$, 0.2, 0	0.35, $\frac{1}{2}$, 0
sod-y*	$Pn\bar{3}m$	0.31, $\frac{1}{2}$, 0.69	0, 0.19, 0.69
ana-y*	$Ia\bar{3}d$	0.17, 0.30, 0.89	0.20, 0.39, 1.17
pcu-y	$Pm\bar{3}n$	0.1, 0.4, $\frac{3}{4}$	0.9, 0.4, $\frac{3}{4}$

6.4.5 Linked polyhedra. These structures (Figure 6.46) are beyond our restriction to those made up solely of 2-c corners and sticks. However, one might argue that they are the true 3-periodic analogs of chainmail.
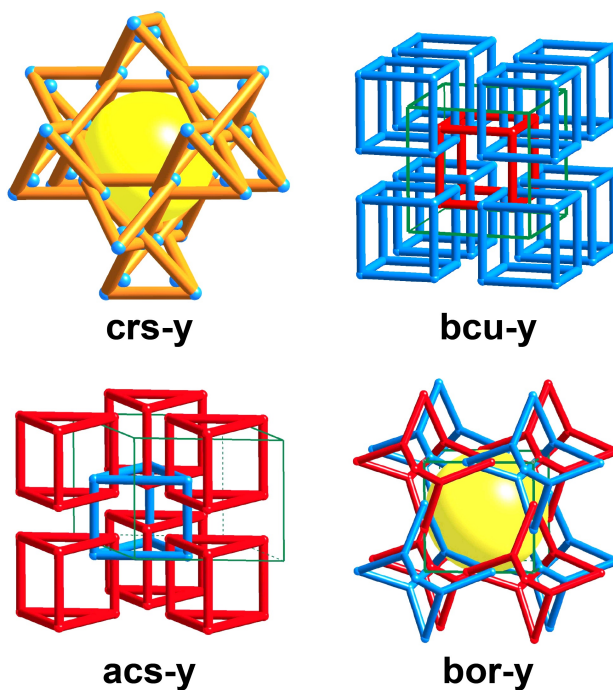
Figure 6.46. Simple examples of 3-periodic 'chainmail' formed by linking polyhedra into 3-periodic frameworks.

crs-y (linked tetrahedra) and **bcu-y** (linked cubes) are the only ones with one kind of edge and one kind of vertex. **acs-y** has two kinds of stick (edge). **bor-y** is derived from the boracite net (**bor**) and can be considered as linked adamantane units with 2-c and 3-c vertices. It is included as it forms the basis for a rare example of a crystal structure based on 3-periodic chainmail.[49]

6.4.6 Mixed threads and rings

Shown in this section are some examples of structures with interwoven threads and rings (Figure 6.47). They all have the minimal possible transitivity (2 2 2) and, as in earlier examples of dinemal weavings, one kind of link point. Symbols are **abc-wy** for structures derived from **abc**.
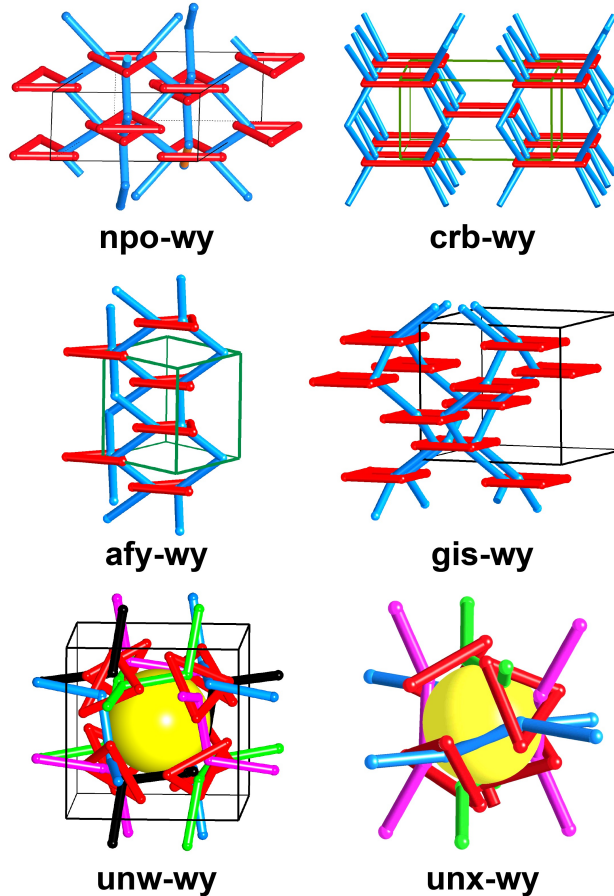

Figure 6.47. Examples of interwoven combinations of threads and rings with transitivity 2 2 2. Those with parallel threads and parallel rings are: **npo-wy** triangles and zigzags; **crb-wy** squares and zigzags; **afw-wy** triangles and 3_1 (or 3_2) helices; **gis-wy** squares and 4_1 and 4_3 helices.

In addition, **unw-wy** is formed from triangles and 3_1 (or 3_2) helices. The helix axes are in the Ω rod packing as in **sod-w** but now linked with triangles as shown in the figure. Finally, **unx-wy** has again triangles in four orientations (parallel to <111>) but now the threads are 4_1 (or 4_3) helices. The structure is hard to illustrate but can be appreciated by the observation that the yellow ball in the figure is part of a **dia** (diamond) array of such balls.

Table 6.10. Geometric data for 3-periodic thread plus ring weavings with transitivity 2 2 2. The vertex in the 'stick' column is linked to the one in the 'corner' column.

Symbol	Symmetry	Corner	Stick
npo-wy	$P6_5/mmc$	0.47, 0.53, ¼	0, 0.53, ¼
		0.41, 0.82, ¼	0.59, 1.18, ¾
crb-wy	$I4/mmm$	0.72, 0.28, ½	0.72, 0.72, ½
		0.17, 0.17, 0	0.33, 0.33, ½
afw-wy	$R32$	0.125, 0, 0	0.542, 0.208, ⅓
		⅓, 0.6, ⅓	0.4, 0.067, ⅓
gis-wy	$I4_1/amd$	0.1, 0.35, ⅞	0.4, 0.35, ⅝
		0.1, 0.45, ⅞	0.2, 0.05, ⅞
unw-wy	$I432$	¼, 0.19, 0.31	0.19, ¼, 0.61
		¼, 0.08, 0.42	0.08, 0.42, ¼
unx-wy	$I4_132$	0.125, 0, ¼	¼, 0.125, 0
		⅛, 0.06, 0.19	⅜, 0.06, 0.31

6.5 References

(1)   Knot Atlas http://katlas.org/wiki/Main_Page.

(2)   Adams, C. C. *The Knot Book*; American Mathematical Soc., 1994.

(3)   Gibson, H. W.; Bheda, M. C.; Engen, P. T. *Prog. Polym. Sci.* **1994**, *19*, 843.

(4)   Niu, Z.; Gibson, H. W. *Chem. Rev.* **2009**, *109*, 6024.

(5)   Yaghi, O. M.; M, O. K.; Ockwig, N. W.; Chae, H. K.; Eddaoudi, M.; Kim, J. *Nature* **2003**, *423*, 705.

(6)   Furukawa, H.; Cordova, K. E.; O'Keeffe, M.; Yaghi, O. M. *Science* **2010**, *9*, 1230444.

(7)   Diercks, C. S.; Yaghi, O. M. *Science* **2017**, *355*, eaal1585.

(8)   O'Keeffe, M. *Acta Crystallogr. Sect. A Found. Crystallogr.* **2008**, *64*, 425.

(9)   O'Keeffe, M.; Peskov, M. A.; Ramsden, S. J.; Yaghi, O. M. *Acc. Chem. Res.* **2008**, *41*, 1782.

(10)   Li, M.; Li, D.; O'Keeffe, M.; Yaghi, O. M. *Chemical Reviews*. 2014, 1343.

(11)   Delgado Friedrichs, O.; O'Keeffe, M.; Yaghi, O. M. *Acta Crystallogr. Sect. A Found. Crystallogr.* **2003**, *59*, 22.

(12)   Delgado-Friedrichs, O.; O'Keeffe, M. *Acta Crystallogr. A* **2003**, *59*, 351.

(13)   Kopský, V.; Litvin, D. B. *International Tables for Crystallography, Volume E: Subperiodic Groups*; International Tables for Crystallography; International Union of Crystallography: Chester, England, 2006; Vol. E.

(14)   Grunbaum, B.; Shephard, G. C. *Am. Math. Mon.* **1988**, *95*, 5.

(15)   Dietrich-Buchecker, C. O.; Sauvage, J. -P. *Angew. Chem. Int. Ed.* **1989**, *28*, 189.

(16)   Nierengarten, J. F.; Dietrich-Buchecker, C. O.; Sauvage, J. P. *J. Am. Chem. Soc.* **1994**, *116*, 375.

(17)   Ayme, J.-F.; Beves, J. E.; Leigh, D. A.; McBurney, R. T.; Rissanen, K.; Schultz, D. *Nat. Chem.* **2011**, *4*, 15.

(18)   Fielden, S. D. P.; Leigh, D. A.; Woltering, S. L. *Angew. Chem. Int. Ed.* **2017**, *56*, 11166.

(19)   Danon, J. J.; Krüger, A.; Leigh, D. A.; Lemonnier, J.; Stephens, A. J.; Vitorica-yrezabal, I. J.; Woltering, S. L. *Science* **2017**, *162*, 159.

(20)   Ponnuswamy, N.; Cougnon, F. B. L.; Pantoş, G. D.; Sanders, J. K. M. *J. Am. Chem. Soc.* **2014**, *136*, 8243.

(21) Dietrich-Buchecker, C.; Sauvage, J.-P. *J. Am. Chem. Soc.* **1984**, *106*, 3043.

(22) Sauvage, J.-P. *Acc. Chem. Res.* **1998**, *31*, 611.

(23) Goldup, S. M.; Leigh, D. A.; Long, T.; McGonigal, P. R.; Symes, M. D.; Wu, J. *J. Am. Chem. Soc.* **2009**, *131*, 15924.

(24) Leigh, D. A.; Pritchard, R. G.; Stephens, A. J. *Nat. Chem.* **2014**, *6*, 978.

(25) Lincheneau, C.; Jean-Denis, B.; Gunnlaugsson, T. *Chem. Commun.* **2014**, *50*, 2857.

(26) Wood, C. S.; Ronson, T. K.; Belenguer, A. M.; Holstein, J. J.; Nitschke, J. R. *Nat. Chem.* **2015**, *7*, 354.

(27) Wu, Q.; Rauscher, P. M.; Lang, X.; Wojtecki, R. J.; de Pablo, J. J.; Hore, M. J. A.; Rowan, S. J. *Science* **2017**, *358*, 1434.

(28) Chichak, K. S.; Cantrill, S. J.; Pease, A. R.; Chiu, S.-H.; Cave, G. W. V.; Atwood, J. L.; Stoddart, J. F. *Science* **2004**, *304*, 1308.

(29) Yang, G.-P.; Hou, L.; Luan, X.-J.; Wu, B.; Wang, Y.-Y. *Chem. Soc. Rev.* **2012**, *41*, 6992.

(30) Han, L.; Zhou, Y. *Inorg. Chem. Comm.* **2007**, *11*, 385.

(31) Champsaur, A. M.; Mézière, C.; Allain, M.; Paley, D. W.; Steigerwald, M. L.; Nuckolls, C.; Batail, P. *J. Am. Chem. Soc.* **2017**, *139*, 11718.

(32) Wang, Z.; Błaszczyk, A.; Fuhr, O.; Heissler, S.; Wöll, C.; Mayor, M. *Nat. Commun.* **2017**, *8*, 14442.

(33) Calcar, P. M. Van; Olmstead, M. M.; Balch, A. L. *J. Chem. Soc. Chem. Commun.* **1995**, 1773.

(34) Li, Y.-H.; Su, C.-Y.; Goforth, A. M.; Shimizu, K. D.; Gray, K. D.; Smith, M. D.; zur Loye, H.-C. *Chem. Commun.* **2003**, 14, 1630.

(35) Lewandowska, U.; Zajaczkowski, W.; Corra, S.; Tanabe, J.; Borrmann, R.; Benetti, E. M.; Stappert, S.; Watanabe, K.; Ochs, N. A. K.; Schaeublin, R.; et al. *Nat. Chem.* **2017**, *9*, 1068.

(36) LaPlantz, S. *The Mad Weave Book an Ancient Form of Triaxial Basket Weaving*; Dover Publications, 2016.

(37) Gailiunas, P. *J. Math. Arts* **2017**, *11*, 40.

(38) Zhang, J.-P.; Qi, X.-L.; He, C.-T.; Wang, Y.; Chen, X.-M. *Chem. Commun.* **2011**, *47*, 4156.

(39) Thorp-Greenwood, F. L.; Kulak, A. N.; Hardie, M. J. *Nat. Chem.* **2015**, *7*, 526.

(40) Evans, M. E.; Robins, V.; Hyde, S. T. *Acta Crystallogr. Sect. A Found. Crystallogr.* **2013**,

69, 262.

(41) Alexandrov, E. V.; Goltsev, A. V.; O'Keeffe, M.; Proserpio, D. M. *Cryst. Growth Des.* **2017**, *17*, 2941.

(42) Rosi, N. L.; Kim, J.; Eddaoudi, M.; Chen, B.; Keeffe, M. O.; Yaghi, O. M. *J. Am. Chem. Soc.* **2005**, *127*, 1504.

(43) Verhoeff, T. ; Verhoeff, K. *Proceedings of Bridges 2011: Mathematics, Music, Art, Architecture, Culture (14th Annual Conference, Coimbra, Portugal, July 2011)*; Tessellations Publishing, 2011, 1.

(44) Stasiak, A.; Katritch, V.; Kauffman, L. H. *Ideal Knots*; World Scientific, 1998; Vol. 19.

(45) Evans, M. E.; Robins, V.; Hyde, S. T. *Proc. R. Soc. A* **2015**, *471*, 20150254.

(46) Li, M.; Ye, C. R.; Huang, X. C.; O'Keeffe, M. *Struct. Chem.* **2017**, *28*, 147.

(47) Liu, Y.; Ma, Y.; Zhao, Y.; Sun, X.; Gandara, F.; Furukawa, H.; Liu, Z.; Zhu, H.; Zhu, C.; Suenaga, K.; et al. *Science* **2016**, *351*, 365.

(48) Zhao, Y.; Guo, L.; Gándara, F.; Ma, Y.; Liu, Z.; Zhu, C.; Lyu, H.; Trickett, C. A.; Kapustin, E. A.; Terasaki, O.; et al. *J. Am. Chem. Soc.* **2017**, *139*, 13166.

(49) Kuang, X. F.; Wu, X. Y.; Yu, R. M.; Donahue, J. P.; Huang, J. S.; Lu, C. Z. *Nat. Chem.* **2010**, *2*, 461.

(50) El-Kaderi, H. M.; Hunt, J. R.; Mendoza-Cortés, J. L.; Côté, A. P.; Taylor, R. E.; O'Keeffe, M.; Yaghi, O. M. *Science* **2007**, *316*, 268.
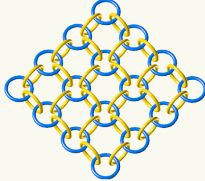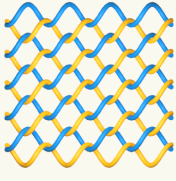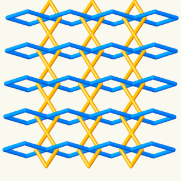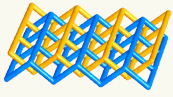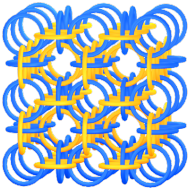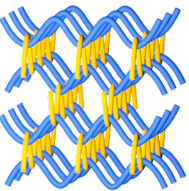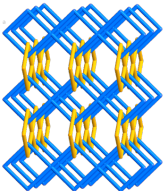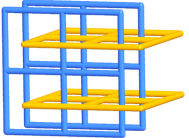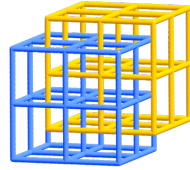
Chapter VII

Future Prospects of Woven Materials

Distinct modes of entanglements can be expected in the chemistry of the framework. The entanglement of 2D and 3D nets into frameworks with the same dimensionality is referred to as interpenetration. Mechanically linked 1D chains are defined as weaving, and mechanical entanglement of discrete (0D) rings as polycatenation. Interlocking can be considered as a broader term and is referred to when catenated rings are present (*e.g.* interlocking of rods, Table 7.1).

Controlling the mechanical entanglement in the solid state is not only of fundamental interest; it also can lead to more flexible, dynamic materials that are important synthetic targets. It is anticipated that the dynamics of entangled materials is inversely correlated with the dimensionality of their respective constituents. In the case of 2D and 3D interpenetration, the potential for motion of the fragments with respect to each other is limited because the entire extended 3D or 2D frameworks would have to be dislocated in a synchronized manner. The formation of extended structures based on structural motifs with lower dimensions has thus been sought after, as the many degrees of freedom of their building units allow for large spatial deviations to take place without deteriorating the overall structure.

Table 7.1. Distinct modes of entanglement by structural constituents of lower or the same dimensionality in extended frameworks. From left to right: Polycatenanes refer to the entanglement of 0D rings, and the formation of mechanical bonds between 1D chains is defined as weaving. Extended structures can be achieved by interlocking of rods. The entanglement of 2D or 3D nets into structures with the same dimensionality is referred to as interpenetration.

The design principles of reticular synthesis, together with metal templation strategy towards COF synthesis can provide a powerful and general approach to access materials with these different modes of entanglement (Table 7.1). It is no coincidence that the first examples of woven COFs feature a **dia-w** topology. The synthetic route toward the structure relies on the initial formation of a framework of **dia** topology, which is only subsequently demetalated to yield the derived woven framework. Since the diamond net is the default topology for tetrahedral nets it is the most likely to form in the context of reticular synthesis. The advantage of using COFs to target woven or polycatenated extended structures is however that the directional covalent bonds and the rigid organic building blocks allow for the precise adjustment of angles and therefore for targeting of topologies other than the default nets. A target compound is chosen and the topology of the framework is determined. The crossover points in the structure can be templated with molecular building blocks that already encode this information. It must be noted that topologies do not have a symmetry *per se* and their highest symmetry embeddings are considered here. As such, these angles must not be understood as a strict necessity for the formation of the desired topologies but more as a rational guideline for their design. Exemplary we illustrate this based on the case of woven and polycatenated structures derived from the sodalite (**sod**) net, namely **sod-w**, **sod-y**, and **sod-y***. Each of them can be formed from tetrahedral metal complexes with two bidentate ligands. For the case of an angle of $\phi = 90°$ between the respective points of extension within each ligand and a dihedral angle $\varphi = 38.9°$ between the two such ligands of each complex is expected to yield a framework of **sod-w** topology. Similarly an angle of $\phi = 90°$ and $\varphi = 90°$ codes for a **sod-y** topology structure and angles of $\phi = 120°$ and $\varphi = 70.5°$ will yield a material with an underlying **sod-y*** net (Figure 7.1).

In Table 7.2, a concise list of regular woven and polycatenated nets has been compiled with the angles ϕ and ψ derived from their highest symmetry embeddings. In addition, the highest possible space groups of both are enumerated, the parent nets as well as the different possible derived nets. This list alongside the general design considerations outlined in the previous chapters will serve as a guideline for the targeted synthesis of a large variety of woven and polycatenated frameworks of different structure types.
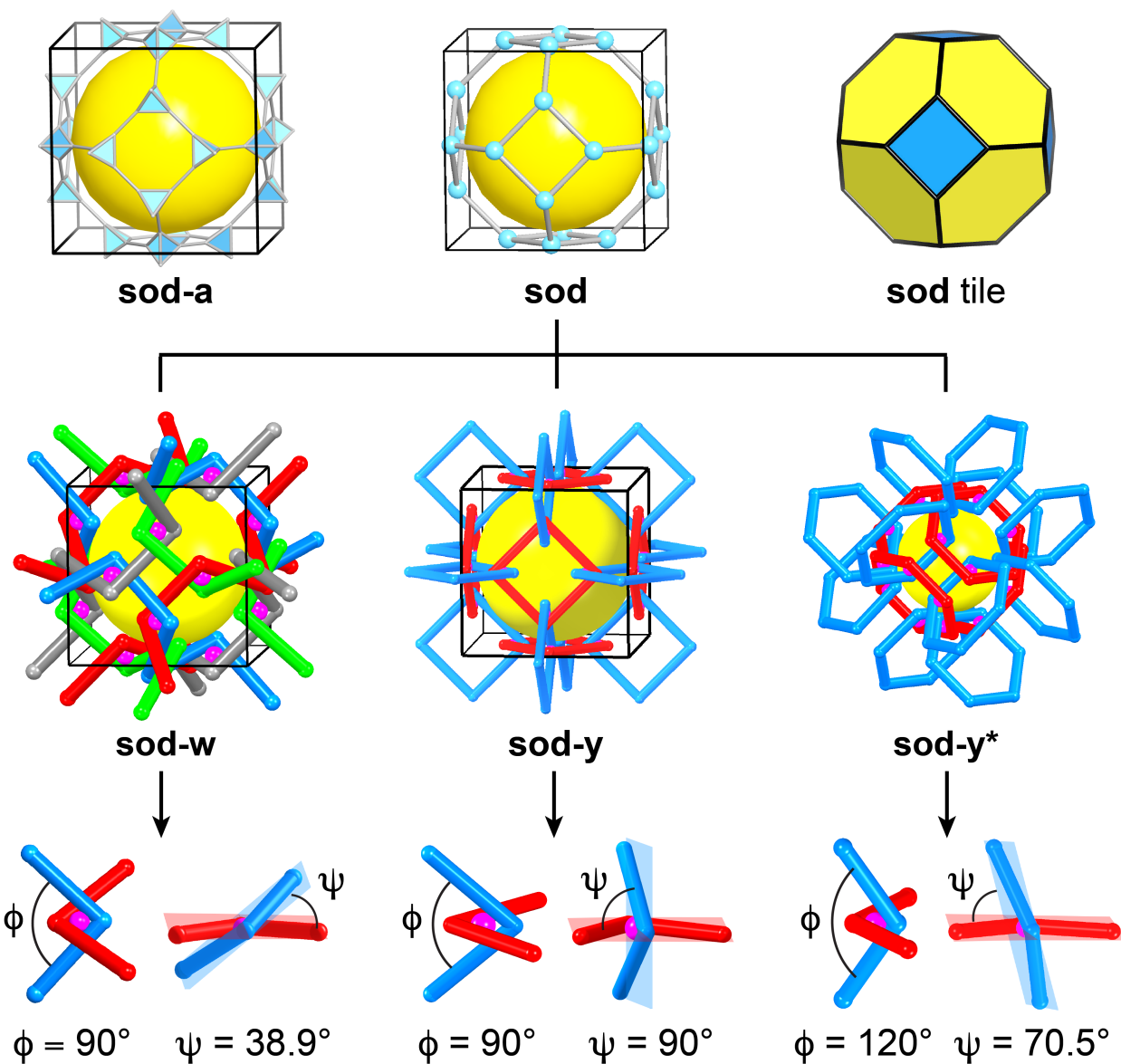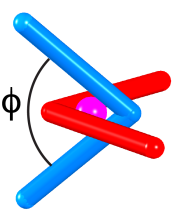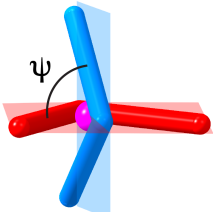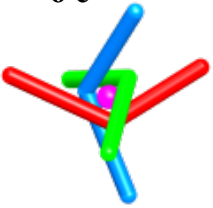
sod-a **sod** **sod** tile

sod-w **sod-y** **sod-y***

$\phi = 90°$ $\psi = 38.9°$ $\phi = 90°$ $\psi = 90°$ $\phi = 120°$ $\psi = 70.5°$

Figure 7.1. Deriving **sod** net into woven and polycatenated forms- **sod-w**, **sod-y**, **sod-y*** by converting the 4-c corners (illustrated in **sod-a**) into tetrahedral metal complexes. By selecting the exact angles between the points of extension (ϕ) and those between the dihedral planes of the ligands (ψ), the synthesis of targeted topologies can be directed.

Table 7.2. The angles in the regular (transitivity 1 1 1) 3-periodic polycatenanes (**-y**) and weavings (**-w**).

Building block	Symbol	Symmetry (parent net)	Symmetry (derived net)	Angle ϕ [°]	Angle ψ [°]
4 c	**dia-w**	$Fd\bar{3}m$	$I4_1/amd$	90.6	90
	dia-w*		$I4_122$	100.5	67.4
	qtz-w	$P6_222$	$P6_222$	88.7	50.0
	qtz-w*		$P6_222$	62.9	86.6
	qtz-w**		$P6_222$	129.0	68.5
	nbo-w	$Im\bar{3}m$	$Fd\bar{3}c$	157.8	90
	sod-w	$Im\bar{3}m$	$I432$	90	38.9
	sod-y		$Im\bar{3}m$	90	90
	sod-y*		$Im\bar{3}m$	120	70.5
	lcs-w	$Ia\bar{3}d$	$Ia\bar{3}d$	109.5	90
	lcv-w		$Pn\bar{3}m$	120.0	22.8
	lcv-w*	$I4_132$	$I4_132$	114.7	10.4
	lcv-y		$I4_132$	60	70.5
	ana-y	$Ia\bar{3}d$	$Ia\bar{3}d$	78.8	72.1
	ana-y*		$Ia\bar{3}d$	109.9	54.4
6 c	**lcy-w**	$P4_132$	$P4_132$	110.0	72.9
	lcy-w*		$P4_132$	70.5	60
	acs-w	$P6_3/mmc$	$P6_322$	127.6	78.1
	crs-w	$Fd\bar{3}m$	$F4_132$	135.5	62.9
	pcu-w	$Pm\bar{3}m$	$I432$	121.0	60
	pcu-y		$Pm\bar{3}n$	90	90